Die approbierte Originalversion dieser Dissertation ist an der Hauptbibliothek der Technischen Universität Wien aufgestellt (http://www.ub.tuwien.ac.at).

The approved original version of this thesis is available at the main library of the Vienna University of Technology (http://www.ub.tuwien.ac.at/englweb/).

DISSERTATION

Contributions to an Efficient Numerical Analysis of the Plastic Collapse Behaviour of Thin-Walled Structures

ausgeführt zum Zwecke der Erlangung des akademischen Grades eines
Doktors der technischen Wissenschaften unter der Leitung von

o.Univ.Prof. Dipl.-Ing. Dr.techn. Franz G. Rammerstorfer
E317
Institut für Leichtbau und Flugzeugbau

eingereicht an der Technischen Universität Wien
Fakultät für Maschinenbau

von

Dipl.-Ing. Markus SEITZBERGER
Matr.Nr.: 8406833
Steinbachmauer 10
A-3345 Göstling/Ybbs

Wien, im September 1999 *Markus Seitzberger*

Kurzfassung

Ziel der vorliegenden Arbeit ist es, Beiträge für eine numerisch effiziente Simulation des Kollapsverhaltens dünnwandiger Strukturen zu liefern. Dazu wird zunächst ein Überblick über die Literatur zu dieser Thematik gegeben. Anschließend werden die theoretischen Grundlagen für die vorgeschlagenen Simulationsalgorithmen dargelegt. Dabei wird, neben einer Einführung in die Grundlagen der Kontinuumsmechanik bei großen Deformationen und einer Darstellung plastischer Extremalprinzipien, besonderes Augenmerk auf die Herleitung und Beschreibung der exakten Ilyushin Fließfläche gelegt. Diese auf der von Mises Fließbedingung basierende Fließfläche beschreibt den Grenzzustand einer voll durchplastizierten Platte/Schale bei ideal-plastischem Materialverhalten in Abhängigkeit von spannungs- bzw. verzerrungsbezogenen resultierenden Größen und erlaubt, insbesondere in Verbindung mit kinematisch-orientierten Berechnungsmethoden der Plastizitätstheorie (z.B. Markov Theorem oder oberer Traglastsatz), eine sehr genaue und effiziente Berechnung der inneren Energiedissipation. Die exakte Ilyushin Fließfläche stellt daher einen wesentlichen Bestandteil für die in dieser Arbeit vorgeschlagenen Simulationsalgorithmen dar.

Um einen Einblick in das Kollapsverhalten dünnwandiger Strukturen zu geben, werden anschließend Ergebnisse von experimentellen Untersuchungen präsentiert sowie in der Literatur vorgeschlagene semi-analytische Kollapsmechanismen für das quasistatische progressive Beulen von dünnwandigen kreisförmigen und prismatischen Profilen unter axialer Druckbeanspruchung analysiert. Aufbauend auf diesen Untersuchungen wird im folgenden ein Computerprogramm zur vereinfachten numerischen Simulation des Kollapsverhaltens axialsymmetrischer Strukturen entwickelt und programmtechnisch umgesetzt. Der definierte Algorithmus basiert auf dem oberen Traglastsatz der Plastizitätstheorie, wobei die aktuelle Traglast für einen augenblicklichen Verformungszustand als Lösung eines Optimierungsproblems gefunden wird. Ein gesamter Kollapsprozeß kann dabei als Folge solcher Optimierungsprobleme simuliert werden ("sequential limit analysis method"). Die

kinematische Beschreibung, der eine Diskretisierung in Teilbereiche ("Finite Elemente") zugrunde liegt, erlaubt sowohl das Auftreten kontinuierlicher als auch diskontinuierlicher plastischer Deformationen ("Fließgelenkslinien"). Bezüglich des Materialverhaltens wird die exakte Form der Ilyushin-Fließfläche verwendet, in deren Rahmen eine sehr genaue Berechnung der inneren Energiedissipation ermöglicht wird. Es wird weiters gezeigt, daß mit der vorgeschlagenen Methodik innerer Kontakt auf einfache und numerisch effiziente Weise berücksichtigt werden kann. Anhand mehrerer Beispiele wird die Allgemeinheit der Methode, aber auch deren Eignung für vereinfachte Kollapsanalysen, bestätigt.

Zur numerisch effizienten Kollaps- und Traglastanalyse von Schalenstrukturen mit Hilfe der Methode der Finiten Elemente wird anschließend ein Schalen-Plastizitätsalgorithmus, basierend auf der exakten Ilyushin Fließbedingung, untersucht. Hauptprobleme dabei ergeben sich v.a. aufgrund der speziellen Darstellungsform der Fließfläche, die keine Anwendung von Standardalgorithmen ermöglicht, sowie numerisch sehr sensibler Bestimmungsgleichungen. Lösungsmöglichkeiten für eine numerisch stabile und effiziente algorithmische Umsetzung werden vorgeschlagen, und dabei auftretende Probleme werden diskutiert. Die erzielten Ergebnisse bestätigen, daß der vorgeschlagene implizite Plastizitätsalgorithmus für einen praktischen Einsatz in FE-Strukturanalysen prinzipiell geeignet ist und bei geeigneter Implementierung des Materialgesetzes auch tatsächlich Rechenzeitvorteile gegenüber einer numerischen Dickenintegration zu erwarten sind.

Abstract

The subject of the work is to provide contributions towards an efficient numerical analysis of the plastic collapse process of thin-walled structures. Starting from a survey on the state of research the theoretical foundations underlying the proposed algorithms are summarized. Here, besides large deformation continuum mechanics and plastic extremum and bounding principles, special emphasis is put on the derivation and description of the exact Ilyushin yield criterion, providing an important ingredient for the proposed algorithms. This plastic limit yield criterion (which is based on perfectly plastic material behaviour obeying the von Mises yield condition) provides a number of advantageous features, rendering the definition of both accurate and numerically efficient simulation tools for plastic collapse analysis of slender beams, thin plates and shells possible. Furthermore, due to the assumptions underlying the derivation of the yield surface it is fully consistent with plastic extremum and bounding principles, where it may in particular be utilized in combination with kinematics-oriented theorems, e.g. the Markov theorem or the upper bound theorem of limit analysis.

To gain more insight into the principles of the crushing phenomenon in a next step experimental results are presented and simplified analytically based collapse mechanisms proposed in the literature, which describe the quasistatic progressive buckling process of circular and multicornered prismatic profiles, are investigated in some detail. As a generalization of these simplified tools a computational model based on the upper bound theorem of limit analysis ("sequential limit analysis method") in combination with a finite element discretization is presented afterwards, which allows to study the large deformation crushing behaviour of general axisymmetric shell structures. The kinematic description is chosen such that both continuous and discontinuous plastic deformations can be considered. The large deformation process is described in an incremental manner, where each increment is solved by mathematical programming techniques. Within the framework of the application of the exact Ilyushin yield surface the power of internal forces can be taken into account very accurately. It is also shown that frictionless internal contact can be accounted for easily in the algorithm developed in this thesis. Several examples confirming the generality and suitability of this novel method for simplified plastic collapse analysis are included, too.

For conventional finite element based collapse and limit load analyses of shell structures a “full section material model”, which is based on the exact Ilyushin yield criterion, is investigated afterwards. Many features considered as being essential for the definition of both a numerically stable and a computationally efficient formulation are proposed and the main difficulties concerned with the implementation are discussed. This not only includes the reformulation of standard plasticity algorithms (being required, because the exact Ilyushin yield criterion may only be stated in parametric form), but also an appropriate definition and choice of internal parameters used for the local stress update. The test examples confirm that the proposed full section material routine is in principle applicable for general finite element analyses and even has the potential of speeding up FE based limit and collapse analyses.

Acknowledgments

This work was carried out in the course of my employment at the Institute of Lightweight Structures and Aerospace Engineering (ILFB) at the Vienna University of Technology. I am deeply indebted to my thesis advisor, Prof. Dr. F.G. Rammerstorfer, head of the above Institute, who encouraged me to work in this field. In particular, I want to express my gratitude for his invaluable assistance in preparing the thesis, but also for his patience and motivating support each time I had to overcome a “dry patch”, all being decisive for the completion of the work.

I also want to thank Prof. Dr. H. Troger from the Institute of Mechanics for acting as coadvisor for this thesis.

The financial support of the work by the Austrian “Fonds zur Förderung der wissenschaftlichen Forschung (FWF)”, contract number P12092-MAT, is gratefully acknowledged. This support has been substantial in allowing me the unhindered completion of the thesis. Further thanks go to the Institute for Testing and Research in Materials Technology (TVFA), Vienna University of Technology, for the provision of their test facilities. The preparatory and additional work on the topic done by Dipl.-Ing. S. Wintschnig and Dipl.-Ing. S. Willminger within their diploma theses at the ILFB is also gratefully acknowledged.

Additionally, I would like to express my thanks to Prof. Dr. H.J. Böhm, especially for his critical review of the present text, and to the system administrator of the ILFB, Ing. G. Schneider, due to whose efforts an optimal working environment at the Institute is being provided as a matter of course.

Last but not least, special thanks go to all the former and current colleagues at the ILFB (the “ILFB-gang”) for many valuable discussions and for making my work at the “Institut für Leichtbau und Flugzeugbau” an inspiring and interesting experience.

Contents

1 **Introduction** **1**

1.1 A Brief Overview on Vehicle Crashworthiness 2

1.1.1 Some Principles of a Crashworthy Vehicle Design 3

1.2 Objectives of the Work 7

2 **Literature Overview** **9**

2.1 Experimental Methods 10

2.2 Numerical Methods 12

2.3 Analytically Based Methods 16

2.4 Summary 20

3 **Theory** **22**

3.1 Notation 22

3.2 Some Basic Principles of Continuum Mechanics 23

3.2.1 Deformation, Rate of Deformation and Strain Increment 23

3.2.2 Equilibrium Statements 25

3.2.3 Work Conjugacy 28

3.2.4 The Additive Strain Rate Decomposition 29

3.3 Plastic Extremum and Bounding Principles 30

3.3.1 Principle of Maximum Plastic Dissipation 31

3.3.2 Kinematic Extremum and Bounding Theorems 32

3.4 Exact Ilyushin Yield Surface 36
3.4.1 Definitions 36
3.4.2 Derivation 37
3.4.3 Three-Dimensional Representations 39
3.4.4 Normality Rule 45
3.4.5 Power of Internal Forces 46

4 Experiments **48**
4.1 Experimental Setup 48
4.2 Test Results 50

5 Folding Mechanisms **56**
5.1 General Formulation 56
5.2 Axisymmetric Crushing of Circular Tubes 59
5.2.1 Model of Alexander 59
5.2.2 Refined Single Active Fold Models 62
5.2.3 Two Active Folds Model of Wierzbicki et al. 70
5.3 Axial Crushing of Multicorner Columns 73
5.4 Conclusions 77

6 Sequential Limit Analysis Method **80**
6.1 Fundamentals 81
6.1.1 Upper Bound Theorem 81
6.1.2 Large Deformation Analysis 82
6.1.3 Internal Energy Dissipation 83
6.2 Sequential Limit Analysis of Axisymmetric Shells 85
6.2.1 Kinematic Description 85
6.2.2 Internal Energy Dissipation 91

6.2.3 Consideration of Contact 93
6.2.4 Outline of the Solution Procedure 98
6.2.5 Examples 101
6.3 Summary, Conclusions 112

7 A Stress Resultant Constitutive Law 115
7.1 Introduction 116
7.2 Algorithmic Structure 117
7.2.1 Description of the Plastic Corrector Step 119
7.2.2 Determination of the Tangential Stiffness Matrix 134
7.3 Examples 138
7.3.1 Single Element Tests 139
7.3.2 Uniformly Loaded, Simply Supported Plate 140
7.3.3 Axial Crushing of a Square Tube 144
7.4 Summary, Concluding Remarks 150

8 Summary and Conclusions 152

Appendices 154

A Folding Mechanisms — Details 155
A.1 Axial Crushing of Multicorner Columns 155

B Exact Ilyushin Yield Surface — Details 159
B.1 Normalized Shell Quantities 159
B.2 Algorithmic Details 162
B.3 Continuum Tangential Stiffness Matrix 166

Bibliography 169

Chapter 1

Introduction

The study of the energy absorption and crashworthiness behaviour of structures and structural components has received considerable attention in recent years. This field is of particular interest for the design of all kinds of vehicles (cars, buses, trains, aircraft, ships, etc.) for transport of both passengers and goods, but also for the design of devices which have to withstand collisions with moving objects (e.g. offshore structures) and for a wide range of safety components. Continuing progress towards the optimization of engineering structures, leading to lighter components and vehicles (driven, among others, by environmental issues), again increases the importance of crashworthy designs, and the requirement to estimate the actual failure loads of various systems. Thus it is likely that the field of structural crashworthiness, and its numerical simulation in particular, will continue to grow in the future.

Motivated by these facts, the present work mainly aims at providing contributions to a simplified numerical analysis of crush elements (forming an essential part in many energy absorption devices), which are intended to assist the future development of reliable, yet weight efficient crashworthy structures. Before the main objectives of the work are presented in detail, however, a brief overview on structural vehicle crashworthiness for cars, trains and aircraft as well as certain considerations for a crashworthy vehicle design are given.

1.1 A Brief Overview on Vehicle Crashworthiness

In the automotive field systematic crash safety research started in the early 1950's and crash protection has meanwhile become a well established car design requirement. Mainly driven by consumer pressure and legislation, a crashworthy automotive structure in combination with active and passive crash safety systems is substantial for the today's vehicle design process. Full scale tests prescribed by law (e.g. frontal and side impact tests), which typically are performed with impact velocities ranging from 4 to 50-55 km/h, have to validate the effectiveness of occupant protection, but must also ensure some functionality of the vehicle structural components (e.g. the fuel system must remain sealed, doors should still to be opened, etc.). In the last years crashworthiness also has become a strong marketing argument and automotive industry, consumer consulting services and trade journals have defined and are performing additional testing to provide consumers with further information with respect to the impact performance of cars [Anselm, 1997; Seiffert, 1997].

Over the last decade the subjects of passive safety and the crashworthy characteristics of structural components have also become issues of growing importance for the railway industry. Administrations and railway research institutes are currently active in defining relevant recommendations and standards, and in many countries requirements are already mandatory for the crashworthy design of new rail vehicles (see e.g. [Lewis, 1998]). An analysis of "structurally significant" railway accidents reveals that most fatalities and serious injuries of occupants occur as a result of end-on collisions, where the collision speeds are generally less than 60 km/h, often accompanied by overriding of the coach bodies [Lewis, 1994]. Consequently, the most effective means of reducing passenger and crew casualties in railway accidents is to concentrate on the design of crashworthy vehicle body ends and to avoid overriding, which is also reflected in the mandatories. For example, the current design requirements for new rail vehicles in the UK, set out in the *Railway Group Standard GM/RT 2100* [GMRT2100, 1997] stipulate that, before any deformation of the main body takes place, a minimum of 1 MJ must be absorbed by the end section over a maximum collapse distance of 1 m. The impact force must not exceed a certain limit (3000 kN) in order to keep the maximal deceleration forces sufficiently low and thus to avoid fatalities for the passengers [Kirk et al., 1998].

Particular emphasis with respect to passive safety of rail vehicles has to be put on high speed trains, which have become more and more popular in recent years (TGV, ICE, Shinkansen, etc.). Although high speed rail is accepted to be one of the safest forms of transport (such types of trains use modern equipment and the design already includes advanced safety concepts, see e.g. [Cléon, 1993]), their high cruising speeds (typically more than 200–250 km/h) are mainly responsible for the fact that even minor defects may end in fatal accidents. This was unfortunately proven to be true in summer 1998 in Germany, where more than 100 people lost their lives, when an ICE high speed train traveling at a speed of about 200 km/h was derailed and struck a road overbridge.

Crashworthiness is also a topic of increasing interest in aeronautics. Experience with crashes of small aircraft (light fixed-wing general aviation aircraft, small passenger airplanes, helicopters, etc.) shows that there are a number of accidents that could possibly be survived by the passengers if certain sources of danger were eliminated. Besides excessively high deceleration peak loads such events are e.g. fire, collapse of the cabin structure or collision of hard protruding objects with occupants bodies [Bisagni, 1998]. However, there is the problem that small aircraft, especially with retracted landing gear, in general have little crushable airframe structure. Therefore, besides designing crashworthy fuel systems, passenger cabins, energy absorbing landing gears, etc., particular emphasis must be put on the design of crashworthy subfloor systems. The structural collapse of the subfloor structure shall allow for a controlled energy dissipation and also limit the vertical loads to human tolerance levels for potentially survivable accidents [Kindervater and Georgi, 1993; Bisagni, 1998]. With respect to the definition of standards first structural design requirements for better crash protection of aircraft were established for military helicopters and light fixed-wing aircraft in the form of the *MIL-STD-1290 A* [MilStd1290, 1988] and the *Aircraft Crash Survival Design Guide* [Desjardins et al., 1989]. For all other aircraft categories further progress can be expected in the future to improve the requirements for structural crash resistance [Kindervater et al., 1998].

1.1.1 Some Principles of a Crashworthy Vehicle Design

The main goals of a crashworthy structural design are to limit vehicle deformation to areas where there are no passengers, and to absorb the kinetic energy of the collision in these regions in a controlled way. In practice, very often a modular design concept is adopted, which has to ensure that, depending on the impact velocity and the kinetic energies, respectively, different parts of these energy absorption devices are activated. In Figure 1.1 the optimal overall impact force versus deformation characteristics for a rail vehicle during a frontal collision is sketched, which reflects this necessity for a modular crash design concept of the vehicle body ends. At the beginning (and for small impact forces, respectively) energy should be dissipated mainly by buffers and couplers without

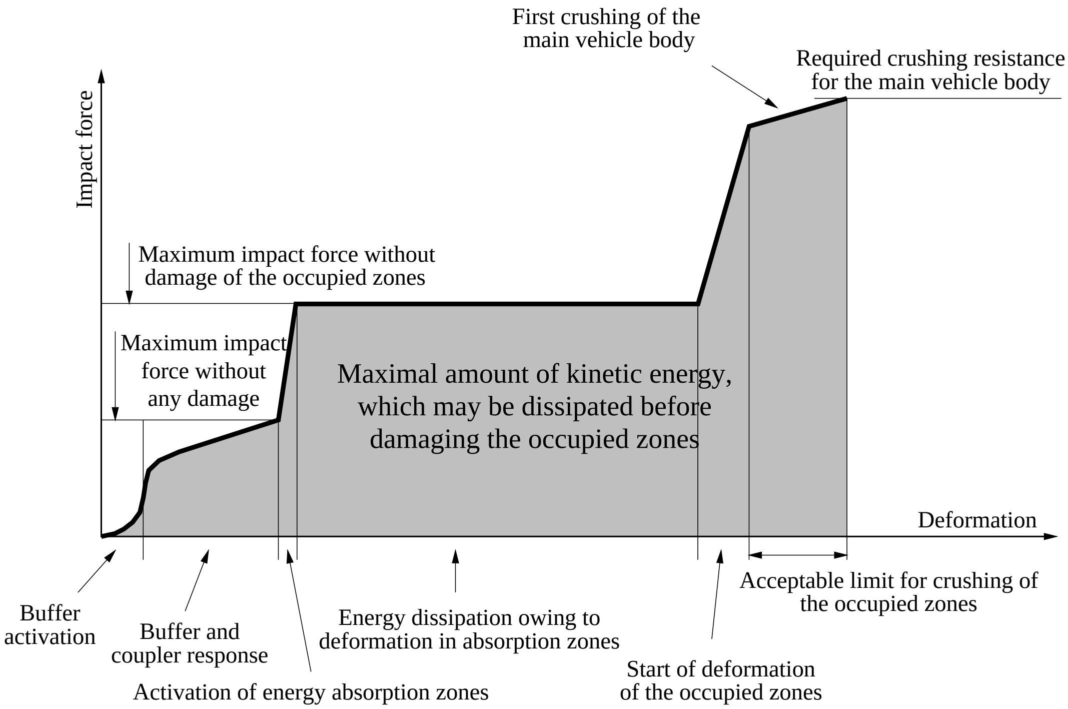
First crushing of the main vehicle body
Required crushing resistance for the main vehicle body
Impact force
Maximum impact force without damage of the occupied zones
Maximum impact force without any damage
Maximal amount of kinetic energy, which may be dissipated before damaging the occupied zones
Deformation
Buffer activation
Buffer and coupler response
Activation of energy absorption zones
Energy dissipation owing to deformation in absorption zones
Start of deformation of the occupied zones
Acceptable limit for crushing of the occupied zones

Figure 1.1: Optimal impact force versus deformation characteristics for a rail vehicle (from [Cléon and Lagneau, 1993])

any damage to the vehicle structure. Larger kinetic energies are to be dissipated in energy absorption zones, ideally having a constant force level over a wide range of deformations. In order to efficiently protect the part of the rail coach which is occupied by passengers, the required crushing resistance of the main vehicle body must markedly exceed the crushing force level of the energy absorption zones [Cléon and Lagneau, 1993].

In a similar manner, Anselm [1997] points out recommendations for the design of the optimal energy dissipation management for a modern car structure with respect to a frontal impact against a rigid wall:

- between 0–8 km/h collision speed the whole energy should be absorbed in a reversible way (e.g. by applying hydraulic, pneumatic or elastomeric systems) without causing any damage of the car structure,
- from 8–12 km/h the kinetic energy should be dissipated in plastically deforming energy absorption elements, which are easily exchangeable,
- between 12–15 km/h the capacity of the energy absorption elements will in general

be exhausted and the frontal part of the side members will also start to deform,

- above 15 km/h the whole side members of the frontal chassis will deform plastically.

Whereas the first three requirements rather come from demands of an easy and inexpensive repair of the car structure, the energy absorption and deformation characteristics of the frontal side members are essential for an effective occupant protection at higher collision speeds. A crashworthy design of these primary structural parts (they also have to carry the motor, etc.) ensures that a large amount of energy is dissipated by controlled plastic deformations in the frontal area of the vehicle. In order to ensure such a controlled deformation behaviour, however, the individual parts of the frontal chassis are in general composed of thin-walled structures (open and closed sectioned tubular members, etc.), where plastic collapsing (postbuckling, crushing) leads to efficient energy dissipation in well defined, localized regions.

As an example (where the above mentioned collapse speed limits are already exceeded), Figure 1.2 shows the all-aluminium space frame of the Audi A8. The frontal chassis is arranged such that up to 8 km/h collision speed a front bumper with impact absorber dissipates the kinetic energy without damaging any structural parts. Up to 20 km/h the energy is dissipated by plastic buckling of a tubular crush element. Permanent deformations of the frontal side member (essentially having a hexagonal cross-section) occur after a collision speed of 20 km/h [Paefgen et al., 1994]). Even higher critical collision speeds are reported for the frontal chassis of the BMW 850i, where specifically designed frontal side members with octagonal cross-sections are stated to be able to suffer collapse speeds of up to 30 km/h without essentially damaging the frontal area of the car [Haberl and Eichinger, 1990].

The practical design of the energy absorption zones at the front and rear ends of the engine of the french TGV 2N high speed train is shown in Figure 1.3. These crash zones (and also the energy absorption zones at the front and rear ends of the passenger car set) are also composed to a great extent of thin-walled tubular structures. During frontal crashes these components are to absorb the essential part of the kinetic energy by plastic buckling in an efficient, yet controlled way, before the region occupied by passengers is affected.

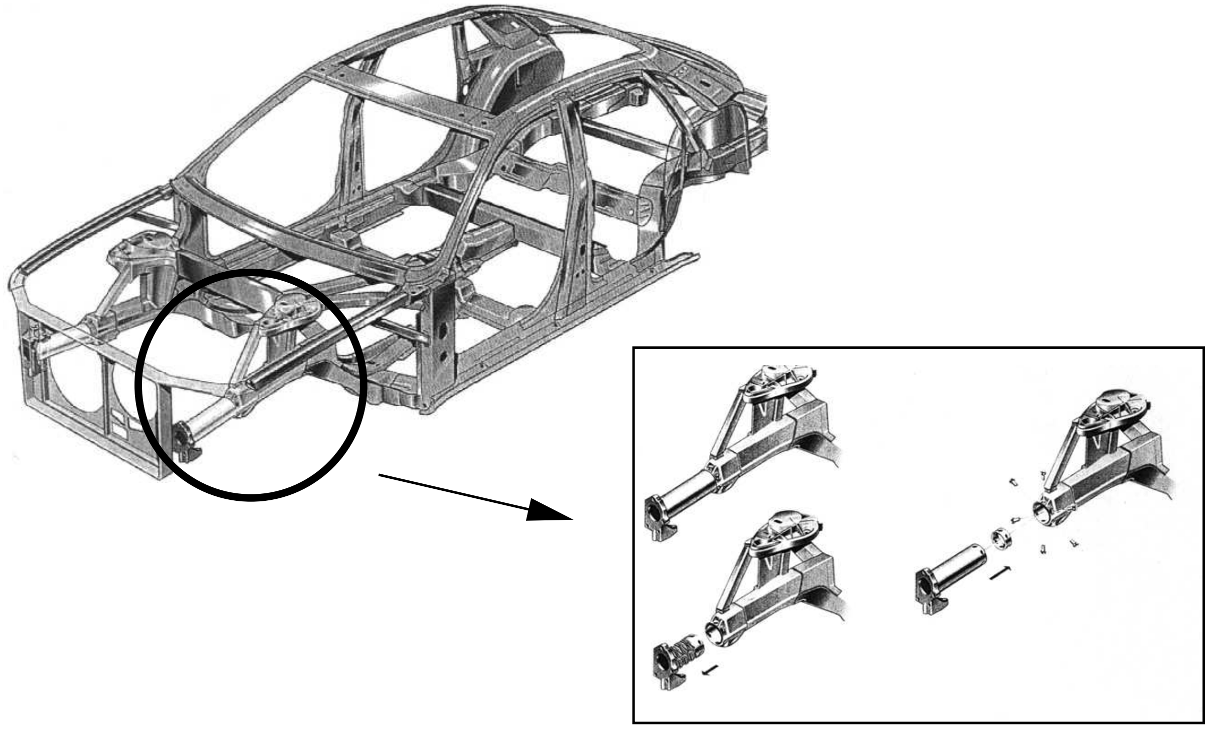

Figure 1.2: Audi A8: aluminium chassis (space frame concept) and repair of front chassis member after 15 km/h frontal impact (from [Paefgen et al., 1994])

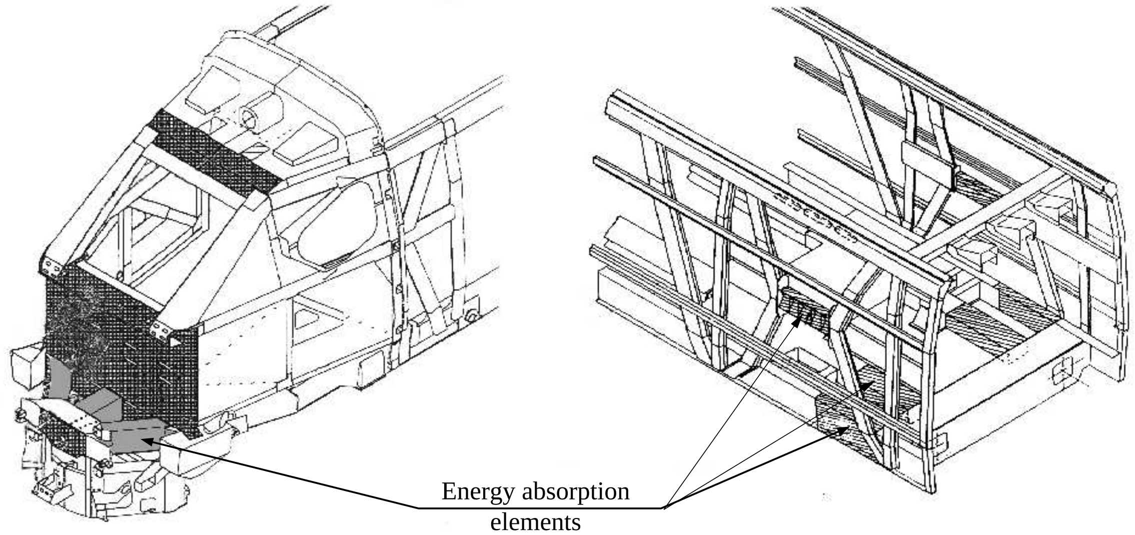

Figure 1.3: TGV 2N: energy absorption zones at the frontal and rear ends of the locomotive (from [Cléon, 1993])

1.2 Objectives of the Work

The present work aims at providing contributions to an efficient (i.e. simplified, but still sufficiently accurate) numerical analysis of the collapse process of thin-walled structures. Starting from a survey on the state of research (chapter 2) the theoretical foundations are summarized in chapter 3. To gain more insight into the principles of the crushing phenomenon in a next step experimental results are presented (chapter 4) and simplified analytically based collapse mechanisms proposed in the literature, which describe the quasistatic progressive buckling process of circular and multicornered prismatic profiles, are investigated (chapter 5). Comparisons with experiments and FE computations show that the ability of such mechanisms to describe the force-deflection characteristics of the whole deformation process is rather limited, even if the underlying kinematics seem to be well suited for the description of actual crushing processes. When the requirement for obtaining analytical solutions is dropped, several refinements and generalizations are possible. These essentially include:

- a refined description of the constitutive behaviour by application of a general stress resultant yield surface instead of simplified yield conditions (in the present work the Ilyushin yield surface, which is exact for rigid-perfectly plastic material behaviour, is applied),
- a more generalized kinematic description of the deformation mechanisms (e.g. an “FE-like” discretization of the geometry and the deformation field, respectively).

Starting from these considerations a “sequential limit analysis method” is presented in chapter 6 for the axisymmetric collapse analysis of general axisymmetric shells. Herein the large deformation process is described in an incremental manner, where each increment is solved by mathematical programming techniques. Due to the application of the exact Ilyushin yield surface the power of internal forces can be taken into account very accurately. It is also shown that with the proposed method frictionless internal contact can be accounted for easily. Furthermore, most of the analytically based kinematic mechanisms proposed in the literature for the concertina mode buckling of cylindrical shells can be regarded as special cases, thus allowing to study the effects of different simplifications used in these models.

In order to study the principal phenomena and to keep the kinematic description as simple as possible, the refinements and derivations are restricted to axisymmetric shells.

The description of the exact Ilyushin yield surface (chapter 3), however, is given for general shell geometries and it is worth studying if this yield criterion could also be used advantageously for the definition of a material law for FE-shell elements. Besides the fact that such a stress resultant constitutive model is interesting from the theoretical point of view, its application in FE-based collapse and limit load analyses could eventually speed up the FE calculations (because no numerical thickness integration must be performed), while retaining the necessary accuracy for these types of problems. This topic is investigated in some detail in chapter 7.

Conclusions are finally summarized in chapter 8.

Chapter 2

Literature Overview

In the past, certain types of crush elements have been developed which dissipate energy in a variety of ways, e.g. by friction, fracture, plastic bending or torsion, crushing, cyclic plastic deformation, metal cutting, etc. However, as was already pointed out in the introduction, the elastoplastic buckling and postbuckling behaviour of thin-walled structures (collapse, crushing) may in particular be utilized to define efficient and versatile energy absorption devices. Thin-walled structures (and axially compressed tubular members in particular) are capable of carrying substantial loads for deflections far beyond those corresponding to ultimate or buckling loads. These large deflections can be accommodated through the formation of deformation mechanisms that concentrate the energy dissipation in relatively narrow zones, while the remainder of the structure is almost unaffected from plastic strains. Due to this advantageous plastic postbuckling behaviour such types of structures meet several requirements of an optimal energy absorption device:

- the crushing loads do not exceed certain limits over a long crushing distance (e.g. for axially compressed, progressively buckling tubes the forces fluctuate around more or less constant values),
- the stroke lengths, i.e. the maximal distances that may be utilized for energy dissipation, may reach markedly high values (e.g. up to 80% of the original length may be used for the progressive buckling of axially compressed cylindrical shells),
- deformations are localized in well defined regions (the locations may additionally be triggered by a proper design of the crush elements),
- thin-walled structures made of conventional materials (steel, aluminium, etc.) are

inexpensive and versatile and, for many applications, they may also be designed to carry operational loads,

- thin-walled structures are weight efficient, thus fulfilling demands for a lightweight vehicle design for both operational and crash loading conditions.

In the following, a survey on the state of research is given on methods and solution techniques, used for studying the deep plastic collapse behaviour of thin-walled structures. In addition, special attention is focused on methods which have the potential (but are not applied up to now) to set up some basis for the future development of numerically efficient simulation tools for crashworthiness calculations. The overview, which is essentially restricted to metallic structural devices, is classified into experimental, numerical and analytically based methods.

2.1 Experimental Methods

Besides crash tests, which are prescribed by law, there are a number of reasons why in practice a lot of time and cost intensive testing is still inevitable, even if numerical analyses are carried out. These include:

- The complexity of crashworthiness simulation results from the underlying problems of arbitrary geometries, large deformations with contact, nonlinear, strain rate sensitive constitutive behaviour, dynamic loading, fracture, etc. Because crushing is affected by so many parameters, there arises the difficulty of obtaining and considering all the relevant data for general numerical analyses. For example, much effort is required for obtaining material data related to high rates of strain, see [Harding, 1991; Nemat-Nasser et al., 1994]).
- Even solely mechanically based numerical algorithms have to be validated by experiments [Haug et al., 1983; Berstad et al., 1995; Zaouk et al., 1998].
- Analytically based solution methods in general have to use many simplifying assumptions or are even based on experimental observations. Therefore, testing is inevitable for the definition and validation of these types of simulation strategies.
- In some cases selected component testing may still be more appropriate (and reliable) than performing detailed numerical simulations [Kecman, 1997]. This holds especially

true, if there are to investigate simple geometries in combination with very restricted parameter variations.

Test methods with respect to crashworthiness of structures may principally be divided into static and dynamic test procedures. The main reason why (quasi-)static testing can also be appropriate for approximately investigating dynamic processes is that the unstable response of structural members at relatively low impact velocities often is closely related to their static behaviour – that means, the pattern of deformation is similar for both static and dynamic loading [Jones, 1989a; Kecman, 1983; Aamlid et al., 1993]. The reason for this is that inertia effects do not yet play a significant role (even if some strain rate sensitivity of the material may cause differences). Accordingly, for moderate impact velocities tests can often be done quasistatically, which considerably simplifies the testing procedures (e.g. uniaxial universal testing machines can be used for axial compression of tubular members). Furthermore, it follows that analytical and numerical models can be derived excluding inertia forces (quasistatically) and applied to quasistatic dynamic simulation, possibly considering some strain rate sensitivity [Kecman, 1983; Jones, 1989b]. Examples for "static crash testing" can, among many others, be found in [Gupta and Khullar, 1993; Gupta and Velmurugan, 1995; Cimpoeru and Murray, 1993]. Analytically based simulation techniques often rely on experimental results obtained from static tests. The experiments which were conducted for the present work (axial compression of tubular crush elements), and also the proposed simplified numerical methods, are, therefore, restricted to quasistatic loading conditions.

Besides the crash tests performed e.g. in the automotive industry, which are prescribed by law and typically are full scale dynamic tests under well defined conditions (frontal, side or rear impact test, rollover test, etc. — for an overview on currently required test methods in Europe and the US see e.g. [Anselm, 1997] — dynamic component testing can be carried out in different ways. One method is the "drop weight" or "drop hammer" test, where some rigid weight falls down on the test specimen (e.g. [Berstad et al., 1995; Bravo et al., 1993; McGregor et al., 1993]). Although this kind of testing is relatively simple to use there are uncertainties in the measured results arising from interaction between the rigid mass and the specimen (e.g. uncontrolled stress wave propagation effects may markedly influence the measurements). To obtain more accurate experimental results (e.g. for comparison with numerical analyses), more advanced test methods were developed. Maier et al. [1990] describe test arrangements for dynamic crash testing, where the rigid mass and the specimen become decoupled immediately after impact. Albertini et al. [1993] use the Hopkinson bar method, which was originally developed for high strain rate characterization of materials, for a more accurate measurement of the load-displacement characteristics of full scale thin sheet metal structures. The authors state that such a specialized arrangement allows control and clear measurement of the stress waves due to impact loading.

2.2 Numerical Methods

Finite element programs today offer the most general way of simulating the crash behaviour of structures. From the methods point of view there are no intrinsic limitations, and practical constraints are rather due to computer resources and the huge amount of data generated with fine meshes. In fact even on supercomputers a compromise has to be achieved between "accuracy" and efficiency.

There are a number of specialized finite element codes, designed especially for modelling the large deformation dynamic response of inelastic solids and structures, e.g. DYNA-3D, LS-DYNA3D, MSC/DYTRAN, PAM-CRASH, PLEXIS-3C or ABAQUS/Explicit.

The time integration of the nonlinear equations of motion in these programs is generally based on explicit schemes, usually using the central difference method [Chung and Lee, 1994]. One main advantage of an explicit formulation is that no assembling of a stiffness matrix and only simple vector calculations are required (provided mass and damping matrices are diagonal). Therefore, storage and computational costs per time step are generally much less than for implicit methods. Furthermore, no iterations have to be carried out. Because the explicit scheme is only conditionally stable, however, severe time step size restrictions apply. The time step has to be smaller than the travel time of a stress wave across the smallest element within a given FE discretization (Courant limit). In general this results in an extremely large number of increments, but each increment is relatively inexpensive [Haug et al., 1983; HKS, 1998b].

Due to the dynamic nature of impact explicit codes offer an economical way of carrying out crash calculations (as compared to implicit time integration codes). Furthermore, static and slow motion dynamic problems, which are highly nonlinear or even discontinuous (very large deformations and strains, rate dependent plasticity, and frictional contact), also require small time steps, and, hence, they are also often solved efficiently by using explicit codes (see e.g. [Hu et al., 1994]). But even for slow motion smooth nonlinear problems the explicit procedure may become more economical for very large models. The reason for this is that due to the efficient incremental solution technique of explicit methods (without the need of matrix inversions, etc.) the computation time increases in a direct proportion to the problem size, whereas implicit methods become less efficient for larger problems [HKS, 1997].

Much effort has been put into the development of efficient element formulations, especially for plates and shells which are mainly used for modelling thin-walled structures. These elements have to be simple and computationally "cheap", must handle large rotations properly, should work for thick and thin shell applications, must be robust, i.e. free of unnatural stiffening effects such as shear locking, and should consider thickness changes due to in-plane deformations. An example for such an element formulation can be found in [HKS, 1998a]. Whereas this element uses a numerical through thickness integration, formulations working only in terms of stress resultants, even for plastic deformations, are desirable. Among others, Simo et al. [Simo and Fox, 1989; Simo et al., 1989, 1990a,b; Simo and Kennedy, 1992; Simo et al., 1992; Simo, 1993a], Ibrahimbegović and Frey [1993, 1994] and Auricchio and Taylor [1994] presented plate and shell elements, where the elastoplastic constitutive models are formulated directly in terms of stress resultants. Using such formulations for the constitutive behaviour may lead to improvements in computational costs, but is often accomplished at the expense of introducing considerably more complex functional forms in the constitutive response functions and restricts the generality of the material description. Furthermore, most stress resultant yield criteria are approximate because the spreading of the plastic zone over the thickness of the shell section is neglected (plastic limit yield functions) or is considered only in a simplified way (see e.g. [Crisfield, 1980; Başar and Krätzig, 1985]). In addition, the theoretical derivations of such yield criteria are mostly based on perfectly plastic material behaviour, even if extensions to include hardening have been proposed (see e.g. [Chou et al., 1994] or the FE plate and shell formulations cited above). Crisfield [1997] suggests to use full section yield criteria for quick approximate studies — for final detailed analyses (as well as for very imperfection sensitive shell structures) a numerical thickness integration should always be used.

Despite all these disadvantages the application of elastoplastic stress resultant constitutive laws may be suitable for a certain type of problems — limit and collapse analyses of thin-walled structures, which are dominated by plastic deformations. Because the present work just deals with the simplified analysis of the plastic collapse behaviour of thin-walled shells, the application of approximate stress resultant constitutive laws appears to be highly appropriate. In section 3.4, therefore, the derivation and description of the exact Ilyushin yield surface (which is applied for these purposes) is presented in detail. With respect to FE analyses, an algorithmic structure for the definition of a full section constitutive model, based on the exact Ilyushin yield surface, is proposed, too (chapter 7).

Notwithstanding all the progress made in further developing the conventional, displacement based finite element method there exists the principal problem that strain localization (for crushing this corresponds to the development of plastic hinges or yield lines) can only be considered properly through very fine meshing, and in general the localization zone will not be known a priori. For strain localization representable by displacement (strong) discontinuities (e.g. shear bands) Larsson et al. [1993] used mesh adaption or mesh realignment procedures, where regularized displacement discontinuities are allowed along inter-element boundaries. A further strategy for displacement discontinuities, which in recent years became the subject of considerable research, is the formulation of enhanced assumed strain elements, where the continuous deformation field inside an element domain is enriched by discontinuous displacements. With such a formulation mesh size and mesh alignment dependencies can be removed when computing strong displacement discontinuities [Larsson et al., 1995; Armero and Garikipati, 1995; Oliver, 1995]. Although these developments seem to be very useful for analyses of displacement discontinuities (shear bands, slip lines, ...), in general the material behaviour must fulfill certain conditions (damaging, softening, see [Armero and Garikipati, 1995; Oliver, 1995]) and it is questionable if this methodology is applicable to the analysis of plastic hinge or yield line mechanisms, where the displacements remain continuous and generally no material softening occurs.

Toi et al. [Toi and Yang, 1991; Toi and Isobe, 1996] proposed a technique to consider plastic hinges in framed structures by shifting the integration points in linear and cubic beam elements. This procedure is based on the comparison of the strain energy approximations of these finite element formulations with rigid body – spring models, which are the discrete elements suitable for plastic collapse analysis.

Shi and Atluri [1988] presented a stress based element formulation for space frames, where plastic hinges can develop at discrete points and the rest of the element remains purely elastic. Shi and Voyiadjis [1992] extended this plastic node technique to assumed strain elements for shear flexible plates. In their work a modified Ilyushin yield function considering transverse shear as well as the progress of yielding across the plate thickness is used. The plastic deformations, however, are restricted to the positions of the nodes of the element whereas the interior always remains elastic. Eventhough the beam element is valid for large deformations, the plate element formulation is based on the assumption of small strains and, therefore, not applicable to crushing analysis. In [Vasudevan et al., 1995], however, a brief outline for the formulation of a frame element, which is also based on a mixed variational principle and stated to be specialized for crash analysis, was proposed (following the definition of the hybrid frame element cited above).

Rather classical methods for computing the ultimate loads of plastically deforming structures are a direct outcome of the theory of plasticity. Plastic extremal and bounding principles (Hill theorem, Markov theorem, limit analysis theorems, ... , see e.g. [Washizu, 1968; Ismar and Mahrenholtz, 1979; Lubliner, 1990]) may serve to find solutions for the plastic limit state and may also provide estimates for the actual collapse loads.

The bounding principles of limit analysis (lower and upper bound theorem) are generally based on rigid-perfectly plastic material behaviour, small deformations, monotonic and proportional loading conditions, etc. The problem consists in finding statically and plastically admissible stress configurations (lower bound theorem) and/or kinematic mechanisms (upper bound theorem), which are as close as possible to the actual configuration at collapse. Jones [1989b] used the theorems to investigate the limit behaviour of beams, plates and shells under static as well as dynamic loads and different boundary conditions. Gao [1995] presented bounding theorems for plastic shells undergoing large deformations and suggested a penalty-duality variational technique for the numerical evaluation of the optimal load factor. A "sequential limit analysis" method for large deformation analysis of truss and frame structures, which is based on a duality theorem, was proposed by Yang [1993]. There the solutions for large deformations are obtained in an incremental manner without losing the advantages of limit analysis which are numerical stability, efficiency, modelling simplicity, etc. Furthermore, hardening or softening, loading-unloading, bifurcation of solutions, etc., can be accounted for in this method.

The numerical implementation of limit analysis in general leads to mathematical programming methods (e.g. [Smith, 1990; Zouain et al., 1993; Zhang et al., 1994; de Buhan and Maghous, 1995; Turgeman et al., 1998]), often combined with some finite element discretization of the geometry [Lü et al., 1993; Yu et al., 1994; Zhang et al., 1994; Zwoliński, 1995; Borges et al., 1996; Seitzberger and Rammerstorfer, 1998a]. The FE formulation, which is mostly based on the upper bound theorem or (in a very similar, but more general way) on the Markov theorem and related extremum principles [Washizu, 1968; Ismar and Mahrenholtz, 1979; Smith, 1990], may also be used advantageously to set up a nonlinear system of equations in the unknown velocity parameters instead of directly solving an optimization problem [Kobayashi, 1977; Ismar and Mahrenholtz, 1979; Tsuta et al., 1993; Mori et al., 1996; Hwan, 1997; Capsoni and Corradi, 1997a,b]. Besides the numerical efficiency, which is stated to be achievable by such a solution method, its formulation and programming are in general simpler than those for conventional elastoplastic FE codes.

Non-steady-state large deformation problems (which even may include frictional contact, see e.g. [Ismar and Mahrenholtz, 1979; Hwan, 1997]) are generally solved by adopting a step-by-step procedure. Discontinuous velocity fields can also be accounted for without fundamental difficulties. The rigid plastic finite element method is widely applied to the simplified numerical simulation of metal forming processes (see e.g. [Kobayashi, 1977; Feng and de Saxcé, 1996; Mori et al., 1996; Hwan, 1997; Bonet, 1998]).

The methods discussed in the present section are concentrated on the finite element method and on plastic extremum and bounding principles. The reason for this is that the first methodology offers a very general and widely used tool. Extremum and bounding principles, however, are intended for investigating plastic limit states and ultimate loads, respectively, and, therefore, serve as a direct and natural approach to collapse analysis of structures. In the subsequent chapters, contributions to both types of numerical methods are given. Besides the full section constitutive model for conventional FE analyses, which was mentioned above, a sequential limit analysis method is investigated in the present work. Chapter 6 includes the description of a computer program for the simulation of the large deformation collapse behaviour of axisymmetric shells (including internal contact), which is based on the upper bound theorem of limit analysis. In order to retain some modeling generality (and to restrict the programming effort), however, the incremental solutions are found by applying general mathematical programming techniques instead of resorting to a (numerically certainly more efficient) direct solution method (see also [Seitzberger and Rammerstorfer, 1998a,b]).

2.3 Analytically Based Methods

Experiments show that the collapse process of thin-walled structures is in general accompanied by the development of localized plastic mechanisms, i.e. the formation of a more or less complicated pattern of folds and wrinkles. Based on these observations simplified kinematic mechanisms were proposed for predicting the crushing response of thin-walled members of simple geometry under different loading conditions. Many of these models lead to simple computer codes or even to closed-form solutions and, therefore, can be used efficiently in the preliminary design of energy absorbing systems.

The proposed models are mostly based on kinematics-oriented methods of plasticity, suitably generalized to large deformation problems. Starting point is the selection of a kinematically admissible velocity field, which is piecewise continuous allowing stationary and moving yield lines to develop. Taking into account the constitutive behaviour the internal rate of energy dissipated within such a collapse mechanism can be computed (mostly rigid-perfectly plastic material behaviour is assumed). Global equilibrium is in general expressed by the power equation, from which external loads and load parameters, respectively, are obtained, after the unknown parameters (if there are any) are determined by some minimization procedure. This minimization may be based on a power principle, e.g. the Markov theorem or the upper bound theorem. For progressive buckling processes, however, often an energy principle is applied, leading to the minimization of the mean crushing force over one crushing cycle (see e.g. [Abramowicz, 1996]). Depending on the kinematic description and on simplifications with respect to the computation of the power of internal forces closed-form solutions may be obtained, which can be solved analytically [Wierzbicki and Abramowicz, 1989].

Many mechanisms were proposed for describing the axisymmetric progressive buckling of circular tubes ("concertina" mode buckling). Examples can be found in [Alexander, 1960; Abramowicz and Jones, 1986; Grzebieta, 1990; Wierzbicki et al., 1992; Gupta and Velmurugan, 1995] — see also section 5.2.

Wierzbicki and Abramowicz [1983] and Hayduk and Wierzbicki [1984] presented two basic folding elements (collapse modes) for the axial crushing of thin-walled structural members, which can account for internal energy dissipation not only due to local bending but also due to membrane deformations in the corner regions. These elements were used to predict the axial collapse behaviour of a cruciform member [Hayduk and Wierzbicki, 1984] and the symmetric collapse of rectangular and square box columns [Wierzbicki and Abramowicz, 1983]. In [Abramowicz and Wierzbicki, 1989] a combined mechanism was proposed for multicorner prismatic columns with an even number of corners, where both collapse modes are allowed to act in series (also denoted as "superfolding element" by the authors). A further extension of this generalized model to square tubes filled with polyurethane foam is described in [Abramowicz and Wierzbicki, 1988]. An application (and further extension) of the latter to study the axial crushing behaviour of square, hexagonal and octagonal members, which are fully or partially filled with aluminium foam, is described in [Willminger, 1999]. Wierzbicki and Huang [1991] presented a model which is able to describe the transition from the postbuckling phase (immediately following the bifurcation) to the crushing deformation phase (leading to localized plastification) in box columns. Reddy and Al-Hassani [1993] and Reid [1993] suggested (among other energy absorbing systems) simplified kinematic mechanisms for the progressive crushing of axially compressed square metal tubes filled with polyurethane foam and wood. In contrast to the model proposed by Abramowicz and Wierzbicki [1988], however, these kinematic mechanisms are not able to account for some interaction between filler and tube.

Concerning the force-deflection characteristics during the formation of a single fold in progressive crushing of tubes it must be said that none of the cited mechanisms is able to describe this behaviour sufficiently accurately. Therefore, for practical use and comparison with experiments mostly the mean force-deflection characteristics or only parts of this curve are used.

Kecman [1983] investigated the characteristics of the bending collapse of rectangular and square section tubes experimentally as well as theoretically and presented a kinematic mechanism for the prediction of the moment-rotation curve of such tubes. In [Kotelko and Królak, 1993] the collapse behaviour of triangular cross-section girders subject to pure bending was examined. Wierzbicki et al. [1994a,b] proposed a model for combined bending/compression loading of multicorner columns based on a purely axial compression mechanism [Abramowicz and Wierzbicki, 1989]. It is interesting to note that they used not only experimental observations but also the finite element method to study the crushing process in detail and to propose their mechanism (which in analogy to the underlying "superfolding element" for axial compression, is denoted as "superbeam element").

The "superfolding" and the "superbeam" elements essentially form the basis of CRASH-CAD [CrashCad, 1995], a simplified design code intended for rapid prototyping and design of energy absorbing components and structural arrangements. The design code in its current version not only includes the axial and bending response of tubular members, but may also be used to investigate torsional as well as combined loading conditions. Furthermore, the main variables of influence are suggested for a preliminary design of whole structural devices (including the choice of the optimal cross-section, the wall thickness, the location of spot welds, etc.). However, CRASH-CAD has been set on a commercial basis and, though still being developed further, theoretical foundations of progress have not been published since the early 90's. An example for the use of CRASH-CAD for a preliminary design study of energy absorption devices made of aluminium can be found in [McGregor et al., 1993].

Murray [1985] presented results for the collapse behaviour of different open and closed sections. He proposed that even the most complicated local plastic mechanisms can be decomposed into a number of basic mechanisms. Following Murray [1995] two general principles can be stated which determine what kind and shape of mechanism will be adopted during collapse. The first principle is that the mechanism becomes locked into a certain shape determined by the location of the zones of first yielding (influenced by initial imperfections). Therefore, the actual mechanism is not necessarily the one which would minimize the load during collapse. The second principle is that the structure always tries to develop a mechanism which is dominated by bending and avoids membrane yielding.

Most of the mechanisms cited above assume rigid-perfectly plastic material behaviour. Elasticity, hardening, strain rate effects, etc., could eventually be considered, but often at the expense of obtaining much more complex equations, and closed-form solutions can in general no longer be obtained.

Many of the kinematic models use moving hinges or yield lines to describe the deformation process. Lu and Sherbourne [1992] and Sherbourne and Lu [1993] presented contributions towards the physical understanding of the moving hinge concept in large-displacement problems.

Many of the analytically based models give rise to closed-form solutions for the force-displacement or moment-rotation characteristics of thin-walled tubes and, therefore, are well suited for use as special elements in numerical algorithms as described in section 2.2 (but often only the mean force-deflection behaviour is used in practice, see the remarks above). For example, Drazétic et al. [1993, 1995] used the compression and pure bending models developed by Abramowicz and Wierzbicki [1989] and Kecman [1983] as translational and rotational springs in connection with elastoplastic beam elements as well as with rigid elements for the evaluation of the global crash behaviour of an "S"-frame undergoing a collision against a rigid block. In [Drazétic et al., 1995] a modelling tool was described, which allows the determinination of the number and locations of the springs in the rigid body-spring model. Sonzogni and Géradin [1994] presented a hinge model for transient beam response analysis allowing a variety of moment-rotation characteristics. For considering section instability of rectangular thin-walled sections they also employed Kecman's bending mechanism. The combined compression/bending element presented in [Wierzbicki et al., 1994a,b] is also intended as special beam element for simplified crushing analysis of arbitrary framework structures (and as such is used in the design code CRASH-CAD, see above).

Due to the fact that most mechanisms based on analytical techniques generally use many simplifying assumptions, results are mainly useful for preliminary design studies (see e.g. [McGregor et al., 1993]). In [Wierzbicki and Abramowicz, 1989] a scenario for linking the proposed analytically based folding elements with the finite element method is sketched. It is stated that for practical use the folding elements have to be suitably generalized to allow an incorporation into “hybrid” FE codes. Directions of future research have to include improvements of existing mechanisms, e.g. by removing the requirement of obtaining analytical solutions. Such a formulation may open the way for extensions of the existing mechanisms (elastic behaviour, inertia forces, hardening, etc., could be accounted for) to form a hybrid shell model for efficient crash calculations of arbitrarily shaped shells. This task, however, requires deeper insight into the plastic folding process of thin-walled metal structures.

2.4 Summary

The goal of the present research work is to provide contributions towards an effective numerical simulation of the collapse process of thin-walled structures. From the summary on the state of research presented above some conclusions may be drawn, which seem to be important for obtaining this goal:

- In a first step the development of simplified numerical tools can be performed without considering dynamic effects. However, this restriction to static problems should not be stringent, i.e. the possibility of including dynamic effects (at least in an approximate way) should be provided by the chosen methodology.
- A definition of effective and accurate algorithms should be based on stress resultant yield surfaces, which can account for some interaction between the stress resultant components while avoiding a numerical thickness integration. The application of plastic limit yield surfaces is in particular suited for rigid plastic solution methods, because the definitions of such surfaces usually also rely on the assumption that elastic deformations can be neglected, thus being consistent with rigid plastic analysis.
- The application of approximate “full section” constitutive laws, which are based on stress resultant yield surfaces, is appropriate for conventional FE collapse analyses of shells, which are dominated by plastic deformations.
- The kinematic description of crushing processes of thin-walled structures, either within analytically based models or within a more general finite element discretization, should allow for the development of stationary or moving plastic hinges and yield lines. For FE-based solution techniques this ensures that relatively coarse meshes can be used while still considering localization of plastic deformations.

- For simplified plastic collapse analyses kinematics-oriented extremum or bounding principles (Markov theorem, upper bound theorem of limit analysis) are ideally suited and, therefore, mainly applied in practice. A generalization of the analytically based simulation models will certainly lead to some kind of a sequential limit analysis or rigid plastic finite element method, respectively (both methodologies are essentially based on the same theoretical foundations, see chapter 3). The sequential limit analysis method for axisymmetric shells presented in chapter 6 shows that many of the analytically based mechanisms can be regarded as special cases, while the generalized method is able to deliver results which are comparable to that of conventional elastoplastic FE analyses.

- With respect to the conventional, displacement based FE method especially hybrid element formulations, which are set on the basis of multifield variational principles, seem promising (see e.g. [Shi and Atluri, 1988; Vasudevan et al., 1995; Seki and Atluri, 1995]). For example, the beam element proposed by Shi and Atluri [1988] is based on assumed stress resultants within the element and allows plastic hinges to develop on a number of fixed positions within the element domain in order to account for plasticity. With proper extensions concerning the position of the plastic hinges as well as the kinematics this formulation could also serve as a basis for defining a hybrid axisymmetric shell element where plastic hinges are allowed and elasticity as well as dynamic behaviour can be accounted for. This approach, however, though very interesting, is not investigated further in the present work.

Chapter 3

Theory

In the following, several theoretical foundations are stated, which are needed for the developments in the subsequent chapters. Starting with a brief introduction into large deformation continuum mechanics (section 3.2) some principles of the mechanics of rigid plastic materials, including the kinematics-oriented plastic extremum and bounding principles, are presented in section 3.3. Furthermore, the derivation and description of the exact Ilyushin yield criterion is summarized in section 3.4.

The theoretical fundamentals included in this chapter are mainly taken from [Malvern, 1969; Lai et al., 1993; Crisfield, 1997; HKS, 1998a] (continuum mechanics) and [Washizu, 1968; Ismar and Mahrenholtz, 1979; Lubliner, 1990; Kreißig, 1992] (plastic material behaviour), respectively. The representation of the exact Ilyushin yield surface is closely related to the work of Burgoyne and Brennan [1993b].

3.1 Notation

In the next two sections on continuum mechanics and the plastic extremum and bounding principles (sections 3.2 and 3.3) tensors and vectors are denoted in boldface letters without, in general, referring to the individual components (e.g. $\boldsymbol{a}$, $\mathbf{A}$). This kind of notation ("direct matrix notation") allows a very compact and convenient representation of tensorial quantities without reference to a particular coordinate system. For the main body of the work, however, matrix notation is used, being more convenient for the formulation and computer implementation of several algorithms. According to this kind of notation the components of second and fourth order tensors are arranged as vectors and matrices, respectively (where vectors and matrices are again written in boldface).

In any case, all quantities are defined and designated when first used, and the type of notation will in general be obvious from the context.

3.2 Some Basic Principles of Continuum Mechanics

3.2.1 Deformation, Rate of Deformation and Strain Increment

A material particle of a body in its reference configuration is given by the position vector $\boldsymbol{X}$. The motion of this material particle is described by the mapping

$$\boldsymbol{x} = \boldsymbol{x}(\boldsymbol{X}, t) \ , \tag{3.1}$$

where $\boldsymbol{x}$ stands for the current position of the material particle at time t. The relation between a material element in the current and in the reference configuration ($d\boldsymbol{x}$ and $d\boldsymbol{X}$, respectively) is given by

$$d\boldsymbol{x} = \frac{\partial \boldsymbol{x}}{\partial \boldsymbol{X}} d\boldsymbol{X} = \mathbf{F} \; d\boldsymbol{X} \ , \tag{3.2}$$

where the unsymmetric second order tensor $\mathbf{F}$ is the deformation gradient. Because of the one-to-one correspondence between particles in the reference and the current configuration (material cannot appear or disappear) the deformation gradient is invertible and accordingly, the determinant $J = \det \mathbf{F} \neq 0$. The determinant of $\mathbf{F}$ may be shown to be a measure for the volume change between current (dv) and reference (dV) infinitesimal volumes:

$$dv = J \; dV \ , \tag{3.3}$$

from which it becomes evident that not only $J \neq 0$ but also $J > 0$ holds. The deformation gradient $\mathbf{F}$ in general includes both continuum deformations and rigid body motions and, therefore, is not suited to directly describe strains in continuum mechanics. However, most common strain measures for large deformation problems may be defined via the deformation gradient (for details see e.g. [Lai et al., 1993]).

Due to the path dependency of plastically deforming materials constitutive equations (of the flow theory of plasticity) are typically stated in rate form, thus requiring the definition of a measure for the strain rate. The velocity of a material particle is given by

$$\boldsymbol{v} = \frac{\partial \boldsymbol{x}}{\partial t} \ . \tag{3.4}$$

The velocity difference between two neighbouring particles in the current configuration is

$$d\boldsymbol{v} = \frac{\partial \boldsymbol{v}}{\partial \boldsymbol{x}}\, d\boldsymbol{x} = \nabla \boldsymbol{v}\, d\boldsymbol{x} = \boldsymbol{l}\, d\boldsymbol{x} \ , \tag{3.5}$$

where $\boldsymbol{l}$ is the velocity gradient in the current configuration. It is noted, however, that by applying the definition of the deformation gradient (see Eq. (3.2)) one may alternatively obtain the velocity gradient as

$$\boldsymbol{l} = \dot{\mathbf{F}}\mathbf{F}^{-1} \ , \tag{3.6}$$

where $\dot{\mathbf{F}}$ denotes the time derivative of $\mathbf{F}$.

$\boldsymbol{l}$ is in general an unsymmetric tensor, which may be decomposed into a symmetric and a skew-symmetric part,

$$\boldsymbol{l} = \boldsymbol{d} + \boldsymbol{\omega} \ , \tag{3.7}$$

with

$$\boldsymbol{d} = \frac{1}{2}\left(\boldsymbol{l} + \boldsymbol{l}^T\right) = \frac{1}{2}\left(\nabla \boldsymbol{v} + \nabla \boldsymbol{v}^T\right) \ , \tag{3.8}$$

$$\boldsymbol{\omega} = \frac{1}{2}\left(\boldsymbol{l} - \boldsymbol{l}^T\right) = \frac{1}{2}\left(\nabla \boldsymbol{v} - \nabla \boldsymbol{v}^T\right) \ . \tag{3.9}$$

The skew-symmetric part $\boldsymbol{\omega}$ is the spin tensor, characterizing the rate of rotation of $d\boldsymbol{x}$ without changing its length (rigid body rotation), whereas the symmetric tensor $\boldsymbol{d}$ is denoted as the spatial rate of deformation tensor (sometimes also called stretching tensor, velocity strain, etc.). It is an appropriate measure of strain rate. Omitting the proof the following relation holds ($ds = \sqrt{d\boldsymbol{x}^T d\boldsymbol{x}}$):

$$\frac{d}{dt}(ds) = \frac{1}{ds} d\boldsymbol{x}^T \boldsymbol{d}\, d\boldsymbol{x} \ , \tag{3.10}$$

that means that the rate of change of an infinitesimal material element ds is determined by the spatial rate of deformation tensor $\boldsymbol{d}$. Furthermore, from Eq. (3.8) it may be seen that for small deformation problems the definition of $\boldsymbol{d}$ corresponds to the elementary definition of the time rate of "small strains". However, whereas the time derivative of the "small strain tensor" is based on the assumption that the displacements and the displacement increments are small (and thus, the strain definition is related to the (undeformed) reference state) the rate of deformation tensor $\boldsymbol{d}$ is related to the current configuration and is also useable in situations where the displacements are not small, e.g. fluid flow or metal forming such as drawing, extrusion, etc. [Malvern, 1969].

For the special case that the principal strain directions do not rotate with respect to the material, $\boldsymbol{d}$ is integrable into a common strain measure, namely the logarithmic or natural strain. For example, in one dimension, the rate of deformation is given by

$$d_{11} = \frac{dv_1}{dx_1} \; , \tag{3.11}$$

from which (with the stretch $\lambda_1 = dx_1/dX_1$) the logarithmic strain follows as

$$\varepsilon_{11} = \int_0^t d_{11} \, dt = \ln \lambda_1 \; . \tag{3.12}$$

3.2.2 Equilibrium Statements

A body (or a part of a body), given in its current configuration (volume v, boundary surface a), is loaded by surface tractions $\boldsymbol{t}$ (force per unit of current area) and body forces $\boldsymbol{f}$ (force per unit of current volume). Then, (static) force equilibrium of the body is written as

$$\int_a \boldsymbol{t} \; da + \int_v \boldsymbol{f} \; dv = \mathbf{0} \; . \tag{3.13}$$

The "true" or Cauchy stress tensor $\boldsymbol{\sigma}$ at a point of the surface is defined by

$$\boldsymbol{t} = \boldsymbol{\sigma} \boldsymbol{n} \; , \tag{3.14}$$

where $\boldsymbol{n}$ is the unit outward normal to a at the point. Using this definition, Eq. (3.13) may be expressed as

$$\int_a \boldsymbol{\sigma} \boldsymbol{n} \; da + \int_v \boldsymbol{f} \; dv = \mathbf{0} \; . \tag{3.15}$$

In order to transform a surface integral into a volume integral, the integral identity

$$\int_a \mathbf{T} \boldsymbol{n} \; da = \int_v \mathrm{div} \mathbf{T} \; dv \; , \tag{3.16}$$

with $\mathbf{T}$ being a tensor field, may be applied (for the integral transformation of a vector instead of the tensor field this is known as the Gauß theorem). Using this, it follows for Eq. (3.15):

$$\int_v [\mathrm{div} \boldsymbol{\sigma} + \boldsymbol{f}] \; dv = \mathbf{0} \; . \tag{3.17}$$

Since the volume is arbitrary, this equation must apply pointwise in the body, thus providing the differential equation of translational equilibrium:

$$\mathrm{div}\boldsymbol{\sigma} + \boldsymbol{f} = \boldsymbol{0}\ . \tag{3.18}$$

Moment equilibrium for the body under consideration, written as

$$\int_a (\boldsymbol{x} \times \boldsymbol{t})\ da + \int_v (\boldsymbol{x} \times \boldsymbol{f})\ dv = \boldsymbol{0}\ , \tag{3.19}$$

finally simply delivers that the Cauchy stress tensor is symmetric, i.e.

$$\boldsymbol{\sigma} = \boldsymbol{\sigma}^T\ , \tag{3.20}$$

so that at each point there are only six independent stress components. Conversely, by taking the stress tensor to be symmetric, moment equilibrium is identically satisfied, and, therefore, Eq. (3.18) is sufficient to explicitly write the equilibrium equations.

Principle of Virtual Velocities

A scalar equilibrium statement for the entire body (a "weak form") may be obtained by multiplying Eq. (3.18) with a suitable vector-valued test function and integrating over the whole body. If the test function is imagined to be a "virtual" velocity field $\delta\boldsymbol{v}$ (which is completely arbitrary except that it must obey any prescribed kinematic constraints and have sufficient continuity — i.e., it must be "kinematically admissible"), then the "principle of virtual velocities" may first be stated as

$$\int_v [\mathrm{div}\boldsymbol{\sigma} + \boldsymbol{f}]\ \delta\boldsymbol{v}\ dv = 0\ . \tag{3.21}$$

With the chain rule

$$\mathrm{div}(\boldsymbol{\sigma}\delta\boldsymbol{v}) = \mathrm{div}\boldsymbol{\sigma}\delta\boldsymbol{v} + \boldsymbol{\sigma} : \nabla\delta\boldsymbol{v} \tag{3.22}$$

it follows for Eq. (3.21)

$$\int_v \left[\mathrm{div}(\boldsymbol{\sigma}\delta\boldsymbol{v}) - \boldsymbol{\sigma} : \nabla\delta\boldsymbol{v} + \boldsymbol{f}\delta\boldsymbol{v}\right]\ dv = 0\ . \tag{3.23}$$

The first term of this equation may be transformed using the Gauß theorem. By additionally considering the definition and the symmetry for the Cauchy stresses (Eqs. (3.14) and (3.20)) this gives

$$\int_v \mathrm{div}(\boldsymbol{\sigma}\delta\boldsymbol{v})\ dv = \int_a (\boldsymbol{\sigma}\delta\boldsymbol{v})\boldsymbol{n}\ da = \int_a \boldsymbol{t}\delta\boldsymbol{v}\ da\ . \tag{3.24}$$

From the definition of the spatial velocity gradient (see Eq. (3.5)) it follows that $\nabla\delta\boldsymbol{v}$ is the virtual velocity gradient in the current configuration, which may, according to Eq. (3.7), be partitioned into a virtual strain rate and a virtual rate of spin:

$$\nabla\delta\boldsymbol{v} = \delta\boldsymbol{l} = \delta\boldsymbol{d} + \delta\boldsymbol{\omega}\ . \tag{3.25}$$

Since $\boldsymbol{\sigma}$ is symmetric and $\delta\boldsymbol{\omega}$ is skew-symmetric, the relation

$$\boldsymbol{\sigma} : \nabla\delta\boldsymbol{v} = \boldsymbol{\sigma} : (\delta\boldsymbol{d} + \delta\boldsymbol{\omega}) = \boldsymbol{\sigma} : \delta\boldsymbol{d} + 0 = \boldsymbol{\sigma} : \delta\boldsymbol{d} \tag{3.26}$$

holds, and the principle of virtual velocities may finally be written as

$$\int_a \boldsymbol{t}\delta\boldsymbol{v}\ da + \int_v \boldsymbol{f}\delta\boldsymbol{v}\ dv = \int_v \boldsymbol{\sigma} : \delta\boldsymbol{d}\ dv\ . \tag{3.27}$$

Equation (3.27) represents an integral or “weak” form of static equilibrium for a body — the rate of work done by the external forces subjected to any virtual velocity field is equal to the rate of work done by the equilibrating stresses on the rate of deformation of the same virtual velocity field.

It is remarkable that no restrictions are placed on the magnitudes of the virtual velocities, that means they may be arbitrary finite values. Because the virtual velocity field may be regarded as the difference between two kinematically admissible velocity fields, however, (with each one fulfilling the kinematic boundary conditions), $\delta\boldsymbol{v}$ vanishes on the part of the boundary, where velocities are prescribed ($a_v \subset a$). Therefore, the surface integral in Eq. (3.27) has to be evaluated only over a_σ, where surface tractions are given (here and in the following it is assumed that the whole boundary may be partitioned into $a = a_v \cup a_\sigma$).

Power Principle

Instead of applying a virtual velocity field $\delta\boldsymbol{v}$ for deriving an integral equilibrium statement a kinematically admissible velocity field $\boldsymbol{v}^*$ may directly be used in Eq. (3.21). Following the same derivation procedure as sketched above this finally delivers

$$\int_a \boldsymbol{t}\boldsymbol{v}^*\ da + \int_v \boldsymbol{f}\boldsymbol{v}^*\ dv = \int_v \boldsymbol{\sigma} : \boldsymbol{d}^*\ dv\ , \tag{3.28}$$

with

$$\boldsymbol{d}^* = \frac{1}{2}\left(\nabla\boldsymbol{v}^* + (\nabla\boldsymbol{v}^*)^T\right) \tag{3.29}$$

and the given boundary conditions

$$\begin{aligned} \boldsymbol{t} &= \boldsymbol{\sigma n} \quad \text{on } a_\sigma \text{ (static boundary conditions) ,} \\ \boldsymbol{v}^* &= \boldsymbol{v} \quad \text{on } a_v \text{ (kinematic boundary conditions) .} \end{aligned} \tag{3.30}$$

In contrast to the principle of virtual velocities, Eq. (3.27), however, the surface integral now additionally has to include reaction forces that do work, i.e. the integration must be performed not only over a_σ, but also over that part of the surface a_v where the velocities are not constrained to be zero. Furthermore, it is to be noted that the left and right hand sides of Eq. (3.28) will only equate the actual external and internal power, respectively, if $\boldsymbol{v}^*$ coincides with the actual velocity field $\boldsymbol{v}$ at each material point of the body.

3.2.3 Work Conjugacy

The principle of virtual velocities, Eq. (3.27), expresses equilibrium in terms of Cauchy ("true") stresses and the conjugate virtual strain rate, the spatial rate of deformation tensor (where conjugate means that the product of stress and strain rate defines the rate of work per current volume). For the definition of constitutive models (e.g. in a displacement based finite element formulation), however, it is often more convenient to describe the equilibrium conditions in a state to which the body would return upon unloading (an elastic reference state). Then, work conjugate quantities should rather be referred to this elastic reference state than to the actual configuration. With this the internal power may be rewritten as an integral over the natural reference volume V (now represented by actual instead of virtual quantities) as

$$D_{\text{int}} = \int_v \boldsymbol{\sigma} : \boldsymbol{d} \, dv = \int_V J\boldsymbol{\sigma} : \boldsymbol{d} \, dV \ , \tag{3.31}$$

where J is the ratio of the material's volume in the current and the elastic reference configuration (see Eq. (3.3)). The stress measure defined by

$$\boldsymbol{\tau} = J\boldsymbol{\sigma} \tag{3.32}$$

is (with respect to the reference state) conjugate to the spatial rate of deformation tensor $\boldsymbol{d}$. This measure of stress, which is often used for constitutive developments (see e.g. [Simo, 1993a,b; HKS, 1998a]) is called Kirchhoff stress. Other conjugate stress and strain rate measures are e.g. the (unsymmetric) first Piola-Kirchhoff stress tensor and the time derivative of the deformation gradient, $\dot{\mathbf{F}}$, or the often used second Piola-Kirchhoff stress tensor and the rate of the Green-Lagrange strain tensor (see e.g. [Malvern, 1969]).

3.2.4 The Additive Strain Rate Decomposition

In chapter 7 a full section constitutive model for elastoplastic shells is presented, which is implemented into the nonlinear FE code ABAQUS/Standard. For the definition of such a user defined material routine the (corotational) stress/strain quantities provided by ABAQUS are by default measured in a local, orthonormal coordinate system. According to the work conjugacy considerations mentioned above the Kirchhoff stress together with the spatial rate of deformation tensor are used for geometrically nonlinear analyses. Furthermore, it is assumed that for small amounts of elastic strain the elastic and inelastic parts of the strain rates (and increments, respectively) may be decomposed in an additive way — analogous to the "classical" strain rate decomposition of small deformation plasticity. The argumentation for this and the basic definition of the elastic and plastic parts is as follows [HKS, 1998a]:

In (elastoplastic) large deformation plasticity the total deformation is decomposed multiplicatively:

$$\mathbf{F} = \mathbf{F}^e \mathbf{F}^p \, , \tag{3.33}$$

where $\mathbf{F}^e$ and $\mathbf{F}^p$ denote elastic and plastic part of the deformation gradient, respectively. The spatial velocity gradient $\boldsymbol{l}$, which may be expressed as a function of the deformation gradient (see Eq. (3.6)), can thus be written as

$$\boldsymbol{l} = \dot{\mathbf{F}}\mathbf{F}^{-1} = \dot{\mathbf{F}}^e(\mathbf{F}^e)^{-1} + \mathbf{F}^e\dot{\mathbf{F}}^p(\mathbf{F}^p)^{-1}(\mathbf{F}^e)^{-1} \, . \tag{3.34}$$

The elastic and plastic velocity gradients are (according to Eq. (3.6)) defined as

$$\boldsymbol{l}^e = \dot{\mathbf{F}}^e(\mathbf{F}^e)^{-1} \qquad \text{and} \qquad \boldsymbol{l}^p = \dot{\mathbf{F}}^p(\mathbf{F}^p)^{-1} \, , \tag{3.35}$$

and Eq. (3.34) may be expressed as

$$\boldsymbol{l} = \boldsymbol{l}^e + \mathbf{F}^e \boldsymbol{l}^p (\mathbf{F}^e)^{-1} \, . \tag{3.36}$$

The definition of $\boldsymbol{l}^p$ in this way, however, in fact means that $\boldsymbol{l}^p$ is related to some intermediate configuration instead of the final configuration. Essentially based on the assumption that the difference between these two configurations is given by the elastic deformations (and these are assumed to be small), the spatial velocity gradient in the current position may finally be written approximately as

$$\boldsymbol{l} \approx \boldsymbol{l}^e + \boldsymbol{l}^p \, . \tag{3.37}$$

From this it follows immediately that the spatial strain rate tensor $\boldsymbol{d}$ may also be decomposed additively to give

$$\boldsymbol{d} \approx \boldsymbol{d}^e + \boldsymbol{d}^p \; , \tag{3.38}$$

where

$$\boldsymbol{d}^e = \frac{1}{2}\left(\boldsymbol{l}^e + (\boldsymbol{l}^e)^T\right) \qquad \text{and} \qquad \boldsymbol{d}^p = \frac{1}{2}\left(\boldsymbol{l}^p + (\boldsymbol{l}^p)^T\right) \tag{3.39}$$

are defined according to Eq. (3.8).

A slightly different argumentation for the additive strain rate decomposition is given in [Crisfield, 1997, chapter 19]. Starting from Eq. (3.34) the plastic velocity gradient in the current configuration is directly defined as

$$\boldsymbol{l}^p = \mathbf{F}^e \dot{\mathbf{F}}^p (\mathbf{F}^p)^{-1} (\mathbf{F}^e)^{-1} \; , \tag{3.40}$$

concluding that by using this definition the above relations, Eq. (3.37) and (3.38), are fulfilled not only in an approximative but even in an exact way.

A formulation and algorithmic treatment of finite strain plasticity for isotropic materials based on the multiplicative decomposition (Eq. (3.33)) was presented by Simo [1992], which leads to a format identical to the standard return mapping algorithms of the infinitesimal theory (thus including the additive strain rate decomposition). Besides the appropriate choice of stress and strain rate measures the key point therein is the transformation of the finite strain plasticity problem to the principal stress and strain directions of the current configuration, which coincide for isotropic materials.

For more details concerning these topics see e.g. [Simo, 1992; Crisfield, 1997; HKS, 1998a]. The main conclusion which may be drawn for the present work, however, is that, essentially based on the assumption of small elastic deformations, the algorithmic structure of a material routine for ABAQUS/Standard is not affected whether geometrically linear or nonlinear theory is concerned, thus considerably simplifying the constitutive description (see chapter 7).

3.3 Plastic Extremum and Bounding Principles

The computational models presented in the subsequent chapters for the simplified analysis of collapse processes of thin-walled structures are essentially based on kinematics-oriented plastic extremum and bounding principles, respectively. These are, therefore, stated in the following. Before, however, the principle of maximum plastic dissipation is specified, forming the basis for the validity and proof of the theorems.

For the following it is assumed that the material is rigid-perfectly plastic, isotropic and incompressible. Rigid or plastic states of stress are determined by the inequality

$$f(\boldsymbol{\sigma}) \leq 0 \, , \tag{3.41}$$

where the boundary $f(\boldsymbol{\sigma}) = 0$ is the (general form of the) yield condition, which describes a convex surface in stress space. All states of stress lying inside this surface denote rigid material behaviour, whereas stress states on the yield surface characterize a plastic state of stress for the material point under consideration.

For a given plastic stress state the flow rule determines the direction of the (plastic) strain rates $\boldsymbol{d}$. For the following the normality rule is assumed to be valid, which means that (in the coaxial space of stresses and strain rates) the direction of the plastic strain rates is directed towards the outward normal of the yield surface f:

$$\boldsymbol{d} = \dot{\xi} \frac{df}{d\boldsymbol{\sigma}} \, . \tag{3.42}$$

The consistency parameter $\dot{\xi}$ is a positive scalar, which again may be expressed as a function of the (plastic) strain rate tensor $\boldsymbol{d}$.

3.3.1 Principle of Maximum Plastic Dissipation

For rigid plastic materials the maximum plastic dissipation principle (stating a necessary condition for stable materials, see e.g. [Lubliner, 1990]) may be written as

$$(\boldsymbol{\sigma} - \boldsymbol{\sigma}^*) : \boldsymbol{d} \geq 0 \, . \tag{3.43}$$

The stress $\boldsymbol{\sigma}$ denotes a point on the yield surface ($f(\boldsymbol{\sigma}) = 0$) and is associated with the (plastic) strain rate $\boldsymbol{d}$. $\boldsymbol{\sigma}^*$ is any plastically admissible state of stress, lying on or within the yield surface ($f(\boldsymbol{\sigma}^*) \leq 0$). With the definition of plastic dissipation per unit volume,

$$D_{\mathrm{p}}(\boldsymbol{d}) = \boldsymbol{\sigma} : \boldsymbol{d} \, , \tag{3.44}$$

Eq. (3.43) may alternatively be written as

$$D_{\mathrm{p}}(\boldsymbol{d}) \geq \boldsymbol{\sigma}^* : \boldsymbol{d} \, . \tag{3.45}$$

For a given (plastic) strain rate $\boldsymbol{d}$ the actual stress state $\boldsymbol{\sigma}$ delivers, among all plastically admissible stress states, a maximum of plastic dissipation ("principle of maximum plastic dissipation"). From Eq. (3.43) both the normality rule and the convexity of the yield surface can be derived.

D_{p} is a pure function of the plastic deformations and does not depend on the stress $\boldsymbol{\sigma}$. This dependency can be explained from geometrical considerations concerning the convexity of the yield surface and the normality rule. For example, if the yield surface is strictly convex at $\boldsymbol{\sigma}$, then this is the only stress that corresponds to a given strain rate $\boldsymbol{d}$. If the yield surface has a flat portion, however, then all points of this portion have the same normal, that is, the different stresses correspond to the same plastic strain rate, and the scalar product $\boldsymbol{\sigma} : \boldsymbol{d}$ is the same for all of them. Such states of stress are called plastically equivalent. For a material obeying the von Mises yield criterion plastically equivalent stresses differ at most by a hydrostatic pressure, but in a "Tresca material" all stresses, which lie on the same facet of the hexagonal cylinder in the principal stress space, are plastically equivalent.

3.3.2 Kinematic Extremum and Bounding Theorems

Kinematic Extremum Principle

The kinematic extremum principle, first proposed by Markov [1947] for a von Mises material, may be stated as:

> Among all kinematically admissible velocity fields $\boldsymbol{v}^*$ (satisfying the conditions of compatibility and incompressibility, as well as the geometrical boundary conditions on a_v) the actual solution renders the functional
>
> $$\Gamma(\boldsymbol{v}^*) = \int_v D_{\mathrm{p}}(\boldsymbol{d}^*)\, dv - \int_v \boldsymbol{f}\boldsymbol{v}^*\, dv - \int_{a_\sigma} \boldsymbol{t}\boldsymbol{v}^*\, da \tag{3.46}$$
>
> to become an absolute minimum.

To prove this theorem at first the power principle, Eq. (3.28), is stated for the actual and some kinematically admissible velocity field ($\boldsymbol{v}$ and $\boldsymbol{v}^*$) as

$$\begin{aligned}
\int_v \boldsymbol{\sigma} : \boldsymbol{d}\, dv &= \int_{a_\sigma} \boldsymbol{t}\boldsymbol{v}\, da + \int_{a_v} \boldsymbol{t}\boldsymbol{v}\, da + \int_v \boldsymbol{f}\boldsymbol{v}\, dv\ , \\
\int_v \boldsymbol{\sigma} : \boldsymbol{d}^*\, dv &= \int_{a_\sigma} \boldsymbol{t}\boldsymbol{v}^*\, da + \int_{a_v} \boldsymbol{t}\boldsymbol{v}\, da + \int_v \boldsymbol{f}\boldsymbol{v}^*\, dv\ .
\end{aligned} \tag{3.47}$$

where for the second relation the kinematic boundary conditions ($\boldsymbol{v}^* = \boldsymbol{v}$ on a_v) have already been taken into account. Elimination of the surface integral over a_v gives

$$\int_v \boldsymbol{\sigma} : \boldsymbol{d}^* \, dv = \int_v \boldsymbol{\sigma} : \boldsymbol{d} \, dv + \int_{a_\sigma} \boldsymbol{t}(\boldsymbol{v}^* - \boldsymbol{v}) \, da + \int_v \boldsymbol{f}(\boldsymbol{v}^* - \boldsymbol{v}) \, dv \ . \tag{3.48}$$

Now, by subtracting this equation from the identity

$$\int_v \boldsymbol{\sigma}^* : \boldsymbol{d}^* \, dv = \int_v \boldsymbol{\sigma}^* : \boldsymbol{d}^* \, dv \ , \tag{3.49}$$

where $\boldsymbol{\sigma}^*$ and $\boldsymbol{d}^*$ are associated via the normality rule[1], the relation

$$\int_v (\boldsymbol{\sigma}^* - \boldsymbol{\sigma}) : \boldsymbol{d}^* \, dv = \int_v \boldsymbol{\sigma}^* : \boldsymbol{d}^* \, dv - \int_v \boldsymbol{\sigma} : \boldsymbol{d} \, dv - \int_{a_\sigma} \boldsymbol{t}(\boldsymbol{v}^* - \boldsymbol{v}) \, da - \int_v \boldsymbol{f}(\boldsymbol{v}^* - \boldsymbol{v}) \, dv \geq 0 \tag{3.50}$$

is delivered. Because the integrand on the left side just states the principle of maximum plastic dissipation (Eq. (3.43)), it follows that each side of Eq. (3.50) may not become negative. Consequently,

$$\int_v \boldsymbol{\sigma}^* : \boldsymbol{d}^* \, dv - \int_{a_\sigma} \boldsymbol{t}\boldsymbol{v}^* \, da - \int_v \boldsymbol{f}\boldsymbol{v}^* \, dv \geq \int_v \boldsymbol{\sigma} : \boldsymbol{d} \, dv - \int_{a_\sigma} \boldsymbol{t}\boldsymbol{v} \, da - \int_v \boldsymbol{f}\boldsymbol{v} \, dv \tag{3.51}$$

holds, and because $\boldsymbol{\sigma}^*$ and $\boldsymbol{d}^*$as well as $\boldsymbol{\sigma}$ and $\boldsymbol{d}$ are associated via the normality rule, this gives

$$\int_v D_{\mathrm{p}}(\boldsymbol{d}^*) \, dv - \int_{a_\sigma} \boldsymbol{t}\boldsymbol{v}^* \, da - \int_v \boldsymbol{f}\boldsymbol{v}^* \, dv \geq \int_v D_{\mathrm{p}}(\boldsymbol{d}) \, dv - \int_{a_\sigma} \boldsymbol{t}\boldsymbol{v} \, da - \int_v \boldsymbol{f}\boldsymbol{v} \, dv \tag{3.52}$$

and

$$\Gamma(\boldsymbol{v}^*) \geq \Gamma(\boldsymbol{v}) \ , \tag{3.53}$$

respectively, thus proving the kinematic extremum principle stated above. It is to be noted, however, that it is not possible, in general, to strengthen the inequality (3.53) by asserting that the equality only holds when $\boldsymbol{v}^* = \boldsymbol{v}$, but only that such a solution is plastically equivalent to the actual one. For example, for the von Mises yield criterion (or any other plastically incompressible material with a smooth yield surface) this means that the entire deformation-rate field is determined to within a scale factor. The indeterminacy, however, may be eliminated if a nonzero velocity is prescribed anywhere on a_v [Lubliner, 1990].

---

[1] If the velocity fields involves regions that move as rigid bodies (rigid regions), then the strain rate there is, of course, zero and the question of association does not arise.

Upper Bound Theorem of Limit Analysis

The upper bound theorem of limit analysis (kinematic theorem) may directly be derived from the kinematic extremum principle. If from each side of Eq. (3.51) the power of external forces acting on a_v (with $\boldsymbol{v}^* = \boldsymbol{v}$),

$$\int_{a_v} \boldsymbol{t}\boldsymbol{v}^* \, da = \int_{a_v} \boldsymbol{t}\boldsymbol{v} \, da \; , \tag{3.54}$$

is subtracted, then one obtains

$$\int_v \boldsymbol{\sigma}^* : \boldsymbol{d}^* \, dv - \int_a \boldsymbol{t}\boldsymbol{v}^* \, da - \int_v \boldsymbol{f}\boldsymbol{v}^* \, dv \geq \int_v \boldsymbol{\sigma} : \boldsymbol{d} \, dv - \int_a \boldsymbol{t}\boldsymbol{v} \, da - \int_v \boldsymbol{f}\boldsymbol{v} \, dv = 0 \; , \tag{3.55}$$

where the right hand side of this inequality just represents the difference between actual internal and external power, which equals zero. Therefore, the upper bound theorem may first be expressed as

$$\int_v \boldsymbol{\sigma}^* : \boldsymbol{d}^* \, dv \geq \int_a \boldsymbol{t}\boldsymbol{v}^* \, da + \int_v \boldsymbol{f}\boldsymbol{v}^* \, dv \; . \tag{3.56}$$

If all external forces acting on the body can be expressed in terms of a single load parameter and a given set of reference loads (i.e. surface forces $\boldsymbol{t} = \lambda \boldsymbol{t}_0$, volume forces $\boldsymbol{f} = \lambda \boldsymbol{f}_0$), then the upper bound theorem may alternatively be written as

$$\overline{\lambda} \leq \lambda^+(\boldsymbol{v}^*) = \frac{D_{\text{int}}(\boldsymbol{v}^*)}{D_{\text{ext},0}(\boldsymbol{v}^*)} = \frac{\int_v \boldsymbol{\sigma}^* : \boldsymbol{d}^* \, dv}{\int_a \boldsymbol{t}_0\boldsymbol{v}^* \, da + \int_v \boldsymbol{f}_0\boldsymbol{v}^* \, dv} \; , \tag{3.57}$$

where λ^+ is an upper bound for the actual limit load multiplier $\overline{\lambda}$, which is obtained by dividing the power of internal forces, D_{int}, by the power of external reference forces, $D_{\text{ext},0}$.

The relation

$$\int_v \boldsymbol{\sigma}^* : \boldsymbol{d}^* \, dv = \lambda^+ (\int_a \boldsymbol{t}_0\boldsymbol{v}^* \, da + \int_v \boldsymbol{f}_0\boldsymbol{v}^* \, dv) \tag{3.58}$$

and

$$D_{\text{int}}(\boldsymbol{v}^*) = \lambda^+ D_{\text{ext},0} \; , \tag{3.59}$$

respectively, formally introduced in Eq. (3.57), is known as the power equation, which is often used as a statement of global equilibrium of a structure.

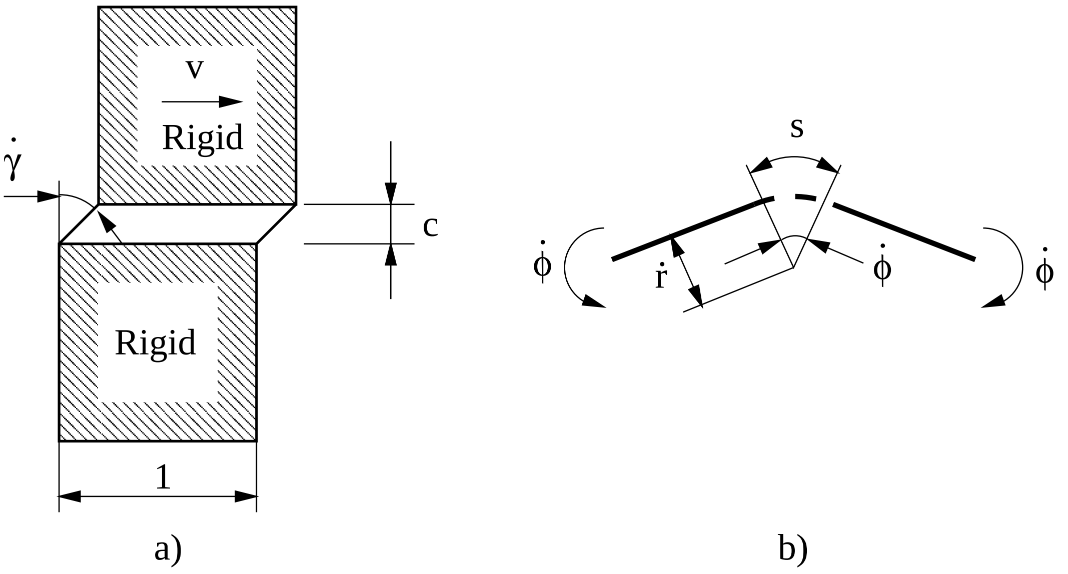

Figure 3.1: Transition zones for pure shear (a) and bending deformations (b)

Remarks

The principles stated above have been derived under the assumption that the kinematically admissible velocity fields are continuous and continuously differentiable. Plastic deformations, however, are typically characterized by a strong localization of deformations, which practically leads to the formation of discontinuous velocity fields (e.g. shear bands) and derivatives (e.g. plastic hinges and yield lines), respectively. These types of discontinuities, however, are just idealizations of a continuous distribution in which the velocity rapidly changes across a very small region. Consequently, the theorems remain valid in the limit as the dimensions of such deformation regions approach zero, with the rate of dissipation approaching finite values. For example, a transition zone for pure shear is sketched in Figure 3.1a. The plastic dissipation due to these deformations is given by

$$D_\mathrm{p} = k\dot\gamma c = k\frac{v}{c}c = kv \tag{3.60}$$

(herein k means the yield stress in simple shear, $\dot\gamma$ and c are defined in Figure 3.1a). In a similar way, a beam subjected to pure bending is sketched in Figure 3.1b. With the plastic bending moment M_0 the whole energy dissipation D_arc of the deforming circular part is given by

$$D_\mathrm{arc} = M_0\dot\kappa s = M_0\frac{\dot\varphi}{s}s = M_0\dot\varphi \ , \tag{3.61}$$

where $\dot{\kappa}$ is the time derivative of the curvature, $\dot{\varphi}$ the angular velocity and s the arc length of the plastically deforming part.

In both cases it can be seen that the evaluation of the plastic energy dissipation does not depend on the dimensions of the plastic zone and thus can be performed even for vanishing lengths c and s, respectively.

3.4 Exact Ilyushin Yield Surface

In 1948, Ilyushin published the derivation of a stress resultant yield surface (in Russian), describing the case where a point of a shell is fully plastified and thus reaches its load capacity. This yield surface, however, may only be described in parametric form and the parametrization originally proposed by Ilyushin [1948] is not amenable to structural application. This is the main reason why in practice mostly approximations have been used up to now, e.g. a linear approximation proposed by Ilyushin himself (which in many publications is simply denoted as "Ilyushin yield surface"), the Ivanov yield surface, etc. The derivation and description of the exact Ilyushin yield surface presented in this section is closely related to the work of Burgoyne and Brennan [1993b]. In their work the authors propose a reparametrization of the yield surface, allowing a more convenient description, which opens the way for practical use of the exact Ilyushin yield surface in structural calculations. In a companion paper [Burgoyne and Brennan, 1993a] a strategy for calculating elastoplastic rigidities (and the tangential stiffness matrix, respectively) when using the exact Ilyushin yield surface, is discussed and presented. This work, however, will be referred to when describing the full section constitutive model in section 7.

3.4.1 Definitions

With the yield stress σ_y and a reference strain ε_0 stresses and strain increments are expressed in normalized vectorial form as

$$\overline{\boldsymbol{\sigma}} = \frac{1}{\sigma_y}\begin{pmatrix}\sigma_{11}\\ \sigma_{22}\\ \sigma_{12}\end{pmatrix} \quad \text{and} \quad d\boldsymbol{e} = \frac{1}{\varepsilon_0}\begin{pmatrix}d\varepsilon_{11}\\ d\varepsilon_{22}\\ 2d\varepsilon_{12}\end{pmatrix} . \qquad (3.62)$$

Herein $\sigma_{\alpha\beta}$ and $d\varepsilon_{\alpha\beta}$ $(\alpha, \beta \in \{1,2\})$ are the components of the physical stress and of the strain increment tensor for a state of plane stress.[2] The position along the normal coordinate of the shell (thickness h) is described by a dimensionless coordinate $\overline{z} \in [-1/2, 1/2]$.

According to the definition of normalized stresses and strain increments generalized normalized stress and strain increment vectors are introduced:

$$\boldsymbol{n} = \frac{1}{N_0}\begin{pmatrix} N_{11} \\ N_{22} \\ N_{12} \end{pmatrix}, \quad \boldsymbol{m} = \frac{1}{M_0}\begin{pmatrix} M_{11} \\ M_{22} \\ M_{12} \end{pmatrix}, \quad d\overline{\boldsymbol{e}} = \frac{1}{\varepsilon_0}\begin{pmatrix} d\overline{\varepsilon}_{11} \\ d\overline{\varepsilon}_{22} \\ 2d\overline{\varepsilon}_{12} \end{pmatrix}, \quad d\boldsymbol{k} = \frac{1}{\kappa_0}\begin{pmatrix} d\kappa_{11} \\ d\kappa_{22} \\ 2d\kappa_{12} \end{pmatrix}, \tag{3.63}$$

with $N_0 = \sigma_y h$ and $M_0 = \sigma_y h^2/4$ being the sectional limit load in uniaxial tension and uniaxial bending, respectively. For convenience, the reference curvature κ_0 is chosen such that it fulfills the condition $N_0 \varepsilon_0 = M_0 \kappa_0$ (from which it follows that $\kappa_0 = 4\varepsilon_0/h$). $N_{\alpha\beta}$, $M_{\alpha\beta}$, $d\overline{\varepsilon}_{\alpha\beta}$ and $d\kappa_{\alpha\beta}$ are the physical section force and bending moment as well as the midplane strain and curvature increment components of a Kirchhoff shell, respectively ($d\overline{\boldsymbol{e}} = d\boldsymbol{e}(\overline{z} = 0)$).

A summary concerning the definition of the normalized quantities, its use to state several equations of shell theory, and the derivation of the relations between physical and normalized values are given in Appendix B.1.

3.4.2 Derivation

The derivation of the exact Ilyushin yield surface is based on the following assumptions:

- perfectly plastic isotropic material behaviour obeying the von Mises yield criterion,
- validity of the normality rule for the plastic deformations,[3]

---

[2] In order to keep consistent with the presentation of the exact Ilyushin yield surface in [Burgoyne and Brennan, 1993b], incremental instead of strain rate quantities are used in the following. It is to be noted, however, that the stated relations are not affected, if strain rate quantities are used throughout, provided the reference values ε_0 and κ_0 are replaced by reference strain and curvature rates $\dot{\varepsilon}_0$ and $\dot{\kappa}_0$, respectively (thus ensuring that dimensionless quantities are used throughout).

[3] For the derivation and representation of the yield surface, an additive decomposition of the strain increments into elastic and plastic parts, $d\boldsymbol{e} = d\boldsymbol{e}^e + d\boldsymbol{e}^p$, is assumed, which is used for the description of the FE full section constitutive model in chapter 7. For rigid plastic material behaviour, however, $d\boldsymbol{e}^e$ vanishes and, accordingly, $d\boldsymbol{e}^p$ equates $d\boldsymbol{e}$ (in terms of strain rates: $\boldsymbol{d}^p = \boldsymbol{d}$).

- plane stress conditions in each material point,
- validity of the Kirchhoff hypothesis for both total and plastic strains.

In the limit, each material point through the thickness has plastic material behaviour. Therefore, both the von Mises yield condition and the normality rule, are valid:

$$f(\overline{\boldsymbol{\sigma}}) = \overline{\boldsymbol{\sigma}}^T \mathbf{P} \overline{\boldsymbol{\sigma}} - 1 = 0 \; , \qquad \mathbf{P} = \begin{pmatrix} 1 & -\frac{1}{2} & 0 \\ -\frac{1}{2} & 1 & 0 \\ 0 & 0 & 3 \end{pmatrix} \; , \tag{3.64}$$

$$d\boldsymbol{e}^p = d\xi \frac{\partial f}{\partial \overline{\boldsymbol{\sigma}}} \; . \tag{3.65}$$

From Eqs. (3.64) and (3.65) $\overline{\boldsymbol{\sigma}}$ and $d\xi$ can be expressed as functions of $d\boldsymbol{e}^p$:

$$\overline{\boldsymbol{\sigma}}(d\boldsymbol{e}^p) = \frac{1}{2d\xi(d\boldsymbol{e}^p)} \mathbf{P}^{-1} \, d\boldsymbol{e}^p \tag{3.66}$$

and

$$d\xi(d\boldsymbol{e}^p) = \sqrt{\frac{1}{4} \, (d\boldsymbol{e}^p)^T \, \mathbf{P}^{-1} \, d\boldsymbol{e}^p} \; . \tag{3.67}$$

The Kirchhoff hypothesis in normalized form is expressed as (see Appendix B.1, Eq. (B.14))

$$d\boldsymbol{e}(\overline{z}) = d\overline{\boldsymbol{e}} + 4\overline{z} \, d\boldsymbol{k} \; . \tag{3.68}$$

Now, it is assumed that the plastic strain increment resultants also obey the Kirchhoff hypothesis.[4] Therefore:

$$d\boldsymbol{e}^p(\overline{z}) = d\overline{\boldsymbol{e}}^p + 4\overline{z} \, d\boldsymbol{k}^p \; . \tag{3.69}$$

This equation can be used to express $d\boldsymbol{e}^p$ in Eq. (3.67), resulting in

$$d\xi = \frac{1}{\sqrt{3}} \sqrt{P_\varepsilon + 2P_{\varepsilon\kappa}\overline{z} + P_\kappa \overline{z}^2} \; , \tag{3.70}$$

with

$$\begin{aligned} P_\varepsilon &= \frac{3}{4} (d\overline{\boldsymbol{e}}^p)^T \mathbf{P}^{-1} \, d\overline{\boldsymbol{e}}^p \quad (\geq 0) \; , \\ P_{\varepsilon\kappa} &= 3 (d\overline{\boldsymbol{e}}^p)^T \mathbf{P}^{-1} \, d\boldsymbol{k}^p \; , \\ P_\kappa &= 12 (d\boldsymbol{k}^p)^T \mathbf{P}^{-1} \, d\boldsymbol{k}^p \quad (\geq 0) \; . \end{aligned} \tag{3.71}$$

---

[4] This distinction, however, must only be made for nonvanishing elastic strain increments — for rigid plastic material behaviour Eq. (3.69) is identically satisfied by Eq. (3.68).

These incremental plastic strain resultant intensities are subject to the condition

$$P_\varepsilon P_\kappa \geq P_{\varepsilon\kappa}^2 \; . \tag{3.72}$$

Substitution of Eqs. (3.70) and (3.69) in Eq. (3.66) gives

$$\overline{\boldsymbol{\sigma}} = \frac{\sqrt{3}}{2} \frac{1}{\sqrt{P_\varepsilon + 2P_{\varepsilon\kappa}\overline{z} + P_\kappa \overline{z}^2}} \mathbf{P}^{-1}(d\overline{\boldsymbol{e}}^p + 4\overline{z}\, d\boldsymbol{k}^p) \; , \tag{3.73}$$

from which the non-dimensional stress resultants can be obtained. With

$$\boldsymbol{n} = \int_{-1/2}^{1/2} \overline{\boldsymbol{\sigma}}\, d\overline{z} \qquad \text{and} \qquad \boldsymbol{m} = 4 \int_{-1/2}^{1/2} \overline{\boldsymbol{\sigma}}\overline{z}\, d\overline{z} \tag{3.74}$$

(see Appendix B.1, Eqs. (B.7)) the stress resultants may finally be written as

$$\begin{pmatrix} \boldsymbol{n} \\ \boldsymbol{m} \end{pmatrix} = \frac{3}{2} \begin{pmatrix} J_0 \mathbf{P}^{-1} & 4J_1\mathbf{P}^{-1} \\ 4J_1\mathbf{P}^{-1} & 16J_2\mathbf{P}^{-1} \end{pmatrix} \begin{pmatrix} d\overline{\boldsymbol{e}}^p \\ d\boldsymbol{k}^p \end{pmatrix} , \tag{3.75}$$

where the integrals J_i depend only on the incremental plastic strain resultant intensities P_ε, $P_{\varepsilon\kappa}$ and P_κ:

$$J_i = \frac{1}{\sqrt{3}} \int_{-1/2}^{1/2} \frac{\overline{z}^i}{\sqrt{P_\varepsilon + 2P_{\varepsilon\kappa}\overline{z} + P_\kappa \overline{z}^2}}\, d\overline{z} \; , \tag{3.76}$$

which may be evaluated analytically.

Equation (3.75) can be regarded as a six-dimensional stress resultant yield surface for the limit that the shell is wholly plastic and thus in each point over the thickness the von Mises yield criterion and the normality rule are satisfied. If the direction of the plastic strain increment resultants is given, the stress resultants can be obtained from Eq. (3.75), provided the integrals J_i can be evaluated numerically (if $P_\varepsilon P_\kappa - P_{\varepsilon\kappa}^2 = 0$ and $P_\kappa > 0$, then these integrals may become infinite — for a numerical treatment of this case see Appendix B.2).

3.4.3 Three-Dimensional Representations

The set of six equations given in Eq. (3.75) can be reduced to three by introducing quadratic stress resultant intensities

$$\begin{aligned} Q_t &= \boldsymbol{n}^T \mathbf{P} \boldsymbol{n} \quad (\geq 0) \; , \\ Q_{tm} &= \boldsymbol{n}^T \mathbf{P} \boldsymbol{m} \; , \\ Q_m &= \boldsymbol{m}^T \mathbf{P} \boldsymbol{m} \quad (\geq 0) \; . \end{aligned} \tag{3.77}$$

Together with the definition of P_ε, $P_{\varepsilon\kappa}$ and P_κ (Eq. (3.71)) this leads to

$$\begin{pmatrix} Q_t \\ Q_{tm}/4 \\ Q_m/16 \end{pmatrix} = 3 \begin{pmatrix} J_0^2 & J_0 J_1 & J_1^2 \\ J_0 J_1 & (J_0 J_2 + J_1^2)/2 & J_1 J_2 \\ J_1^2 & J_1 J_2 & J_2^2 \end{pmatrix} \begin{pmatrix} P_\varepsilon \\ 2P_{\varepsilon\kappa} \\ P_\kappa \end{pmatrix} . \tag{3.78}$$

The yield surface is subject to the condition

$$Q_t Q_m \geq Q_{tm}^2 , \tag{3.79}$$

with the boundary given by the equality sign (and corresponding to the case that $P_\varepsilon P_\kappa - P_{\varepsilon\kappa}^2 = 0$). Equation (3.78) describes a surface in the three-dimensional Q-space and, therefore, can be represented in parameter form as a function of two independent parameters. An implicit form of Eq. (3.78), i.e. $F = F(Q_t, Q_{tm}, Q_m) = 0$, however, cannot be obtained. In order to avoid the complexity of the parametrized exact form of the yield surface proposed by Ilyushin (see below), in practical computations mainly approximations, leading to implicit forms, where used up to now. Ilyushin [1948] himself proposed a linear approximation, consisting of two planes in Q-space:

$$F_1 = Q_t + \frac{1}{\sqrt{3}} |Q_{tm}| + Q_m - 1 = 0 . \tag{3.80}$$

This often used approximation introduces a discontinuity at the line $Q_{tm} = 0$. Figure 3.2 shows a graphical representation of the exact and the linear approximation of the yield surface in Q-space. As can be seen, the surface is symmetrical with respect to the Q_t-Q_m-plane. It can also be plotted in two-dimensional form as Q_{tm} against $Q_t - Q_m$ without loss of clarity [Burgoyne and Brennan, 1993b], see Figure 3.3.

A quadratic approximation of the exact Ilyushin yield surface was proposed by Ivanov [1967]:

$$F_2 = Q_t + \frac{Q_m}{2} + \sqrt{Q_m^2/4 + Q_{tm}^2} - \frac{1}{4} \left(\frac{Q_t Q_m - Q_{tm}^2}{Q_t + 0.48 Q_m} \right) - 1 = 0 . \tag{3.81}$$

The yield surface F_2 always lies within 1% of the exact one and avoids discontinuities at $Q_{tm} = 0$ (except at the point $Q_t = 1$, where the exact yield surface also has a slope discontinuity).

Further suggestions of approximate full plasticity yield surfaces, partly including the effect of transverse shear as well as hardening effects, can be found e.g. in [Robinson, 1971]. In order to take into account the spreading of the plastic zone over the thickness, stress resultant based approximations where suggested, too (see e.g. [Crisfield, 1980, 1997; Başar and Krätzig, 1985; Auricchio and Taylor, 1994]).

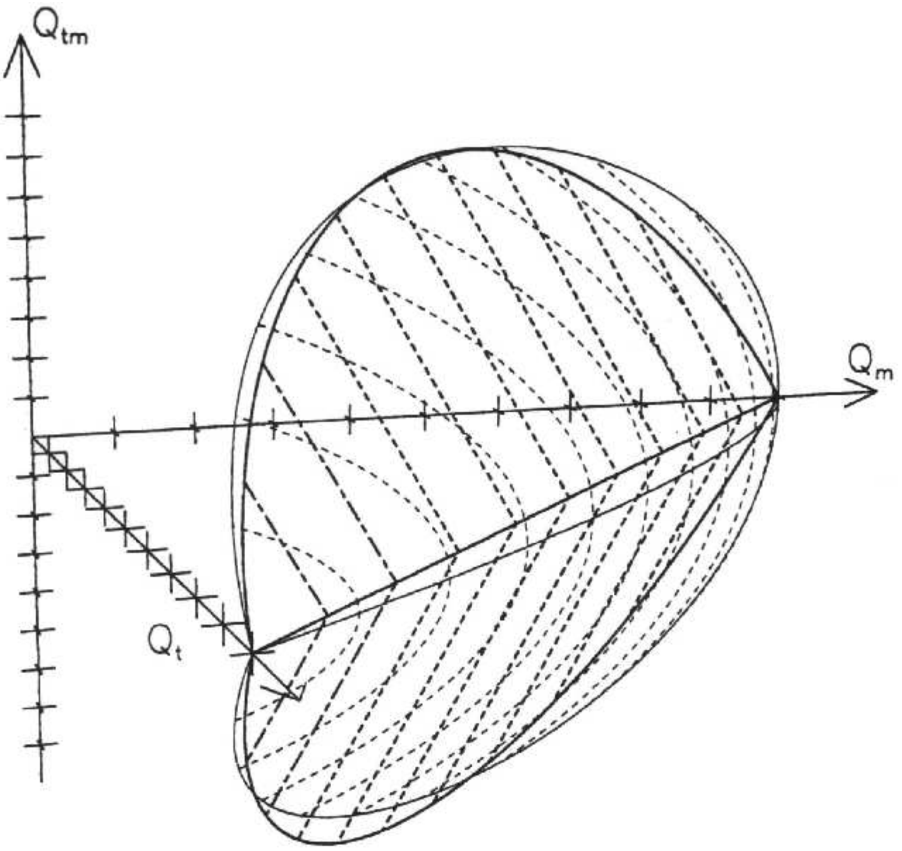

Figure 3.2: Three-dimensional view of the exact and the linear approximation of the Ilyushin yield surface (from [Burgoyne and Brennan, 1993b])

Ilyushin's Parametrization

For the description of the exact Ilyushin yield surface in parametrized form, Ilyushin [1948] introduced the following parameters:

$$\begin{aligned} \zeta &= \left(\frac{P_\varepsilon - P_{\varepsilon\kappa} + P_\kappa/4}{P_\varepsilon + P_{\varepsilon\kappa} + P_\kappa/4} \right)^{1/2} , \\ \mu &= \left(\frac{P_\varepsilon P_\kappa - P_{\varepsilon\kappa}^2}{P_\kappa (P_\varepsilon + P_{\varepsilon\kappa} + P_\kappa/4)} \right)^{1/2} . \end{aligned} \tag{3.82}$$

The resulting equations for the exact yield surface are:

$$\begin{aligned} Q_t &= \frac{1}{{\Delta_1}^2}(\mu^2\psi^2+\varphi^2)\ , \\ Q_{tm} &= \frac{2}{{\Delta_1}^3}(\mu^2\Delta\psi^2+\Delta\varphi^2+\mu^2\varphi\psi+\varphi\chi)\ , \\ Q_m &= \frac{4}{{\Delta_1}^4}(\mu^2\psi^2(\mu^2+\Delta^2)+\varphi^2(4\mu^2+\Delta^2)+2\mu^2\Delta\varphi\psi-2\mu^2\psi\chi+2\Delta\varphi\chi+\chi^2)\ , \end{aligned} \tag{3.83}$$

where

$$\begin{aligned} \varphi &= \zeta - 1\ , \\ \psi &= \left| \ln\frac{(1+\sqrt{1-\mu^2})}{\mu} \pm \ln\frac{(\zeta+\sqrt{\zeta^2-\mu^2})}{\mu} \right|\ , \\ \chi &= \left|\sqrt{1-\mu^2}\pm\zeta\sqrt{\zeta^2-\mu^2}\right|\ , \\ \Delta_1 &= \sqrt{1-\mu^2}\pm\sqrt{\zeta^2-\mu^2}\ , \\ \Delta &= \frac{1-\zeta^2}{\Delta_1}\ , \end{aligned} \tag{3.84}$$

subject to the conditions

$$\begin{aligned} 0 \le \mu \le 1\ , \\ \mu \le \zeta \le 1\ . \end{aligned} \tag{3.85}$$

The boundary is given by $\mu = 0$. Ilyushin's original parametrization makes it necessary to divide the surface into four regions, each region characterized by different equations (due to the alternative signs). Within one half of the surface (e.g. $Q_{tm} \ge 0$) one has to divide into "in-plane dominant" and "bending dominant" regions. Besides, lines of constant ζ and μ are virtually parallel in many cases and, therefore, a numerical algorithm based on these parameters will be ill-conditioned and numerically unstable [Burgoyne and Brennan, 1993b].

Parametrization of Burgoyne and Brennan

In order to overcome some of the problems arising with the parametrization described above, Burgoyne and Brennan [1993b] introduced the parameters

$$\alpha = \frac{P_\varepsilon}{P_\kappa}\ , \qquad \beta = -\frac{P_{\varepsilon\kappa}}{P_\kappa} \quad \text{and} \quad \gamma = \alpha - \beta^2\ , \tag{3.86}$$

and proposed to apply β and γ as independent parameters for the description of the yield surface. β has the physical meaning of being the position within the thickness of the shell, where the consistency parameter $d\xi$ (being a measure for the equivalent plastic strain increment) is a minimum. With β and γ the yield surface takes the following form:

$$\begin{aligned} Q_t &= (\beta K_0 - K_1)^2 + \gamma {K_0}^2 \ , \\ Q_{tm} &= 4(\beta K_0 - K_1)(\beta K_1 - K_2) + 4\gamma K_0 K_1 \ , \\ Q_m &= 16(\beta K_1 - K_2)^2 + 16\gamma {K_1}^2 \ , \end{aligned} \tag{3.87}$$

where the integrals K_i are given by

$$K_i = \sqrt{3P_\kappa} \cdot J_i = \int_{-1/2}^{1/2} \frac{\overline{z}^i}{\sqrt{(\overline{z}-\beta)^2+\gamma}} d\overline{z} \ . \tag{3.88}$$

The yield surface (Eq. (3.87)) is subject to the limits

$$\begin{aligned} &0 \le \beta^2 \le \alpha \le \infty \ , \\ &0 \le \gamma \le \infty \ . \end{aligned} \tag{3.89}$$

Figure 3.3 shows a two-dimensional representation of one half of the yield surface ($Q_{tm} \le 0$) in terms of the two parameters β and γ.

The integrals K_i (Eq. (3.88)) may be integrated analytically to give

$$\begin{aligned} K_0 &= \ln \left| \frac{\sqrt{(0.5-\beta)^2+\gamma} + (0.5-\beta)}{\sqrt{(0.5+\beta)^2+\gamma} - (0.5+\beta)} \right| \ , \\ K_1 &= \sqrt{(0.5-\beta)^2+\gamma} - \sqrt{(0.5+\beta)^2+\gamma} + \beta K_0 \ , \\ 2K_2 &= (0.5+\beta)\sqrt{(0.5-\beta)^2+\gamma} + (0.5-\beta)\sqrt{(0.5+\beta)^2+\gamma} + 2\beta K_1 - \gamma K_0 \ . \end{aligned} \tag{3.90}$$

The boundary curve is given by $Q_t Q_m = Q_{tm}^2$ and $\gamma = 0$, respectively.[5] For $\gamma = 0$ and $|\beta| \le 0.5$ the factors K_i become

$$\begin{aligned} K_0 &= \infty \ , \\ K_1 &= -2\beta + \beta K_0 \ , \\ K_2 &= 0.25 - 3\beta^2 + \beta^2 K_0 \ . \end{aligned} \tag{3.91}$$

---

[5] Physically, the boundary represents the case, when the directions of $d\overline{\boldsymbol{e}}^p$ and $d\boldsymbol{k}^p$ and $\boldsymbol{n}$ and $\boldsymbol{m}$, respectively, coincide ($d\overline{\boldsymbol{e}}^p \sim d\boldsymbol{k}^p$, $\boldsymbol{n} \sim \boldsymbol{m}$).

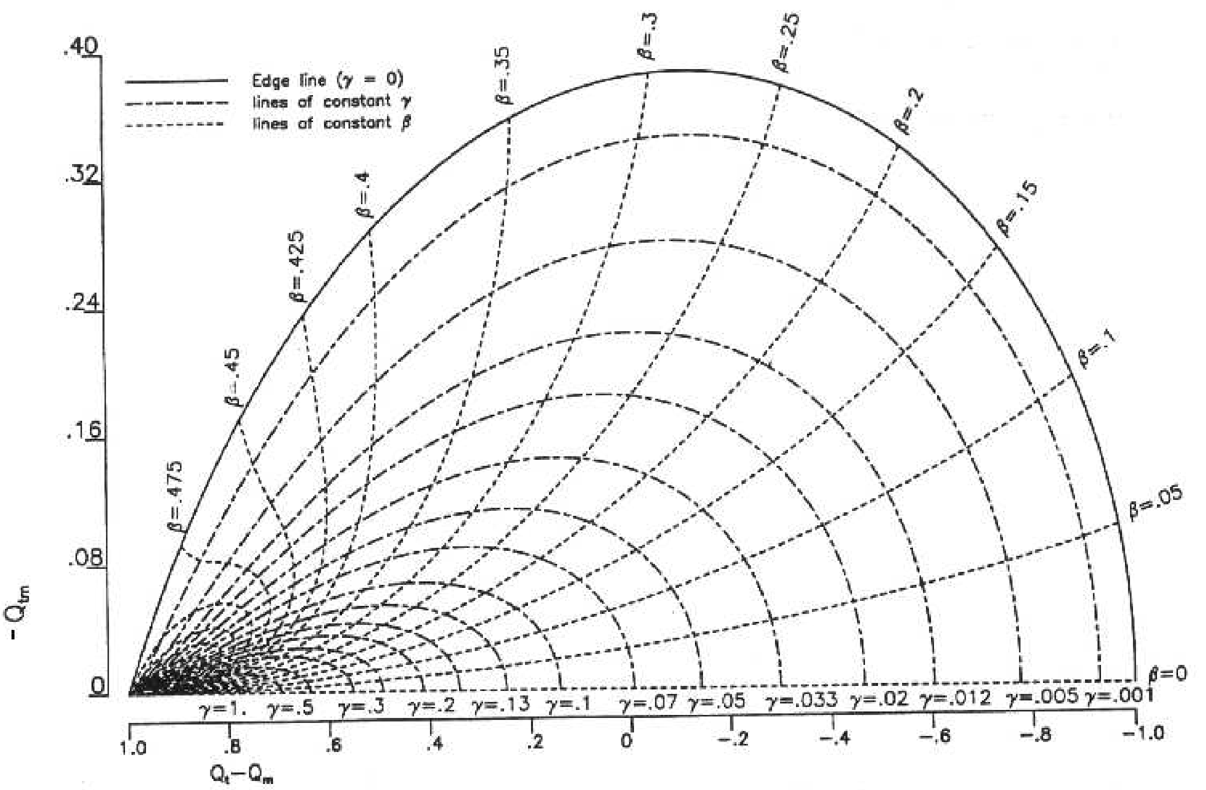

Figure 3.3: One half of the exact Ilyushin yield surface ($Q_{tm} \leq 0$) constructed in terms of β and γ (from [Burgoyne and Brennan, 1993b])

By inserting these values into the definition for the yield surface, Eq. (3.87), the K_0-term cancels and the yield surface can be expressed as

$$\begin{aligned} Q_t &= 4\beta^2 \,, \\ Q_{tm} &= -2\beta(1-4\beta^2) \,, \\ Q_m &= (1-4\beta^2)^2 \,, \end{aligned} \tag{3.92}$$

or in implicit form as[6]

$$Q_m = (1-Q_t)^2 \,. \tag{3.93}$$

In all cases, when $\gamma > 0$ or $|\beta| > 0.5$, the integrals K_i are well defined and thus can be evaluated numerically (even if precautions must be taken to avoid numerical difficulties, which may arise for in-plane dominant loading conditions — for details see the proposed algorithmic structure for the numerical evaluation of the J_i-integrals in Appendix B.2).

---

[6] The interaction between axial force and bending moment of an uniaxially loaded rectangular beam (see e.g. [Chen and Han, 1988]) is also contained in Eq.(3.93). With n_1 and m_1 being the only components of the generalized stress vectors $\boldsymbol{n}$ and $\boldsymbol{m}$, which are not equal to zero, Eq.(3.93) just delivers the yield criterion $|m_1| + n_1^2 - 1 = 0$.

3.4.4 Normality Rule

Regarding the normality rule Burgoyne and Brennan [1993b] have shown that this also holds in stress resultant space.

In the three-dimensional Q-space the normal direction onto the yield surface may be found as

$$\begin{aligned} F_t &= \frac{\partial F}{\partial Q_t} = C(16K_2) \ , \\ F_{tm} &= \frac{\partial F}{\partial Q_{tm}} = C(-8K_1) \ , \\ F_m &= \frac{\partial F}{\partial Q_m} = C(K_0) \ , \end{aligned} \tag{3.94}$$

where C is a constant defining the magnitude of the normal vector. Using this, the normality rule in stress resultant space is expressed as

$$\begin{aligned} \begin{pmatrix} d\overline{\boldsymbol{e}}^p \\ d\boldsymbol{k}^p \end{pmatrix} &= d\overline{\xi} \begin{pmatrix} \partial F/\partial \boldsymbol{n} \\ \partial F/\partial \boldsymbol{m} \end{pmatrix} = d\overline{\xi} \begin{pmatrix} 2F_t\mathbf{P} & F_{tm}\mathbf{P} \\ F_{tm}\mathbf{P} & 2F_m\mathbf{P} \end{pmatrix} \begin{pmatrix} \boldsymbol{n} \\ \boldsymbol{m} \end{pmatrix} = \\ &= 2Cd\overline{\xi} \begin{pmatrix} 16K_2\mathbf{P} & -4K_1\mathbf{P} \\ -4K_1\mathbf{P} & K_0\mathbf{P} \end{pmatrix} \begin{pmatrix} \boldsymbol{n} \\ \boldsymbol{m} \end{pmatrix} . \end{aligned} \tag{3.95}$$

This six-dimensional form of the normality rule (with $d\overline{\xi}$ already determined), however, can directly be obtained from the six-dimensional representation of the exact Ilyushin yield surface. Inversion of Eq. (3.75) to get $d\overline{\boldsymbol{e}}^p$ and $d\boldsymbol{k}^p$ delivers

$$\begin{pmatrix} d\overline{\boldsymbol{e}}^p \\ d\boldsymbol{k}^p \end{pmatrix} = \frac{1}{24(J_0J_2 - J_1^2)} \begin{pmatrix} 16J_2\mathbf{P} & -4J_1\mathbf{P} \\ -4J_1\mathbf{P} & J_0\mathbf{P} \end{pmatrix} \begin{pmatrix} \boldsymbol{n} \\ \boldsymbol{m} \end{pmatrix} , \tag{3.96}$$

and because the J_i-integrals are directly related to the K_i-terms by Eq. (3.88), this form is just an alternative statement of the normality rule given in Eq. (3.95).

It is remarkable that the terms $\overline{J}_i = J_i/(J_0J_2 - J_1^2)$ are definite values at any point of the yield surface, including the boundary. For $\gamma = 0$ and $|\beta| \leq 0.5$ one obtains (using Eqs.

(3.91))

$$\begin{aligned}\overline{J}_0 &= \sqrt{3P_\kappa}\frac{K_0}{K_0K_2 - K_1^2} = \sqrt{3P_\kappa}\frac{1}{0.25+\beta^2} \ ,\\ \overline{J}_1 &= \sqrt{3P_\kappa}\frac{K_1}{K_0K_2 - K_1^2} = \sqrt{3P_\kappa}\frac{\beta}{0.25+\beta^2} \ ,\\ \overline{J}_2 &= \sqrt{3P_\kappa}\frac{K_2}{K_0K_2 - K_1^2} = \sqrt{3P_\kappa}\frac{\beta^2}{0.25+\beta^2} \ .\end{aligned} \tag{3.97}$$

In all other cases the integrals for J_i can be evaluated numerically and even the factors $\overline{J}_i$ are well defined. For the special point $P_\kappa = 0$ (and $Q_t = 1$, respectively), describing pure in-plane loading, the J_i- and $\overline{J}_i$-terms take the simple form

$$\begin{aligned} J_0 &= \frac{1}{\sqrt{3P_\varepsilon}} \ , & J_1 &= 0 \ , & J_2 &= \frac{1}{12\sqrt{3P_\varepsilon}} \ ,\\ \overline{J}_0 &= \frac{1}{J_2} = 12\sqrt{3P_\varepsilon} \ , & \overline{J}_1 &= 0 \ , & \overline{J}_2 &= \frac{1}{J_0} = \sqrt{3P_\varepsilon} \ . \end{aligned} \tag{3.98}$$

With regard to changes of the slope Burgoyne and Brennan [1993b] have shown that there is a strong but continuous change of the normal directions along the boundary of the yield surface — at the point $Q_t = 1$, however, there is a true slope discontinuity (see also chapter 7).

3.4.5 Power of Internal Forces

The derivation and description of the exact Ilyushin yield surface presented above was performed with incremental strain quantities. For the evaluation of the power of internal forces, however, a description in terms of strain rate quantities is more convenient. As was already mentioned above, the consistent use of strain rate quantities (instead of the actually used strain increments) does not affect the stated relations, provided the reference values ε_0 and κ_0 are substituted by reference strain and curvature rates $\dot{\varepsilon}_0$ and $\dot{\kappa}_0$, respectively. According to Eq. (3.63), therefore, dimensionless generalized strain rate vectors $\dot{\overline{\boldsymbol{e}}}^p$ and $\dot{\boldsymbol{k}}^p$ are defined:

$$\dot{\overline{\boldsymbol{e}}} = \frac{1}{\dot{\varepsilon}_0}\begin{pmatrix}\dot{\overline{\varepsilon}}_{11}\\ \dot{\overline{\varepsilon}}_{22}\\ 2\dot{\overline{\varepsilon}}_{12}\end{pmatrix} \ , \quad \dot{\boldsymbol{k}} = \frac{1}{\dot{\kappa}_0}\begin{pmatrix}\dot{\kappa}_{11}\\ \dot{\kappa}_{22}\\ 2\dot{\kappa}_{12}\end{pmatrix} \ , \tag{3.99}$$

replacing the generalized strain increments $d\overline{\boldsymbol{e}}$ and $d\boldsymbol{k}$.

The plastic dissipation for a shell-like structure may be written as

$$\overline{d}_{\mathrm{p}} = \frac{\overline{D}_{\mathrm{p}}}{N_0 \dot{\varepsilon}_0} = \begin{pmatrix} \boldsymbol{n} \\ \boldsymbol{m} \end{pmatrix}^T \begin{pmatrix} \dot{\boldsymbol{e}}^p \\ \dot{\boldsymbol{k}}^p \end{pmatrix} , \tag{3.100}$$

where $\overline{D}_{\mathrm{p}}$ is the physical and $\overline{d}_{\mathrm{p}}$ the normalized plastic dissipation per unit area of the shell's midplane (herein, the validity of the condition $N_0 \dot{\varepsilon}_0 = M_0 \dot{\kappa}_0$ is assumed). With the six-dimensional representation of the exact Ilyushin yield surface, Eq. (3.75) (written in rate form), $\overline{d}_{\mathrm{p}}$ may be expressed as a pure function of the strain rate resultant quantities $\dot{\boldsymbol{e}}^p$ and $\dot{\boldsymbol{k}}^p$:

$$\overline{d}_{\mathrm{p}}(\dot{\boldsymbol{e}}^p, \dot{\boldsymbol{k}}^p) = \frac{3}{2} \begin{pmatrix} \dot{\boldsymbol{e}}^p \\ \dot{\boldsymbol{k}}^p \end{pmatrix}^T \begin{pmatrix} J_0 \mathbf{P}^{-1} & 4J_1 \mathbf{P}^{-1} \\ 4J_1 \mathbf{P}^{-1} & 16 J_2 \mathbf{P}^{-1} \end{pmatrix} \begin{pmatrix} \dot{\boldsymbol{e}}^p \\ \dot{\boldsymbol{k}}^p \end{pmatrix} . \tag{3.101}$$

Analytical evaluation of this relation delivers

$$\overline{d}_{\mathrm{p}} = 2 \left(J_0 P_\varepsilon + 2 J_1 P_{\varepsilon\kappa} + J_2 P_\kappa \right) = \frac{2}{\sqrt{3}} \int_{-1/2}^{1/2} \sqrt{P_\varepsilon + 2 P_{\varepsilon\kappa} \overline{z} + P_\kappa \overline{z}^2} \, d\overline{z} , \tag{3.102}$$

which finally may be written as

$$\overline{d}_{\mathrm{p}} = \begin{cases} 2\sqrt{\frac{P_\varepsilon}{3}} & \text{for } P_\kappa = 0 , \\ \sqrt{\frac{P_\kappa}{3}} \left(\beta_1 \sqrt{\beta_1^2 + \gamma} + \beta_2 \sqrt{\beta_2^2 + \gamma} + \gamma K_0 \right) & \text{for } P_\kappa > 0 . \end{cases} \tag{3.103}$$

Herein, besides the parameters γ and K_0 the auxiliary variables

$$\beta_1 = \frac{1}{2} - \beta \qquad \text{and} \qquad \beta_2 = \frac{1}{2} + \beta \tag{3.104}$$

have been used. For cases, in which K_0 may become infinite ($\gamma \to 0$), it can be shown that the term γK_0 cancels, and hence, Eq. (3.103) is amenable to a numerical evaluation for all values of $\dot{\boldsymbol{e}}^p$ and $\dot{\boldsymbol{k}}^p$ (even without regularization of points at the boundary).

Equation (3.103) is formulated such that a direct numerical evaluation of the plastic dissipation is possible, once the generalized plastic strain rates are given. For the sequential limit analysis method presented in chapter 6, which relies on a general numerical optimization of the power of internal forces, this equation is, therefore, directly applied. It is to be noted, however, that this method may also be formulated analogously to the conventional displacement based finite element method, leading to the solution of a set of nonlinear equations for the unknown velocity parameters (see e.g. [Kobayashi, 1977; Ismar and Mahrenholtz, 1979; Capsoni and Corradi, 1997b]). For such a formulation, it will certainly be more convenient to directly use the quadratic form, Eq. (3.101), for deriving and stating the relevant finite element equations.

Chapter 4

Experiments

This chapter summarizes results of experiments, which have been conducted in order to study the progressive buckling behaviour of axially compressed circular and square steel tubes under quasistatic loading conditions. In order to provide material data for the cold deformed (and strain hardened) profiles, results of uniaxial tension tests, which have been performed on the actual tube materials, are included, too. The test results presented in the following are mainly intended to show several phenomena related to progressive buckling of tubes and to allow some validation of the numerical simulation tools described later on. Further experimental studies as well as comparisons with analytical and numerical analyses are summarized in [Wintschnig, 1996; Seitzberger et al., 1997b]. In addition, results of an extensive experimental (and a restricted numerical) study on the axial crushing behaviour of foam-filled crush elements, where empty profiles of different cross-sectional shapes and dimensions were also investigated, may be found in [Seitzberger et al., 1997a, 1999].

4.1 Experimental Setup

The tested steel tubes were obtained from square and circular profiles. The outer side length of the cross-section of the cold deformed and welded square tubes was 40 mm, the wall thickness 1.4 mm. The weldless, extruded cylindrical tubes had an outside diameter of 40 mm and a wall thickness of 1.0 mm. All samples used for the compression tests had a length of 155 mm.

The profiles were made of different grades of mild steel. Material tests, which were performed on the actual tube materials (uniaxial tension tests on sheet samples taken from

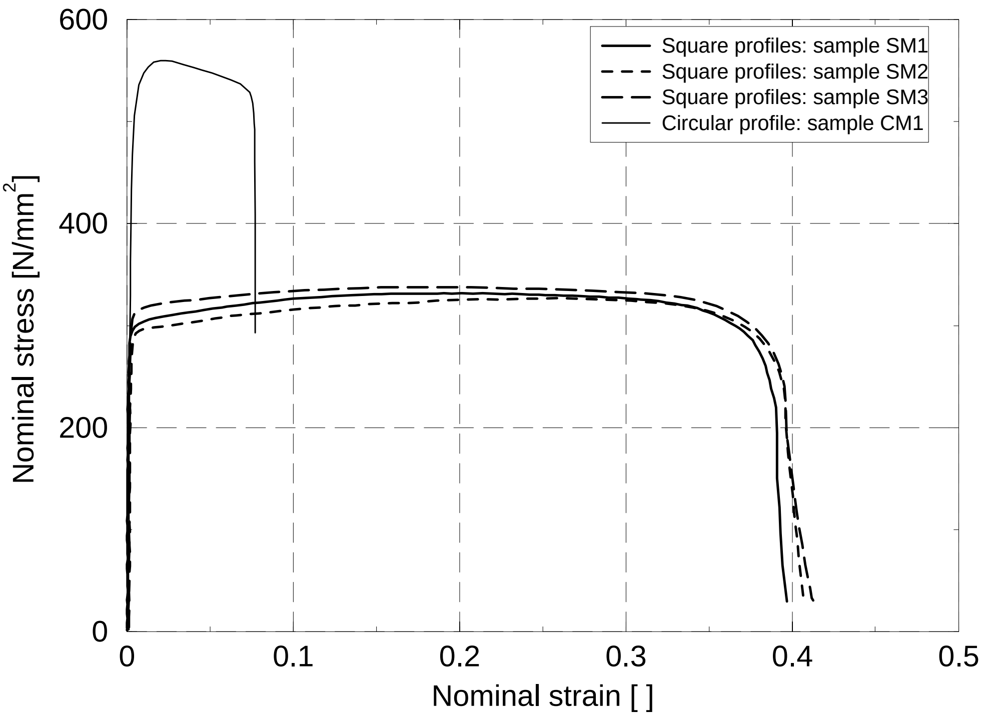

Figure 4.1: Square and circular steel tubes: actual uniaxial tension behaviour

the square tubes, uniaxial tension tests on the circular members themselves) according to the standard ÖEN 10002-1, are summarized in Figure 4.1 and Table 4.1.

A uniaxial universal testing machine was employed for carrying out the experiments. Axial force and crossbeam displacement were measured using PC based data recording equipment. Special constraints at the ends were mostly used to ensure well defined, clamped boundary conditions.

Two different loading velocities, 1 mm/s and 8.4 mm/s were applied for performing the compression tests. With respect to the deformation behaviour these loading rates can certainly be regarded as quasistatic, i.e. inertia effects will not influence the buckling patterns. Nevertheless, the velocities are sufficiently high to reveal some strain rate sensitivity of the materials, leading to somewhat elevated force values when compared to static compression tests (and for the circular tubes even changing the mode of progressive buckling, see below).

Table 4.1: Square and circular steel tubes: summary of uniaxial tension test results ($\sigma_{0.2}$ … yield stress, σ_u … ultimate strength, $A_{5.65}$, $A_{11.3}$ … strain at break, A_g … strain corresponding to σ_u)

Sample	$\sigma_{0.2}$ [N/mm^2]	σ_u [N/mm^2]	$A_{5.65}$ [%]	$A_{11.3}$ [%]	A_g [%]
Square tubes					
SM1	296	333	—	39.6	21.1
SM2	288	328	—	40.6	24.0
SM3	311	339	—	41.2	16.3
Circular tubes					
CM1	509	563	9.79	—	1.74

4.2 Test Results

Photographs of some deformed specimens are shown in Figures 4.2 to 4.4, and Figures 4.5 and 4.6 contain the measured force-compression curves for the square and circular tubes, respectively. A summary of some characteristic quantities describing the collapse process of the investigated tubular members is given in Table 4.2.

All tested samples showed the typical progressive buckling behaviour, characterized by the sequential formation of adjacent local folding patterns, with the buckling always starting at one of the two ends. A folding mode characteristic for multicorner columns, which is dominated by inextensional bending deformations (where the individual lobes around the circumference alternatively move inwards and outwards, this way avoiding large hoop strains), can be seen from the crushed square tube shown in Figure 4.2. Concerning the buckling modes of the circular profiles, marked differences are observed for the two different loading rates. Although the geometry of these specimens has been chosen such that an axisymmetric "concertina mode" buckling could be expected,[1] only those samples tested with higher loading rate showed this buckling mode throughout the deformation process (Figure 4.4). The specimens subjected to the lower loading rate (1 mm/s) started to buckle axisymmetrically. However, after the formation of the first lobes they switched to a non-axisymmetric "diamond mode", as can be seen in Figure 4.3. The

---

[1] For thicker tubes with a radius to thickness ratio of less than 40-45, approximately, axisymmetric buckling is likely to occur, whereas thinner tubes rather tend to buckle into a non-axisymmetric "diamond mode" [Jones, 1989b].

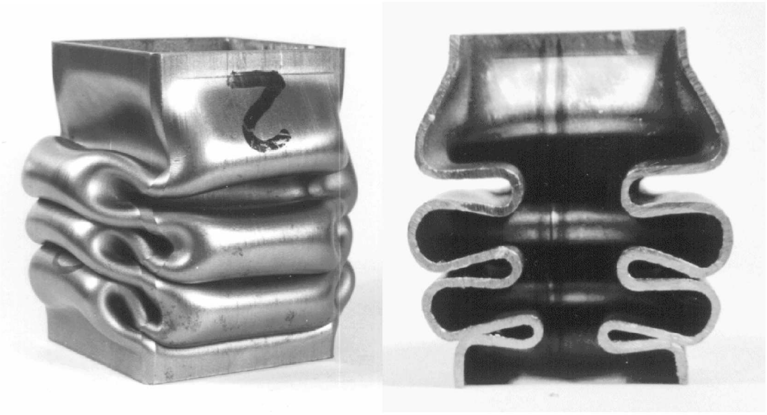

Figure 4.2: Square tubes: axially crushed specimen S2

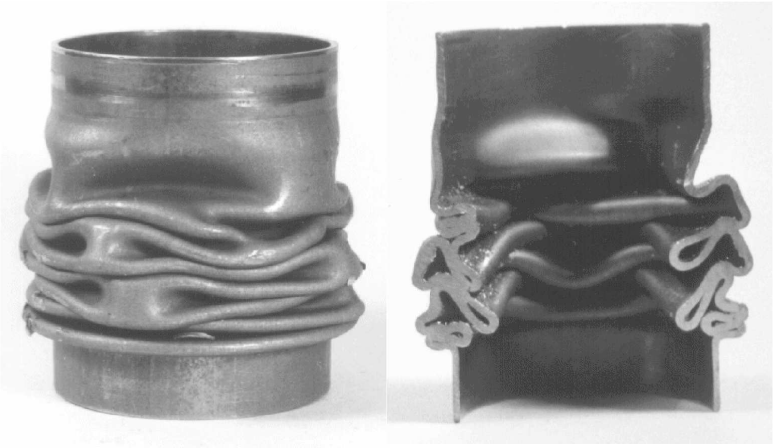

Figure 4.3: Circular tubes: axially crushed specimen C2

strain rate sensitivity of the material was the reason that no switching into this mode (which is accompanied by larger local strain rates due to the development of strongly deformed "corner regions") occurred for the specimens loaded at 8.4 mm/s.

From the measured force-compression curves, shown in Figures 4.5 and 4.6, several features, which are characteristic for progressive buckling processes, immediately become obvious:

- the first load peak F^1_{max}, being associated with first local collapse of the crush element, markedly exceeds the load maxima according to the formation of the subsequent folds,
- the progressive formation of the subsequent folds is associated with a more or less re-

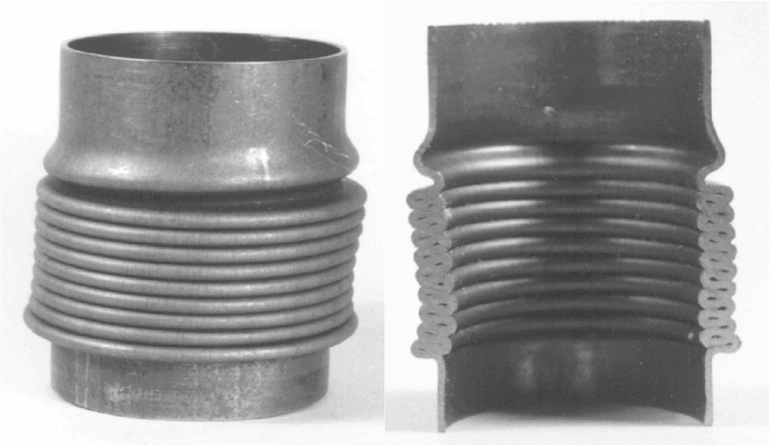

Figure 4.4: Circular tubes: axially crushed specimen C3

peated force-deflection pattern, fluctuating around an approximately constant mean force value,

- very similar force-deflection curves are obtained for those specimens, which buckle into the same modes, affecting not only the local force maxima and minima, but even the effective crushing distances u_{eff}, i.e. the compression distances between these repeated local load peaks,
- quite large compression distances (as compared to the total length of the specimens) may be utilized without essentially changing the mean force levels.[2]

A comparison of the results for the different test samples, listed in Table 4.2, clearly reveals the strain rate sensitivity of the material, where markedly higher first load maxima, but for the (comparable) square tubes also slightly elevated mean force levels, are observed for the higher loading velocity. The reproducibility of the measurements within the individual test configurations is also reflected by the results.

In order to directly compare the energy absorption capacity of the investigated profiles, the structural effectiveness parameter η, defined here as the mean force F_{m} with respect to the ultimate load $A\sigma_{\text{u}}$ (A is the cross-sectional area, σ_{u} the ultimate strength of the material) can be used [Jones, 1989b]. From this it can be seen that the energy absorption

---

[2] With respect to this it is to be noted, however, that none of the tested samples was loaded up to the stroke length (i.e. the maximum compression distance, which may be utilized for energy dissipation before the crushing forces begin to increase steeply).

Table 4.2: Summary of compression test results for square and circular steel tubes (v_c … loading rate, F^1_max … first load peak, F_m … mean force, η … structural effectiveness parameter, A … cross-sectional area, σ_u … ultimate strength, u_eff … effective crushing distance)

Sample	v_c [mm/s]	F^1_max [kN]	F_m [kN]	η $(= F_\mathrm{m}/A\sigma_\mathrm{u})$	u_eff[a] [mm]	Remarks
			Square tubes			
S1	1.0	74.9	26.5	0.37	33	
S2	– ”–	75.2	26.9	0.37	33	
S3	– ”–	75.1	27.1	0.38	33	
S7	8.4	79.0	28.1	0.39	30	ends not constrained
S8	– ”–	79.2	28.4	0.39	35.5	
			Circular tubes			
C1	1.0	70.8	32.0	0.46	14.5	switching to diamond mode
C2	– ”–	70.9	32.4	0.47	15.5	– ”–
C3	8.4	73.0	33.2	0.48	9	concertina mode
C4	– ”–	72.7	33.3	0.48	9	– ”–

[a] The values of the effective crushing distances are taken as the distance between two repeated load-compression patterns in the postbuckling range.

capacity of the circular profiles is distinctly higher than that of the square ones. The difference between diamond and concertina mode buckling of the circular tubes, however, is much less pronounced.

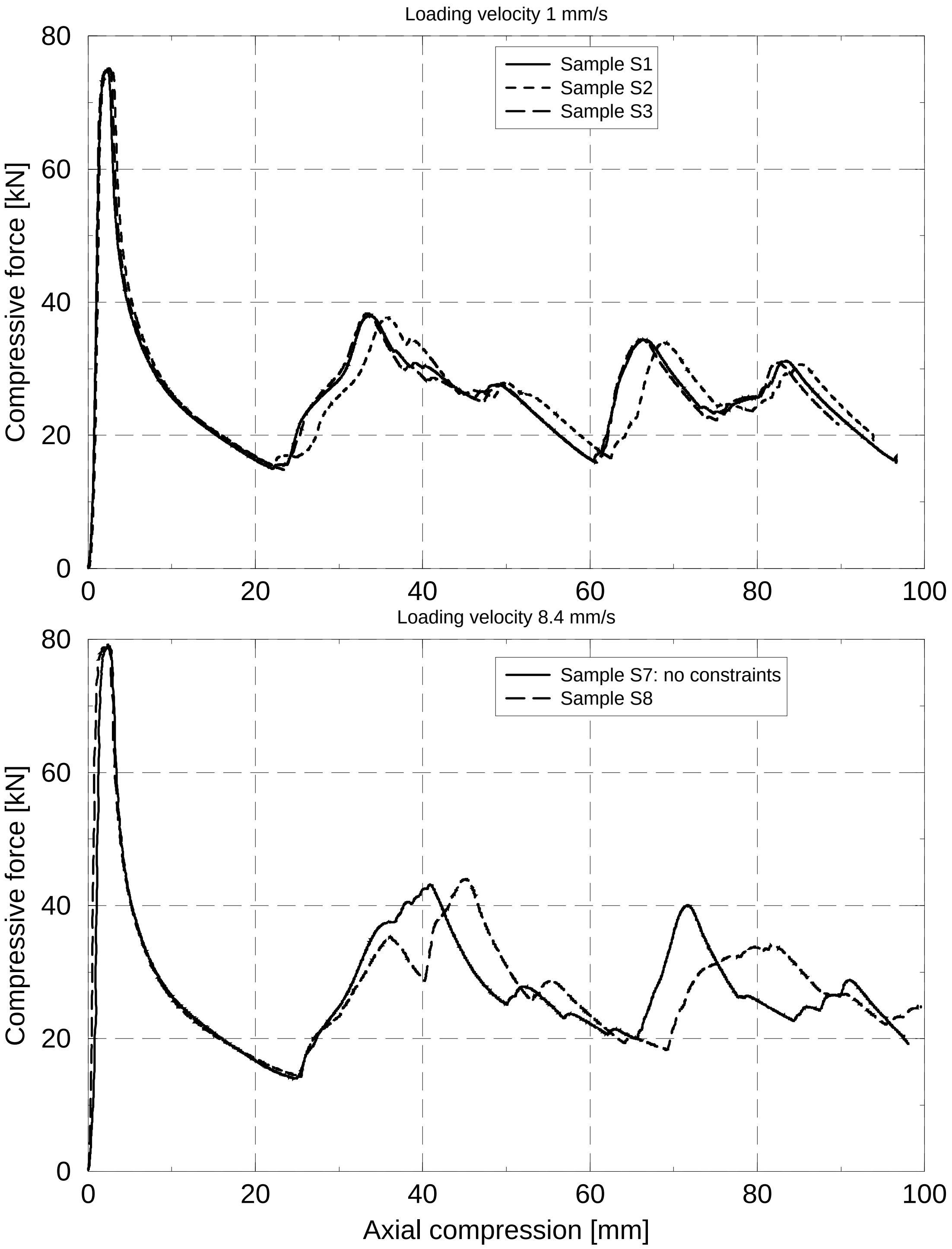

Figure 4.5: Load versus compression curves for square steel tubes

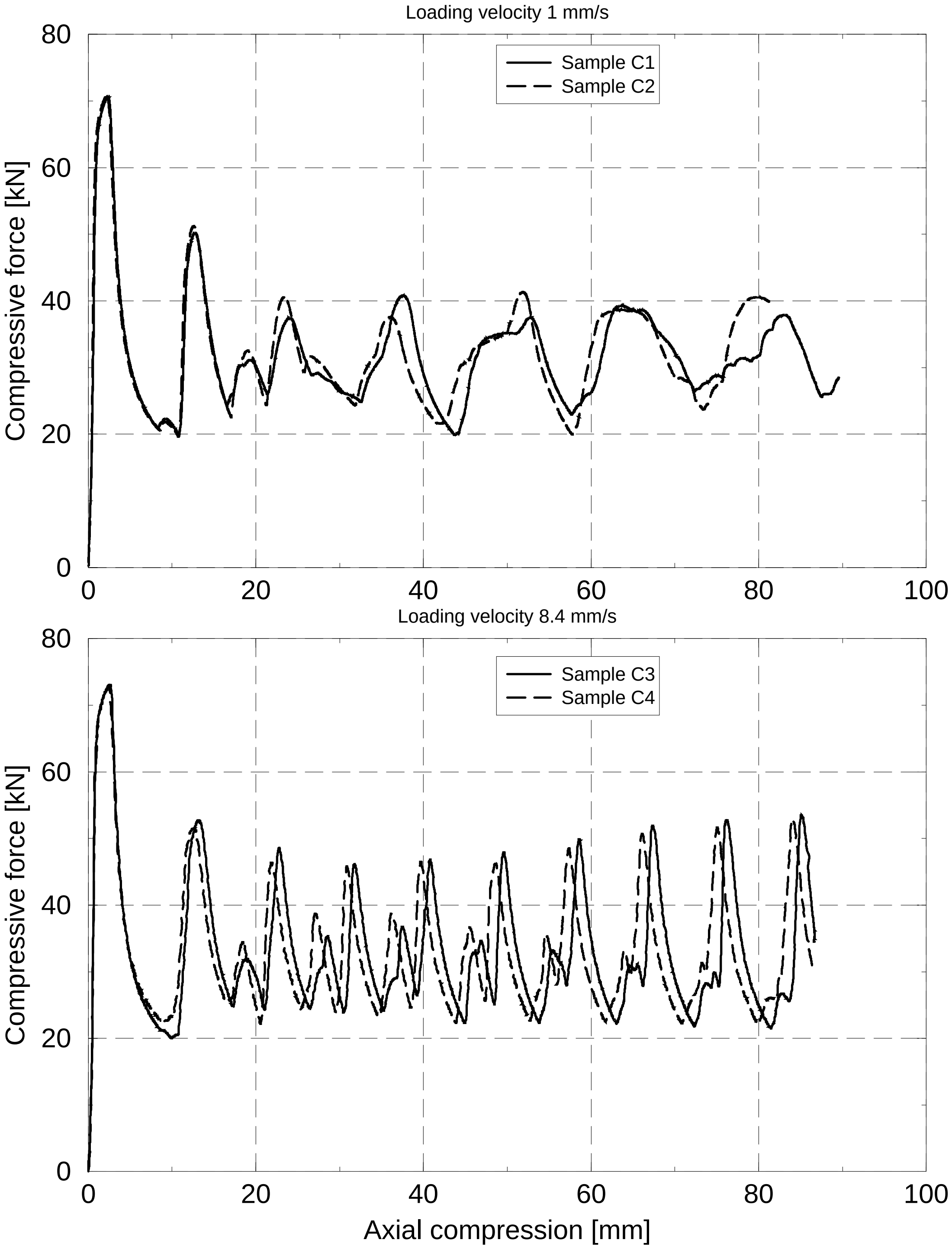

Figure 4.6: Load versus compression curves for circular steel tubes

Chapter 5

Folding Mechanisms

Experiments show that the collapse process of thin-walled structures is, in general, accompanied by the development of localized plastic mechanisms, i.e. the formation of a more or less complicated pattern of folds and wrinkles (see chapter 4). Based on these observations simplified kinematic mechanisms were proposed to predict the crushing response of thin-walled members of simple geometry under different loading conditions. Many of these models lead to small computer codes or even to closed-form solutions and therefore can be used efficiently in the preliminary design of energy absorbing systems (see section 2.3 for an overview).

In the following, several collapse mechanisms describing the concertina mode buckling of circular tubes [Abramowicz and Jones, 1986; Grzebieta, 1990; Wierzbicki et al., 1992; Gupta and Velmurugan, 1995] and the progressive crushing of multicornered prismatic columns [Abramowicz and Wierzbicki, 1989] are sketched and discussed. Besides pointing out the principles of the underlying theory (for a more detailed description see e.g. [Wierzbicki and Abramowicz, 1989]), the suitability and accuracy of these approaches for crushing analysis of structures is investigated with respect to both the axial force-compression characteristics and the prediction of the mean force levels. The test results presented in the last chapter are used for assessing the numerical results.

5.1 General Formulation

All of the investigated collapse models are based on a kinematics oriented method of plasticity, suitably generalized to large deformation problems (i.e., according to the statement of the plasticity theorems in section 3.3, spatial integrations are performed over the current configuration, and the Cauchy stress tensor $\boldsymbol{\sigma}$ together with the work conjugate spatial rate of deformation tensor $\boldsymbol{d}$ are used for the constitutive description). Starting point is the selection of a kinematically admissible velocity field $\boldsymbol{v}^*(\boldsymbol{x}, \boldsymbol{\chi}, t)$, describing the formation of individual folds. This velocity field may be chosen to be piecewise continuous, thus allowing stationary and moving yield lines to develop, and in general is fully determined or described by only a few degrees of freedom (collected in general form by the n-dimensional vector $\boldsymbol{\chi}$ used above). The spatial rate of deformation tensor $\boldsymbol{d}^* = \boldsymbol{d}(\boldsymbol{v}^*)$ is obtained from the underlying velocity field according to Eq. (3.8).

Taking into account the constitutive behaviour,[1] the plastic dissipation per unit volume, $D_\mathrm{p}(\boldsymbol{d}^*)$, and thus the total internal rate of energy dissipated within such a collapse mechanism,

$$D_\mathrm{int}(\boldsymbol{v}^*) = \int_v \boldsymbol{\sigma}^* : \boldsymbol{d}^* \, dv = \int_v D_\mathrm{p}(\boldsymbol{d}^*) \, dv \; , \tag{5.1}$$

can be computed. For axial crushing processes, the power of external forces is given by

$$D_\mathrm{ext} = F_\mathrm{a} v_\mathrm{c} \; , \tag{5.2}$$

where F_a is the axial crushing force and v_c the conjugate compression velocity. With the upper bound theorem, Eq. (3.57), it follows

$$\overline{F}_\mathrm{a} v_\mathrm{c} \leq F_\mathrm{a} v_\mathrm{c} = D_\mathrm{int}(\boldsymbol{v}^*) \tag{5.3}$$

and

$$|\overline{F}_\mathrm{a}| \leq |F_\mathrm{a}| = \frac{D_\mathrm{int}(\boldsymbol{v}^*)}{|v_\mathrm{c}|} \; , \tag{5.4}$$

respectively, being a condition of the minimum of the actual instantaneous crushing force, $|\overline{F}_\mathrm{a}|$. The unknown kinematic parameters (if there are any) may thus be obtained for each instant by minimizing $|F_\mathrm{a}|$ according to Eq. (5.4). Because for the progressive buckling processes described herein, however, the unknown parameters (e.g. the length of a folding wave) are assumed not to change with time, an alternative principle was postulated for the determination of $\boldsymbol{\chi}$. Time integration of Eq. (5.3) over the whole crushing process (time limits $t = 0$ to $t = t_\mathrm{f}$) delivers

$$\overline{F}_\mathrm{m} u_\mathrm{f} \leq F_\mathrm{m} u_\mathrm{f} = W_\mathrm{int} = \int_0^{t_\mathrm{f}} D_\mathrm{int}(\boldsymbol{v}^*) \, dt \; , \tag{5.5}$$

---

[1] The formulation described herein is based on the plastic extremum and bounding principles stated in section 3.3. Accordingly, the same constitutive description, namely rigid-perfectly plastic, isotropic and incompressible material behaviour with a convex yield surface and an associated flow rule, is assumed.

and

$$|\overline{F}_{\mathrm{m}}| \leq |F_{\mathrm{m}}| = \frac{W_{\mathrm{int}}}{|u_{\mathrm{f}}|} \; . \tag{5.6}$$

Herein $\overline{F}_{\mathrm{m}}$ and F_{m} denote minimum and upper bound for the mean crushing force, respectively, u_{f} is the axial shortening and W_{int} the internal plastic work for the deformation cycle under consideration. According to Eq. (5.6), the unknown parameters $\boldsymbol{\chi}$ may therefore be obtained by extremization of the mean crushing force, i.e.

$$\frac{\partial}{\partial \boldsymbol{\chi}} \left(|F_{\mathrm{m}}| \right) = \frac{\partial}{\partial \boldsymbol{\chi}} \left(\frac{W_{\mathrm{int}}}{|u_{\mathrm{f}}|} \right) = 0 \; , \tag{5.7}$$

leading to a set of n equations for the n degrees of freedom.

Once the kinematics of the deformation process is fully determined, the instantaneous crushing force (and thus the axial force-compression curve) is given by the power equation (see Eqs. (5.3) and (5.4)).

The minimum condition stated in Eq. (5.5) is a requirement for the minimum of the total internal work dissipated over a plastic deformation process. For arbitrary large deformation processes, however, it may not be assumed that this global minimum condition holds in general. Some considerations justifying the validity of Eqs. (5.5) to (5.7) for the special case of steady-state and quasi steady-state deformation processes (with special emphasis put onto the progressive crushing of tubes), however, are presented and discussed in [Abramowicz, 1996].

So far the strategy for treating plastic collapse of axially compressed tubular members is quite general. Depending on the appropriate choice of deformation mechanisms, numerical solutions quite close to the actual crushing behaviour may be obtained. A major concern for the definition of most of the proposed collapse models, however, was to state simple techniques for estimating the global parameters of the crushing process (folding wave length, mean crushing force, etc.), which are computationally inexpensive or even lead to closed-form solutions. Therefore, a number of simplifying assumptions are used in general, affecting both the kinematic description and the computation of the internal energy dissipation. For example, many of the proposed collapse models are based on the assumption that only one fold is forming at a time and thus may be isolated from the rest of the structure, which is assumed to behave in a rigid manner. Furthermore, interaction effects between the individual stress (and strain rate) components are often treated in a simplified way or are even totally disregarded, this way delivering simplified, but analytically tractable relations between the main variables of influence.

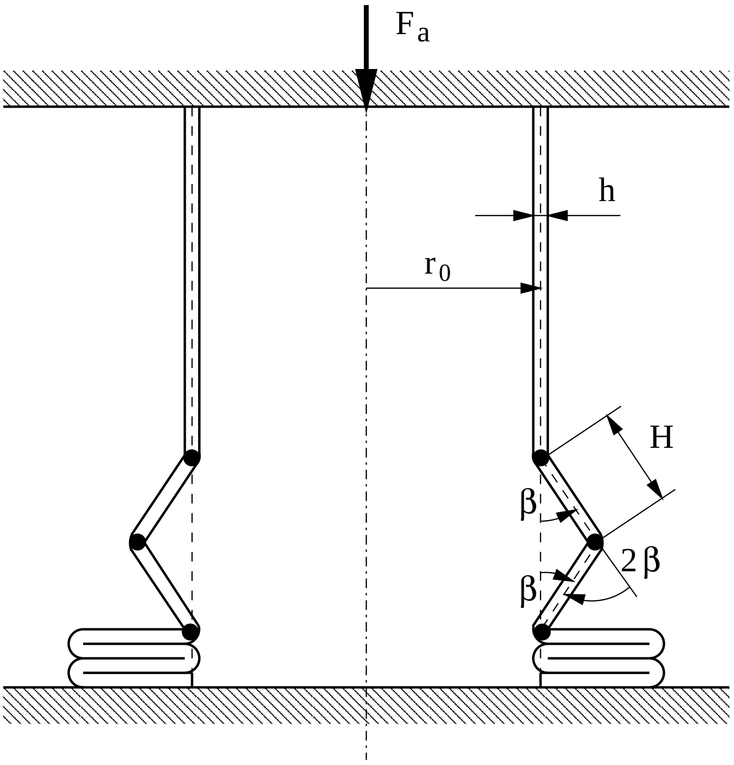

Figure 5.1: Axisymmetric collapse model of Alexander [1960]

The principles of this strategy are illustrated in the next section by first discussing the model of Alexander [1960], who proposed a rather simple deformation pattern for the axisymmetric crushing behaviour of axially compressed circular tubes (Figure 5.1). Extensions of this collapse model to cater for various effects, but also a (geometrically much more involved) kinematic model for the axial crushing of multicornered prismatic columns, are sketched afterwards.

5.2 Axisymmetric Crushing of Circular Tubes

5.2.1 Model of Alexander

The deformation pattern underlying the first of the proposed collapse mechanisms for axisymmetric crushing of axially compressed circular tubes is shown in Figure 5.1. Starting from an initially straight meridional curve, Alexander assumed that the meridian of the active fold may be idealized by two straight line elements and three circumferential plastic hinge lines. The "folding half wave length", H, used in Figure 5.1, is an initially unknown parameter, which has to be determined in the course of the analysis.

With regard to the internal energy dissipation, it is assumed that this can be decomposed into two parts,

$$D_{\mathrm{int}} = D_{\mathrm{b}} + D_{\mathrm{m}} \ , \tag{5.8}$$

owing to bending at the plastic hinge lines and circumferential membrane stretching of the line segments.

The contribution due to bending, D_{b}, is given by

$$D_{\mathrm{b}} = 2 \times 2\pi r_0 M_h \dot{\beta} + 2\pi(r_0 + H\sin\beta) M_h 2\dot{\beta} \ . \tag{5.9}$$

For the plastic bending moment at the hinge lines the validity of the von Mises yield condition and constrained circumferential deformations are assumed. With this, M_h is given by

$$M_h = \frac{2}{\sqrt{3}} M_0 = \frac{2}{\sqrt{3}} \frac{\sigma_y h^2}{4} \ . \tag{5.10}$$

The energy dissipation due to bending is then written as

$$D_{\mathrm{b}} = 4\pi \frac{2}{\sqrt{3}} \frac{\sigma_y h^2}{4} (2r_0 + H\sin\beta)\dot{\beta} \ . \tag{5.11}$$

For the determination of the contribution of membrane deformations to the internal energy dissipation, a mean circumferential strain rate in the line segments is assumed (the parallel action of all other generalized stress and strain rate components in the line segments, however, is disregarded). With the circumferential strain rate

$$d_{22} = \frac{\dot{r}}{r} = \frac{\frac{\partial}{\partial t}\left(r_0 + \frac{H}{2}\sin\beta\right)}{r_0 + \frac{H}{2}\sin\beta} = \frac{\frac{H}{2}\cos\beta\ \dot{\beta}}{r_0 + \frac{H}{2}\sin\beta} \ , \tag{5.12}$$

there follows

$$\begin{aligned} D_{\mathrm{m}} &= N_0 d_{22} 2\pi (r_0 + \frac{H}{2}\sin\beta) 2H \\ &= \sigma_y h \frac{\frac{H}{2}\cos\beta\ \dot{\beta}}{r_0 + \frac{H}{2}\sin\beta} 2\pi (r_0 + \frac{H}{2}\sin\beta) 2H \ , \end{aligned} \tag{5.13}$$

and finally

$$D_{\mathrm{m}} = 2\pi\sigma_y h H^2 \cos\beta\ \dot{\beta} \ . \tag{5.14}$$

With Eqs. (5.11) and (5.14) the internal energy dissipation may be expressed as

$$D_{\text{int}} = D_{\text{b}} + D_{\text{m}} = 2\pi\sigma_y h \left[\frac{h}{\sqrt{3}}(2r_0 + H\sin\beta) + H^2\cos\beta\right]\dot{\beta}\ . \tag{5.15}$$

The total internal energy dissipated within one crushing cycle is then given by

$$\begin{aligned} W_{\text{int}} &= \int_0^{t_{\text{f}}} D_{\text{int}}\, dt \\ &= 2\pi\sigma_y h \int_0^{\pi/2} \left[\frac{h}{\sqrt{3}}(2r_0 + H\sin\beta) + H^2\cos\beta\right] d\beta \\ &= 2\pi\sigma_y h \left[(\frac{h}{\sqrt{3}}(r_0\pi + H) + H^2\right]\ . \end{aligned} \tag{5.16}$$

According to Eq. (5.6), the folding length H is determined by minimization of the mean crushing force, i.e. by extremization of the function

$$F_{\text{m}} = \frac{W_{\text{int}}}{2H} = \pi\sigma_y h \left[\frac{hr_0\pi}{\sqrt{3}H} + \frac{h}{\sqrt{3}} + H\right]\ . \tag{5.17}$$

With

$$\frac{\partial F_{\text{m}}}{\partial H} = \pi\sigma_y h \left[-\frac{hr_0\pi}{\sqrt{3}H^2} + 1\right] = 0 \tag{5.18}$$

the optimal folding length follows as

$$H = \sqrt{\frac{hr_0\pi}{\sqrt{3}}} = 1.347\sqrt{hr_0}\ , \tag{5.19}$$

and the mean crushing force is finally given by

$$F_{\text{m}} = \pi\sigma_y h \left[2H + \frac{h}{\sqrt{3}}\right] = \pi\sigma_y h \left[2\sqrt{\frac{hr_0\pi}{\sqrt{3}}} + \frac{h}{\sqrt{3}}\right]\ . \tag{5.20}$$

In addition to the collapse mode shown in Figure 5.1, where all folds go outwards, Alexander [1960] investigated an alternative collapse mechanism with all lobes moving inwards. In view of the approximative character of the analysis, however, the author proposed that for the computation of the mean crushing force an average value between these two folding modes should be used,[2] which is given by

$$F_{\text{m}} = 2\pi\sigma_y hH = 2\pi\sigma_y h\sqrt{\frac{hr_0\pi}{\sqrt{3}}}\ . \tag{5.21}$$

---

[2] A comparison of the plastic wave length H with that of an elastic buckling analysis on axially compressed circular tubes led to further slight modifications for F_{m} which, however, are not discussed here (for details see [Alexander, 1960]).

For the determination of the axial force-compression curve (which, however, was not considered in [Alexander, 1960]) the power equation may be used. With the axial shortening

$$u_\mathrm{c} = 2H(1-\cos\beta) \tag{5.22}$$

the compression velocity follows as

$$v_\mathrm{c} = 2H\sin\beta\dot{\beta}\ . \tag{5.23}$$

Application of the power equation

$$F_\mathrm{a}v_\mathrm{c} = D_\mathrm{int}\ , \tag{5.24}$$

and insertion of Eqs. (5.15) and (5.23) finally delivers for the instantaneous axial crushing force:

$$F_\mathrm{a}(\beta) = \pi\sigma_y h\left[\frac{h}{\sqrt{3}}\left(\frac{2r_0}{H\sin\beta}+1\right)+\frac{H}{\tan\beta}\right]\ . \tag{5.25}$$

The corresponding axial compression, $u_\mathrm{c}(\beta)$, is given by Eq. (5.22).

A typical axial force-compression curve obtained this way is shown in Figure 5.25, sketched for several folding cycles. At the beginning of each deformation cycle ($\beta = 0$) the crushing load starts at infinity, and reduces to quite small values when β approaches $\pi/2$, with the minimal load values lying markedly below those of comparable experimental results. From Eq. (5.20) the mean crushing force follows as 19.9 kN, which underestimates the measured values (33.3 kN, see Table 4.2) by about 40%. The measured crushing distance $u_\mathrm{eff} = 9$ mm, however, is overestimated by the collapse model which predicts a value of $2H = 11.9$ mm.

5.2.2 Refined Single Active Fold Models

In order to overcome some drawbacks of the Alexander model (strongly idealized deformation pattern, neglecting of the meridional stress components, underestimation of the mean force levels, etc.), several refinements were proposed. In the following three single active fold models are discussed, which retain the assumption that only one fold is forming at a time ("single active fold models"):

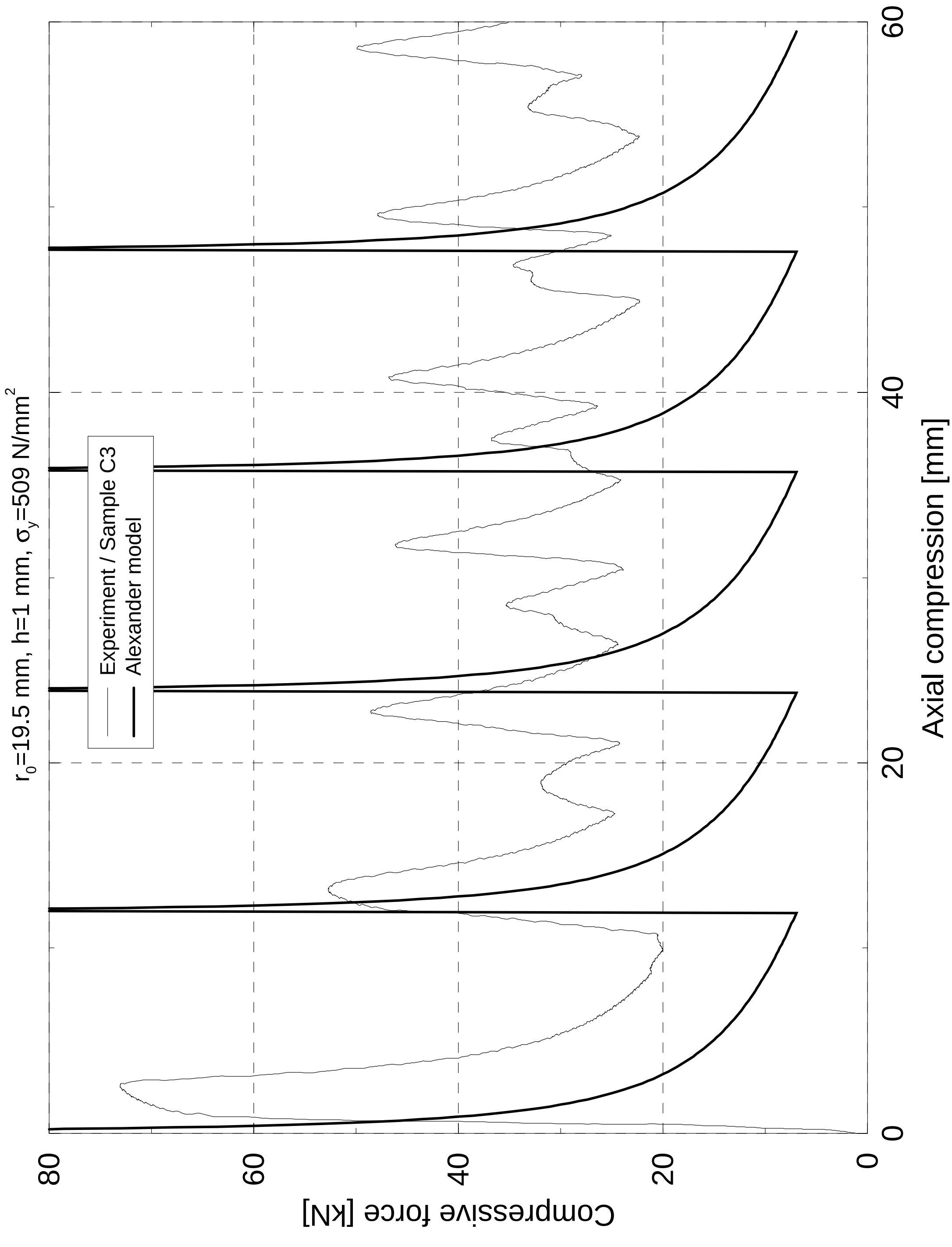

Figure 5.2: Model of Alexander: comparison of measured and predicted load versus compression curves

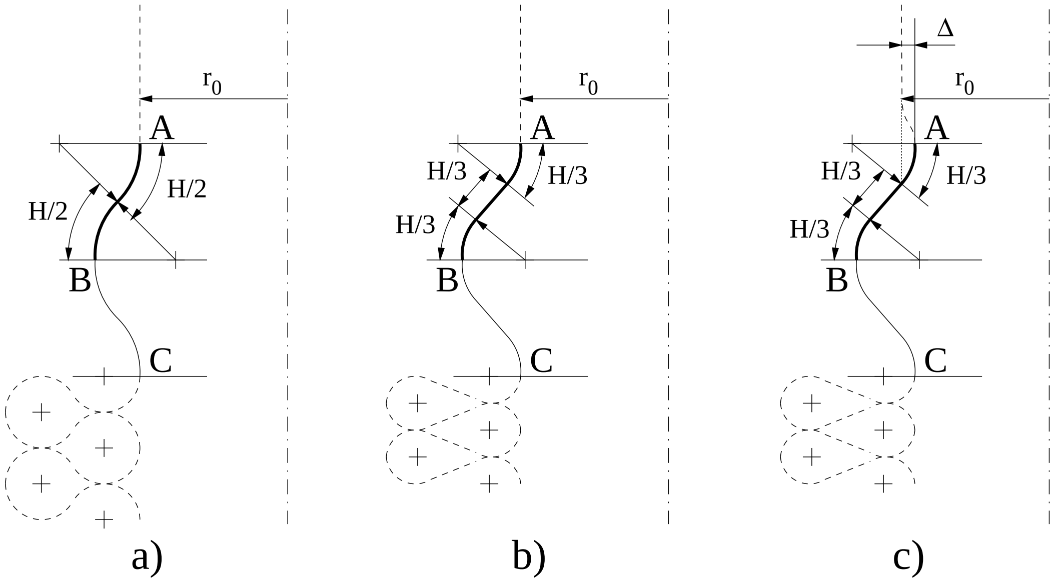

Figure 5.3: Circular tubes: deformation profiles for axisymmetric crushing: a) model of Abramowicz and Jones [1986], b) model of Grzebieta [1990], c) model of Gupta and Velmurugan [1995]

AMC1: model of Abramowicz and Jones [1986],[3]

AMC2: model of Grzebieta [1990],

AMC3: model of Gupta and Velmurugan [1995].

A further collapse model for concertina mode buckling of circular tubes, which suggests that folding is characterized by the simultaneous deformation of two folds,

AMC4: model of Wierzbicki et al. [1992],

is presented in the next section.

The kinematics underlying the single active fold models AMC1 to AMC3 are shown in Figure 5.3. What immediately becomes obvious is that, due to the use of circular arc segments for discretizing the meridional curves, more realistic deformation patterns (compared to the model of Alexander, Figure 5.1) are obtained. AMC1 describes the

---

[3] In [Abramowicz and Jones, 1986] only the mean crushing load is examined. In order to determine the load-deflection curve the method described in [Grzebieta, 1990] is used here and also applied for the evaluation of the mean crushing force.

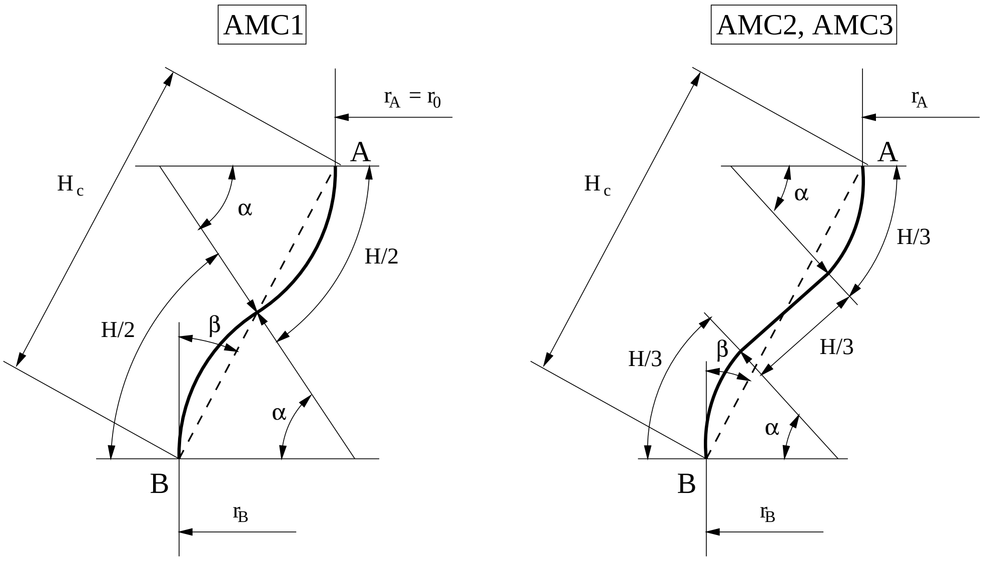

Figure 5.4: Single active fold models AMC1 to AMC3: variables definition

collapse process with meridional arc segments of a length of $H/2$ and H, respectively, whereas the other two models assume this circumferential bending to be more concentrated (with a meridional length of $H/3$ and $2H/3$), which should be more realistic for thinner tubes ($r_0/h > 20$). The main difference between AMC2 and AMC3 is that the latter assumes a small amount of deformation inwards to account for the predeformation due to the last folding cycle. Furthermore, the length of one arm of the plastic folds, H, is assumed to be given by the formula derived by Alexander, Eq. (5.19), and thus, the kinematics of these collapse models is fully determined and may be described by a single process parameter $\alpha(t)$.

For the computation of the internal energy dissipation the strategy proposed by Alexander [1960] is essentially retained. This means that plastic hinge lines are assumed at points A, B and C (see Figure 5.3), where the bending deformations are determined by the time rate of the angle α subtended by an arc element (for the definition of the kinematic variables used in the following see Figure 5.4). Hence, D_b is given by

$$D_\mathrm{b} = 4\pi M_h (r_A + r_B)\dot{\alpha} \ . \tag{5.26}$$

Concerning the membrane deformations, an idealization of the deformation pattern by straight line segments of length H_c each, is assumed for the kinematic models AMC1 and AMC2. Because, however, such a collapse pattern just coincides with that proposed by Alexander, Eq. (5.14) may directly be applied for evaluating the energy dissipation caused by the hoop stresses σ_{22}:

$$D_{\mathrm{m}} = 2\pi\sigma_{22} h H_c^2 \cos\beta\,\dot{\beta} \tag{5.27}$$

(the variable β is a given function of α, see Figure 5.4). For AMC3, however, no such idealization is assumed. Here, the energy dissipation due to membrane deformations in circumferential direction is given by

$$D_{\mathrm{m}} = 2\pi\sigma_{22} h \frac{H^2}{3} \cos\beta\,\dot{\beta}\ . \tag{5.28}$$

The derivation of this expression, however, is also based on the assumption that a mean hoop strain rate acts over the folding half wave length H.

In the Alexander model no reductions of the plastic bending moments M_h and the hoop stresses σ_{22} due to the parallel action of the meridional stresses are accounted for (leading to infinite axial load values for the starting configuration, $\beta = 0$). In order to take into account these effects, somewhat "specialized" yield conditions are applied for the investigated single active fold models. The moment capacity of the hinge lines is coupled with the external axial force according to

$$M_h = \frac{2M_0}{\sqrt{3}}\left[1 - \frac{3}{4}\left(\frac{F_{\mathrm{a}}}{F_0}\right)^2\right] \tag{5.29}$$

($F_0 = 2\pi r_0 N_0$ is the axial "squashing load" of the tubular member), and with the relation

$$\frac{\sigma_{11}}{\sigma_y} = -\frac{F_a}{F_0}\cos\alpha = -\overline{F}\cos\alpha \tag{5.30}$$

(σ_{11} denotes the meridional stress component) and the plane stress von Mises yield condition

$$\sigma_y^2 = \sigma_{11}^2 - \sigma_{11}\sigma_{22} + \sigma_{22}^2 \tag{5.31}$$

the (reduced) hoop stresses σ_{22} are finally given as

$$\sigma_{22} = \frac{\sigma_y}{2}\left[-\overline{F}\cos\alpha + \sqrt{4 - 3\overline{F}^2\cos^2\alpha}\right]\ . \tag{5.32}$$

Accordingly, finite values for the axial force are obtained even if the tube is perfectly straight.[4]

---

[4] Concerning the derivation of Eq. (5.32) it is to be noted that Eq. (5.30) utilized therein in fact is a condition of local equilibrium. With the theory underlying the kinematics-oriented solution strategy, however, local equilibrium will in general not be enforced, but equilibrium is rather fulfilled in a global sense. The advantageous use of Eq. (5.30) for stating the problem, therefore, is to be regarded as an additional input entering the solution procedure, but as such is not really consistent with the general description of the solution strategy sketched in section 5.1.

Because for a given fold length H the whole deformation process and, hence, the internal energy dissipation may be described as a function of the process parameter α only (which also determines the axial compression velocity $v_\mathrm{c} = v_\mathrm{c}(\alpha(t))$, the power equation

$$F_\mathrm{a} v_\mathrm{c} = D_\mathrm{b} + D_\mathrm{m} \tag{5.33}$$

may be used to set up a scalar nonlinear equation in terms of F_a,

$$g(F_\mathrm{a}, \alpha) = 0 \ , \tag{5.34}$$

from which the instantaneous crushing force for each (predetermined) configuration α may be obtained numerically.

In order to determine a complete load-compression curve, however, Grzebieta [1990] proposed that the mechanisms are only used for describing the descending part of one load cycle, and further assumptions are made to determine the remaining parts of the curve, including the first load cycle (associated with first local collapse of the crush element) as well as the lower and upper load peaks in each subsequent crushing cycle — in order to fit the models to experimental results. A typical "constructed" force-compression curve is shown in Figure 5.5. The essential assumptions used therein are (for details see [Grzebieta, 1990] or the diploma thesis [Wintschnig, 1996]):

- After an elastic response at the beginning first yielding is described by an axial force $F_y = F_0$.
- The load maximum for the first loading cycle is determined by $F^1_\mathrm{max} = 2F_y/\sqrt{3}$.
- The effective crushing distance u_eff is assumed to be given by $2H - h$. This value, however, is quite larger than the "crushable amount" of axial deformation due to the underlying kinematic deformation pattern, u_f.
- Concerning the evaluation of the descending part of the curve, which is determined by the kinematics of the collapse model used, the authors propose to replace the yield stress, σ_y ($= \sigma_{0.2}$), by the ultimate strength of the material, σ_u (in order to account for hardening).
- the upper peak load for each but the first crushing cycle, F_u, is determined by a small amount of radial predeformations Δ. Suggested values are: $r_0/h < 20$: $\Delta = h$, $r_0/h \geq 20$: $\Delta = 1.5h$.

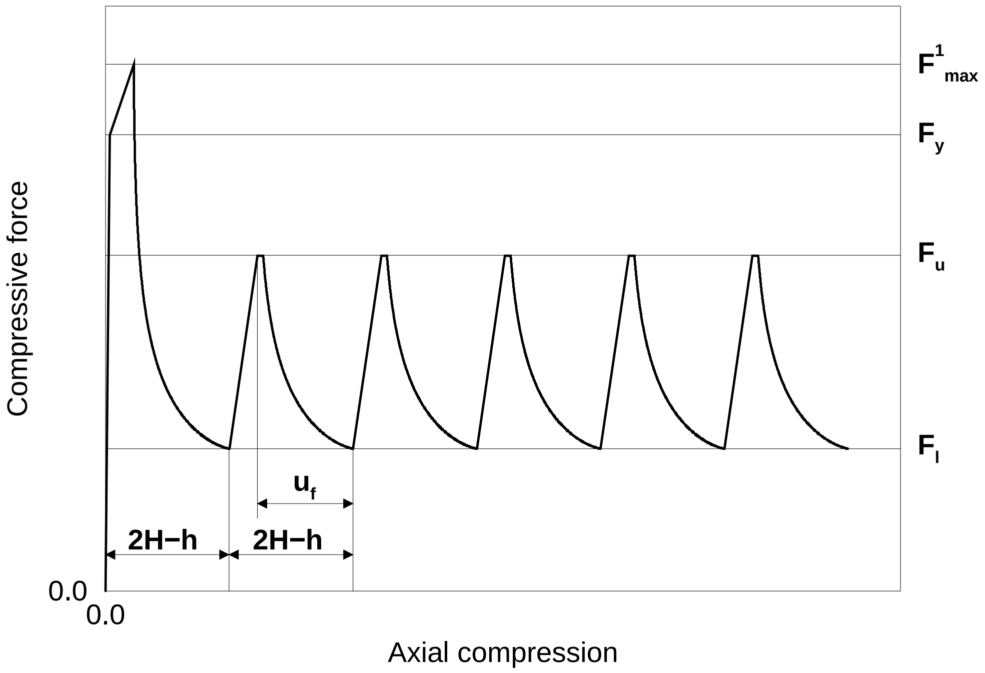

Figure 5.5: Single active fold models AMC1 to AMC3: details for the “construction” of the axial load versus compression curves

In Figure 5.6 the axial force-compression curves obtained this way for the different single active fold models are compared with each other and with a typical experimental result. Table 5.1 lists several characteristic quantities related to the measurements and the numerical predictions. It becomes obvious from the results that, due to the use of the additional assumptions described above, the force-compression behaviour can be fitted relatively closely to experiments. A comparison between models AMC1 and AMC2 reveals only slight differences in the force-compression curves, whereas the load fluctuation as well as the mean crushing force of model AMC3 are clearly higher (the mean forces in Table 5.1 are evaluated here directly via the force-deflection diagrams). The maximal differences between measured and predicted mean force values are about 10%, and also the effective crushing distances agree reasonably well with the experimental observations.

Essentially based on a refined evaluation of the internal energy dissipation, which takes into account the parallel action of the axial crushing force and the corresponding meridional stresses, respectively, the collapse models are shown to be able to describe the unloading part of a crushing cycle with some realism. The very beginning of each loading cycle, however, may not be captured by the collapse models itself — this must, therefore, be

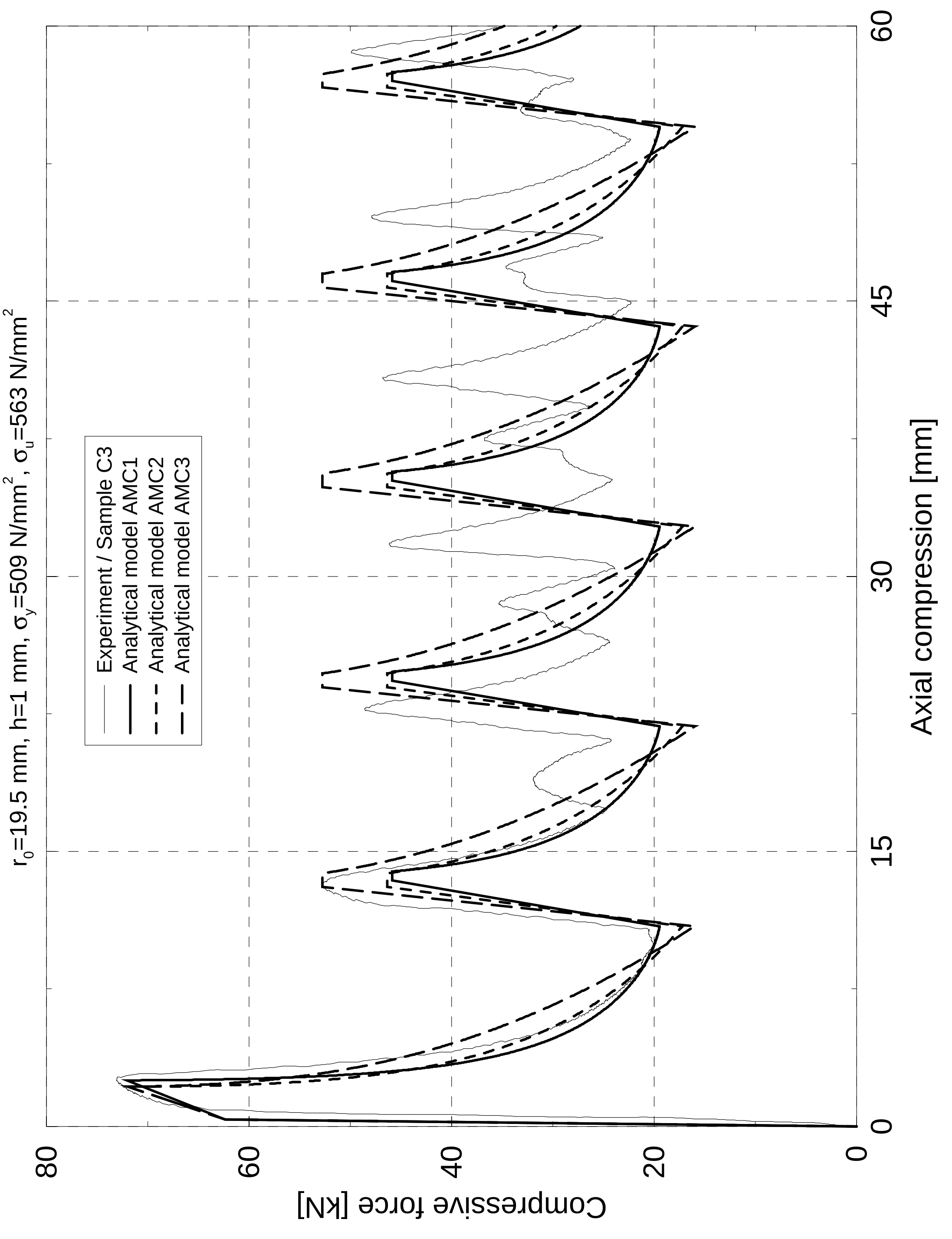

Figure 5.6: Single active fold models AMC1 to AMC3: comparison of measured and predicted load versus compression curves

Table 5.1: Single active fold models for circular tubes: summary of results

Sample / Model	F^1_{max} [kN]	F_{m} [kN]	u_{eff} [mm]
Experiments			
C3	73.0	33.2	9
C4	72.7	33.3	9
Analytical models			
AMC1	72.0	29.5	10.9
AMC2	– ”–	30.3	– ”–
AMC3	– ”–	33.6	– ”–

approximated by additional assumptions as sketched above.

5.2.3 Two Active Folds Model of Wierzbicki et al.

In contrast to the single active fold models AMC1 to AMC3 the mechanism proposed by Wierzbicki et al. (AMC4) suggests that folding is characterized by the simultaneous deformation of two (half) folds, described by two circular arcs of fixed length $\overline{H}$ each (Figure 5.7).[5] This initially unknown length is determined through minimization of the mean crushing force, whereas the eccentricity, i.e. the inward movement Δ, has to be assumed in advance. Corresponding to outside and inside folding, a total repeated folding cycle is to be divided into two parts, accompanied by a shifting of the active transition region by $2\overline{H}$, after the first fold has formed completely. This is shown schematically in Figure 5.8, where several subsequent deformation stages during the formation of one repeated crushing cycle are sketched. Each of these subcycles, however, may be described by a single process parameter $\alpha(t)$.

In order to obtain closed form solutions for $\overline{H}$ and the mean crushing force F_{m}, membrane forces and bending moments are assumed not to interact and are decoupled from the external axial force. Furthermore, (small deformation) engineering definitions are used for the hoop strain rates, and spatial integrations are performed over the initial undeformed configuration, both essentially being based on the assumption that the fold lengths are sufficiently small, and $r \approx r_0$ may be set for simplicity.

---

[5] Note that now the total folding wave length is described by $4\overline{H}$ instead of $2H$ as done before.

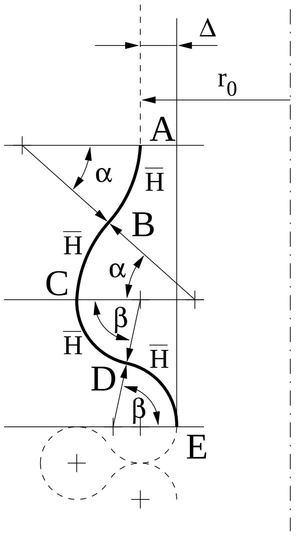
Δ
r_0
A
α
$\overline{H}$
B
$\overline{H}$
α
C
β
$\overline{H}$
$\overline{H}$
D
β
E

Figure 5.7: Circular tubes: deformations profile for axisymmetric crushing: model of Wierzbicki et al. [1992]

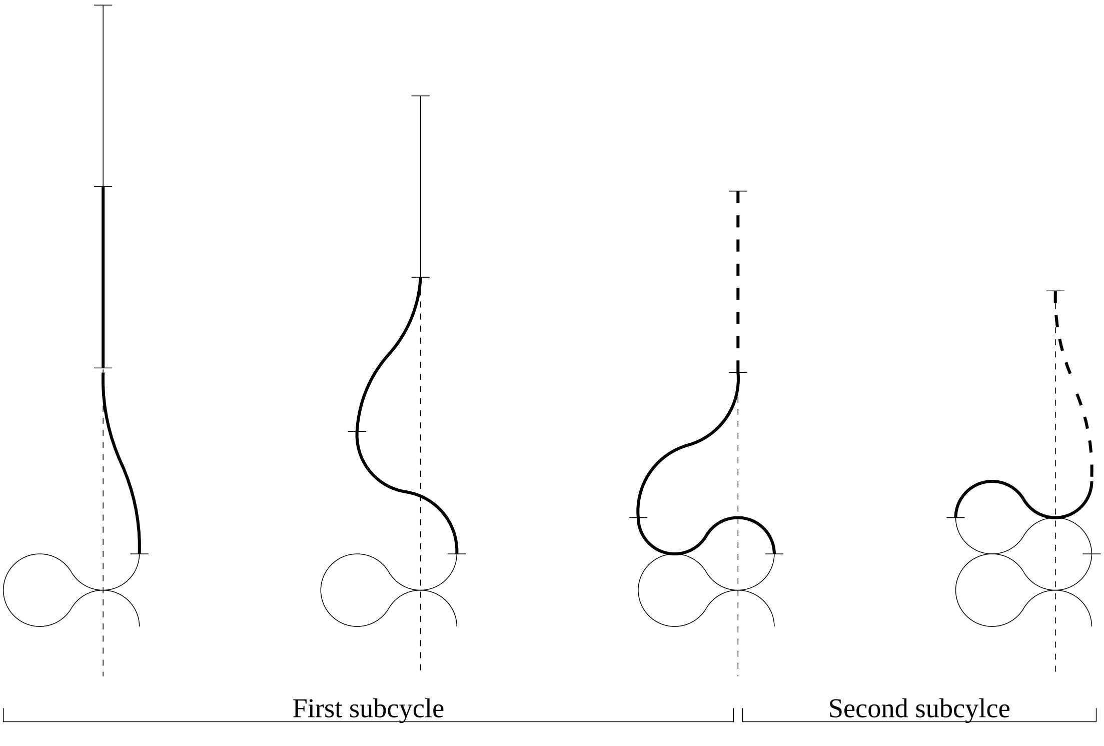
First subcycle
Second subcylce

Figure 5.8: Model of Wierzbicki et al. [1992]: subsequent deformation stages for one repeated crushing cycle

With the meridional curvature rate $\dot{\kappa}_{22}$ (and the local meridional coodinate s) the energy dissipation due to bending is given by

$$D_\mathrm{b} = \int_{ABCDE} |M_0 \dot{\kappa}_{22}| 2\pi r_0 \, ds = 4\pi r_0 M_0 (|\dot{\alpha}| + |\dot{\beta}|) \; , \tag{5.35}$$

and the energy dissipation owing to membrane deformations in hoop direction follows as[6]

$$D_\mathrm{m} = \int_{ABCDE} \left| N_0 \frac{\dot{r}}{r_0} \right| 2\pi r_0 \, ds = 2\pi N_0 \int_{ABCDE} |\dot{r}| \, ds \; , \tag{5.36}$$

where, according to the different active arc elements, the spatial integration for D_m (which is not described here) must be performed by parts.

After stating all geometric dependencies in terms of the process parameter α, the power equation is used for defining the instantaneous crushing force, which may formally be expressed as

$$\frac{F_a}{M_0} = p_1(\alpha) \frac{2\overline{H}}{h} + p_2(\alpha) \frac{r_0}{\overline{H}} \; . \tag{5.37}$$

Here $p_1(\alpha)$ and $p_2(\alpha)$ are known functions of α. The unknown parameter $\overline{H}$ is obtained by extremizing the mean crushing force. After some calculation, the final values for $\overline{H}$ and F_m, which are found not to depend on the chosen eccentricity Δ, are found as

$$\begin{aligned} \overline{H} &= 0.9263 \sqrt{h r_0} \\ F_\mathrm{m} &= 44.89 M_0 \sqrt{\frac{r_0}{h}} \; . \end{aligned} \tag{5.38}$$

The advantage of the kinematic description underlying AMC4 is that several features of a crushing cycle, observed in experiments, can be captured. These are finite values of load peaks and predeformations at the beginning of one load cycle (provided $\Delta \neq 0$), two peaks, which may be unequally spaced and of different heights (corresponding to contact of the folds inside and outside of the tube) and (at least for thicker tubes) a realistic deformed shape of the crushed members. However, as can be seen from Figure 5.9, the two active folds model must be stated to fail in describing the force-deflection curve of an actual crushing cycle. The peak loads are in general markedly higher than the squash loads of the tube (for the chosen eccentricity $\Delta = 1.5h$ a peak load of 165.3 kN is obtained, whereas the maximal measured force value is 73 kN) and even the effective crushing distance is overestimated ($u_{\text{eff}} = 13.3$ mm). According to Eq. (5.38) the mean force prediction is 25.2 kN, which underestimates the measured values by about 25%.

---

[6] It is to be noted, however, that with respect to the membrane contributions the final expression would not be affected if the spatial rate of deformation is used for defining the hoop strain rates and the spatial integration is performed over the current configuration. In any case, the radius cancels out from the integrand function.

Although this model shows shortcomings the kinematics seem to be well suited for describing the crushing process of thicker tubes. In comparison to the other models no additional assumptions have to be made to account for several phenomena which are typical for progressive buckling processes of tubular members, but cannot be captured by the single active fold models. The main drawback, however, is that, in order to obtain closed-form solutions, a very simple material description is used, which totally disregards interaction effects between different stress and strain rate components. Without changing the kinematic description, essential improvements of the two active folds model are therefore expected by removing the requirement for obtaining analytical solutions and resorting to a numerical solution strategy — this way allowing the application of more refined yield conditions while still keeping the computational effort sufficiently low.

5.3 Axial Crushing of Multicorner Columns

As a further example for the application of the solution strategy described in section 5.1, a single active fold model for the progressive buckling of multicornered prismatic columns is outlined in the following.

Starting from two basic collapse modes, a quasi-inextensional [Wierzbicki and Abramowicz, 1983] and an extensional deformation mode [Hayduk and Wierzbicki, 1984], Abramowicz and Wierzbicki [1989] proposed a kinematic model, which combines the features of both mechanisms and allows the description of the crushing process of axially compressed columns having an even number of corners. The deformation pattern of a representative corner element, which is shown in Figure 5.10, is composed of rigid flat parts and continuously deforming elements, which are connected by stationary and moving hinge lines. During the first phase of deformation ($0 < \alpha < \overline{\alpha}$) the quasi-inextensional mode, as sketched in Figure 5.10a, is assumed to act. This mode consists of four trapezoidal elements each moving as a rigid body, a section of a toroidal surface, subjected to extensional deformations, two sections of a cylindrical surface with horizontal moving hinge lines and two sections of a cylindrical surface, in which material is bent and rebent again

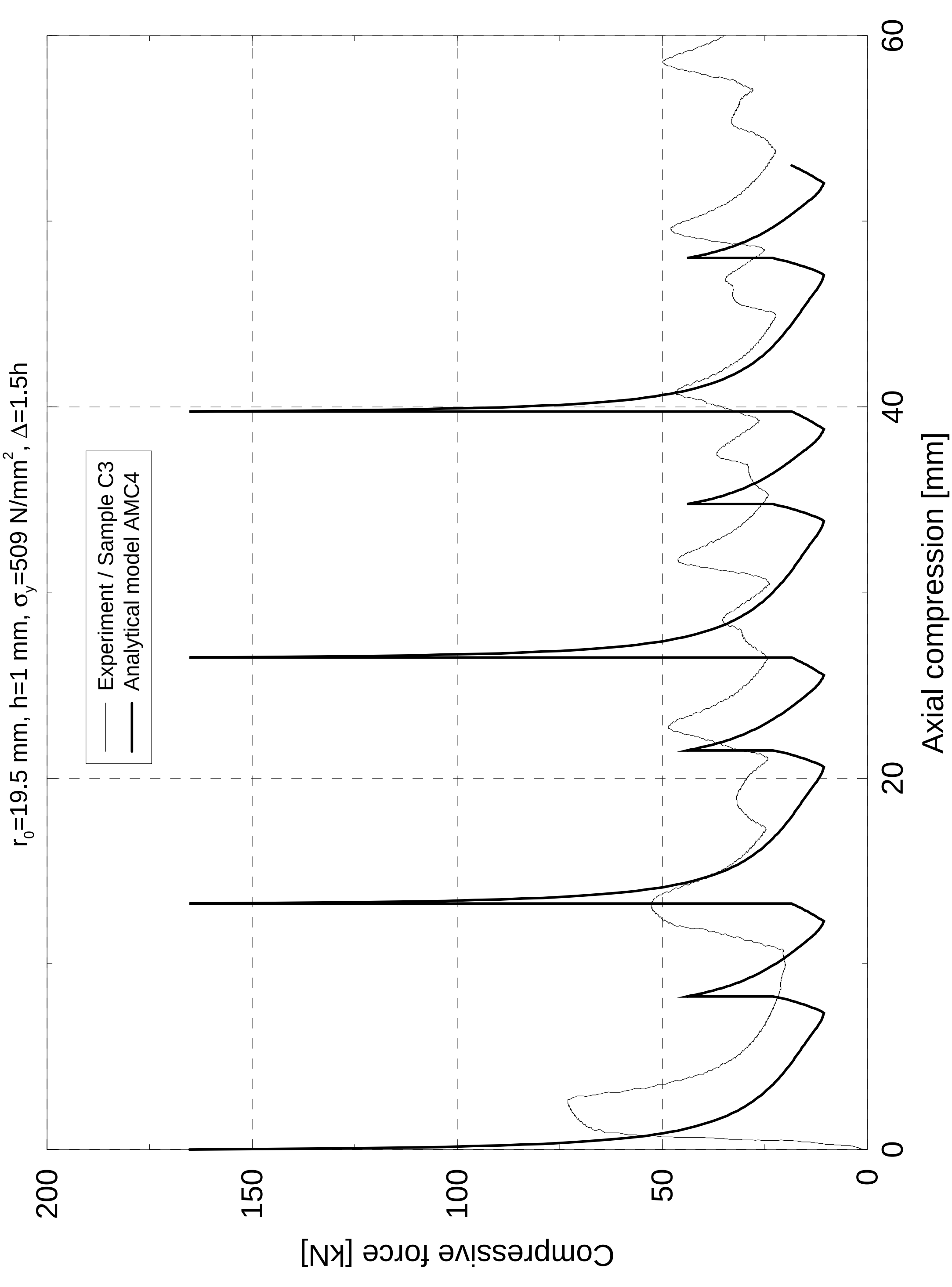

Figure 5.9: Two active folds model AMC4: comparison of measured and predicted load versus compression curves

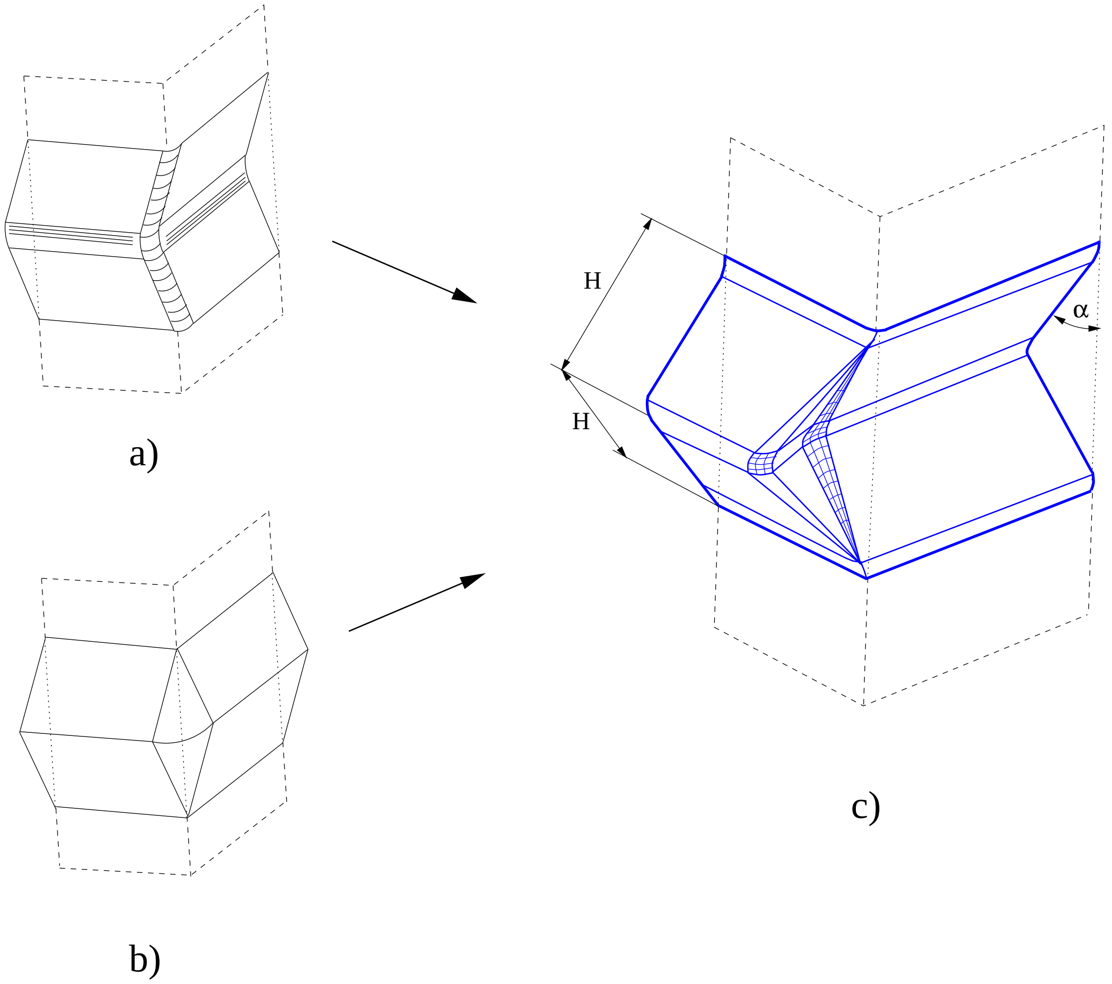

Figure 5.10: Multicorner columns: deformation modes: a) quasi-inextensional, b) extensional, c) generalized folding mechanism

by moving hinge lines, inclined between the trapezoidal elements.[7] At the configuration $\overline{\alpha}$ the inclined travelling hinge lines cease to move (i.e. they become stationary with respect to the material), and an extensional folding mode takes over for the second part of the crushing process ($\overline{\alpha} \leq \alpha \leq \alpha_f = \pi/2$), characterized by the (additional) formation of two conical surfaces, as shown in Figure 5.10c.

Unknown parameters of the deformation process are the fold length H, the switching angle $\overline{\alpha}$ between the two modes and a small bending radius b, used for describing the cylindrical and toroidal surfaces. Because all these variables are assumed not to change with time, they may (according to Eq. (5.7)) again be determined by minimization of the mean crushing force.

---

[7] Likewise, a conical surface, as sketched in Figure 5.10c, could also be assumed for the latter part without affecting the energy dissipation (see e.g. [Wierzbicki and Abramowicz, 1983]).

The use of elements with moving instead of fixed boundaries allows to describe a rather complex deformation behaviour, inherent to this type of failure, with a very limited number of degrees of freedom by the proposed collapse model, and even the (approximate) evaluation of the internal energy dissipation may be performed very efficiently. Without going into details of the derivation (the final expressions for the individual energy and energy rate terms are summarized in Appendix A.1), the internal energy dissipation for each folding mode may be confined to only three different contributions:

- Mode 1 (quasi-inextensional mode, $0 < \alpha < \overline{\alpha}$):

  D_1: flow over the toroidal surface,

  D_2: bending along horizontal hinge lines,

  D_3: bending along inclined travelling hinge lines,

- Mode 2 (extensional mode, $\overline{\alpha} \leq \alpha \leq \alpha_f$):

  D_4: stretching in a conical surface,

  D_5: bending along horizontal hinge lines,

  D_6: bending along inclined stationary hinge lines.

With respect to the evaluation of these terms, most effort has to be put on a convenient kinematic description for defining the strain rates acting in the individual parts. In order not to complicate the analysis, however, it is assumed that for each of the contributions D_i the rates of plastic deformation may be restricted to one dimension, and N_0 and M_0, respectively, act in the directions of these nonzero plastic strain and curvature rates. Details of the derivation, however, are omitted here. These may e.g. be found in [Abramowicz and Wierzbicki, 1989] or the diploma theses [Wintschnig, 1996; Willminger, 1999].

With D_1 to D_6 the power equation is formally written as

$$F_{\mathrm{a}} v_{\mathrm{c}} = \begin{cases} n_{\mathrm{c}} \sum_{i=1}^{3} D_i & \text{for } 0 < \alpha < \overline{\alpha} \; , \\ n_{\mathrm{c}} \sum_{i=4}^{6} D_i & \text{for } \overline{\alpha} < \alpha < \alpha_f \; , \end{cases} \tag{5.39}$$

where n_c denotes the number of corners of the column under consideration. Integration over the whole crushing cycle delivers

$$F_\mathrm{m} u_\mathrm{f} = n_\mathrm{c} \left[\sum_{i=1}^{3} \int_{0}^{\overline{\alpha}} \frac{D_i}{\dot{\alpha}} d\alpha + \sum_{i=4}^{6} \int_{\overline{\alpha}}^{\alpha_f} \frac{D_i}{\dot{\alpha}} d\alpha \right] \tag{5.40}$$

and

$$F_\mathrm{m}(H, \overline{\alpha}, b) = \frac{n_\mathrm{c}}{u_\mathrm{f}} \sum_{i=1}^{6} W_i \ , \tag{5.41}$$

respectively, from which the unknown kinematic parameters may be obtained by applying a numerical optimization procedure. Analytical derivations, however, have also been provided for special configurations, see e.g. [Abramowicz and Wierzbicki, 1989; Wierzbicki and Abramowicz, 1989]. Having determined the unknown variables, F_m is finally given by Eq. (5.41), and the instantaneous crushing forces follow from Eq. (5.39).

A force-compression curve obtained with this collapse model, together with a typical experimental curve, is shown in Figure 5.11., where the actual yield stress $\sigma_{0.2}$ is replaced by $\sigma_y = 0.92\sigma_\mathrm{u}$ (as proposed for mild steel) in order to account for hardening of the material, and the crushing distance u_f $(= 2H)$ is replaced by an effective crushing distance of $u_\mathrm{eff} = 0.73 \cdot 2H$ [Abramowicz and Wierzbicki, 1989]. A comparison of the predicted and experimental curves reveals that, without additional considerations, this model must also be stated to fail to describe the actual force-deflection behaviour of the progressive crushing process. The instantaneous crushing force starts with an infinite load peak (provided the tube is perfectly straight) which is followed by a strong decrease of the forces down to values below the measured ones at the end of each crushing cycle. The effective crushing distances, however, agree reasonably well with the experimental observations, and also the mean force predictions have some value for design purposes. The mean force predicted by the model is 22.6 kN, which is about 15% lower than the measured ones (if compared to the results for loading rate 1 mm/s, see Table 4.2).

5.4 Conclusions

A comparison of the different investigated single active fold models for describing the crushing process of circular and multicorner columns has shown that without additional assumptions (mainly based on experimental observations) they are not suited for describing complete load-compression curves. For a prediction of the mean forces, however, these

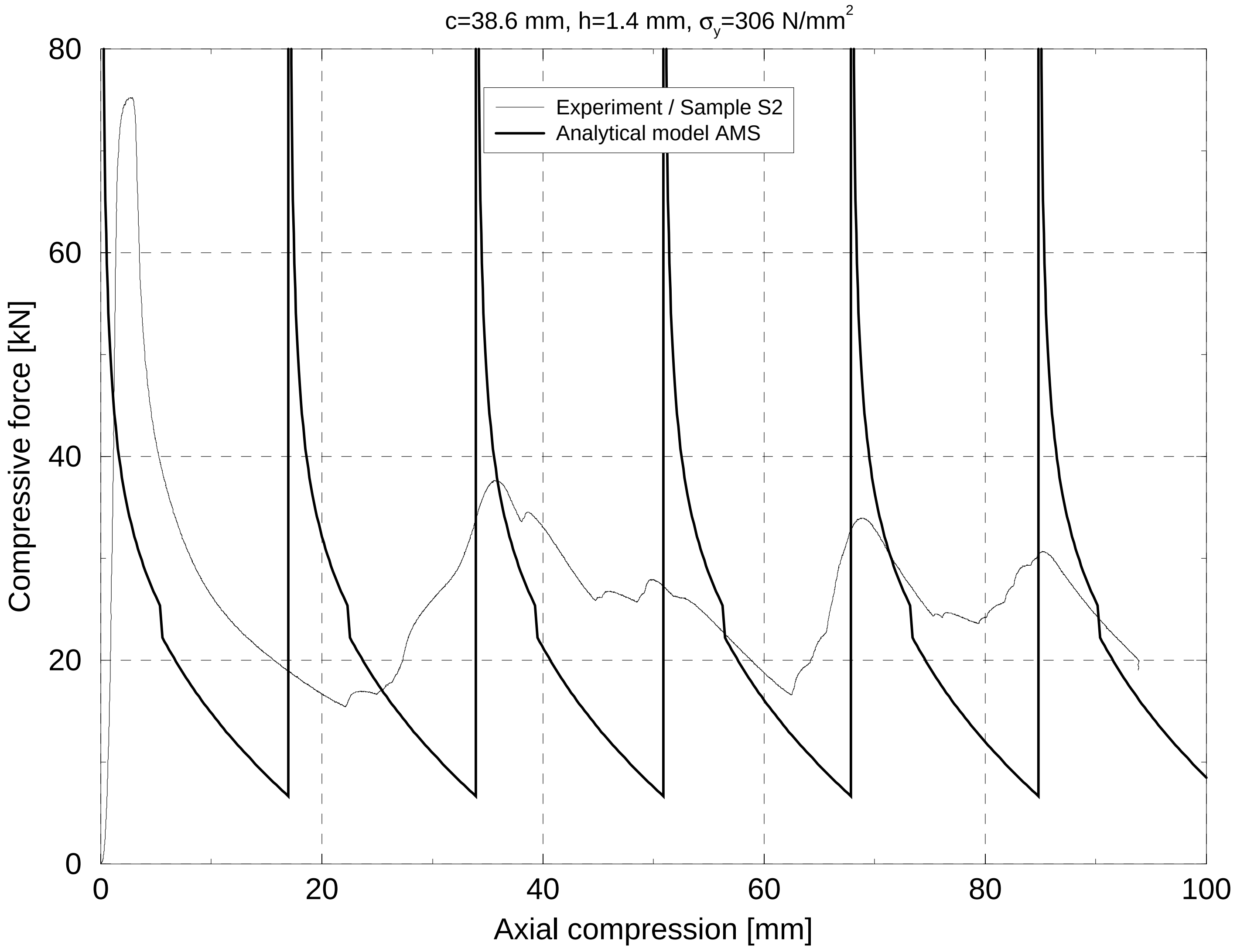

Figure 5.11: Multicorner model AMS: comparison of measured and predicted load versus compression curves for square tubes

models are applicable. If additional considerations are taken into account, then even relatively simple kinematic descriptions allow quite accurate predictions of the load-deflection behaviour. The two active folds model for circular tubes, proposed by Wierzbicki et al. [1992], seems to be highly qualified for the kinematic description of the whole crushing process, but without further improvements it is also only applicable for the prediction of mean crushing forces. A generalization of this model, however, is expected to deliver more accurate predictions even for a complete load cycle. When the requirement for obtaining analytical solutions is dropped, essential improvements are expected by using a more refined stress resultant yield surface. In a first step this could be realized by utilizing yield conditions like those used for the single active fold models AMC1 to AMC3 (Eqs. (5.29) and (5.32)). If set on a proper numerical foundation, however, further improvements are possible. These essentially include:

- application of a general yield condition (e.g. the exact Ilyushin yield condition described in section 3.4),
- consideration of all active strain rate components, i.e. not only bending and hoop strain rates, but also meridional strain rates and bending rates in circumferential direction,
- generalization of the kinematic description to a system of more degrees of freedom.

A simulation strategy taking into account all these refinements, which is based on the upper bound theorem of limit analysis in combination with an incremental solution procedure, is proposed in the next chapter ("sequential limit analysis method").

Chapter 6

Sequential Limit Analysis Method

The comparisons of the simplified axial crushing mechanisms with experiments, which are presented in the previous chapter, reveal that the ability of these semi-analytical models to describe the force-deflection characteristics of the whole deformation process is rather limited, even if the underlying kinematics seem to be well suited. When the requirement for analytical solutions is dropped, however, several improvements can be obtained. To account for the interaction between the different stress resultant components, a general yield criterion (e.g. the exact Ilyushin yield criterion, described in section 3.4, which is exact for rigid-perfectly plastic material behaviour) instead of simplified yield conditions can be used. Furthermore, there is no need to describe the kinematics of a single fold by only one degree of freedom, so the division into “finite elements”, where the boundaries may be described by plastic hinge lines (which even could be allowed to move), should lead to further improvements.

Starting from these considerations a “sequential limit analysis method” for the axial collapse analysis of general axisymmetric shells (i.e. not restricted to cylindrical ones) is proposed in the present chapter. Herein the large deformation process is described in an incremental manner, where each increment is solved by mathematical programming techniques. Due to the application of the exact Ilyushin yield surface the power of internal forces can be taken into account very accurately. It is also shown that with the proposed method frictionless internal contact can be accounted for easily, fitting into the kinematics-oriented solution strategy. Furthermore, the kinematic description is chosen such that most of the analytically based kinematic mechanisms proposed in the literature for the concertina mode buckling of cylindrical shells can be regarded as special cases, thus allowing to study the effects of different simplifications used in these models.

6.1 Fundamentals

As mentioned in the literature overview the plastic extremum and bounding principles, which are intended for investigating plastic limit states and ultimate loads, respectively, may serve as a direct and natural approach to collapse analysis of structures. Advantages of these methods (which use an inequality form of the constitutive equations), compared to the conventional FE method, are that the ultimate loads are evaluated directly without considering details of incremental elasto-plastic constitutive relations and internal loading and unloading conditions, thus delivering computational attractivity. In particular, the kinematics-oriented theorems (Markov theorem, upper bound theorem of limit analysis, see section 3.3) are conceptually simple and may be applied to advantage for defining numerical (rigid-plastic) simulation tools. Due to the kinematics-driven formulation stresses do not explicitly enter the algorithmic problem, and the methods fit very well into the basic concepts of the conventional kinematics-oriented finite element method. Examples are FE based upper bound limit analysis or the rigid-plastic finite element method mentioned in section 2.2, but also the semi-analytical collapse models described in chapter 5 are essentially based on the same theoretical foundations.

The numerical implementation of the upper bound theorem for axisymmetric shells, which is proposed in the following, also relies on a finite element discretization of the underlying structure. Numerical solutions, however, are directly found by applying general optimization routines instead of resorting to a specialized solution procedure, this way maintaining modeling generality while restricting the coding effort. Before details of the kinematic description as well as the algorithmic structure are given, however, the basics of the method are sketched in the following.

6.1.1 Upper Bound Theorem

The upper bound theorem of limit analysis (the derivation of which is given in section 3.3), is stated in its traditional form (Eq. (3.57)) as

$$\overline{\lambda} \leq \lambda^{+}(\boldsymbol{v}^{*}) = \frac{D_{\text{int}}(\boldsymbol{v}^{*})}{D_{\text{ext},0}(\boldsymbol{v}^{*})} \, . \tag{6.1}$$

Because both the power of internal and external reference forces, D_{int} and $D_{\text{ext},0}$, are functions of the velocity field $\boldsymbol{v}^{*}$ only, the problem of calculating the optimal load proportionality factor $\overline{\lambda}$ reduces to the search for the optimal (kinematically admissible) collapse mechanism $\boldsymbol{v}$ $(= \boldsymbol{v}^*_{\text{opt}})$, leading to a (constrained) minimum of λ^+. If the power of the external reference forces is kept constant,[1] then the upper bound theorem may alternatively be written as the constrained optimization problem [Capsoni and Corradi, 1997b]:

$$\begin{aligned} & D_{\text{int}}(\boldsymbol{v}^*) \longrightarrow \min \ , \\ \text{subject to:} \quad & D_{\text{ext},0}(\boldsymbol{v}^*) = \text{const} \ , \\ & \boldsymbol{v}^* = 0 \qquad \text{at } a = a_v \ , \end{aligned} \tag{6.2}$$

which may be solved directly by applying general optimization routines. It is to be noted, however, that in general the objective function $D_{\text{int}}(\boldsymbol{v}^*)$, although convex, is not only nonlinear, but may also become non-smooth,[2] and special optimization routines, which are able to treat such problems, must be adopted for such cases (see below).

6.1.2 Large Deformation Analysis

The upper bound theorem, Eq. (6.2), is used to determine the "optimal" instantaneous velocity field $\boldsymbol{v}$ describing the actual collapse behaviour for a given geometrical configuration $\boldsymbol{x}$ at time t. In order to simulate a large deformation solution, however, a stepwise procedure may be adopted. In each step, a limit analysis problem is solved and afterwards the velocity field is integrated in a small time step $t \rightarrow t + \Delta t$ to update the geometry:

$$\boldsymbol{x}(t + \Delta t) \approx \boldsymbol{x}(t) + \Delta t \ \boldsymbol{v} \ . \tag{6.3}$$

This way a "sequential limit analysis" [Yang, 1993; Hwan, 1997], which produces a nonlinear cumulative sequence of (quasistatic) deformations, may be performed. Since stress quantities do not enter the upper bound formulation explicitly, the sequence involves geometrical updating only, which may be achieved relatively simply, and in general larger time steps as compared with those used in an incremental analysis based on stress updating may be used. If contact has to be considered, too, then after each geometrical update kinematic contact search algorithms must be applied for locating regions of contact and interpenetrations, respectively. If regions of interpenetrations are found, the time step Δt is reduced accordingly (in order to ensure valid contact without interpenetrations), and additional constraints are activated for the optimization problem to be solved in the next step. These kinematic constraint inequalities have to ensure that (for frictionless contact) the time derivative of the normal distance between the contacting surfaces does not become negative, this way maintaining the purely kinematic characteristics of the methodology. It is worth noting, however, that hardening could also be accounted for in an incremental manner by updating the local yield stress step by step with the deformation history. In a similar way, material strain rate sensitivities, and even inertia forces (and thus dynamic effects) could approximately be considered without giving rise to leading to fundamental difficulties.

---

[1] Without loss of generality $D_{\text{ext},0} = 1$ may be assumed.

[2] This is the case if some regions of the structure do not deform plastically but move as rigid bodies. Then, depending on the kinematic description, the partial derivatives of the objective function become discontinuous.

6.1.3 Internal Energy Dissipation

Concerning the application of the upper bound limit analysis method for shell structures it is necessary to evaluate the power of internal forces as a function of kinematic quantities only. For a Kirchhoff shell obeying the von Mises yield criterion, however, this may advantageously be achieved by applying the energy dissipation function according to the exact Ilyushin yield criterion, the derivation of which is given in section 3.4.5 (see Eqs. (3.100) to (3.103)).

Provided the shell structure under consideration (described by its (current) middle surface S) can be decomposed into continuously and discontinuously deforming regions, the total internal energy dissipation D_{int} is given by

$$D_{\text{int}} = D_{\text{int}}^{(c)} + D_{\text{int}}^{(d)} = \int_S \left(N_{\alpha\beta} \dot{\bar{\varepsilon}}_{\alpha\beta} + M_{\alpha\beta} \dot{\kappa}_{\alpha\beta} \right) dS + \sum_j |M_j \dot{\beta}_j| l_j \, . \tag{6.4}$$

$N_{\alpha\beta}$ and $M_{\alpha\beta}$ denote the stress resultants (section forces and moments) and $\dot{\bar{\varepsilon}}_{\alpha\beta}$ and $\dot{\kappa}_{\alpha\beta}$ are the rates of the work conjugate (plastic) midplane strains and curvatures, respectively,[3] with $(\alpha, \beta) \in (1, 2)$ for Kirchhoff shells (see also section 3.4). The second part sums up all contributions with respect to energy dissipation due to the presence of plastic hinge lines. Here it is already assumed that the angular velocities, i.e. the jumps in the rate of rotation, $\dot{\beta}_j$, as well as the corresponding plastic moments, M_j, are constant over the length l_j of each yield line j.

With the normalized power of internal forces of a shell section, $\overline{d}_{\text{p}}$ (Eq. (3.103)), the internal energy dissipation follows as

---

[3] Due to the basic assumption of rigid-plastic material behaviour no distinction between total and plastic strains is made.

$$D_{\text{int}} = \int_S N_0 \dot{\varepsilon}_0 \, \overline{d}_{\text{p}}(\dot{\boldsymbol{e}}, \dot{\boldsymbol{k}}) \, dS + \sum_j |M_j \dot{\beta}_j| l_j \, , \tag{6.5}$$

and because the normalized midplane strain and curvature rate vectors $\dot{\boldsymbol{e}}$ and $\dot{\boldsymbol{k}}$ are given functions of the underlying velocity field, Eq. (6.5) is a convenient definition for the objective function in terms of kinematic quantities only.

With respect to a discretization of the geometry into a number of (continuously deforming) elements, Eq. (6.5) may be written as

$$D_{\text{int}} = \sum_e \int_{S_e} N_0 \dot{\varepsilon}_0 \overline{d}_{\text{p}}(\dot{\boldsymbol{e}}, \dot{\boldsymbol{k}}) \, dS_e + \sum_j |M_j \dot{\beta}_j| l_j \tag{6.6}$$

(element related quantities are denoted by a subscript e), where, as in the conventional finite element method, the element integrations may be performed numerically (e.g. by applying a Gauß integration procedure).

From a computational point of view it is worth mentioning that the evaluation of $\overline{d}_{\text{p}}(\dot{\boldsymbol{e}}, \dot{\boldsymbol{k}})$ according to section 3.4.5 not only avoids a numerical thickness integration, but also gives the exact power of internal forces for the shell section under consideration.

Remarks

For the special case of a shell with constant thickness and consisting of one material only, a dimensionless form for the objective function may also be obtained:

$$d_{\text{int}} = \frac{D_{\text{int}}}{N_0 \dot{\varepsilon}_0} = \sum_e \int_{S_e} \overline{d}_{\text{p}}(\dot{\boldsymbol{e}}, \dot{\boldsymbol{k}}) \, dS_e + \frac{1}{\dot{\kappa}_0} \sum_j |m_j \dot{\beta}_j| l_j \, , \tag{6.7}$$

with the dimensionless plastic moments m_j being defined as $m_j = M_j / M_0$ (and assuming that $N_0 \dot{\varepsilon}_0 = M_0 \dot{\kappa}_0$ holds, see section 3.4). An interesting fact becoming obvious from this equation is that the normalized internal energy dissipation of the shell structure, d_{int}, does not depend on the actual yield stress of the material. Because, in addition, the power of the external reference forces, $D_{\text{ext},0}$ (entering the optimization problem (6.2) as an equality constraint), is not affected by σ_y, it is furthermore found that solutions of the upper bound limit analysis problem may be obtained as pure functions of the geometrical configuration of the structure, with the actual yield stress just acting as a scaling factor ($N_0 = \sigma_y h$). For large deformation collapse analysis of structures this, however, implies that the predicted characteristics of the whole system response (e.g. the progression of the force-deflection curve during axial crushing) is fully determined by the geometrical configuration of the underlying structure, regardless of the material actually used.

6.2 Sequential Limit Analysis of Axisymmetric Shells

The sequential limit analysis method sketched above (which is applicable to shell structures of general geometry) is implemented in a specialized computer program to analyze the crushing behaviour of axisymmetric shells. Herein, the main emphasis is put on the numerical generalization of simplified kinematic mechanisms for the concertina mode buckling of circular cylindrical shells proposed in the literature (as those described in chapter 5). Therefore, the meridian of the shell structure is discretized using circular arc elements (which are also used in analytically based mechanisms), and the external loading is restricted to axial compression only. Further assumptions, used in the current version of the computer program, are:

- the shell structure consists of one material only and has a constant thickness,
- the thickness does not change with time,
- meridional strain rates are constant within each element (this is realized by treating the meridional length of each element as an independent parameter, which may change with time),
- between the arc elements stationary plastic hinge lines may be allowed.

The Kirchhoff hypothesis (together with the assumptions of rigid-perfectly plastic material behaviour and the validity of the von Mises yield criterion) furthermore ensures that the energy dissipation function according to the exact Ilyushin yield surface, Eq. (3.103), may be applied for the evaluation of the internal energy dissipation.

6.2.1 Kinematic Description

Nodal Quantities

The geometry of the meridional curve of the axisymmetric shell structure is described using n circular arc elements. The discretization of an arbitrary intermediate configuration

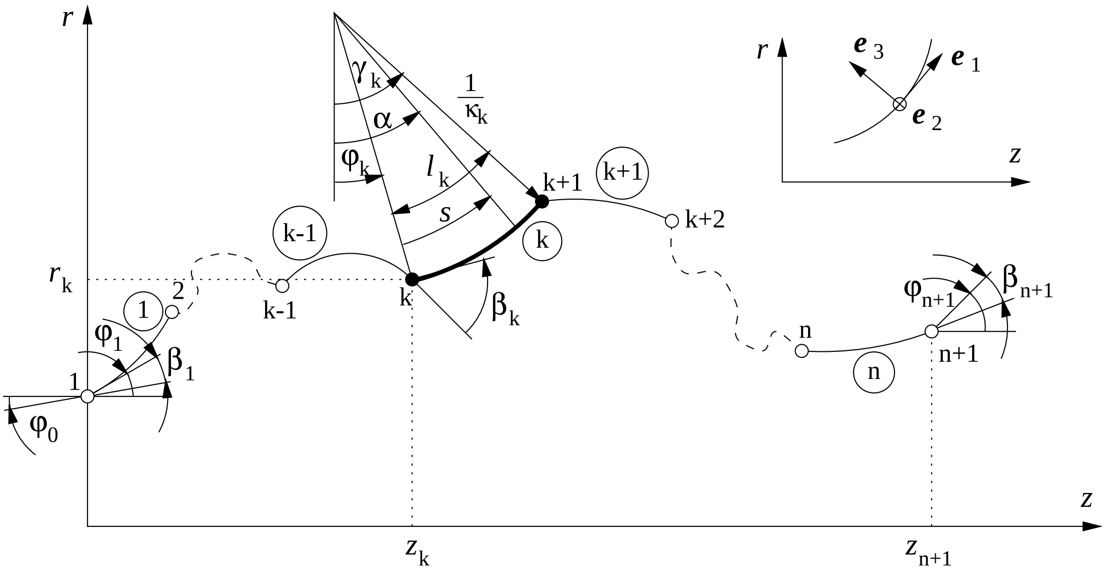
r
z
r_k
z_k
z_{n+1}
1
2
k-1
k
k+1
k+2
n
n+1
(1)
(k-1)
(k)
(k+1)
(n)
φ_0
φ_1
β_1
γ_k
α
φ_k
l_k
s
$\frac{1}{\kappa_k}$
β_k
φ_{n+1}
β_{n+1}
e_1
e_2
e_3

Figure 6.1: Finite element discretization of the meridional curve

(which is, starting from the initial geometry, given in advance for each time step) can be seen schematically in Figure 6.1, where the used variables (and the orientation of the element's local coordinate system, given by the unit vectors $\boldsymbol{e}_1$ to $\boldsymbol{e}_3$) are also shown. The stationary plastic hinges, which may be allowed between individual elements, are characterized for node k by an angle β_k. Starting from node 1, the position of each node k (up to node $n+1$) is described using the curvatures κ_i and the lengths l_i of the elements as well as the nodal angles β_i ($i \in [1,k]$) as independent parameters (the rates of these quantities are used as the degrees of freedom for the optimization problem, see below). For given values of φ_0, r_1 and z_1 (and with $\varphi_1 = \varphi_0 + \beta_1$) the following equations hold ($k \in [1,n]$):

$$\begin{aligned} \gamma_k &= \varphi_k + \kappa_k l_k \ , \\ \varphi_{k+1} &= \gamma_k + \beta_{k+1} \ , \\ r_{k+1} &= r_k + \frac{1}{\kappa_k} \left(\cos\varphi_k - \cos\gamma_k\right) \ , \\ z_{k+1} &= z_k - \frac{1}{\kappa_k} \left(\sin\varphi_k - \sin\gamma_k\right) \ . \end{aligned} \tag{6.8}$$

The time derivatives of these equations have the form

$$
\begin{aligned}
\dot{\gamma}_k &= \dot{\varphi}_k + \dot{\kappa}_k l_k + \kappa_k \dot{l}_k \ , \\
\dot{\varphi}_{k+1} &= \dot{\gamma}_k + \dot{\beta}_{k+1} \ , \\
\dot{r}_{k+1} &= \dot{r}_k - \frac{\dot{\kappa}_k}{\kappa_k^2} \left(\cos\varphi_k - \cos\gamma_k\right) - \frac{1}{\kappa_k} \left(\dot{\varphi}_k \sin\varphi_k - \dot{\gamma}_k \sin\gamma_k\right) \ , \\
\dot{z}_{k+1} &= \dot{z}_k + \frac{\dot{\kappa}_k}{\kappa_k^2} \left(\sin\varphi_k - \sin\gamma_k\right) - \frac{1}{\kappa_k} \left(\dot{\varphi}_k \cos\varphi_k - \dot{\gamma}_k \cos\gamma_k\right) \ ,
\end{aligned}
\tag{6.9}
$$

where the boundary values at node 1 are given by $\dot{\varphi}_0$ ($\Rightarrow \dot{\varphi}_1 = \dot{\varphi}_0 + \dot{\beta}_1$), $\dot{r}_1$ and $\dot{z}_1$, which, in the general case, are active degrees of freedom.[4]

For a straight element ($\kappa_k = 0$) the above equations for r, z, $\dot{r}$ and $\dot{z}$ are indeterminate. Application of the de L'Hospital rule, however, delivers simplified expressions in this case, which are given as

$$
\begin{aligned}
r_{k+1} &= r_k + l_k \sin\varphi_k \ , \\
z_{k+1} &= z_k + l_k \cos\varphi_k \ ,
\end{aligned}
\tag{6.10}
$$

and

$$
\begin{aligned}
\dot{r}_{k+1} &= \dot{r}_k + \left(\dot{\varphi}_k l_k + \frac{\dot{\kappa}_k l_k^2}{2}\right) \cos\varphi_k + \dot{l}_k \sin\varphi_k \ , \\
\dot{z}_{k+1} &= \dot{z}_k - \left(\dot{\varphi}_k l_k + \frac{\dot{\kappa}_k l_k^2}{2}\right) \sin\varphi_k + \dot{l}_k \cos\varphi_k \ ,
\end{aligned}
\tag{6.11}
$$

respectively.

With respect to the definition of the constraint equations for the optimization problem (kinematic boundary conditions, power of external reference forces, but also the contact constraints derived in section 6.2.3) it is interesting to note that all relations defined in Eqs. (6.9) and (6.11) show a linear dependence between the different velocity quantities. This functional dependence, however, is also reflected by the linearity of the constraint equations entering the optimization problems, which all are defined in rate form.[5]

Element Quantities — Strain Rate Definition

The strain rate measure used for stating the kinematics-oriented plastic extremum and bounding theorems is the spatial rate of deformation tensor $\boldsymbol{d}$, defined in general form in

---

[4] For the investigations described here, however, clamped boundary conditions are assumed at node 1, which means that $\dot{\varphi}_0$, $\dot{r}_1$ and $\dot{z}_1$ are (without restriction to generality) all set to zero.

[5] For example, a radial fixation of point $n+1$ is enforced by the constraint equation $\dot{r}_{n+1} = 0$, etc.

Eq. (3.8). Using this (and considering that the meridional strain rates are assumed to be constant within an element), the midplane strain rates for an axisymmetrically deforming shell section are given by

$$\begin{aligned}\dot{\bar{\varepsilon}}_{11} &= \frac{\dot{l}_k}{l_k}\ ,\\ \dot{\bar{\varepsilon}}_{22} &= \frac{\dot{r}}{r}\ ,\\ \dot{\bar{\varepsilon}}_{12} &= 0\ ,\end{aligned} \tag{6.12}$$

where 1 denotes the meridional and 2 the circumferential direction (see Figure 6.1). Because of the assumption of constant meridional strain rates within an element, however, $\dot{\bar{\varepsilon}}_{11}$ may likewise be stated as

$$\dot{\bar{\varepsilon}}_{11} = \frac{\dot{l}_k}{l_k} = \frac{\dot{s}}{s}\ , \tag{6.13}$$

from which the relation

$$\dot{s} = \frac{s}{l_k}\dot{l}_k \tag{6.14}$$

(which is needed below) is obtained.

The curvature vector for the current configuration is defined by the components

$$\begin{aligned}\kappa_{11} &= -\kappa_k\ ,\\ \kappa_{22} &= \frac{\cos\alpha}{r}\ ,\\ \kappa_{12} &= 0\ ,\end{aligned} \tag{6.15}$$

and thus the curvature rates follow as

$$\begin{aligned}\dot{\kappa}_{11} &= -\dot{\kappa}_k\ ,\\ \dot{\kappa}_{22} &= -\dot{r}\frac{\cos\alpha}{r^2} - \dot{\alpha}\frac{\sin\alpha}{r}\ ,\\ \dot{\kappa}_{12} &= 0\ .\end{aligned} \tag{6.16}$$

According to Eqs. (6.12) and (6.16), the following kinematic quantities must, therefore, be evaluated at some point s in element k ($s \in [0, l_k]$) in order to fully determine the midplane strain and curvature rates (and thus the vectors $\dot{\bar{\boldsymbol{\varepsilon}}}$ and $\dot{\boldsymbol{k}}$, used for computing the internal energy dissipation of the shell section):

$$\begin{aligned}\alpha(s) &= \varphi_k + \kappa_k s\ ,\\ r(s) &= r_k + \frac{1}{\kappa_k}\left(\cos\varphi_k - \cos\alpha\right)\ ,\end{aligned} \tag{6.17}$$

Table 6.1: Evaluation sequence for the determination of the position related quantities

1.	Independent variables	φ_0, r_1, z_1 $\boldsymbol{\kappa} = (\kappa_1, \ldots, \kappa_n)^T$ $\boldsymbol{l} = (l_1, \ldots, l_n)^T$ $\boldsymbol{\beta} = (\beta_1, \ldots, \beta_{n+1})^T$
2.	Compute node related position vectors (Eqs. (6.8) and (6.10), resp.)	$\boldsymbol{\gamma} = (\gamma_1, \ldots, \gamma_n)^T$ $\boldsymbol{\varphi} = (\varphi_0, \ldots, \varphi_{n+1})^T$ $\boldsymbol{r} = (r_1, \ldots, r_{n+1})^T$ $\boldsymbol{z} = (z_1, \ldots, z_{n+1})^T$
3.	Evaluate element quantities (Eqs. (6.17) and (6.19), resp.)	$\alpha(s), r(s)$

$$\begin{aligned} \dot{\alpha}(s) &= \dot{\varphi}_k + \dot{\kappa}_k s + \kappa_k \dot{s} \ , \\ \dot{r}(s) &= \dot{r}_k - \frac{\dot{\kappa}_k}{\kappa_k^2} \left(\cos\varphi_k - \cos\alpha\right) - \frac{1}{\kappa_k} \left(\dot{\varphi}_k \sin\varphi_k - \dot{\alpha}\sin\alpha\right) \ . \end{aligned} \tag{6.18}$$

Again, simplified formulas for r and $\dot{r}$ are valid for straight elements ($\kappa_k = 0$):

$$r(s) = r_k + s\sin\varphi_k \ , \tag{6.19}$$

$$\dot{r}(s) = \dot{r}_k + \left(\dot{\varphi}_k s + \frac{\dot{\kappa}_k s^2}{2}\right)\cos\varphi_k + \dot{s}\sin\varphi_k \ . \tag{6.20}$$

The quantity $\dot{s}$ used in Eqs. (6.18) and (6.20) is given by Eq. (6.14).

A summary concerning the evaluation of the kinematic quantities, required for determining the midplane strain and curvature rate vectors $\dot{\boldsymbol{e}}(s)$ and $\dot{\boldsymbol{k}}(s)$ (and thus the normalized internal energy dissipation for the shell section, $\overline{d}_{\mathrm{p}}(s)$) is contained in Tables 6.1 and 6.2 (divided into position and velocity related quantities). Due to the fact that no displacement changes take place within an increment (i.e. the geometrical configuration is fixed for each step of the sequential limit analysis algorithm), the dependent position quantities listed in Table 6.1 must only be evaluated once per increment. The velocity terms summarized in Table 6.2, however, have to be computed for each iteration step of the optimization process.

Table 6.2: Evaluation sequence for the determination of the velocity related quantities and the internal energy dissipation, respectively

1.	Independent variables (degrees of freedom for the optimization problem)	$\dot{\varphi}_0, \dot{r}_1, \dot{z}_1$ $\dot{\boldsymbol{\kappa}} = (\dot{\kappa}_1, \dots, \dot{\kappa}_n)^T$ $\dot{\boldsymbol{l}} = (\dot{l}_1, \dots, \dot{l}_n)^T$ $\dot{\boldsymbol{\beta}} = (\dot{\beta}_1, \dots, \dot{\beta}_{n+1})^T$
2.	Compute node related velocity vectors (Eqs. (6.9) and (6.11), resp.)	$\dot{\boldsymbol{\gamma}} = (\dot{\gamma}_1, \dots, \dot{\gamma}_n)^T$ $\dot{\boldsymbol{\varphi}} = (\dot{\varphi}_0, \dots, \dot{\varphi}_{n+1})^T$ $\dot{\boldsymbol{r}} = (\dot{r}_1, \dots, \dot{r}_{n+1})^T$ $\dot{\boldsymbol{z}} = (\dot{z}_1, \dots, \dot{z}_{n+1})^T$
3.	Evaluate element quantities (Eqs. (6.18) and (6.20), resp., with Eq. (6.14))	$\dot{\alpha}(s), \dot{r}(s)$
4.	Determine midplane strain and curvature rate vectors (Eqs. (6.12), (6.16), (3.99))	$\dot{\bar{\boldsymbol{e}}}(s), \dot{\boldsymbol{k}}(s)$
5.	Evaluate the normalized plastic dissipation of the shell section (Eq. (3.103))	$\bar{d}_{\mathrm{p}}(s)$

Remarks

It was mentioned in section 3.2 that time integration of the spatial rate of deformation tensor (used here) does in general not deliver a strain measure. For the special case that the principal strain directions do not rotate with respect to the material, however, the logarithmic or natural strain is obtained. For the axisymmetric shells considered here, the (nonzero) midplane strains are, therefore, given as

$$\begin{aligned} \bar{\varepsilon}_{11} &= \ln \frac{l_k(t)}{l_k(t_0)} \, , \\ \bar{\varepsilon}_{22} &= \ln \frac{r(s,t)}{r(s,t_0)} \end{aligned} \tag{6.21}$$

(time t_0 denotes an arbitrary, but fixed reference state), and differentiation with respect to time just delivers the strain rate components stated in Eq. (6.12). Likewise, the sequential limit analysis method could also be regarded as being based on small deformation theory, where (regardless of the deformation history) for each step an upper bound solution (which is related to the current "reference configuration" at time t_c) is to be solved. In this case, the midplane strains would be defined as

$$\begin{aligned} \overline{\varepsilon}_{11} &= \frac{l_k(t) - l_k(t_c)}{l_k(t_c)} \ , \\ \overline{\varepsilon}_{22} &= \frac{r(s,t) - r(s,t_c)}{r(s,t_c)} \ , \end{aligned} \tag{6.22}$$

and time differentiation yields exactly the same results as above.

6.2.2 Internal Energy Dissipation

According to Eq. (6.7) the internal energy dissipation of the discretized axisymmetric shell is given by

$$\begin{aligned} d_{\mathrm{int}} &= \sum_{k=1}^{n} d_{\mathrm{int},k}^{(c)} + \sum_{j=1}^{n+1} d_{\mathrm{int},j}^{(d)} \\ &= \sum_{k=1}^{n} 2\pi \int_0^{l_k} \overline{d}_{\mathrm{p}}(s) r(s)\ ds + \sum_{j=1}^{n+1} \frac{2\pi}{\dot{\kappa}_0} |m_j \dot{\beta}_j| r_j \ , \end{aligned} \tag{6.23}$$

where $d_{\mathrm{int},k}^{(c)}$ and $d_{\mathrm{int},j}^{(d)}$ denote the normalized internal energy dissipation owing to continuous deformations of element k and discontinuous deformations of the plastic hinge line j, respectively.

Element Contributions

For the numerical evaluation of the element integrals an m-point Gauß-Legendre integration is applied. With the Gauß-Legendre points $s_{k,i}$ and the corresponding weights $c_{k,i}$ (for details see e.g. [Press et al., 1992; Bronstein et al., 1995]) $d_{\mathrm{int},k}^{(c)}$ follows as

$$d_{\mathrm{int},k}^{(c)} = 2\pi \sum_{i=1}^{m} c_{k,i} \overline{d}_{\mathrm{p}}(s_{k,i}) r(s_{k,i}) \ . \tag{6.24}$$

This numerical integration procedure is implemented such that the integration order m may be chosen arbitrarily.[6]

---

[6] For the examples presented below, however, $m = 5$ is set in all cases.

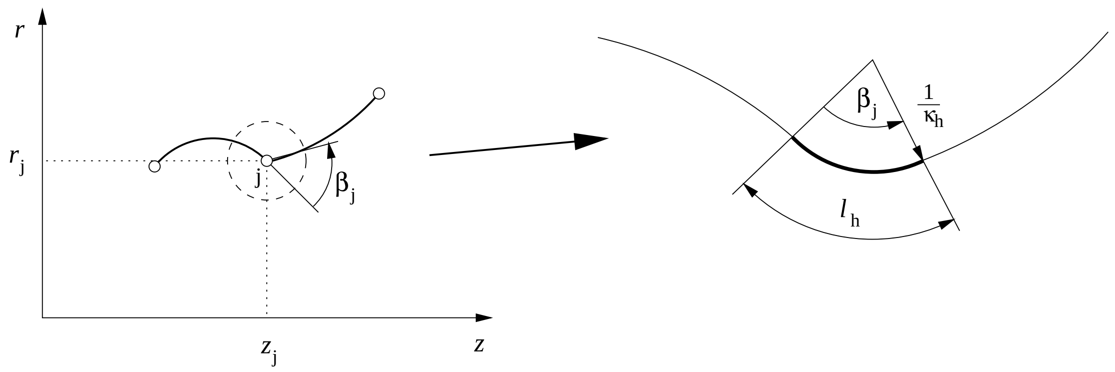

Figure 6.2: Approximation of plastic hinge line j by a continuously deforming transition region

Contributions of the Plastic Hinge Lines

When totally disregarding the effects of interacting stresses at the plastic hinge lines, m_j is equal to one (i.e. $M_j = M_0$). Because for axisymmetric shells, however, deformations in circumferential directions are constrained, a rotation rate $\dot{\beta}_j$ at the plastic hinge will induce plastic moments also along the circumference. When accounting for this bending interaction, the plastic bending moment M_j is given by $M_j = \frac{2}{\sqrt{3}} M_0$ (see also the collapse model of Alexander, described in the preceding chapter). Accordingly, $d^{(d)}_{\mathrm{int},j}$ follows as

$$d^{(d)}_{\mathrm{int},j} = \frac{4\pi}{\sqrt{3}\dot{\kappa}_0} |\dot{\beta}_j| r_j \ , \tag{6.25}$$

and this relation is implemented in the current version of the sequential limit analysis program.

The main drawback of Eq. (6.25), however, is that no reduction of the bending moments due to the additional action of in-plane forces is accounted for. Especially for higher section forces Eq. (6.25) must, therefore, be regarded as a crude approximation, essentially overestimating the energy dissipation at the yield line. A possible refinement, which also fits into the algorithmic structure of the proposed solution strategy, is to treat the plastic hinge line as a small, but continuous transition region of meridional length l_h, as sketched in Figure 6.2. When approximately assuming midplane strain and curvature rates as constant within the element,[7] the "hinge element" integration can be reduced to a one-point integration, thus keeping the additional computational costs sufficiently low while considering interaction of stress components in the most general way. For the limiting case of pure bending at the yield line (i.e. $\dot{\kappa}_h = \dot{\beta}_j / l_h$ is the only term, which is not equal to zero), however, it may be shown that this strategy just delivers the currently used definition for $d^{(d)}_{\text{int},j}$, Eq. (6.25).

---

[7] Without activating additional degrees of freedom, the unknown parameters $\dot{\bar{\varepsilon}}_1$ and $\dot{\alpha}$, needed for fully determining $\dot{\bar{\boldsymbol{e}}}(s)$ and $\dot{\boldsymbol{k}}(s)$, could possibly be estimated from the corresponding values of the adjacent "large" arc elements.

6.2.3 Consideration of Contact

Typical progressive crushing processes of tubular structures show self contact of both outer and inner surfaces due to the formation of subsequent folds and wrinkles. In order to account for these phenomena within the proposed, kinematics-oriented limit analysis procedure for axisymmetric shells, an algorithm based on the master-slave concept (see e.g. [Zhong, 1993]) is applied for the location of active contact regions. Geometric constraint inequalities are activated afterwards in order to ensure that (frictionless) contact is accounted for in the next step of the analysis. Without going into details of implementation, the principles of the applied strategy are sketched in the following.

Kinematic Contact Search

The contact search algorithm uses a spatial discretization, where each arc element is subdivided into a number of straight lines (with the auxiliary nodes lying on the elements, see Figure 6.3). All nodes connected with these contact segments (i.e. auxiliary and elemental nodes) form the contact node set.[8] The position of slave node j (given as point $\boldsymbol{p}_j$) with respect to a master element i is determined using the relations

$$g_{ij} = \pm(\boldsymbol{p}_j - \boldsymbol{p}_i)^T \boldsymbol{e}_{3,i} \,, \qquad s_{ij} = (\boldsymbol{p}_j - \boldsymbol{p}_i)^T \boldsymbol{e}_{1,i} \,. \tag{6.26}$$

Here, g_{ij} denotes the normal distance between slave node and master element (positive and negative signs are used for outside and inside contact, respectively), and s_{ij} gives the corresponding tangential offset on the master element (Figure 6.3). Vectors $\boldsymbol{e}_{1,i}$ and $\boldsymbol{e}_{3,i}$ are tangential and normal unit vectors of line segment i. In terms of the slope α_i these are

---

[8] All quantities used for describing contact are functions of the underlying shell kinematics and may conveniently be derived when adopting the relations given in section 6.2.1. The individual expressions for obtaining these values are, therefore, omitted in the following.

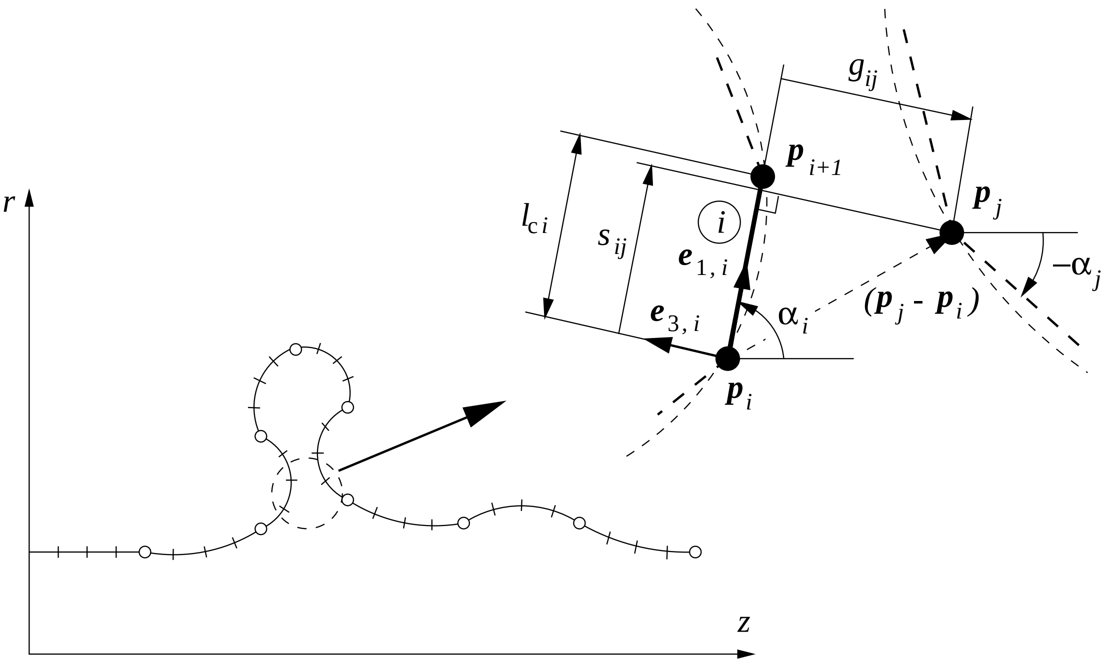

Figure 6.3: Basic configuration of the master-slave contact algorithm (inside contact)

given as

$$e_{1,i} = \begin{pmatrix} \cos\alpha_i \\ \sin\alpha_i \end{pmatrix} \quad , \qquad e_{3,i} = \begin{pmatrix} -\sin\alpha_i \\ \cos\alpha_i \end{pmatrix} \quad . \tag{6.27}$$

One problem when applying Eqs. (6.26) for checking contact is that in general it is not known in advance whether the contact node under consideration approaches the contact element from outside or from inside (and thus, wether the + or − sign has to be used when computing the normal distances g_{ij}). For the kinematic description used here, however, a quite simple strategy may be applied, which allows to distinguish both cases and even enables a common treatment of both outside and inside contact.

Provided the angles α_i are determined without a 2π-modulation,[9] these may be used to advantage for deciding whether outside or inside contact occurs. As can be seen from Figure 6.4, outside contact requires that the angle α_j (i.e. the directional slope of the contact segment, which is connected to slave node $\boldsymbol{p}_j$) is larger than α_i, whereas for inside

---

[9] That means that, starting from a reference angle α_0, each angle α_i is uniquely given by the evolution of the meridional curvature of the shell structure (see e.g. the definition of $\alpha(s)$ in Eq. (6.17)). The α_i-values meeting these requirements may conveniently be derived from the kinematics of the underlying arc elements, because the angles φ_k and γ_k are defined in the same unique manner (see Eq. (6.8)).

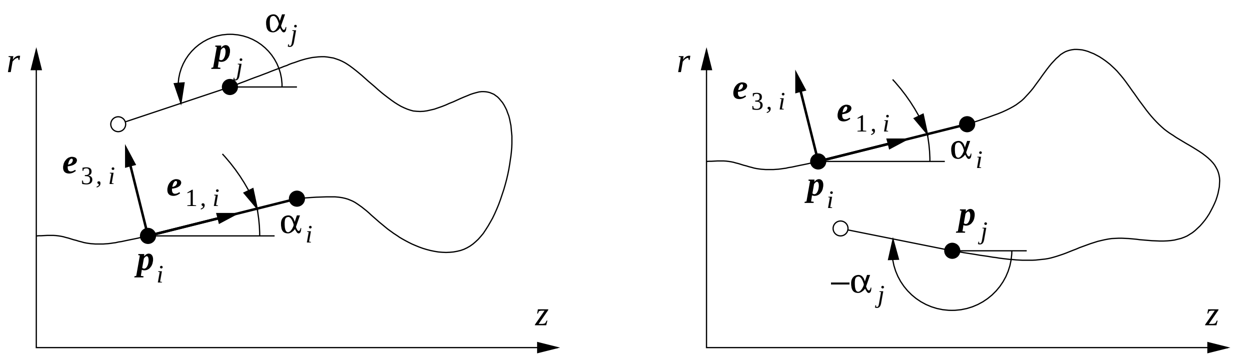

Figure 6.4: Evolution of the slope α for outside (left) and inside contact (right)

contact the difference between these angles,

$$\Delta\alpha_{ij} = \alpha_j - \alpha_i, \tag{6.28}$$

must be less than zero. With this, a simple combined criterion for checking both outside and inside contact may be expressed as

$$g_{ij} = \text{sign}(\Delta\alpha_{ij})(\boldsymbol{p}_j - \boldsymbol{p}_i)^T \boldsymbol{e}_{3,i} \ . \tag{6.29}$$

The flowchart presented in Figure 6.5 summarizes the algorithmic structure of such a combined contact search strategy, which allows to locate active outside/inside contact pairs and interpenetrations, respectively. Because with the sequential limit analysis method changes of the geometrical configuration are restricted to incremental updates between the individual steps (see Eq. (6.3)), these contact checks are of pure incremental nature, too. Intersections (i.e. $g_{ij} < 0$) may, therefore, simply be removed by reducing the time step Δt such that at the end of the increment the minimum of the normal distances of all active contact pairs just equals zero.[10]

Definition of Contact Constraints

Once an active contact pair $[i, j]$ has been located, it must be ensured that g_{ij} does not become negative for the next increment (which is a sufficient condition for frictionless contact). Therefore, inequalities of the form

$$\dot{g}_{ij} = \text{sign}(\Delta\alpha_{ij}) \left[(\dot{\boldsymbol{p}}_j - \dot{\boldsymbol{p}}_i)^T \boldsymbol{e}_{3,i} + (\boldsymbol{p}_j - \boldsymbol{p}_i)^T \dot{\boldsymbol{e}}_{3,i}\right] \geq 0 \ , \tag{6.30}$$

---

[10] Provided the geometrical configuration at the start of the increment does not have any interpenetrations (and all contact pairs active at this time are constrained not to penetrate each other) a time step fulfilling these requirements can always be found.

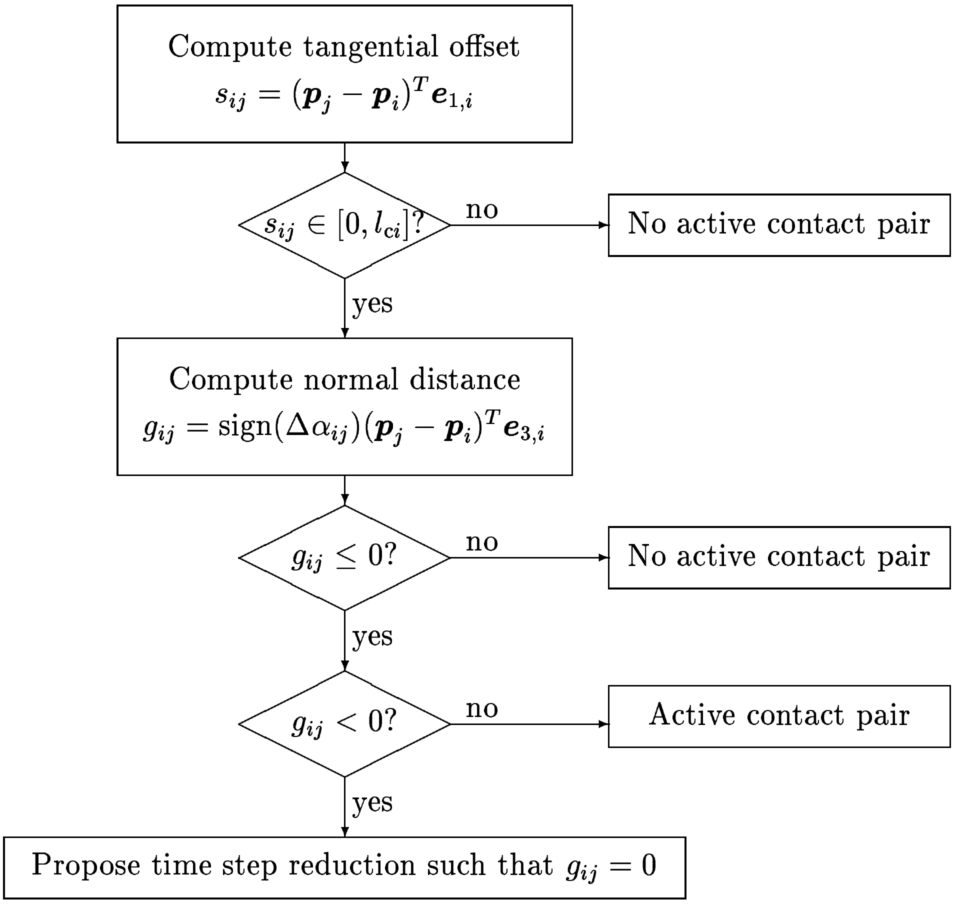
Compute tangential offset
$s_{ij} = (\boldsymbol{p}_j - \boldsymbol{p}_i)^T \boldsymbol{e}_{1,i}$
$s_{ij} \in [0, l_{ci}]?$
no
No active contact pair
yes
Compute normal distance
$g_{ij} = \mathrm{sign}(\Delta\alpha_{ij})(\boldsymbol{p}_j - \boldsymbol{p}_i)^T \boldsymbol{e}_{3,i}$
$g_{ij} \leq 0?$
no
No active contact pair
yes
$g_{ij} < 0?$
no
Active contact pair
yes
Propose time step reduction such that $g_{ij} = 0$

Figure 6.5: Algorithmic structure of the kinematic contact search algorithm for locating both outside and inside contact

which linearly depend on the chosen velocity degrees of freedom, pass into the following optimization problem.

Remarks

- Despite the conceptual simplicity of the proposed contact procedure the formulation is quite general and suitable for the consideration of (frictionless) internal contact for axisymmetric shell structures of arbitrary geometry. Due to the fact that the contact constraints are linear functions of the velocity degrees of freedom, they also do not complicate the numerical optimization procedure. This is in strong contrast to the solution behaviour of conventional finite element analyses when including contact. Because contact conditions may change within each iteration step there, the global finite element equations to be solved show a strong nonlinear behaviour, strongly affecting the overall convergence behaviour.

- Consideration of the shell thickness (although not implemented yet) is straightforward.
- In a similar manner as described above, the circular arc elements used for discretizing the meridional curve of the axisymmetric shell structure may be used directly for defining contact conditions of the form of Eq. (6.26) without resorting to linear master line segments. Although the kinematic description becomes more complicated in this case, the linear dependence of the resulting inequalities on the velocity degrees of freedom (and thus the convergence behaviour of the optimization routines) is still maintained.
- The contact algorithm sketched above was presented without going into details of implementation. Although the principles of the algorithmic structure are quite simple, however, some additional tuning work has to be done in order to define a numerically robust algorithm. For example, appropriate tolerances must be set to avoid spurious contact changes. The main reasons for such not physically motivated "contact changes" are:
  - Even if an active contact pair would keep closed actually, the numerical solution may deliver $\dot{g}_{ij}$-values that are not exactly zero but small positive numbers. This, however, means that in fact a slight separation of the contact partners will take place within each incremental update.
  - Due to the discretization of the meridional curve by linear master line segments tangential movements of the slave nodes across the boundary nodes of the contact elements may lead to some intermediate "drop off" of the contact nodes from the contact surface.
  - The contact search algorithm may fail to uniquely determine contact pairs, if the slave nodes lie near the points of interpenetration of the contact segments.

The current version of the contact algorithm allows for some control of these problems. However, the main emphasis for the definition of the proposed sequential limit analysis program was put on testing the principles and the suitability of the methodology, and, therefore, its applicability is restricted to small scale problems (which typically consider the formation of individual folds only). Therefore, a rather simplified version of the contact algorithm is currently implemented, which still requires some refinements in order to deliver a numerically robust tool for general axisymmetric crushing problems. The suitability and numerical efficiency of the proposed contact algorithm, when used in combination with the sequential limit analysis method, however, already becomes obvious from simple test runs on small scale problems.

6.2.4 Outline of the Solution Procedure

In the following the flow diagram of the computer code, which was defined for the (large deformation) crushing analysis of axisymmetric shells, is sketched:

1. Read input (initial geometry, FE discretization, control parameters, etc.),
2. set starting values for the independent parameters $\dot{\boldsymbol{l}}$, $\dot{\boldsymbol{\kappa}}$ and $\dot{\boldsymbol{\beta}}$ for the first increment,
3. for each increment do:
    (a) solve the nonlinear optimization problem with linear constraints

$$\begin{aligned} & d_{\mathrm{int}}(\dot{\boldsymbol{l}}, \dot{\boldsymbol{\kappa}}, \dot{\boldsymbol{\beta}}) \rightarrow \min \;, \\ & \text{subject to:} \quad \dot{r}_1 = 0 \;, \\ & \qquad\qquad\qquad \dot{z}_1 = 0 \;, \\ & \qquad\qquad\qquad \dot{\varphi}_0 = 0 \;, \\ & \qquad\qquad\qquad \dot{r}_{n+1} = 0 \;, \\ & \qquad\qquad\qquad \dot{z}_{n+1} + 1 = 0 \;, \\ & \qquad\qquad\qquad \dot{\varphi}_{n+1} = 0 \;, \\ & \qquad\qquad\qquad \dot{g}_{ij} \geq 0 \qquad \text{for all active contact pairs } [i,j] \;, \end{aligned}$$

    (b) perform geometrical update

$$\begin{aligned} \boldsymbol{l}_{new} &= \boldsymbol{l}_{old} + \Delta t \, \dot{\boldsymbol{l}} \;\; (+\frac{\Delta t^2}{2}\ddot{\boldsymbol{l}} + \dots) \;, \\ \boldsymbol{\kappa}_{new} &= \boldsymbol{\kappa}_{old} + \Delta t \, \dot{\boldsymbol{\kappa}} \;\; (+\frac{\Delta t^2}{2}\ddot{\boldsymbol{\kappa}} + \dots) \;, \\ \boldsymbol{\beta}_{new} &= \boldsymbol{\beta}_{old} + \Delta t \, \dot{\boldsymbol{\beta}} \;\; (+\frac{\Delta t^2}{2}\ddot{\boldsymbol{\beta}} + \dots) \;, \end{aligned}$$

    (c) check contact/interpenetration of elements,
        i. if contact without interpenetration appears, activate contact conditions for the next increment,

      ii. if interpenetration appears, reduce time increment Δt accordingly and go to step 3b,

   (d) write incremental output,

   (e) if a break-off condition is satisfied, go to step 4,

   (f) go to step 3a.

4. end of solution.

Discussion

Statement of the Optimization Problem (Step 3a): The definition of the optimization problem is based on the assumption that external loading is restricted to axial compression at node $n+1$ only. With

$$D_{\mathrm{ext},0} = F_{\mathrm{a},0}\dot{z}_{n+1} = 1 \tag{6.31}$$

and an axial reference force $F_{\mathrm{a},0} = -1$ this, however, just delivers the kinematic constraint equation

$$\dot{z}_{n+1} + 1 = 0 \tag{6.32}$$

used above. The axial compressive force $F_{\mathrm{a}}(t)$ may finally be obtained from the converged values for the objective function, $d_{\mathrm{int}}(t)$. Using Eq. (6.31) one obtains

$$\overline{\lambda}(t) = \frac{D_{\mathrm{int}}(t)}{D_{\mathrm{ext},0}} = D_{\mathrm{int}}(t) = N_0\dot{\varepsilon}_0 d_{\mathrm{int}}(t) \ , \tag{6.33}$$

and thus

$$F_{\mathrm{a}}(t) = \overline{\lambda}(t)F_{\mathrm{a},0} = -N_0\dot{\varepsilon}_0 d_{\mathrm{int}}(t) \ . \tag{6.34}$$

Concerning the kinematic boundary conditions, the shell structure is (without restriction to generality) assumed to be clamped at both ends.[11] Other types of boundary conditions, however, may simply be obtained by changing the constraint equations accordingly.

---

[11] Although the boundary conditions fixing node 1 are formally listed as constraint equations, it is to be noted that, because the kinematic description of the meridional curve just starts at node 1, these quantities may directly be substituted into the corresponding equations (see Eqs. (6.9)), this way reducing both the number of active degrees of freedom and the constraint equations entering the optimization problem.

Numerical Solution (Step 3a): It was mentioned earlier that in general the objective function for the optimization problem, d_{int}, is convex but not everywhere differentiable [Capsoni and Corradi, 1997b]. Non-differentiability at the optimal point is typically present if individual elements (and plastic hinge lines, respectively) behave in a rigid manner (for axisymmetric problems this means that only rigid movements in axial direction may occur for such an element). In order to allow a direct solution of the nonlinear, nonsmooth, constrained optimization problem, the freeware SOLVOPT [Kuntsevich and Kappel, 1997] is currently used. This optimization code is based on a minimization method with space dilation, working with subgradients (Shor's r-algorithm [Shor, 1985]). Constraints are taken into account by an exact penalization method (for details see [Kuntsevich and Kappel, 1997]).

For the constrained optimization of smooth problems (but also for a regularized evaluation of non-smooth objective functions), however, further optimization routines were implemented:

- FFSQP [Zhou et al., 1997] is a set of subroutines for the minimization of the maximum of a set of smooth objective functions subject to general smooth constraints.[12] The optimization code is based on the method of "Sequential Quadratic Programming", modified so as to generate iterates feasible with all constraints, yielding a globally convergent, locally superlinearly convergent algorithm.

- A robust but computationally less efficient (compared to FFSQP) smooth optimization code is the optimization algorithm CONMAX, provided via the internet service NETLIB. This set of optimization routines is also intended for solving general (nonlinearly constrained) minimax problems, with the solution strategy resting upon an ODE-based[13] approach (for details see [Kaufman et al., 1995]).

Although these optimization codes are restricted to smooth problems an approximative treatment of non-smooth problems can e.g. be achieved by enforcing that the internal energy dissipation within each element (and plastic hinge line) is strictly positive, thus actually solving a smooth problem instead (see e.g. [Achtziger, 1998]). Because the convergence behaviour of smooth optimization methods is in general superior to that of non-smooth ones, such a strategy may be more computationally efficient than directly solving non-smooth problems.

---

[12] The provision of the optimization routines by the authors is gratefully acknowledged.

[13] ODE ... Ordinary Differential Equations

For the (small scale) test examples presented below, all algorithms were found to work satisfactorily. Concerning a numerically efficient solution of the proposed sequential limit analysis method for larger problems, however, further work remains to be done.

With respect to the starting values for each optimization problem, the vectors of independent parameters of the last increment are taken for each but the first step (which is implicitly included in the above flowchart).

Geometrical Update (Step 3b): A geometrical update, which is restricted to the velocity terms, will deliver accurate results for larger time steps only if the higher derivatives of $\boldsymbol{l}$, $\boldsymbol{\kappa}$ and $\boldsymbol{\beta}$ are sufficiently small. This may generally be assumed for increments, where no changes in the contact conditions take place. However, improvements may be achieved by taking into account the acceleration terms, too. These terms may e.g. be approximated at time t by backward difference quotients of the form

$$\ddot{\boldsymbol{l}}(t) \approx \frac{\dot{\boldsymbol{l}}(t) - \dot{\boldsymbol{l}}(t - \Delta t)}{\Delta t}\,, \quad \text{etc.,} \tag{6.35}$$

and can then additionally be applied for the geometrical update, as indicated in step 3b.

6.2.5 Examples

The test examples presented in the following are mainly intended to point out several features of the proposed sequential limit analysis (SLA) method. First, the formation of an individual fold during concertina mode buckling of an axially compressed circular cylinder is investigated in some detail (including the activation of internal contact, but also demonstrating the possibility of obtaining the internal generalized stress state as a pure postprocessing feature). The generality and achievable accuracy of the method also comes out from the next example, where the large deformation axial compression of a conical shell is presented and compared with a detailed FE analysis. A confirmation that most of the analytically based collapse mechanisms presented in chapter 5 may be regarded as special cases of the proposed SLA program is shown by the last two examples, where both the simple collapse model of Alexander and the two active folds model of Wierzbicki et al. are reexamined.

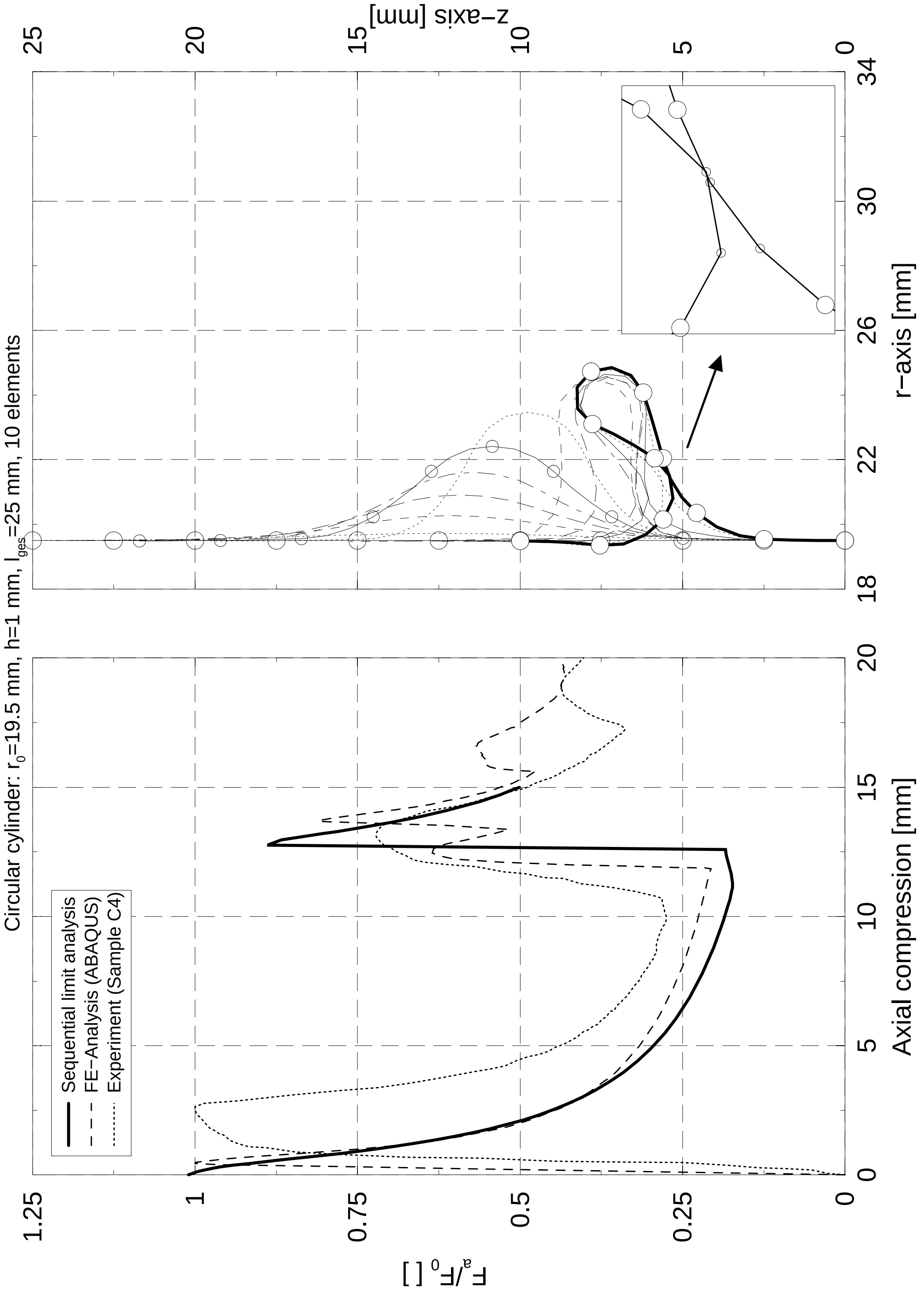

Figure 6.6: Axially compressed circular cylinder: normalized axial force versus compression curve (left), deformation diagram (right)

Axial Crushing of a Circular Cylinder

A numerical crushing simulation for a circular cylinder (cylinder radius $r_0 = 19.5$ mm, wall thickness $h = 1$ mm) was performed, where only continuous deformations were allowed, i.e. no plastic hinge lines could occur at the nodes. The deformable length of the cylinder was assumed to be 25 mm, which was discretized with 10 arc elements, and the cylinder was clamped at both ends. Figure 6.6 shows some results. The normalized axial force versus compression characteristics during the buckling process can be seen in the left diagram, and the right diagram shows a sequence of states of deformation, obtained with the SLA method. The axial force acting on the cylinder, F_a, is normalized with respect to the axial squashing load of the tubular member, $F_0 = 2\pi r_0 N_0$. A comparison of this normalized force versus compression curve with a typical experimental result and results of a conventional FE analysis (which are included in the left diagram) shows a very good agreement with respect to the actual force level as well as the consideration of internal contact, delivering even the fold length accurately. A detail of the active contact region for the last increment, showing the principles of the implemented master-slave contact algorithm, is included in the right diagram, too (the discretization of the arc elements used there corresponds to that applied for considering contact).

The results of this simple example already show that the proposed sequential limit analysis method in principle allows the numerical simulation of axisymmetric crushing processes in a general way, being able to meet the accuracy of conventional FE calculations, even if internal contact has to be taken into account.

One of the features of the upper bound limit analysis method is that the whole solution procedure is kinematically driven, and stresses do not explicitely enter the algorithmic problem. The reason for this is that due to the validity of the principle of maximum plastic dissipation the internal energy dissipation (being the objective function for the optimization problem) is given as a pure function of the plastic strain rates, which in turn are determined by the underlying velocity field. Because the plastic strain rates, however, also determine the corresponding stress state on the yield surface,[14] the internal stresses may, therefore, be evaluated from the converged kinematic quantities within a simple postprocessing step. The relation conveniently used for these purposes for Kirchhoff shells has already been derived in section 3.4. The six-dimensional representation of the exact

---

[14] For plane stress von Mises plasticity this dependence, which is determined by the yield surface in combination with the normality rule, is unique, see section 3.3.

Ilyushin yield criterion, Eq. (3.75), is of a form that, once the (plastic) midplane strain and curvature rate vectors $\dot{\boldsymbol{e}}$ and $\dot{\boldsymbol{k}}$ are given for some shell section, the normalized section force and moment vectors $\boldsymbol{n}$ and $\boldsymbol{m}$ may directly be evaluated.[15] Although the stress state obtained this way will in general not fulfill local equilibrium (in contrast to the lower bound theorem of plasticity this is not enforced for upper bound solutions), approximations quite close to the actual state are usually delivered, provided the kinematic description is chosen suitably. Besides providing information on the stress distribution within the structure, the results may, therefore, also be used for validating the accuracy of the underlying velocity field.

Results of such a postprocessing are shown in Figure 6.7 for an axially compressed circular cylinder, where the total length, 16 mm, was discretized with 4 arc elements. A sequence of several states of deformation is included in the left diagram, and the progression of the corresponding section force and moment components evaluated along the meridional curve of the shell structure can be seen in the right diagram.

Concerning the evaluated force and moment distributions for the investigated example it can be seen that at the beginning (i.e. for a straight shell structure) the meridional section forces n_{11} dominate the energy dissipation, whereas with progressing deformations the meridional moments m_{11} take control over the buckling process. The jumps in the section force components, which occur at the element boundaries, are mainly due to the assumption of constant meridional strain rates within each element, pointing out that future refinements with respect to the assumed meridional strain rate distributions should be made. A further result becoming obvious from the diagrams is that a distinct reduction of the total length of the meridional curve occurs. This may partly be traced back to the axial (and meridional) compression, which, in combination with the extensional circumferential deformations due to the outward folding process, will lead to such a reduction of the meridional length of the shell. Some overestimation of these meridional deformations, however, must also be expected. The reason for this is that in the current version of the SLA program the volume constancy of the rigid-plastic deformations (leading to changes of the shell thickness) is not enforced numerically. Therefore, some volume reduction may take place with the ongoing crushing process.

---

[15] Of course, the validity of this relation is restricted to nonzero plastic deformations, with the (generalized) stress point lying on the yield surface. Stress states within the yield surface (subjected to rigid movements of the corresponding material point) may not be determined with this strategy.

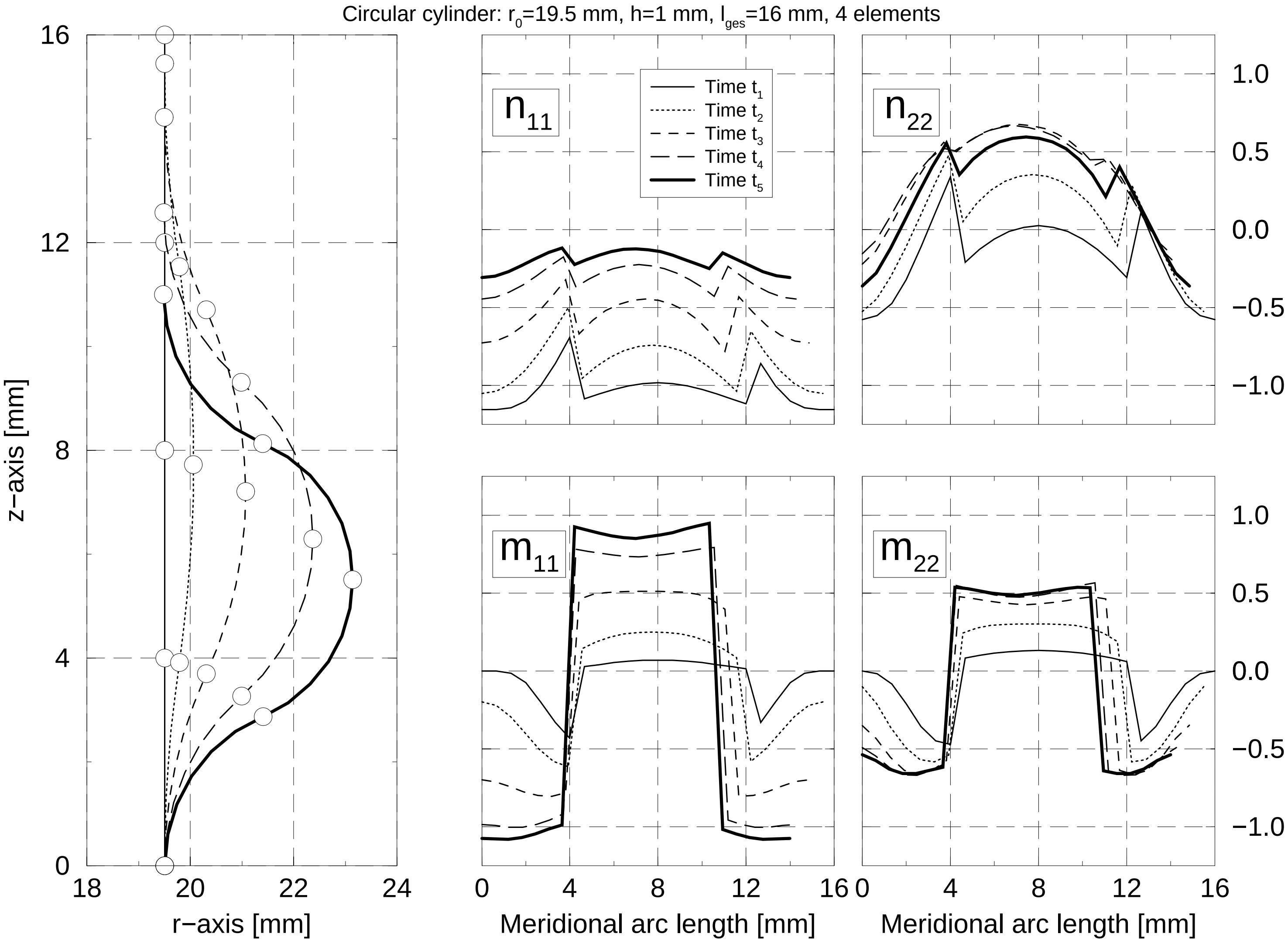

Figure 6.7: Axially compressed circular cylinder: deformation diagram (left), section forces and moments (right)

Plastic Collapse of an Axially Compressed Conical Shell

In order to demonstrate that the proposed sequential limit analysis method is not restricted to circular cylinders, but may be applied for studying the large deformation crushing behaviour of general axisymmetric shells, results for an axially compressed conical shell are shown in Figure 6.8. Again, the ends of the shell structure are clamped, and only continuous deformations are allowed. The reference quantity used for normalizing the axial force is in this example given by $F_0 = 2\pi r_0 N_0$, where r_0 stands for the radius of the smaller end of the cone. The comparison of the SLA simulation with results, which were obtained by a detailed FE analysis (and are included in Figure 6.8), confirms that not only the force-compression behaviour, but also the final deformed configuration are predicted with a high degree of accuracy by the SLA method.

Comparison with Analytically Based Collapse Models

In Figures 6.9 and 6.10 results for two cases are presented, where the SLA program was specialized in order to allow a direct comparison of the proposed numerical scheme with that of analytically based collapse models — the model of Alexander and the two active folds model of Wierzbicki et al. Both collapse models were described in chapter 5 (sections 5.2.1 and 5.2.3).

Model of Alexander: According to the collapse model of Alexander (the kinematics of which is sketched in Figure 5.1) the internal energy dissipation can be decomposed into two parts, owing to bending at concentrated plastic hinge lines and circumferential stretching within the line elements (see section 5.2.1). In order to put these assumptions into the SLA code, the following adaptions have to be made:

- Meridional and curvature rate deformations must be deactivated, i.e. $\dot{\boldsymbol{l}} = \mathbf{0}$, $\dot{\boldsymbol{\kappa}} = \mathbf{0}$.
- Within each element only the hoop strain rates must be taken into account for evaluating the internal energy dissipation. Accordingly, the normalized internal energy dissipation for the shell section under consideration, $\bar{d}_\mathrm{p}$, is given by

$$\bar{d}_\mathrm{p} = \frac{1}{N_0 \dot{\varepsilon}_0} \left| N_0 \dot{\bar{\varepsilon}}_{22} \right| = \frac{1}{\dot{\varepsilon}_0} \left| \frac{\dot{r}}{r} \right| = \left| \dot{\bar{e}}_{22} \right| \ , \tag{6.36}$$

  where $\dot{\bar{\varepsilon}}_{22}$ denotes the physical and $\dot{\bar{e}}_{22}$ the normalized hoop strain rate for the section point.

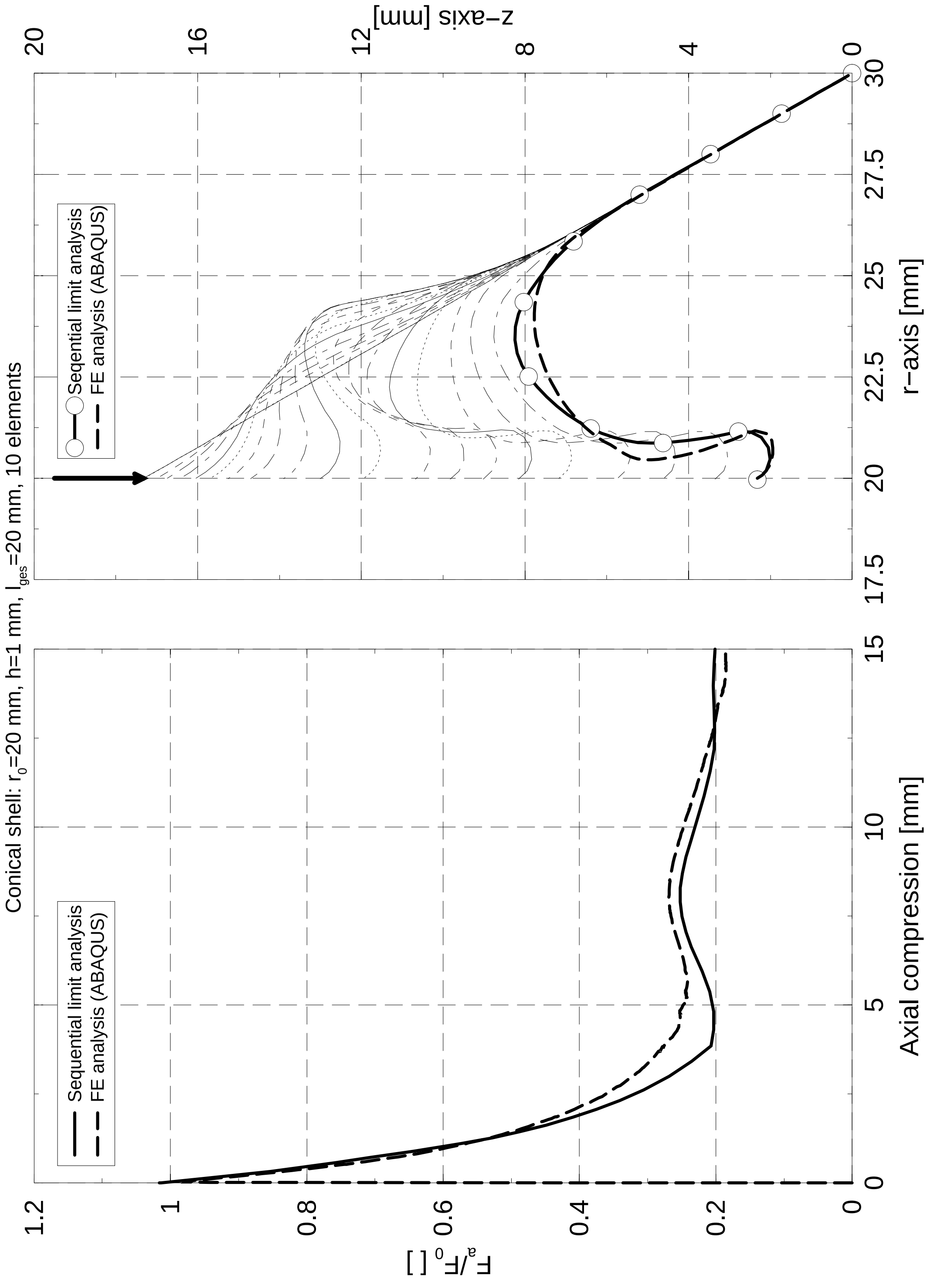

Figure 6.8: Axially compressed conical shell: normalized axial force versus compression curve (left), deformation diagram (right)

- In order to avoid numerical problems for the initially straight meridional curve (where the crushing force would approach infinity), a starting angle of 3° is used for defining the initial geometry.

Concerning the energy dissipation owing to bending at the plastic hinge lines the current implementation coincides with the assumptions used for the collapse model of Alexander (where a constant bending moment of $M_h = 2M_0/\sqrt{3}$ is assumed). Accordingly, no changes have to be made for this. The break-off condition is set such that the analysis stops when first contact is encountered.

The results, which are summarized in graphical form in Figure 6.9, reveal that the numerical simulation delivers exactly the same results as the analytical model (where the force-compression curve is given in closed form by Eq. (5.25)). The optimal folding length, being predicted by the Alexander model as $2H = 11.9$ mm for the given geometry, also comes out from the numerical solution. This may be seen from the right diagram of Figure 6.9, where the numerical prediction for the mean force is shown as a function of the folding length, and again, the minimum is found at 11.9 mm.[16]

In addition to this reexamination of the original Alexander model with the SLA method, a refined investigation was performed. For this instead of applying the simplified relation, Eq. (6.36), for evaluating the internal energy dissipation within the elements, the exact form (considering not only hoop strain rates, but circumferential curvature rates and meridional strain rates as well) is used. It can be seen from the force-compression curve that in this case the axial load no longer starts from infinity,[17] but has a value of $F_a \approx 1.1F_0$, and the minimum of the optimal folding length of the tube is shifted to slightly higher values ($2H \approx 13.6$ mm). A similar progression of the instantaneous crushing force during axial compression (obviously dominated by the localized bending deformations at the hinge lines), however, may also be observed.

Two Active Folds Model of Wierzbicki et al.: For reexamining the two active folds model of Wierzbicki et al. (the deformation sequence of which is sketched in Figure 5.8) some major adaptions must be made to the kinematic description of the SLA program.

---

[16] With regard to the the mean crushing forces shown in the diagram, however, it should be taken into account that because of the predeformations used here the absolute values do not coincide with the analytical predictions (where no such predeformations are assumed).

[17] However, some predeformation at the beginning must also be used, because otherwise the plastic hinge lines (at which currently no moment reduction due to the presence of axial forces is taken into account) would not be activated but the whole structure would only be compressed axially.

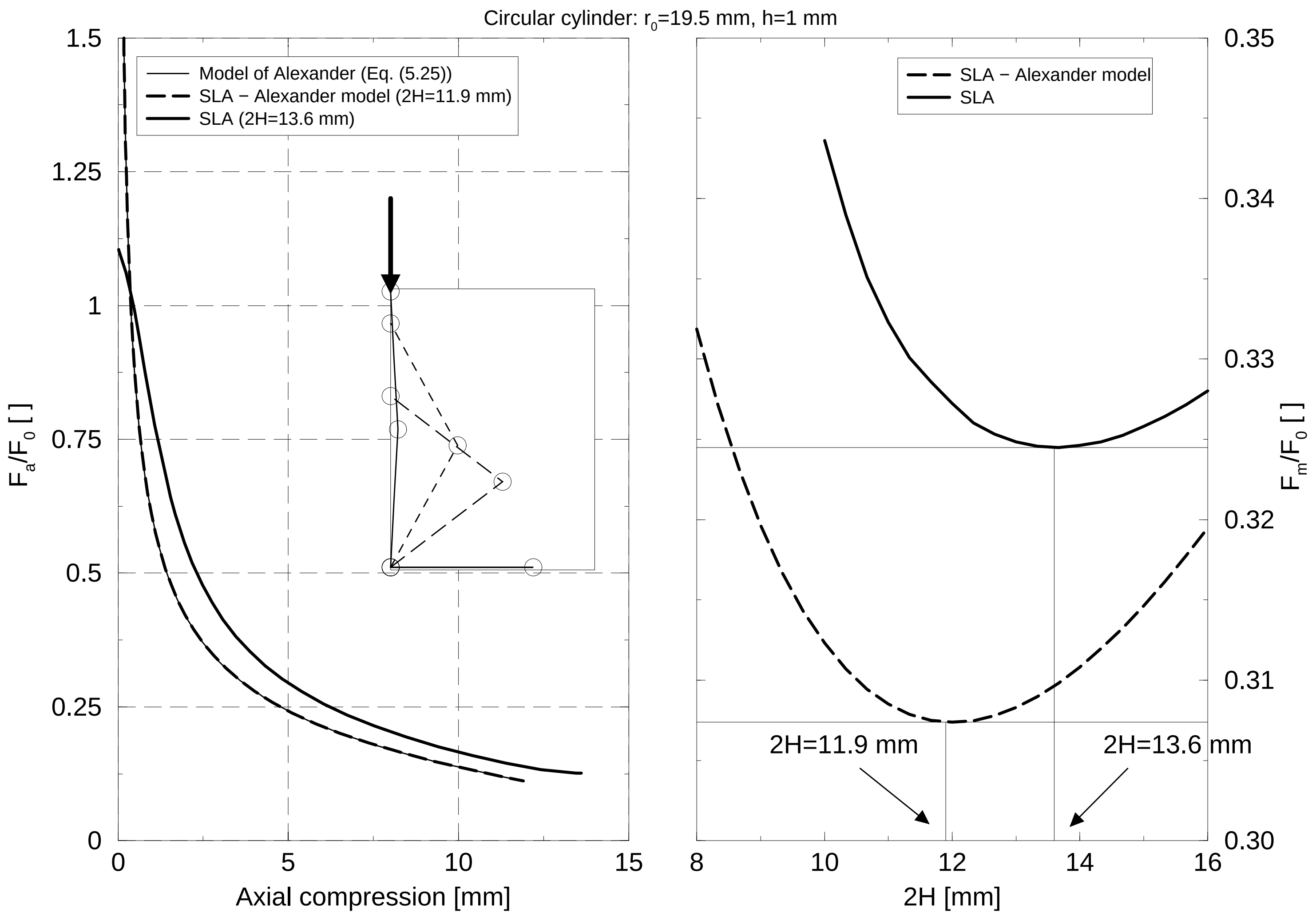

Figure 6.9: Kinematics of the Alexander model: normalized axial force versus compression curve (left), normalized mean force versus folding wave length (right)

Starting from a predeformed geometry (described by the first, i.e. lower four arc elements, see Figure 6.10) the whole structure has to be divided into upper and lower parts moving as rigid bodies, which are connected by some active zone. The deformations in this active zone, which is composed of four elements, are restricted such that pairs of elements share their degrees of freedom (however, with different signs for the meridional curvature rates). With these adaptions the implemented contact algorithm may be applied to determine the end of the first crushing subcycle, at which time the active zone is shifted by two elements and the second subcycle is performed until contact occurs a second time, indicating the end of one total crushing cycle.

Concerning the computation of the internal energy dissipation it is assumed for this collapse model that only the meridional bending moments and the section forces in hoop direction provide contributions — without, however, assuming any interaction between these generalized stress components. Accordingly, the normalized internal energy dissipation is given as

$$\overline{d}_{\mathrm{p}} = \frac{1}{N_0 \dot{\varepsilon}_0} \left(|N_0 \dot{\overline{\varepsilon}}_{22}| + |M_0 \dot{\kappa}_{11}| \right) = |\dot{\overline{e}}_{22}| + |\dot{\overline{k}}_{11}| \, . \tag{6.37}$$

(Here the relation $N_0 \dot{\varepsilon}_0 = M_0 \dot{\kappa}_0$, introduced in section 3.4, has been utilized.) In contrast to the definition of the hoop strain rates used for the general SLA model ($\dot{\overline{\varepsilon}}_{22} = \dot{r}/r$), however, these are now assumed to be based on small deformation theory and hence, they are replaced for this collapse model by $\dot{\overline{\varepsilon}}_{22} = \dot{r}/r_0$ (see section 5.2.3 for details).

The left diagram shown in Figure 6.10 includes several normalized axial force versus compression curves, the computation of which is based on different assumptions. The first curve, denoted as “Model of Wierzbicki et al.”, was obtained with the formulas originally proposed by Wierzbicki et al. [1992], whereas the second one (“SLA – Model of Wierzbicki et al.”) was evaluated with the SLA method considering the adaptions mentioned above. It becomes obvious from these results that both curves in fact coincide, confirming that the two active folds model may be treated as a special case by the proposed SLA program.

The third force-compression curve included in the diagram (“SLA”) is also based on the kinematics of the two active folds model (i.e. a coupling of the velocity degrees of freedom for pairs of elements of the active zone (e.g. $\dot{\kappa}_3 = -\dot{\kappa}_4$, $\dot{l}_3 = \dot{l}_4$, etc.)). The internal energy dissipation, however, is now obtained in an exact way, considering not only all strain and curvature rate components, but also accounting for interaction effects between these quantities. With this it is found that the load peaks, markedly overestimated by the analytically based model, are essentially reduced to reasonable values, being comparable with the measurements. The subsequent crushing force progression according to this refined

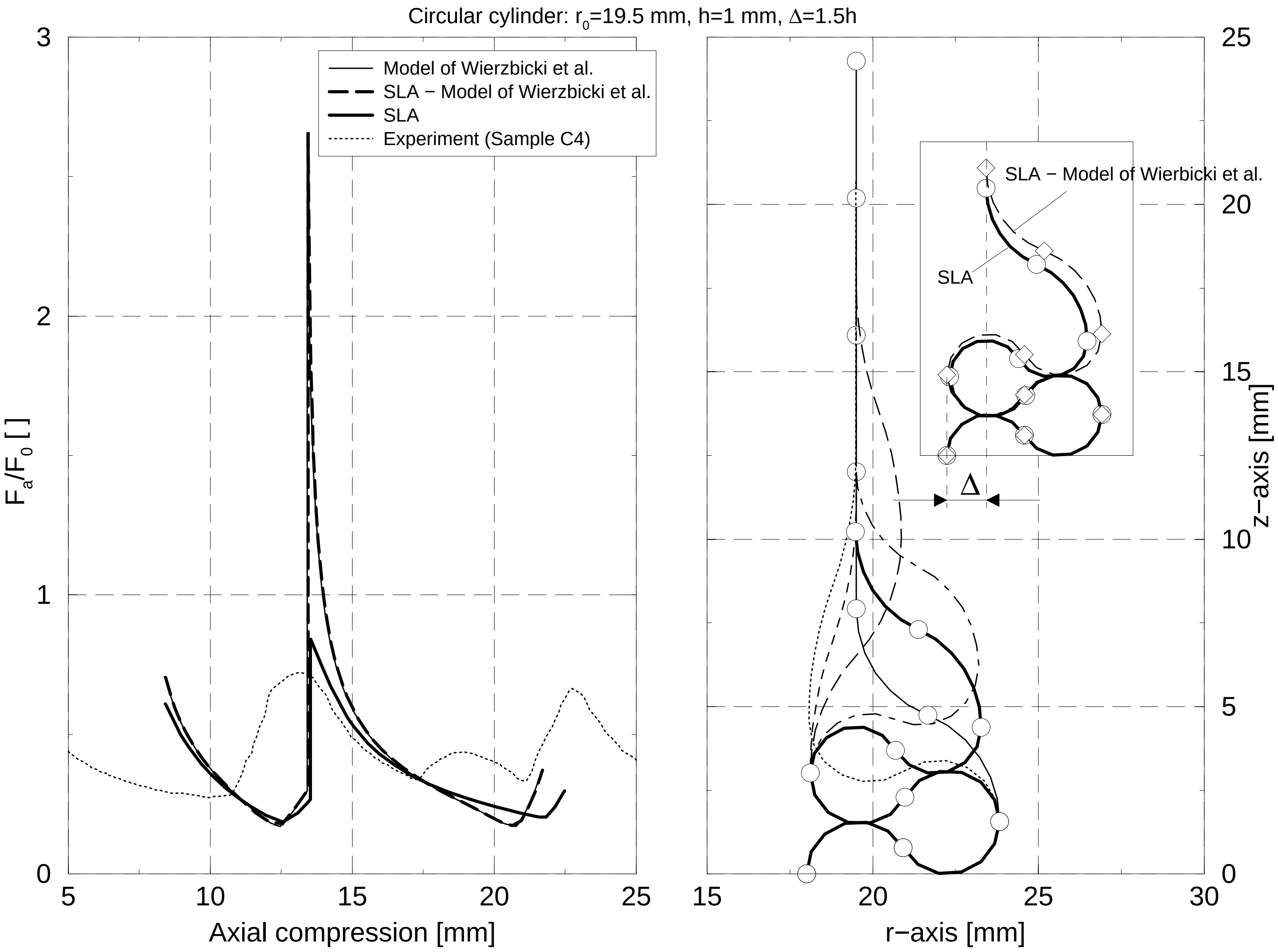

Figure 6.10: Kinematics of the two active folds model of Wierzbicki et al.: normalized axial force versus compression curve (left), deformation diagram (right)

evaluation, however, is comparable to that of the analytically based collapse model.[18] This may certainly be traced back to the fact that with ongoing deformations the energy dissipation becomes dominated by meridional bending — a fact which did already come out from the inspection of the section force and moment distributions shown in Figure 6.7. These bending contributions, however, are an essential part of the energy dissipation taken into account by the analytically based collapse model.

Several stages of one total crushing cycle corresponding to the refined two active folds crushing analysis are shown in the right diagram of Figure 6.10. A comparison of the final deformation states for the original and the refined collapse model (which is also included in the right diagram) again reveals that a considerable meridional shortening is obtained when taking into account meridional strain rates within the elements. This phenomenon, however, has already been discussed above.

6.3 Summary, Conclusions

A major goal of the present study was to work out a possible strategy for an efficient (i.e. simplified but still sufficiently accurate) numerical analysis of the plastic collapse process of thin-walled structures. With regard to this a simulation tool for the axial crushing analysis of axisymmetric shells has been presented in this chapter, which is based on the upper bound theorem of limit analysis in combination with an incremental solution procedure. Several features inherent to this kind of simulation strategy could be demonstrated (or may be concluded). These include:

- Plastic extremum and bounding principles provide a sound theoretical basis for the definition of simplified, though general numerical simulation tools, even if large deformation problems are to be solved. For one parameter loadings these may be based on the upper bound theorem. More general loading conditions, however, are conveniently solved with the more general kinematic extremum principle presented in section 3.3 (Eq. (3.46)), also forming the theoretical basis for rigid-plastic finite element codes proposed in the literature.

- The consideration of (frictionless) contact complicates neither the solution formalism nor the convergence rate of the algorithmic problem in a major way.

---

[18] In both cases the same (initial) folding length, provided by the analytically based collapse model, was assumed (see Eq. (5.38)).

- Plastic hinge lines (or, more generally, discontinuous deformations) may be accounted for without fundamental difficulties. This was shown for stationary hinge lines. Concerning the consideration of moving hinge lines additional degrees of freedom (i.e. the velocities of the moving hinge lines with respect to the material) and additional constraint equations must be activated. The latter have to enforce the compatibility conditions at the lines of discontinuity (see e.g. [Wierzbicki and Abramowicz, 1983]). A kinematic description, where not only continuous but also discontinuous deformations may be accounted for, however, also ensures that relatively coarse meshes may be applied (if compared to a conventional FE analysis) without markedly reducing the accuracy of the results.

- The application of a general numerical solution algorithm opens the way for describing the constitutive behaviour in a quite general way. For thin-walled shell structures the application of the exact Ilyushin yield surface has been shown to be highly suitable, providing an important ingredient for the definition of both an accurate and a numerically efficient simulation tool.[19]

- Due to the incremental solution strategy hardening, material strain-rate sensitivities and even inertia forces could be accounted for in an iterative way without fundamental difficulties.

Although the chosen methodology is quite general, the proposed computational model in its current version is specialized for carrying out detailed studies on axisymmetric buckling processes of axisymmetric shells. With regard to this simulation tool, further improvements may be obtained e.g. by considering changes in the shell thickness due to plastic deformations, allowing the meridional strain rates to change within an element, or to enable moving instead of stationary plastic hinge lines at the nodes. If larger problems are to be solved, then the kinematic description used for conventional axisymmetric finite elements, which is based on nodal degrees of freedom and a local instead of a global kinematic description as used here, may be advantageous. As already mentioned above, multiparameter loadings may conveniently be considered by resorting to the kinematic extremum principle, Eq. (3.46). In conjunction with the proposed kinematic model this delivers the generalized objective function (the "Lagrangian function")

$$L(\dot{r}_1, \dot{z}_1, \dot{\varphi}_0, \dot{\boldsymbol{l}}, \dot{\boldsymbol{\kappa}}, \dot{\boldsymbol{\beta}}, \boldsymbol{F}_v) = D_{\text{int}} - \boldsymbol{F}_\sigma^T \boldsymbol{v}_\sigma - \boldsymbol{F}_v^T \left(\boldsymbol{v} - \overline{\boldsymbol{v}}\right) \longrightarrow \min \ , \tag{6.38}$$

---

[19] This, however, presumes that the Kirchhoff hypothesis and the von Mises yield condition, used for deriving the exact Ilyushin yield criterion, are suitable approximations for the shell structure under consideration.

where the generalized reaction force vector $\boldsymbol{F}_v$ contains the "Lagrange parameters" for the optimization problem, forming part of the solution. The vectorial quantities $\boldsymbol{v}$ and $\overline{\boldsymbol{v}}$ are the corresponding generalized velocity unknowns and prescribed boundary conditions (which e.g. may contain values for $\dot{r}$, $\dot{z}$ and $\dot{\varphi}$ at the boundary nodes 1 and n), respectively. $\boldsymbol{F}_\sigma$ and $\boldsymbol{v}_\sigma$, also used in Eq. (6.38), denote prescribed external loads and their unknown kinematic counterparts, respectively.

Based on such a solution strategy, however, even a connection with the conventional FE method seems possible, where typically the system response (elemental force and stiffness) is to be determined as a function of (increments of) the nodal degrees of freedom. Within such a framework the proposed collapse model could e.g. be applied as a special user defined element, with the global degrees of freedom being given by the displacement and rotation increments at nodes 1 and n. A detailed investigation of the suitability of such an application, however, remains to be done.

Chapter 7

On the Definition of a Stress Resultant Constitutive Law Based on the Exact Ilyushin Yield Surface

In chapter 6 it was shown that plastic collapse simulation of shell-like structures, based on kinematics-oriented extremum or bounding principles, may be performed advantageously when applying the exact Ilyushin yield criterion. Because with this methodology the plastic strain rates are given in advance for each iteration step, the internal energy dissipation may be evaluated in a straightforward manner, without causing numerical difficulties due to the application of this yield criterion. Within an elastoplastic FE material routine, however, the plastic strain increments and the final position on the yield surface during plastic loading are not given in advance, but have to be evaluated within the material routine. This in general requires the solution of (a set of) nonlinear equations for each integration point and it seems worth studying if the exact Ilyushin surface can also be utilized for this purpose, and possibly even offer advantages as compared to other, more approximative full section yield criteria for shells. Besides the fact that such a "material model" is interesting from the theoretical point of view, an efficient implementation could also speed up the calculation time of FE based collapse and limit load analyses and, therefore, be of practical interest. In this chapter a possible algorithmic structure for such a stress resultant constitutive law is proposed and the main difficulties concerned with the implementation are discussed in some detail. Even though first test results are encouraging some problems remain to be solved to make the material model fit for practical use and, therefore, the results presented in this chapter must be regarded as tentative only.

7.1 Introduction

Finite element shell formulations, which are used for elastoplastic analyses, in general rely on a layerwise treatment of plasticity in combination with a numerical thickness integration. This, however, means that the elastoplastic material behaviour has to be evaluated at a number of integration points over the thickness. Accordingly, such a solution strategy, though allowing modeling generality and being able to deliver a high accuracy of results (which, of course, depends on the chosen number of integration points), is computationally expensive. Therefore, element formulations, in which plasticity is treated directly in terms of stress and strain resultant quantities, have been proposed in the past (see section 2.2 of the literature overview).

The application of elastoplastic stress resultant constitutive laws, however, in general restricts both modeling generality and accuracy. As was mentioned in the literature overview, most stress resultant yield criteria are approximate because the spreading of the plastic zone over the thickness of the shell section is neglected (plastic limit yield functions) or is considered only in a simplified way and the derivation of such yield criteria is often based on a specific material behaviour (e.g. isotropic, perfectly plastic). Nevertheless, for a certain class of problems the application of stress resultant constitutive laws is appropriate, namely plastic limit load and collapse analyses of thin-walled structures. Because for such problems the governing plastic behaviour can, in general, be considered with reasonable accuracy, the application of approximate full section constitutive laws is at least suited for quick preliminary analyses with a numerical thickness integration being reserved for final detailed studies. For highly imperfection sensitive shell structures, however, a numerical thickness integration should be used in any case, because in this case loss of stability is often associated with the early loss of stiffness induced by “fibre-yield” [Crisfield, 1997].

In the following, an algorithmic structure for the definition of an elastoplastic constitutive model is discussed, which is based on the exact Ilyushin yield criterion presented in section 3.4. Compared to the application of other full section yield criteria for shells, which have been proposed in the literature and often rely on approximations of this yield surface, its use is expected to deliver more accurate results[1] while retaining their stated numerical efficiency. This, however, first requires that numerical solutions may be obtained at all. The presentation, therefore, mainly intends to point out the basic ingredients for the formulation of an efficient and stable computational algorithm, that is capable of handling a yield surface, which may only be stated in parametric form. This comprises the definition of the system of equations for the plastic correction step (including an appropriate choice of the "free" variables), the numerical treatment of points at the boundary, the definition of the tangential stiffness matrix, etc.

---

[1] Burgoyne and Brennan [1993a] have shown that, although the yield surface itself may be approximated with reasonable accuracy by the Ivanov yield surface, Eq. (3.81), the corresponding surface normals may differ significantly.

The proposed constitutive model is implemented into the commercial finite element code ABAQUS/Standard via the user subroutine UGENS, a "material routine" intended for defining the constitutive behaviour of shells in terms of generalized stress and strain quantities.[2] The formulation of the material routine is based on the use of conjugate stress and strain measures (measured in a local, orthonormal coordinate system) and an additive strain rate decomposition, as generally used for geometrically linear theory. For a discussion of the requirements for the validity of such a formulation for geometrically nonlinear theory see chapter 3.

According to the presentation of the exact Ilyushin yield surface in section 3.4 the algorithmic structure is formulated with normalized stress and strain quantities. In Appendix B.1 several statements with respect to the definition of the normalized quantities and the dependencies between physical and normalized values are summarized, to which it will be referred in the text. In particular, the reference strain ε_0, which was left undetermined in section 3.4, is now set to

$$\varepsilon_0 = \frac{\sigma_y(1-\nu^2)}{E}\,, \tag{7.1}$$

in order to keep consistent with the derivation of the normalized form of Hooke's law used here (see Appendix B.1).

7.2 Algorithmic Structure

The essential task of a finite element material routine is the incremental time integration of the constitutive equations. The subroutine typically is provided with the state at the start of the increment (stresses and strains[3], solution dependent state variables, temperature, predefined fields, etc.), the increments in temperature and predefined field variables, the strain increment and the time increment. The subroutine must perform two functions. It must update the stresses and the solution dependent state variables to their values at the end of the increment, and it must generate the tangential stiffness matrix, which is needed for the compilation of the global finite element equations.

---

[2] Unfortunately, ABAQUS/Explicit, which would be more appropriate for doing structural collapse analyses, has a very limited number of user subroutines and does not offer such an option.

[3] For a full section material routine of shells, of course, generalized (resultant) stress and strain quantities are used.

An often applied method for the time integration of the relevant elastoplastic constitutive equations from increment n to $n+1$ is the elastic predictor/plastic corrector algorithm. An elastic predictor step is performed first by assuming that no plastic strains develop during the increment, i.e. the total strain increment is treated as being elastic. Accordingly, the new stress state may be obtained by applying the elastic constitutive equations (Hooke's law). If the trial stress state obtained this way lies outside the yield surface, then the initial assumption of a purely elastic increment was incorrect, and plastic flow takes place. A plastic correction step has to be performed to account for these plastic deformations and to find the final stress state $n+1$, which necessarily lies on the yield surface. According to this strategy the following flowchart includes the essential steps, which have to be performed within the full section material routine:

1. Normalize the (given) stress/strain resultant quantities:[4]

   $$\Longrightarrow \begin{pmatrix} \boldsymbol{n} \\ \boldsymbol{m} \end{pmatrix}_n , \begin{pmatrix} \Delta\bar{\boldsymbol{e}} \\ \Delta\boldsymbol{k} \end{pmatrix} .$$

2. Compute the elastic predictor:

   $$\begin{pmatrix} \boldsymbol{n} \\ \boldsymbol{m} \end{pmatrix}_{n+1}^{tr} = \begin{pmatrix} \boldsymbol{n} \\ \boldsymbol{m} \end{pmatrix}_n + \begin{pmatrix} \mathbf{E} & \\ & \frac{4}{3}\mathbf{E} \end{pmatrix} \begin{pmatrix} \Delta\bar{\boldsymbol{e}} \\ \Delta\boldsymbol{k} \end{pmatrix} , \qquad \mathbf{E} = \begin{pmatrix} 1 & \nu & 0 \\ \nu & 1 & 0 \\ 0 & 0 & \frac{1-\nu}{2} \end{pmatrix} ,$$

   ($\mathbf{E}$ is the normalized elastic stiffness matrix for plane stress conditions. For the derivation of this normalized form of Hooke's law see Appendix B.1, Eq. (B.19)).

3. Check the yield condition:

   $F_{n+1}^{tr} = F(\boldsymbol{n}_{n+1}^{tr}, \boldsymbol{m}_{n+1}^{tr}) > 0$?

   If ($F_{n+1}^{tr} \leq 0$) go to step 6.

---

[4] To account for the fact that finite instead of infinitesimal increments are considered, in the following the strain increments are denoted as $\Delta\bar{\boldsymbol{e}}$ and $\Delta\boldsymbol{k}$ instead of $d\bar{\boldsymbol{e}}$ and $d\boldsymbol{k}$ (as done in section 3.4).

4. Perform the plastic corrector step (section 7.2.1):

$$\Longrightarrow \begin{pmatrix} \boldsymbol{n} \\ \boldsymbol{m} \end{pmatrix}_{n+1}, \begin{pmatrix} \Delta\bar{\boldsymbol{e}}^p \\ \Delta\boldsymbol{k}^p \end{pmatrix}_{n+1}.$$

5. Define the elastoplastic stiffness matrix $\mathbf{C}_t$ at the end of the increment (section 7.2.2):

$$\begin{pmatrix} d\boldsymbol{n} \\ d\boldsymbol{m} \end{pmatrix}_{n+1} = \mathbf{C}_t \begin{pmatrix} d\bar{\boldsymbol{e}} \\ d\boldsymbol{k} \end{pmatrix},$$

6. Compute the non-normalized stiffness matrix and stress resultants.

The check for yielding of the trial state (step 3) can be performed in a straightforward manner only if the yield condition is described in terms of stresses. Because the exact Ilyushin yield condition may only be stated in parametric form (with the parameters being functions of the plastic strain increments), however, step 3 would require the solution of a nonlinear system of equations. In order to avoid this, the approximate Ivanov yield surface, Eq. (3.81), which lies within 1 % error band of the exact Ilyushin yield surface, is adopted for this initial check.

7.2.1 Description of the Plastic Corrector Step

Concerning the "return mapping" of the trial state onto the yield surface (step 4), the following equations have to be solved:

$$\begin{pmatrix} \boldsymbol{n} \\ \boldsymbol{m} \end{pmatrix}_{n+1} = \begin{pmatrix} \boldsymbol{n} \\ \boldsymbol{m} \end{pmatrix}_{n+1}^{tr} - \begin{pmatrix} \mathbf{E} & \\ & \frac{4}{3}\mathbf{E} \end{pmatrix} \begin{pmatrix} \Delta\bar{\boldsymbol{e}}^p \\ \Delta\boldsymbol{k}^p \end{pmatrix}, \tag{7.2}$$

$$\begin{pmatrix} \boldsymbol{n} \\ \boldsymbol{m} \end{pmatrix}_{n+1} = \frac{3}{2} \begin{pmatrix} J_0\mathbf{P}^{-1} & 4J_1\mathbf{P}^{-1} \\ 4J_1\mathbf{P}^{-1} & 16J_2\mathbf{P}^{-1} \end{pmatrix}_{n+1} \begin{pmatrix} \Delta\bar{\boldsymbol{e}}^p \\ \Delta\boldsymbol{k}^p \end{pmatrix}, \tag{7.3}$$

which, for a general Kirchoff shell, state a nonlinear system of equations in twelve unknown parameters — the components of the vectors $\boldsymbol{n}_{n+1}$, $\boldsymbol{m}_{n+1}$, $\Delta\bar{\boldsymbol{e}}^p$ and $\Delta\boldsymbol{k}^p$.[5]

Equation (7.2) directly follows from the incremental form of Hooke's law,

$$\begin{pmatrix} \boldsymbol{n} \\ \boldsymbol{m} \end{pmatrix}_{n+1} = \begin{pmatrix} \boldsymbol{n} \\ \boldsymbol{m} \end{pmatrix}_{n} + \begin{pmatrix} \mathbf{E} & \\ & \frac{4}{3}\mathbf{E} \end{pmatrix} \left[\begin{pmatrix} \Delta\bar{\boldsymbol{e}} \\ \Delta\boldsymbol{k} \end{pmatrix} - \begin{pmatrix} \Delta\bar{\boldsymbol{e}}^p \\ \Delta\boldsymbol{k}^p \end{pmatrix} \right], \tag{7.4}$$

---

[5] For an axisymmetric Kirchhoff shell the third term in each vector (the "shear" term) is omitted and actually only a reduced system in eight unknown parameters has to be solved. This, however, may be regarded as a special case, without affecting the algorithmic structure of the full section material routine.

and from consideration of the elastic predictor step (step 2 of the above step description), whereas Eq. (7.3) is the six-dimensional form of the yield surface, Eq. (3.75), for the state $n+1$.

General Notes

Equation (7.3) enforces that the stress state at the end of the increment lies on the yield surface, but implicitely also that the flow rule is fulfilled at the end of the increment, i.e. both

$$F_{n+1} = F(\boldsymbol{n}_{n+1}, \boldsymbol{m}_{n+1}) = 0 \qquad \text{and} \qquad \begin{pmatrix} \Delta\bar{\boldsymbol{e}}^p \\ \Delta\boldsymbol{k}^p \end{pmatrix} = \Delta\bar{\xi} \begin{pmatrix} \partial F/\partial\boldsymbol{n} \\ \partial F/\partial\boldsymbol{m} \end{pmatrix}_{n+1} \tag{7.5}$$

are met (see section 3.4). Because, however, the flow rule is included at state $n+1$, the plastic corrector step, given by Eqs. (7.2) and (7.3), in fact represents a backward Euler integration scheme, which, for associated plasticity, is also known as the closest point projection algorithm. This often used implicit time integration algorithm is known to be unconditionally stable provided the elastic region is convex, but it is only first order accurate [Ortiz and Popov, 1985]. Due to the specialized representation of the exact Ilyushin yield surface, however, the backward Euler integration algorithm in the form stated above is a suitable choice for performing the return mapping. The application of a forward Euler integration algorithm, for example, would lead to the necessity of solving a nonlinear system of equations in each subincrement, which, of course, is computationally inattractive (subincrementation is needed because this integration scheme is only conditionally stable).

The two (vectorial) equations, Eqs. (7.2) and (7.3), represent a nonlinear system of equations in twelve unknown parameters. It is shown below that an analytical reduction to six and to a minimum of three[6] independent parameters, respectively, may be performed. Concerning the possible choice of these independent variables several quantities were introduced in section 3.4. Not all of them, however, are qualified for use in a general numerical solution procedure. Although the boundary of the yield surface may be treated in a "regularized" way, the parameters β and γ, but also the integral values K_0, K_1 and K_2 (which all have been introduced by Burgoyne and Brennan [1993b]) are not suitable for treating pure in-plane loading ($P_\kappa = 0$) numerically, because β and γ are not defined for this case.

---

[6] Without regard to the actual choice of these quantities two parameters are always needed for the description of the final stress state on the yield surface (also fixing the normal direction), and a third one determines the "length" of the plastic strain increment vector.

Without regard to any numerical efficiency considerations (convergence behaviour, etc.) a computational algorithm should, therefore, resort to a parametric description in terms of the plastic strain increment intensities P_ε, $P_{\varepsilon\kappa}$ and P_κ, or the integrals $\overline{J}_i$ $(= J_i/(J_0 J_2 - J_1^2))$, delivering well defined values at any point of the yield surface — but also the J_i-terms may be used provided their boundary values are evaluated in a regularized way (see Appendix B.2).

Introduction of Generalized Deviatoric Quantities

Before details concerning the analytical reduction and numerical solution of the plastic correction step are given, "deviatoric" stress/strain vectors are introduced in the following. These quantities may be utilized to rearrange the governing equations and to improve computational efficiency, but also to simplify an analytical treatment of individual steps of the computational algorithm (see also [Simo and Taylor, 1986; Simo and Kennedy, 1992]).

The matrices $\mathbf{P}$ and $\mathbf{E}$, used for stating the von Mises yield condition and Hooke's law for a state of plane stress,

$$\mathbf{P} = \begin{pmatrix} 1 & -\frac{1}{2} & 0 \\ -\frac{1}{2} & 1 & 0 \\ 0 & 0 & 3 \end{pmatrix} \qquad \text{and} \qquad \mathbf{E} = \begin{pmatrix} 1 & \nu & 0 \\ \nu & 1 & 0 \\ 0 & 0 & \frac{1-\nu}{2} \end{pmatrix} , \tag{7.6}$$

both have the same characteristic subspaces:

$$\mathbf{P} = \mathbf{Q}\mathbf{\Lambda}_P\mathbf{Q}^T , \qquad \mathbf{E} = \mathbf{Q}\mathbf{\Lambda}_E\mathbf{Q}^T , \qquad \text{with} \qquad \mathbf{Q} = \frac{1}{\sqrt{2}} \begin{pmatrix} 1 & -1 & 0 \\ 1 & 1 & 0 \\ 0 & 0 & \sqrt{2} \end{pmatrix} . \tag{7.7}$$

$\mathbf{Q}$ is orthogonal ($\mathbf{Q}^{-1} = \mathbf{Q}^T$, $\det \mathbf{Q} = 1$), and the diagonal matrices $\mathbf{\Lambda}_P$ and $\mathbf{\Lambda}_E$ are given by

$$\mathbf{\Lambda}_P = \begin{pmatrix} \frac{1}{2} & 0 & 0 \\ 0 & \frac{3}{2} & 0 \\ 0 & 0 & 3 \end{pmatrix} , \qquad \mathbf{\Lambda}_E = \begin{pmatrix} 1+\nu & 0 & 0 \\ 0 & 1-\nu & 0 \\ 0 & 0 & \frac{1-\nu}{2} \end{pmatrix} . \tag{7.8}$$

If the diagonal matrix $\mathbf{\Lambda}_P$ is written as a product

$$\mathbf{\Lambda}_P = \overline{\mathbf{\Lambda}}_P\overline{\mathbf{\Lambda}}_P , \qquad \overline{\mathbf{\Lambda}}_P = \begin{pmatrix} \sqrt{\frac{1}{2}} & 0 & 0 \\ 0 & \sqrt{\frac{3}{2}} & 0 \\ 0 & 0 & \sqrt{3} \end{pmatrix} , \tag{7.9}$$

and the quantities

$$\begin{aligned} \hat{\boldsymbol{n}} &= \overline{\boldsymbol{\Lambda}}_P \mathbf{Q}^T \boldsymbol{n} \ , & \Delta\hat{\overline{\boldsymbol{e}}}^p &= \overline{\boldsymbol{\Lambda}}_P^{-1} \mathbf{Q}^T \Delta\overline{\boldsymbol{e}}^p \ , \\ \hat{\boldsymbol{m}} &= \overline{\boldsymbol{\Lambda}}_P \mathbf{Q}^T \boldsymbol{m} \ , & \Delta\hat{\boldsymbol{k}}^p &= \overline{\boldsymbol{\Lambda}}_P^{-1} \mathbf{Q}^T \Delta\boldsymbol{k}^p \ , \end{aligned} \tag{7.10}$$

are defined (analogous for the generalized trial stress and the other strain quantities), then the equations to be solved in the plastic correction step, Eqs. (7.2) and (7.3), may be rewritten as

$$\begin{pmatrix} \hat{\boldsymbol{n}} \\ \hat{\boldsymbol{m}} \end{pmatrix}_{n+1} = \begin{pmatrix} \hat{\boldsymbol{n}} \\ \hat{\boldsymbol{m}} \end{pmatrix}_{n+1}^{tr} - \begin{pmatrix} \boldsymbol{\Lambda}_E \boldsymbol{\Lambda}_P & \\ & \frac{4}{3}\boldsymbol{\Lambda}_E \boldsymbol{\Lambda}_P \end{pmatrix} \begin{pmatrix} \Delta\hat{\overline{\boldsymbol{e}}}^p \\ \Delta\hat{\boldsymbol{k}}^p \end{pmatrix} \ , \tag{7.11}$$

$$\begin{pmatrix} \hat{\boldsymbol{n}} \\ \hat{\boldsymbol{m}} \end{pmatrix}_{n+1} = \frac{3}{2} \begin{pmatrix} J_0 \mathbf{I}_3 & 4J_1 \mathbf{I}_3 \\ 4J_1 \mathbf{I}_3 & 16J_2 \mathbf{I}_3 \end{pmatrix}_{n+1} \begin{pmatrix} \Delta\hat{\overline{\boldsymbol{e}}}^p \\ \Delta\hat{\boldsymbol{k}}^p \end{pmatrix} \ , \tag{7.12}$$

where now all submatrices have diagonal form ($\mathbf{I}_3$ is the 3×3-identity matrix). The stress resultant and plastic strain increment intensities (Eqs. (3.77) and (3.71)) are obtained as

$$\begin{aligned} Q_t &= \hat{\boldsymbol{n}}^T \hat{\boldsymbol{n}} \ , & P_\varepsilon &= \frac{3}{4} (\Delta\hat{\overline{\boldsymbol{e}}}^p)^T \Delta\hat{\overline{\boldsymbol{e}}}^p \ , \\ Q_{tm} &= \hat{\boldsymbol{n}}^T \hat{\boldsymbol{m}} \ , & P_{\varepsilon\kappa} &= 3 (\Delta\hat{\overline{\boldsymbol{e}}}^p)^T \Delta\hat{\boldsymbol{k}}^p \ , \\ Q_m &= \hat{\boldsymbol{m}}^T \hat{\boldsymbol{m}} \ , & P_\kappa &= 12 (\Delta\hat{\boldsymbol{k}}^p)^T \Delta\hat{\boldsymbol{k}}^p \ , \end{aligned} \tag{7.13}$$

which means that these parameters are simply defined as (scaled) scalar products of the "deviatoric" stress and plastic strain increment vectors, introduced in Eq. (7.10). All equations and definitions, however, which were based on those intensity values in section 3.4, remain unchanged! Furthermore, it directly follows from Eqs. (7.13) that the parameters Q_t, Q_m, P_ε and P_κ cannot become negative, and also that the conditions (3.79) and (3.72),

$$Q_t Q_m \geq Q_{tm}^2 \qquad \text{and} \qquad P_\varepsilon P_\kappa \geq P_{\varepsilon\kappa}^2 \ , \tag{7.14}$$

bounding the exact Ilyushin yield surface, must hold.[7]

Reduction to a System of Six Nonlinear Equations

An ad hoc way to reduce the number of parameters for the solution of the return mapping algorithm immediately follows from Eqs. (7.11) and (7.12). Elimination of the section forces $\hat{\boldsymbol{n}}$ and $\hat{\boldsymbol{m}}$ (by simply equating both relations) delivers a reduced system of equations in terms of the plastic strain increments, which may be stated as

---

[7] The latter may simply be proved by applying the Schwarz inequality, which, for two arbitrary vectors $\boldsymbol{a}$ and $\boldsymbol{b}$ (having the same dimension) is stated as $|\boldsymbol{a}||\boldsymbol{b}| \geq |\boldsymbol{a}^T \boldsymbol{b}|$.

$$\boldsymbol{g}_1(\Delta\hat{\bar{\boldsymbol{e}}}^p, \Delta\hat{\boldsymbol{k}}^p) = \begin{pmatrix} \hat{\boldsymbol{n}} \\ \hat{\boldsymbol{m}} \end{pmatrix}^{tr} - \begin{pmatrix} \boldsymbol{\Omega}_1 & \boldsymbol{\Omega}_2 \\ \boldsymbol{\Omega}_2 & \boldsymbol{\Omega}_4 \end{pmatrix} \begin{pmatrix} \Delta\hat{\bar{\boldsymbol{e}}}^p \\ \Delta\hat{\boldsymbol{k}}^p \end{pmatrix} \stackrel{!}{=} \boldsymbol{0} \,, \tag{7.15}$$

with the diagonal submatrices $\boldsymbol{\Omega}_i$ being defined as

$$\begin{aligned} \boldsymbol{\Omega}_1 &= \boldsymbol{\Lambda}_E \boldsymbol{\Lambda}_P + \frac{3}{2} J_0 \mathbf{I}_3 \,, \\ \boldsymbol{\Omega}_2 &= 6 J_1 \, \mathbf{I}_3 \,, \\ \boldsymbol{\Omega}_4 &= \frac{4}{3} \boldsymbol{\Lambda}_E \boldsymbol{\Lambda}_P + 24 J_2 \mathbf{I}_3 \,. \end{aligned} \tag{7.16}$$

This system of equations may be solved numerically. In the current version of the full section material routine, a general Newton/Raphson solver – with the Jacobian matrix being replaced by forward difference quotients – is applied. The individual steps, which have to be performed for one function evaluation, are summarized in Figure 7.1.

Definition of a Fixpoint Algorithm

Besides the possibility of solving the return mapping step with a general equation solver (like the Newton/Raphson algorithm mentioned above), Eq. (7.15) may also be utilized for the definition of a fixpoint algorithm, the iteration sequence of which (iteration step $k \to k+1$) is given by

$$\begin{pmatrix} \Delta\hat{\bar{\boldsymbol{e}}}^p \\ \Delta\hat{\boldsymbol{k}}^p \end{pmatrix}^{(k+1)} = \boldsymbol{g}_2(\Delta\hat{\bar{\boldsymbol{e}}}^{p(k)}, \Delta\hat{\boldsymbol{k}}^{p(k)}) \tag{7.17}$$

and

$$\begin{pmatrix} \Delta\hat{\bar{\boldsymbol{e}}}^p \\ \Delta\hat{\boldsymbol{k}}^p \end{pmatrix}^{(k+1)} = \begin{pmatrix} \boldsymbol{\Omega}_1^{(k)} & \boldsymbol{\Omega}_2^{(k)} \\ \boldsymbol{\Omega}_2^{(k)} & \boldsymbol{\Omega}_4^{(k)} \end{pmatrix}^{-1} \begin{pmatrix} \hat{\boldsymbol{n}} \\ \hat{\boldsymbol{m}} \end{pmatrix}^{tr} = \begin{pmatrix} \overline{\boldsymbol{\Omega}}_1^{(k)} & \overline{\boldsymbol{\Omega}}_2^{(k)} \\ \overline{\boldsymbol{\Omega}}_2^{(k)} & \overline{\boldsymbol{\Omega}}_4^{(k)} \end{pmatrix} \begin{pmatrix} \hat{\boldsymbol{n}} \\ \hat{\boldsymbol{m}} \end{pmatrix}^{tr} , \tag{7.18}$$

respectively. The flowchart for this solution strategy is presented in Figure 7.2.[8]

---

[8] It is remarkable that — due to the evaluation of the plastic strain increment intensities P_ε, $P_{\varepsilon\kappa}$ and P_κ as well as the integral terms J_i within the iteration loop — the algorithm could likewise be regarded as being defined with either of these sets of parameters. This way actually a system of equations in only three unknowns is stated.

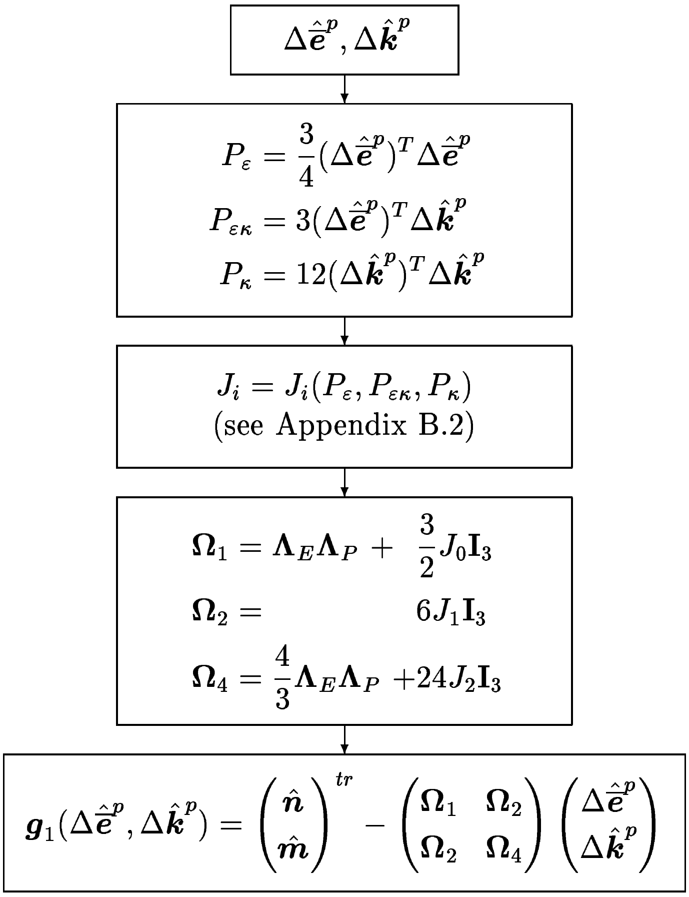
$\Delta\hat{\bar{e}}^p, \Delta\hat{k}^p$
$P_\varepsilon = \frac{3}{4}(\Delta\hat{\bar{e}}^p)^T\Delta\hat{\bar{e}}^p$
$P_{\varepsilon\kappa} = 3(\Delta\hat{\bar{e}}^p)^T\Delta\hat{k}^p$
$P_\kappa = 12(\Delta\hat{k}^p)^T\Delta\hat{k}^p$
$J_i = J_i(P_\varepsilon, P_{\varepsilon\kappa}, P_\kappa)$
(see Appendix B.2)
$\boldsymbol{\Omega}_1 = \boldsymbol{\Lambda}_E\boldsymbol{\Lambda}_P + \frac{3}{2}J_0\mathbf{I}_3$
$\boldsymbol{\Omega}_2 = 6J_1\mathbf{I}_3$
$\boldsymbol{\Omega}_4 = \frac{4}{3}\boldsymbol{\Lambda}_E\boldsymbol{\Lambda}_P + 24J_2\mathbf{I}_3$
$\boldsymbol{g}_1(\Delta\hat{\bar{e}}^p, \Delta\hat{k}^p) = \begin{pmatrix}\hat{n}\\ \hat{m}\end{pmatrix}^{tr} - \begin{pmatrix}\boldsymbol{\Omega}_1 & \boldsymbol{\Omega}_2\\ \boldsymbol{\Omega}_2 & \boldsymbol{\Omega}_4\end{pmatrix}\begin{pmatrix}\Delta\hat{\bar{e}}^p\\ \Delta\hat{k}^p\end{pmatrix}$

Figure 7.1: Return mapping step: flowchart for the evaluation of $\boldsymbol{g}_1(\Delta\hat{\bar{e}}^p, \Delta\hat{k}^p)$

The stated fixpoint algorithm delivers a fairly simple method for solving the plastic correction step without the need for evaluating any derivatives. Furthermore, because all submatrices $\boldsymbol{\Omega}_i$ are given in diagonal form, the matrix inversion to obtain the submatrices $\overline{\boldsymbol{\Omega}}_i$ may be coded very efficiently (see Appendix B.2, Eq. (B.29)), and the computational effort per iteration step is remarkably low. The convergence rate, however, strongly depends on the partial derivatives of $\boldsymbol{g}_2$,[9] and for the given functions it is in general markedly below that of the full Newton/Raphson algorithm (where a quadratic convergence rate is ensured near the solution). Therefore, in general much more iteration steps have to be performed for obtaining solutions with the fixpoint algorithm than with a comparable Newton/Raphson solution procedure. The implementation of this strategy into the full section material routine, however, shows that solutions can be obtained for any point of the yield surface

---

[9] Roughly speaking — the smaller the partial derivatives the higher the rate of convergence [Bronstein et al., 1995].

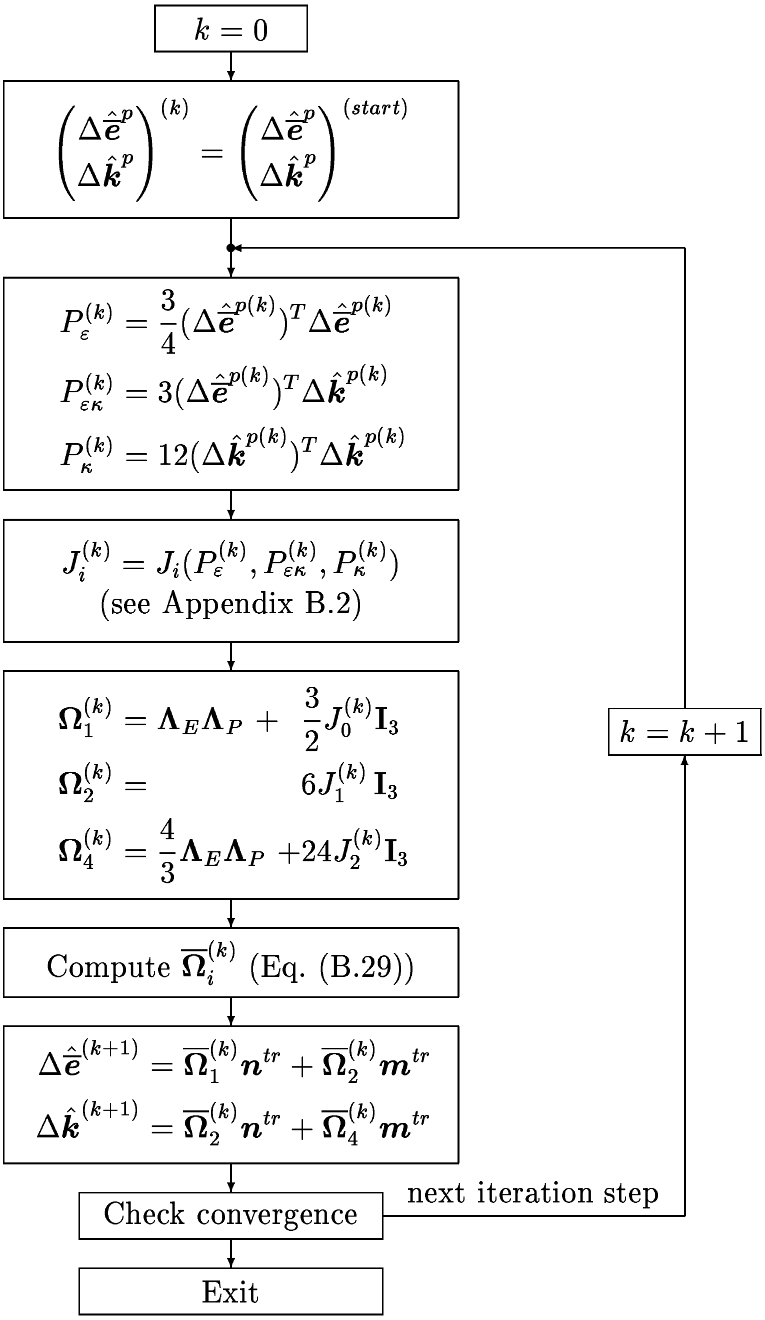
$k = 0$
$\begin{pmatrix} \Delta\hat{\boldsymbol{e}}^p \\ \Delta\hat{\boldsymbol{k}}^p \end{pmatrix}^{(k)} = \begin{pmatrix} \Delta\hat{\boldsymbol{e}}^p \\ \Delta\hat{\boldsymbol{k}}^p \end{pmatrix}^{(start)}$
$P_\varepsilon^{(k)} = \frac{3}{4}(\Delta\hat{\boldsymbol{e}}^{p(k)})^T \Delta\hat{\boldsymbol{e}}^{p(k)}$
$P_{\varepsilon\kappa}^{(k)} = 3(\Delta\hat{\boldsymbol{e}}^{p(k)})^T \Delta\hat{\boldsymbol{k}}^{p(k)}$
$P_\kappa^{(k)} = 12(\Delta\hat{\boldsymbol{k}}^{p(k)})^T \Delta\hat{\boldsymbol{k}}^{p(k)}$
$J_i^{(k)} = J_i(P_\varepsilon^{(k)}, P_{\varepsilon\kappa}^{(k)}, P_\kappa^{(k)})$
(see Appendix B.2)
$\boldsymbol{\Omega}_1^{(k)} = \boldsymbol{\Lambda}_E\boldsymbol{\Lambda}_P + \frac{3}{2}J_0^{(k)}\mathbf{I}_3$
$\boldsymbol{\Omega}_2^{(k)} = 6J_1^{(k)}\mathbf{I}_3$
$\boldsymbol{\Omega}_4^{(k)} = \frac{4}{3}\boldsymbol{\Lambda}_E\boldsymbol{\Lambda}_P + 24J_2^{(k)}\mathbf{I}_3$
Compute $\overline{\boldsymbol{\Omega}}_i^{(k)}$ (Eq. (B.29))
$\Delta\hat{\boldsymbol{e}}^{(k+1)} = \overline{\boldsymbol{\Omega}}_1^{(k)}\boldsymbol{n}^{tr} + \overline{\boldsymbol{\Omega}}_2^{(k)}\boldsymbol{m}^{tr}$
$\Delta\hat{\boldsymbol{k}}^{(k+1)} = \overline{\boldsymbol{\Omega}}_2^{(k)}\boldsymbol{n}^{tr} + \overline{\boldsymbol{\Omega}}_4^{(k)}\boldsymbol{m}^{tr}$
Check convergence
next iteration step
$k = k + 1$
Exit

Figure 7.2: Flowchart for the solution of the return mapping step with a fixpoint algorithm

without fundamental difficulties (except near the singular point $Q_t = 1$, where all solution algorithms presented here run into problems, see below).

An advantage of both formulations sketched above is that the plastic strain increment intensities P_ε, $P_{\varepsilon\kappa}$ and P_κ (which are needed for the numerical evaluation of the J_i-integrals) are obtained directly from the plastic strain increments and thus the constraints imposed onto these parameters:

$$P_\varepsilon \geq 0 \ , \qquad P_\kappa \geq 0 \qquad \text{and} \qquad P_\varepsilon P_\kappa \geq P_{\varepsilon\kappa}^2 \tag{7.19}$$

are fulfilled identically.[10] This may in general not be assumed if a system of equations in terms of only three parameters is formulated. The main disadvantage, however, is the computational inefficiency due to the need for solving a nonlinear system in six variables and, in case of the fixpoint algorithm, a low convergence rate.

Reduction to a System of Three Nonlinear Equations — Preliminaries

It was mentioned above that the return mapping algorithm may be formulated with a minimum number of three independent parameters, e.g. in terms of the plastic strain increment intensities P_ε, $P_{\varepsilon\kappa}$ and P_κ, the integrals J_i or the integral terms $\overline{J}_i$. A comparison with conventional plasticity algorithms in stress space, however, leads to the supposition that a very suitable choice will be given by generalized plastic consistency parameters, which are defined directly via the $\overline{J}_i$-terms. The inverted form of the exact Ilyushin yield surface (and the statement of the normality rule), given in Eq. (3.96), may be written in transformed form as

$$\begin{aligned} \Delta\hat{\boldsymbol{e}}^p &= 2\Delta\xi_t \hat{\boldsymbol{n}} + \Delta\xi_{tm} \hat{\boldsymbol{m}} \ , \\ \Delta\hat{\boldsymbol{k}}^p &= \Delta\xi_{tm} \hat{\boldsymbol{n}} + 2\Delta\xi_m \hat{\boldsymbol{m}} \ , \end{aligned} \tag{7.20}$$

with the $\Delta\xi_i$-terms

$$\Delta\xi_t = \frac{1}{3}\overline{J}_2 \ , \qquad \Delta\xi_{tm} = -\frac{1}{6}\overline{J}_1 \qquad \text{and} \qquad \Delta\xi_m = \frac{1}{48}\overline{J}_0 \tag{7.21}$$

being known functions of the plastic strain increments (and having definite values at any point of the yield surface, see section 3.4.4). This form is quite similar to the normality rule in stress space. For example, for plane stress von Mises plasticity (forming the basis for the derivation of the exact Ilyushin yield surface) the normality rule is given in transformed form by

---

[10] If these constraints are violated during the iteration process, then a further evaluation of the equations, i.e. the integration, which has to be performed to obtain the J_i-values, is no longer possible.

$$\Delta \hat{\boldsymbol{e}}^p = \Delta\xi \frac{\partial f}{\partial \hat{\bar{\boldsymbol{\sigma}}}} = 2\Delta\xi \hat{\bar{\boldsymbol{\sigma}}} \,, \tag{7.22}$$

and $\Delta\xi$ is the usual parameter to be determined within the return mapping step [Simo and Taylor, 1986; Crisfield, 1991].

A physical interpretation (and the subscript nomenclature) for the $\Delta\xi_i$-terms follows from the definition of the normalized incremental plastic work $\Delta\overline{w}_\mathrm{p}$. When using Eq. (7.20), $\Delta\overline{w}_\mathrm{p}$ is expressed as

$$\Delta\overline{w}_\mathrm{p} = \begin{pmatrix} \boldsymbol{n} \\ \boldsymbol{m} \end{pmatrix}^T \begin{pmatrix} \Delta\overline{\boldsymbol{e}}^p \\ \Delta\boldsymbol{k}^p \end{pmatrix} = \begin{pmatrix} \hat{\boldsymbol{n}} \\ \hat{\boldsymbol{m}} \end{pmatrix}^T \begin{pmatrix} \Delta\hat{\overline{\boldsymbol{e}}}^p \\ \Delta\hat{\boldsymbol{k}}^p \end{pmatrix} = \begin{pmatrix} \hat{\boldsymbol{n}} \\ \hat{\boldsymbol{m}} \end{pmatrix}^T \begin{pmatrix} 2\Delta\xi_t\mathbf{I}_3 & \Delta\xi_{tm}\mathbf{I}_3 \\ \Delta\xi_{tm}\mathbf{I}_3 & 2\Delta\xi_m\mathbf{I}_3 \end{pmatrix} \begin{pmatrix} \hat{\boldsymbol{n}} \\ \hat{\boldsymbol{m}} \end{pmatrix} \,, \tag{7.23}$$

from which follows:

$$\Delta\overline{w}_\mathrm{p} = 2(\Delta\xi_t Q_t + \Delta\xi_{tm} Q_{tm} + \Delta\xi_m Q_m) \,, \tag{7.24}$$

revealing that the $\Delta\xi_i$-terms may — in analogy to $\Delta\xi$ in stress space — be regarded as a generalized scalar measure for the plastic strain increments of a plastically deforming Kirchhoff shell section, representing the kinematic counterpart to the generalized stress intensities Q_t, Q_{tm} and Q_m.

Definition of a System of Three Nonlinear Equations

The strategy for the definition of the return mapping algorithm in terms of the three unknown parameters $\Delta\xi_t$, $\Delta\xi_{tm}$ and $\Delta\xi_m$ is closely related to the backward Euler scheme for plane stress von Mises plasticity. The formalism, which is usually applied there for defining the resulting scalar equation (which has to be solved for $\Delta\xi$), is sketched in Table 7.1. However, because the implicit form of the yield surface is applied, Table 7.2 contains a slightly different strategy, where the yield criterion is replaced by the relation between the plastic consistency parameter and the plastic strain increment, i.e. the transformed form of Eq. (3.67) (which, of course, implicitely includes the yield criterion, see section 3.4.2). It is obvious that for plane stress von Mises plasticity both formalisms lead to the same resulting equation for $\Delta\xi$. The strategy sketched in Table 7.2, however, is also convenient for the definition of a return mapping algorithm for the full section material routine in terms of $\Delta\xi_t$, $\Delta\xi_{tm}$ and $\Delta\xi_m$, as described in the following.

Table 7.1: Plane stress von Mises plasticity without hardening: conventional formulation of the backward Euler integration algorithm

1.	Plastic correction	$\hat{\bar{\boldsymbol{\sigma}}} = \hat{\bar{\boldsymbol{\sigma}}}^{tr} - \boldsymbol{\Lambda}_E\boldsymbol{\Lambda}_P\Delta\hat{\boldsymbol{e}}^p$
2.	Normality rule	$\Delta\hat{\boldsymbol{e}}^p = \Delta\xi\dfrac{\partial f}{\partial\hat{\bar{\boldsymbol{\sigma}}}} = 2\Delta\xi\hat{\bar{\boldsymbol{\sigma}}}$
3.	Yield condition	$f(\hat{\bar{\boldsymbol{\sigma}}}) = \hat{\bar{\boldsymbol{\sigma}}}^T\hat{\bar{\boldsymbol{\sigma}}} - 1 = 0$
4.	Use 1 and 2 to express the stresses at the end of the increment	$\hat{\bar{\boldsymbol{\sigma}}}(\Delta\xi) = \boldsymbol{\Sigma}^{-1}\hat{\bar{\boldsymbol{\sigma}}}^{tr}$ $\boldsymbol{\Sigma}(\Delta\xi) = \mathbf{I}_3 + 2\Delta\xi\boldsymbol{\Lambda}_E\boldsymbol{\Lambda}_P$
5.	Use 4 in 3 to set up a scalar equation in terms of $\Delta\xi$	$f(\Delta\xi) = (\hat{\bar{\boldsymbol{\sigma}}}^{tr})^T\boldsymbol{\Sigma}^{-T}\boldsymbol{\Sigma}^{-1}\hat{\bar{\boldsymbol{\sigma}}}^{tr} - 1 \overset{!}{=} 0$ $\Longrightarrow \Delta\xi$

The statement of the algorithmic problem for the full section material routine is given by Eqs. (7.11), (7.20) and the definition of the $\Delta\xi_i$-terms, Eq. (7.21):

$$\begin{pmatrix}\hat{\boldsymbol{n}}\\ \hat{\boldsymbol{m}}\end{pmatrix} = \begin{pmatrix}\hat{\boldsymbol{n}}\\ \hat{\boldsymbol{m}}\end{pmatrix}^{tr} - \begin{pmatrix}\boldsymbol{\Lambda}_E\boldsymbol{\Lambda}_P & \\ & \frac{4}{3}\boldsymbol{\Lambda}_E\boldsymbol{\Lambda}_P\end{pmatrix}\begin{pmatrix}\Delta\hat{\bar{\boldsymbol{e}}}^p\\ \Delta\hat{\boldsymbol{k}}^p\end{pmatrix}, \tag{7.25}$$

$$\begin{pmatrix}\Delta\hat{\bar{\boldsymbol{e}}}^p\\ \Delta\hat{\boldsymbol{k}}^p\end{pmatrix} = \begin{pmatrix}2\Delta\xi_t\mathbf{I}_3 & \Delta\xi_{tm}\mathbf{I}_3\\ \Delta\xi_{tm}\mathbf{I}_3 & 2\Delta\xi_m\mathbf{I}_3\end{pmatrix}\begin{pmatrix}\hat{\boldsymbol{n}}\\ \hat{\boldsymbol{m}}\end{pmatrix}, \tag{7.26}$$

$$\begin{pmatrix}\Delta\xi_t\\ \Delta\xi_{tm}\\ \Delta\xi_m\end{pmatrix} = \begin{pmatrix}\frac{1}{3}\overline{J}_2(\Delta\hat{\bar{\boldsymbol{e}}}^p, \Delta\hat{\boldsymbol{k}}^p)\\ -\frac{1}{6}\overline{J}_1(\Delta\hat{\bar{\boldsymbol{e}}}^p, \Delta\hat{\boldsymbol{k}}^p)\\ \frac{1}{48}\overline{J}_0(\Delta\hat{\bar{\boldsymbol{e}}}^p, \Delta\hat{\boldsymbol{k}}^p)\end{pmatrix}. \tag{7.27}$$

Combining Eqs. (7.25) and (7.26) one obtains

$$\left[\mathbf{I}_6 + \begin{pmatrix}\boldsymbol{\Lambda}_E\boldsymbol{\Lambda}_P & \\ & \frac{4}{3}\boldsymbol{\Lambda}_E\boldsymbol{\Lambda}_P\end{pmatrix}\begin{pmatrix}2\Delta\xi_t\mathbf{I}_3 & \Delta\xi_{tm}\mathbf{I}_3\\ \Delta\xi_{tm}\mathbf{I}_3 & 2\Delta\xi_m\mathbf{I}_3\end{pmatrix}\right]\begin{pmatrix}\hat{\boldsymbol{n}}\\ \hat{\boldsymbol{m}}\end{pmatrix} = \begin{pmatrix}\hat{\boldsymbol{n}}\\ \hat{\boldsymbol{m}}\end{pmatrix}^{tr}. \tag{7.28}$$

Table 7.2: Plane stress von Mises plasticity without hardening: formulation of the backward Euler integration algorithm without explicit use of the yield criterion

1.	Plastic correction	$\hat{\bar{\boldsymbol{\sigma}}} = \hat{\bar{\boldsymbol{\sigma}}}^{tr} - \boldsymbol{\Lambda}_E \boldsymbol{\Lambda}_P \Delta \hat{\boldsymbol{e}}^p$
2.	Normality rule	$\Delta \hat{\boldsymbol{e}}^p = \Delta\xi \dfrac{\partial f}{\partial \hat{\bar{\boldsymbol{\sigma}}}} = 2\Delta\xi \hat{\bar{\boldsymbol{\sigma}}}$
3.	Plastic consistency parameter (Eq. (3.67))	$\Delta\xi^2 = \dfrac{1}{4}(\Delta \hat{\boldsymbol{e}}^p)^T \Delta \hat{\boldsymbol{e}}^p$
4.	Use 1 and 2 to express the stresses at the end of the increment	$\hat{\bar{\boldsymbol{\sigma}}}(\Delta\xi) = \boldsymbol{\Sigma}^{-1} \hat{\bar{\boldsymbol{\sigma}}}^{tr}$ $\boldsymbol{\Sigma}(\Delta\xi) = \mathbf{I}_3 + 2\Delta\xi \boldsymbol{\Lambda}_E \boldsymbol{\Lambda}_P$
5.	Use 4 in 2 to express the plastic strain increment	$\Delta \hat{\boldsymbol{e}}^p(\Delta\xi) = 2\Delta\xi \boldsymbol{\Sigma}^{-1} \hat{\bar{\boldsymbol{\sigma}}}^{tr}$
6.	Use 5 in 3 to set up a scalar equation in terms of $\Delta\xi$	$\Delta\xi^2 = \dfrac{1}{4} 4\Delta\xi^2 (\hat{\bar{\boldsymbol{\sigma}}}^{tr})^T \boldsymbol{\Sigma}^{-T} \boldsymbol{\Sigma}^{-1} \hat{\bar{\boldsymbol{\sigma}}}^{tr}$ $\boldsymbol{g}(\Delta\xi) = (\hat{\bar{\boldsymbol{\sigma}}}^{tr})^T \boldsymbol{\Sigma}^{-T} \boldsymbol{\Sigma}^{-1} \hat{\bar{\boldsymbol{\sigma}}}^{tr} - 1 \overset{!}{=} 0$ $\Longrightarrow \Delta\xi$

With the diagonal submatrices

$$\begin{aligned}
\boldsymbol{\Sigma}_1 &= \mathbf{I}_3 + 2\Delta\xi_t \boldsymbol{\Lambda}_E \boldsymbol{\Lambda}_P \ , \\
\boldsymbol{\Sigma}_2 &= \Delta\xi_{tm} \boldsymbol{\Lambda}_E \boldsymbol{\Lambda}_P \ , \\
\boldsymbol{\Sigma}_3 &= \frac{4}{3}\Delta\xi_{tm} \boldsymbol{\Lambda}_E \boldsymbol{\Lambda}_P \ , \\
\boldsymbol{\Sigma}_4 &= \mathbf{I}_3 + \frac{8}{3}\Delta\xi_m \boldsymbol{\Lambda}_E \boldsymbol{\Lambda}_P \ ,
\end{aligned} \tag{7.29}$$

the stress resultants are given by

$$\begin{pmatrix} \hat{\boldsymbol{n}} \\ \hat{\boldsymbol{m}} \end{pmatrix} = \begin{pmatrix} \boldsymbol{\Sigma}_1 & \boldsymbol{\Sigma}_2 \\ \boldsymbol{\Sigma}_3 & \boldsymbol{\Sigma}_4 \end{pmatrix}^{-1} \begin{pmatrix} \hat{\boldsymbol{n}} \\ \hat{\boldsymbol{m}} \end{pmatrix}^{tr} = \begin{pmatrix} \bar{\boldsymbol{\Sigma}}_1 & \bar{\boldsymbol{\Sigma}}_2 \\ \bar{\boldsymbol{\Sigma}}_3 & \bar{\boldsymbol{\Sigma}}_4 \end{pmatrix} \begin{pmatrix} \hat{\boldsymbol{n}} \\ \hat{\boldsymbol{m}} \end{pmatrix}^{tr} , \tag{7.30}$$

and thus only depend on the parameters $\Delta\xi_t$, $\Delta\xi_{tm}$ and $\Delta\xi_m$ (compare with step 4 in Table 7.2). The stress resultants obtained this way may now be used to evaluate the plastic strain increments $\Delta\hat{\overline{e}}^p$ and $\Delta\hat{k}^p$ from Eq. (7.26), which again, are sufficient to define new values for the plastic consistency parameters $\Delta\xi_t$, $\Delta\xi_{tm}$ and $\Delta\xi_m$ according to Eq. (7.27). This way a nonlinear system of equations of the form

$$\boldsymbol{g}_3(\Delta\xi_t,\Delta\xi_{tm},\Delta\xi_m)=\begin{pmatrix}\Delta\xi_t\\ \Delta\xi_{tm}\\ \Delta\xi_m\end{pmatrix}-\begin{pmatrix}\frac{1}{3}\overline{J}_2(\Delta\xi_t,\Delta\xi_{tm},\Delta\xi_m)\\ -\frac{1}{6}\overline{J}_1(\Delta\xi_t,\Delta\xi_{tm},\Delta\xi_m)\\ \frac{1}{48}\overline{J}_0(\Delta\xi_t,\Delta\xi_{tm},\Delta\xi_m)\end{pmatrix}\overset{!}{=}\mathbf{0} \tag{7.31}$$

is set up, which, in the current version of the full section material routine, is solved with a general Newton/Raphson solver. Again, the partial derivatives are replaced by forward difference quotients.

Figure 7.3 contains a summary of the individual steps, which are to be performed for each function evaluation. Due to the definition of the return mapping with deviatoric stress/plastic strain increment quantities each step of this flowchart is computationally inexpensive, including the matrix inversion to obtain the (diagonal) submatrices $\overline{\boldsymbol{\Sigma}}_i$. Concerning the evaluation of points at the boundary of the exact Ilyushin yield surface it may in addition be utilized that the $\overline{J}_i$-terms (and thus the $\Delta\xi_i$-terms) have definite values there, which may be evaluated without the need for computing regularized values for J_i internally (see section 3.4.4).

Test runs with this return mapping algorithm show that the convergence behaviour is comparable to that of the Newton/Raphson algorithm in terms of the plastic strain increments (i.e. the numerical solution of $\boldsymbol{g}_1(\Delta\overline{\boldsymbol{e}}^p,\Delta\boldsymbol{k}^p)$, Eq. (7.15)). Due to the fact that the independent parameters are integral (and numerically well defined) values, iterative changes remain sufficiently small, and no problems with violating any constraints onto the variables (e.g. $\Delta\xi_t$ and $\Delta\xi_m$ are to be positive (semi)definite values) are observed in general.[11] This is in contrast to a return mapping scheme, which was investigated in terms of the plastic strain increment intensities P_ε, $P_{\varepsilon\kappa}$ and P_κ, where practically no solutions could be obtained without making precautions against violating the constraint equations (7.19).

Definition of Starting Values

According to Crisfield [1991] appropriate starting values for a return mapping algorithm may be found by performing a first-order Taylor expansion of the yield surface about the

---

[11] Except near the singular point $Q_t = 1$ (see restrictions below).

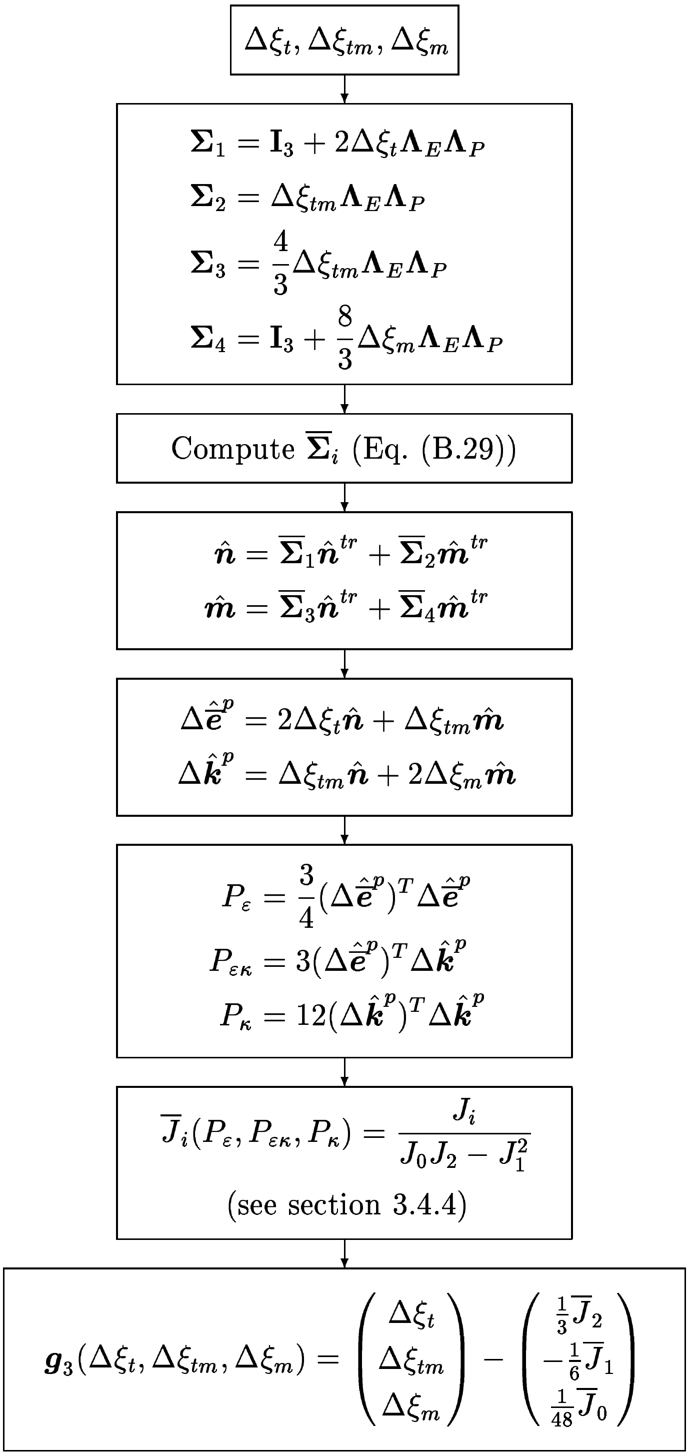
$\Delta\xi_t, \Delta\xi_{tm}, \Delta\xi_m$
$\boldsymbol{\Sigma}_1 = \mathbf{I}_3 + 2\Delta\xi_t \boldsymbol{\Lambda}_E \boldsymbol{\Lambda}_P$
$\boldsymbol{\Sigma}_2 = \Delta\xi_{tm} \boldsymbol{\Lambda}_E \boldsymbol{\Lambda}_P$
$\boldsymbol{\Sigma}_3 = \frac{4}{3}\Delta\xi_{tm} \boldsymbol{\Lambda}_E \boldsymbol{\Lambda}_P$
$\boldsymbol{\Sigma}_4 = \mathbf{I}_3 + \frac{8}{3}\Delta\xi_m \boldsymbol{\Lambda}_E \boldsymbol{\Lambda}_P$
Compute $\overline{\boldsymbol{\Sigma}}_i$ (Eq. (B.29))
$\hat{\boldsymbol{n}} = \overline{\boldsymbol{\Sigma}}_1 \hat{\boldsymbol{n}}^{tr} + \overline{\boldsymbol{\Sigma}}_2 \hat{\boldsymbol{m}}^{tr}$
$\hat{\boldsymbol{m}} = \overline{\boldsymbol{\Sigma}}_3 \hat{\boldsymbol{n}}^{tr} + \overline{\boldsymbol{\Sigma}}_4 \hat{\boldsymbol{m}}^{tr}$
$\Delta\hat{\bar{\boldsymbol{e}}}^p = 2\Delta\xi_t \hat{\boldsymbol{n}} + \Delta\xi_{tm} \hat{\boldsymbol{m}}$
$\Delta\hat{\boldsymbol{k}}^p = \Delta\xi_{tm} \hat{\boldsymbol{n}} + 2\Delta\xi_m \hat{\boldsymbol{m}}$
$P_\varepsilon = \frac{3}{4}(\Delta\hat{\bar{\boldsymbol{e}}}^p)^T \Delta\hat{\bar{\boldsymbol{e}}}^p$
$P_{\varepsilon\kappa} = 3(\Delta\hat{\bar{\boldsymbol{e}}}^p)^T \Delta\hat{\boldsymbol{k}}^p$
$P_\kappa = 12(\Delta\hat{\boldsymbol{k}}^p)^T \Delta\hat{\boldsymbol{k}}^p$
$\overline{J}_i(P_\varepsilon, P_{\varepsilon\kappa}, P_\kappa) = \frac{J_i}{J_0 J_2 - J_1^2}$
(see section 3.4.4)
$\boldsymbol{g}_3(\Delta\xi_t, \Delta\xi_{tm}, \Delta\xi_m) = \begin{pmatrix} \Delta\xi_t \\ \Delta\xi_{tm} \\ \Delta\xi_m \end{pmatrix} - \begin{pmatrix} \frac{1}{3}\overline{J}_2 \\ -\frac{1}{6}\overline{J}_1 \\ \frac{1}{48}\overline{J}_0 \end{pmatrix}$

Figure 7.3: Return mapping step: flowchart for the evaluation of $\boldsymbol{g}_3(\Delta\xi_t, \Delta\xi_{tm}, \Delta\xi_m)$

trial state. For a full section yield criterion this is written as

$$F(\hat{\boldsymbol{n}},\hat{\boldsymbol{m}}) \approx F(\hat{\boldsymbol{n}}^{tr},\hat{\boldsymbol{m}}^{tr}) + \begin{pmatrix} \partial F/\partial\hat{\boldsymbol{n}} \\ \partial F/\partial\hat{\boldsymbol{m}} \end{pmatrix}_{tr}^{T} \begin{pmatrix} d\hat{\boldsymbol{n}} \\ d\hat{\boldsymbol{m}} \end{pmatrix} = 0\ . \tag{7.32}$$

With

$$\begin{pmatrix} d\hat{\boldsymbol{n}} \\ d\hat{\boldsymbol{m}} \end{pmatrix} = \begin{pmatrix} \hat{\boldsymbol{n}} \\ \hat{\boldsymbol{m}} \end{pmatrix} - \begin{pmatrix} \hat{\boldsymbol{n}} \\ \hat{\boldsymbol{m}} \end{pmatrix}^{tr} = - \begin{pmatrix} \boldsymbol{\Lambda}_E\boldsymbol{\Lambda}_P & \\ & \frac{4}{3}\boldsymbol{\Lambda}_E\boldsymbol{\Lambda}_P \end{pmatrix} \begin{pmatrix} \Delta\hat{\bar{\boldsymbol{e}}}^{p} \\ \Delta\hat{\boldsymbol{k}}^{p} \end{pmatrix}\ , \tag{7.33}$$

$$\begin{pmatrix} \Delta\hat{\bar{\boldsymbol{e}}}^{p} \\ \Delta\hat{\boldsymbol{k}}^{p} \end{pmatrix} = \Delta\bar{\xi} \begin{pmatrix} \partial F/\partial\hat{\boldsymbol{n}} \\ \partial F/\partial\hat{\boldsymbol{m}} \end{pmatrix}\ , \tag{7.34}$$

and the abbreviations

$$F_{tr} = F(\hat{\boldsymbol{n}}^{tr},\hat{\boldsymbol{m}}^{tr})\ , \qquad \boldsymbol{a}_{tr} = \begin{pmatrix} \partial F/\partial\hat{\boldsymbol{n}} \\ \partial F/\partial\hat{\boldsymbol{m}} \end{pmatrix}_{tr}\ , \qquad \boldsymbol{\Lambda} = \begin{pmatrix} \boldsymbol{\Lambda}_E\boldsymbol{\Lambda}_P & \\ & \frac{4}{3}\boldsymbol{\Lambda}_E\boldsymbol{\Lambda}_P \end{pmatrix}\ , \tag{7.35}$$

it follows from Eq. (7.32):

$$F_{tr} - \Delta\bar{\xi}\,\boldsymbol{a}_{tr}^{T}\boldsymbol{\Lambda}\boldsymbol{a}_{tr} \approx 0\ . \tag{7.36}$$

The starting values are thus given by

$$\Delta\bar{\xi}^{(start)} = \frac{F_{tr}}{\boldsymbol{a}_{tr}^{T}\boldsymbol{\Lambda}\boldsymbol{a}_{tr}} \tag{7.37}$$

and

$$\begin{pmatrix} \Delta\hat{\bar{\boldsymbol{e}}}^{p} \\ \Delta\hat{\boldsymbol{k}}^{p} \end{pmatrix}^{(start)} = \Delta\bar{\xi}^{(start)}\boldsymbol{a}_{tr}\ , \tag{7.38}$$

respectively. These starting values, however, may only be evaluated if the yield surface is defined implicitely (i.e. as a pure function of the stress state), which is not the case for the exact Ilyushin yield surface. Thus, the approximate Ivanov yield surface is utilized again. For the Ivanov yield surface (Eq. (3.81)) the normal direction is expressed as

$$\begin{pmatrix} \partial F_2/\partial\hat{\boldsymbol{n}} \\ \partial F_2/\partial\hat{\boldsymbol{m}} \end{pmatrix} = \begin{pmatrix} 2F_t\mathbf{I}_3 & F_{tm}\mathbf{I}_3 \\ F_{tm}\mathbf{I}_3 & 2F_m\mathbf{I}_3 \end{pmatrix} \begin{pmatrix} \hat{\boldsymbol{n}} \\ \hat{\boldsymbol{m}} \end{pmatrix}\ , \tag{7.39}$$

with the matrix coefficients given by

$$\begin{aligned} F_t &= \frac{\partial F_2}{\partial Q_t} = 1 - \frac{1}{4}\frac{Q_m}{(Q_t + 0.48Q_m)} + \frac{1}{4}\frac{Q_tQ_m - Q_{tm}^2}{(Q_t + 0.48Q_m)^2}\ , \\ F_{tm} &= \frac{\partial F_2}{\partial Q_{tm}} = \frac{Q_{tm}}{\sqrt{Q_m^2/4 + Q_{tm}^2}} + \frac{1}{2}\frac{Q_{tm}}{(Q_t + 0.48Q_m)}\ , \\ F_m &= \frac{\partial F_2}{\partial Q_m} = \frac{1}{2} + \frac{1}{4}\frac{Q_m}{\sqrt{Q_m^2/4 + Q_{tm}^2}} - \frac{1}{4}\frac{Q_t}{(Q_t + 0.48Q_m)} + \frac{0.12(Q_tQ_m - Q_{tm}^2)}{(Q_t + 0.48Q_m)^2}\ . \end{aligned} \tag{7.40}$$

The sketched method for evaluating starting values can be viewed as a form of the backward Euler scheme, and for three-dimensional von Mises plasticity in fact it coincides with the (first step of the) "radial return mapping algorithm" [Crisfield, 1991]. With respect to the full section material model described here, test runs show that the starting values generated this way deliver approximations quite close to the final state.

Restrictions

All proposed return mapping schemes for the full section material model reveal that solutions may principally be obtained for any point of the yield surface. Use of the pure Newton/Raphson algorithm furthermore ensures a quadratic convergence rate near the solution (which is confirmed by the test runs), and, due to the application of accurate starting values only a few iteration steps are needed in general. This holds not only true for general points on the yield surface, but also for points of the boundary and for pure in-plane and pure bending conditions.

Regardless of the algorithm actually used, however, convergence problems arise for in-plane dominant loading conditions, when approaching the point $Q_t = 1$. This may partly be traced back to an ill-conditioning of the equations to be solved[12] (here an analytical derivation of the Jacobian matrix may become essential). However, as can be seen from Figure 7.4, at $Q_t = 1$ there is even a slope discontinuity and numerical solution algorithms working with derivatives (like a Newton/Raphson procedure) may simply not be able to treat such a case correctly — but also the fixpoint algorithm fails in obtaining valid solutions. The apparent discontinuity along the boundary (i.e. strong, but continuous changes of the normal directions), on the other hand, which is also shown in Figure 7.4, seems to engender no principal numerical difficulties, provided the evaluation points are not too close to the point of singularity. In any case, a detailed investigation of the actual convergence behaviour in terms of $\Delta\xi_t$, $\Delta\xi_{tm}$ and $\Delta\xi_m$ in the in-plane dominant region, but also along the boundary, should be performed. Furthermore, the problem of an appropriate treatment of the slope discontinuity remains to be solved.

---

[12] The parameters β and γ, introduced by Burgoyne and Brennan [1993b], which are used as internal parameters for the return mapping step, become almost parallel near $Q_t = 1$, even if the angles between these curves are quite different for the most part of the yield surface (see Figure 3.3).

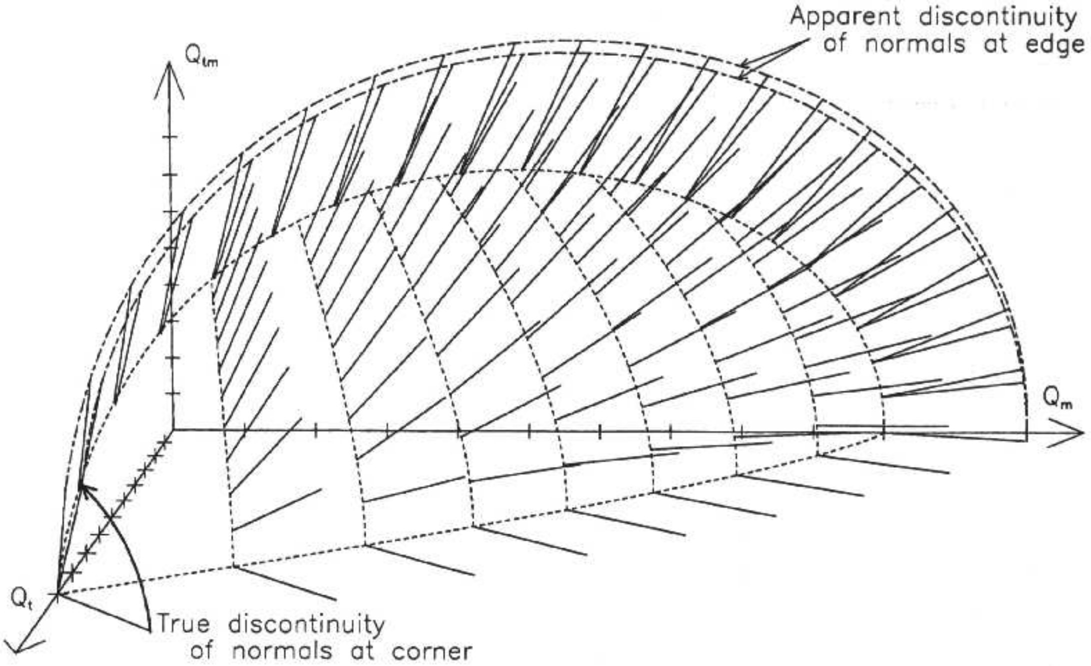

Figure 7.4: Three-dimensional view of the exact Ilyushin yield surface showing normals to the yield surface, discontinuity at one corner and "lip" at the edge (from [Burgoyne and Brennan, 1993b])

7.2.2 Determination of the Tangential Stiffness Matrix

The determination of the tangential stiffness matrix (which provides the contribution of the shell section to the global stiffness matrix) is required when an implicit time integration is used and the Newton/Raphson method is applied for solving the global equilibrium equations. A proper and accurate definition of the elastoplastic section stiffness is the most important factor for a rapid convergence behaviour of the overall equilibrium iterations [HKS, 1998c].

In the following the commonly used strategy for the definition of the tangential stiffness matrix within an elastoplastic material routine is presented (see e.g. [Simo et al., 1988; Crisfield, 1991; Simo and Kennedy, 1992; HKS, 1998a]. By performing an algorithmically consistent linearization of the nonlinear incremental equations (i.e. the backward Euler integration algorithm described above) the "consistent" – as opposed to the continuum – elastoplastic tangent matrix is obtained. This algorithmically consistent linearization, which may be performed in closed form, is essential for retaining the quadratic convergence rate inherent in the full Newton/Raphson procedure also for finite increments of elastoplastic deformations. For the limit of infinitesimally small increments, however, this matrix reduces to the continuum tangential matrix, which relies on the assumption that changes of the plastic strain increments are negligible within an individual increment.

The total differential of

$$\begin{pmatrix} \Delta\boldsymbol{n} \\ \Delta\boldsymbol{m} \end{pmatrix} = \begin{pmatrix} \mathbf{E} & \\ & \frac{4}{3}\mathbf{E} \end{pmatrix} \left[\begin{pmatrix} \Delta\bar{\boldsymbol{e}} \\ \Delta\boldsymbol{k} \end{pmatrix} - \Delta\bar{\xi} \begin{pmatrix} \partial F/\partial\boldsymbol{n} \\ \partial F/\partial\boldsymbol{m} \end{pmatrix} \right] \tag{7.41}$$

gives

$$\begin{pmatrix} d\boldsymbol{n} \\ d\boldsymbol{m} \end{pmatrix} = \mathbf{C}_e \left[\begin{pmatrix} d\bar{\boldsymbol{e}} \\ d\boldsymbol{k} \end{pmatrix} - d(\Delta\bar{\xi}) \begin{pmatrix} \partial F/\partial\boldsymbol{n} \\ \partial F/\partial\boldsymbol{m} \end{pmatrix} - \Delta\bar{\xi} \frac{\partial^2 F}{\partial(\boldsymbol{n},\boldsymbol{m})^2} \begin{pmatrix} d\boldsymbol{n} \\ d\boldsymbol{m} \end{pmatrix} \right] , \tag{7.42}$$

where the elastic stiffness matrix is abbreviated as

$$\mathbf{C}_e = \begin{pmatrix} \mathbf{E} & \\ & \frac{4}{3}\mathbf{E} \end{pmatrix} . \tag{7.43}$$

From Eq. (7.42) it follows that

$$\left[\mathbf{C}_e^{-1} + \Delta\bar{\xi} \frac{\partial^2 F}{\partial(\boldsymbol{n},\boldsymbol{m})^2} \right] \begin{pmatrix} d\boldsymbol{n} \\ d\boldsymbol{m} \end{pmatrix} = \begin{pmatrix} d\bar{\boldsymbol{e}} \\ d\boldsymbol{k} \end{pmatrix} - d(\Delta\bar{\xi}) \begin{pmatrix} \partial F/\partial\boldsymbol{n} \\ \partial F/\partial\boldsymbol{m} \end{pmatrix} \tag{7.44}$$

and

$$\begin{pmatrix} d\boldsymbol{n} \\ d\boldsymbol{m} \end{pmatrix} = \overline{\mathbf{C}}_e \left[\begin{pmatrix} d\bar{\boldsymbol{e}} \\ d\boldsymbol{k} \end{pmatrix} - d(\Delta\bar{\xi}) \begin{pmatrix} \partial F/\partial\boldsymbol{n} \\ \partial F/\partial\boldsymbol{m} \end{pmatrix} \right] , \tag{7.45}$$

respectively. The algorithmic elastic stiffness matrix, $\overline{\mathbf{C}}_e$, defined therein, is given by the expression

$$\overline{\mathbf{C}}_e = \left[\mathbf{C}_e^{-1} + \Delta\bar{\xi} \frac{\partial^2 F}{\partial(\boldsymbol{n},\boldsymbol{m})^2} \right]^{-1} . \tag{7.46}$$

For the determination of $d(\Delta\bar{\xi})$ the plastic consistency condition is used. To remain on the yield surface, the total differential of the yield function must be zero, i.e.

$$\begin{pmatrix} \partial F/\partial\boldsymbol{n} \\ \partial F/\partial\boldsymbol{m} \end{pmatrix}^T \begin{pmatrix} d\boldsymbol{n} \\ d\boldsymbol{m} \end{pmatrix} = 0 . \tag{7.47}$$

With Eq. (7.45) it follows that

$$\begin{pmatrix} \partial F/\partial \boldsymbol{n} \\ \partial F/\partial \boldsymbol{m} \end{pmatrix}^T \overline{\mathbf{C}}_e \begin{pmatrix} d\overline{\boldsymbol{e}} \\ d\boldsymbol{k} \end{pmatrix} = d(\Delta\overline{\xi}) \begin{pmatrix} \partial F/\partial \boldsymbol{n} \\ \partial F/\partial \boldsymbol{m} \end{pmatrix}^T \overline{\mathbf{C}}_e \begin{pmatrix} \partial F/\partial \boldsymbol{n} \\ \partial F/\partial \boldsymbol{m} \end{pmatrix} , \tag{7.48}$$

and

$$d(\Delta\overline{\xi}) = \frac{\begin{pmatrix} \partial F/\partial \boldsymbol{n} \\ \partial F/\partial \boldsymbol{m} \end{pmatrix}^T \overline{\mathbf{C}}_e \begin{pmatrix} d\overline{\boldsymbol{e}} \\ d\boldsymbol{k} \end{pmatrix}}{\begin{pmatrix} \partial F/\partial \boldsymbol{n} \\ \partial F/\partial \boldsymbol{m} \end{pmatrix}^T \overline{\mathbf{C}}_e \begin{pmatrix} \partial F/\partial \boldsymbol{n} \\ \partial F/\partial \boldsymbol{m} \end{pmatrix}} , \tag{7.49}$$

respectively. Inserting Eq. (7.49) into Eq. (7.45) finally delivers the tangential elastoplastic material law

$$\begin{pmatrix} d\boldsymbol{n} \\ d\boldsymbol{m} \end{pmatrix} = \mathbf{C}_{tc} \begin{pmatrix} d\overline{\boldsymbol{e}} \\ d\boldsymbol{k} \end{pmatrix} , \tag{7.50}$$

with the consistent tangential stiffness matrix being given by

$$\mathbf{C}_{tc} = \overline{\mathbf{C}}_e - \frac{\overline{\mathbf{C}}_e \begin{pmatrix} \partial F/\partial \boldsymbol{n} \\ \partial F/\partial \boldsymbol{m} \end{pmatrix} \begin{pmatrix} \partial F/\partial \boldsymbol{n} \\ \partial F/\partial \boldsymbol{m} \end{pmatrix}^T \overline{\mathbf{C}}_e}{\begin{pmatrix} \partial F/\partial \boldsymbol{n} \\ \partial F/\partial \boldsymbol{m} \end{pmatrix}^T \overline{\mathbf{C}}_e \begin{pmatrix} \partial F/\partial \boldsymbol{n} \\ \partial F/\partial \boldsymbol{m} \end{pmatrix}} . \tag{7.51}$$

It is obvious that this definition is not affected by the “length” of the gradient of the yield surface. Therefore, when considering the normality rule, an alternative statement for the algorithmic elastoplastic tangential matrix is given by

$$\mathbf{C}_{tc} = \overline{\mathbf{C}}_e - \frac{\overline{\mathbf{C}}_e \begin{pmatrix} \Delta\overline{\boldsymbol{e}}^p \\ \Delta\boldsymbol{k}^p \end{pmatrix} \begin{pmatrix} \Delta\overline{\boldsymbol{e}}^p \\ \Delta\boldsymbol{k}^p \end{pmatrix}^T \overline{\mathbf{C}}_e}{\begin{pmatrix} \Delta\overline{\boldsymbol{e}}^p \\ \Delta\boldsymbol{k}^p \end{pmatrix}^T \overline{\mathbf{C}}_e \begin{pmatrix} \Delta\overline{\boldsymbol{e}}^p \\ \Delta\boldsymbol{k}^p \end{pmatrix}} . \tag{7.52}$$

This definition may directly be evaluated once the plastic strain increments are obtained from the return mapping step — regardless whether the yield function is given in implicit or in parametric form.

In contrast to the algorithmic or consistent stiffness matrix, which accounts for the fact that finite instead of infinitesimal elastoplastic increments are considered, the continuum tangential stiffness matrix is obtained from Eq. (7.46) by omitting the second derivative of the yield function, i.e. omitting the changes of the gradient of the yield function within the increment. From the derivation procedure sketched above it follows, therefore, that the structure of Eq. (7.51) and (7.52), respectively, remains unchanged — the algorithmic elastic stiffness matrix $\overline{\mathbf{C}}_e$, however, is simply replaced by the elastic stiffness matrix $\mathbf{C}_e$, given by Eq. (7.43).

Remarks

- For the evaluation of the algorithmic elastic stiffness matrix $\overline{\mathbf{C}}_e$ the second derivatives of the exact Ilyushin yield surface are needed. An analytical derivation of $\partial^2 F/\partial(\boldsymbol{n},\boldsymbol{m})^2$ is, however, still lacking. For the current implementation, therefore, a locally quadratic approximation for the yield surface (in $(\boldsymbol{n},\boldsymbol{m})$-space) is assumed, leading to

$$\overline{\mathbf{C}}_e \approx \left[\mathbf{C}_e^{-1} + \begin{pmatrix} 2\Delta\xi_t\mathbf{P} & \Delta\xi_{tm}\mathbf{P} \\ \Delta\xi_{tm}\mathbf{P} & 2\Delta\xi_m\mathbf{P} \end{pmatrix}\right]^{-1} . \tag{7.53}$$

- A drawback of the derivation of the tangential stiffness matrix for a full section material routine is that (regardless if the consistent or the continuum tangential matrix is concerned) the off-diagonal submatrices are in general not symmetrical (although the stiffness matrix itself is). For example, for the continuum tangential stiffness matrix

$$\mathbf{C}_t = \begin{pmatrix} \mathbf{C}^* & \mathbf{B}^* \\ (\mathbf{B}^*)^T & \mathbf{D}^* \end{pmatrix} , \tag{7.54}$$

the submatrices are defined as

$$\begin{aligned} \mathbf{B}^* &= -\frac{4}{3R}\,\mathbf{E}\,\frac{\partial F}{\partial \boldsymbol{n}}\left(\frac{\partial F}{\partial \boldsymbol{m}}\right)^T\mathbf{E}\,, \\ \mathbf{C}^* &= \mathbf{E} - \frac{1}{R}\,\mathbf{E}\,\frac{\partial F}{\partial \boldsymbol{n}}\left(\frac{\partial F}{\partial \boldsymbol{n}}\right)^T\mathbf{E}\,, \\ \mathbf{D}^* &= \frac{4}{3}\mathbf{E} - \frac{16}{9R}\,\mathbf{E}\,\frac{\partial F}{\partial \boldsymbol{m}}\left(\frac{\partial F}{\partial \boldsymbol{m}}\right)^T\mathbf{E}\,, \end{aligned} \tag{7.55}$$

with the scalar factor R given as

$$R = \left(\frac{\partial F}{\partial \boldsymbol{n}}\right)^T\mathbf{E}\,\frac{\partial F}{\partial \boldsymbol{n}} + \frac{4}{3}\left(\frac{\partial F}{\partial \boldsymbol{m}}\right)^T\mathbf{E}\,\frac{\partial F}{\partial \boldsymbol{m}}\,. \tag{7.56}$$

It becomes obvious from Eq. (7.55) that the submatrix $\mathbf{B}^*$ is symmetrical only if

$$\frac{\partial F}{\partial \boldsymbol{n}} = C \frac{\partial F}{\partial \boldsymbol{m}} \,, \tag{7.57}$$

which would occur at the boundary of the yield surface (but there the matrix $\mathbf{B}^*$ should even become zero, see Appendix B.3). Burgoyne and Brennan [1993a] have argued that this unsymmetry comes from incompatible assumptions regarding the relative magnitudes of the elastic and plastic strain increment components.[13] Therefore, the authors proposed a different strategy for determining the tangential stiffness matrix, which is shown to deliver results which are compatible with that of a multilayer analysis. The main deficiency of their revised derivation (which is given in Appendix B.3), however, is that only the continuum tangential material matrix may be obtained in closed-form — for a generalization to determine the consistent tangential material matrix one must resort to a numerical integration procedure.

7.3 Examples

For testing the material routine several single element tests were performed, the results of which are discussed in the next section (section 7.3.1). Results for the numerical simulation of the (bending dominated) collapse behaviour of a simply supported plate under uniform transversal loading conditions (where analytical upper and lower bounds for the limit load are also available) are presented afterwards (section 7.3.2). For all these examples the three-dimensional return mapping algorithm (in terms of $\Delta\xi_i$) was applied. In section 7.3.3, finally, results of a crushing simulation of an axially compressed square tube are shown. In order to obtain valid solutions for this numerically sensitive problem (which, for an initially straight tube, is almost exclusively confined to inplane loading conditions), the numerically more robust six-dimensional Newton/Raphson based return mapping algorithm (for the solution of the system of equations $\boldsymbol{g}_1(\Delta\hat{\boldsymbol{e}}^p, \Delta\hat{\boldsymbol{k}}^p)$) was applied.

For all examples included here the four noded shell elements S4R provided by ABAQUS/Standard with reduced integration and hourglass control were used, which allow for finite membrane strains and thickness changes. Because the S4R elements are, however, shear flexible shells, an (elastic) transverse shear stiffness had also to be defined.[14] Values for this, but also for the hourglass stiffness of the elements, must, therefore, be provided explicitely (see [HKS, 1998c]).

---

[13] For a full section material routine an infinitesimal "movement" in stress resultant space in general does not imply that changes in the plastic strain resultants are of the same order of magnitude, i.e. such changes will in general not be small (for details see [Burgoyne and Brennan, 1993a]).

7.3.1 Single Element Tests

The (displacement driven) single element load cases presented in the following, are:

1. pure inplane loading ($Q_t = 1$ ($P_\kappa = 0$)),
2. pure bending ($Q_m = 1$ ($P_\varepsilon = 0$)),
3. loading at general points at the boundary of the yield surface ($\gamma = 0$, β between 0.39 and 0.45),
4. loading at general points away from the boundary of the yield surface (β between -0.42 and -0.53, γ between 0.005 and 0.35).

The input data as well as the boundary conditions applied for each load case are summarized in Table 7.3. Maximum time increments are prescribed, leading to a total number of 20 (load case 1), 100 (load cases 2 and 3) and 200 (load case 4) equally spaced increments for the individual test examples. Figures 7.5 to 7.8 show the internal section force and moment progressions evaluated with the user subroutine UGENS and comparisons with results being based on a numerical thickness integration.

The approximative character of the full section material routine, where only for pure inplane loading conditions (Figure 7.5) the results of the numerical thickness integration are met, becomes obvious from the numerical results. Uniaxial bending (Figure 7.6) is characterized by neglecting the spreading of the plastic zone over the thickness, i.e. the material behaves elastic up to the point where the moment capacity of the shell section is reached. The numerical thickness integration, however, reveals the gradual stiffness reduction of the shell section due to fibre yield. Similar differences for the section force and moment progressions owing to the (approximative) analytical and the numerical thickness integration can also be seen in Figures 7.7 and 7.8 for load cases 3 and 4, i.e. “boundary loading” and general loading conditions.

---

[14] In ABAQUS/Standard the transverse shear strains of the shear flexible shells are always treated as linear elastic and cannot be used or updated within the user subroutine.

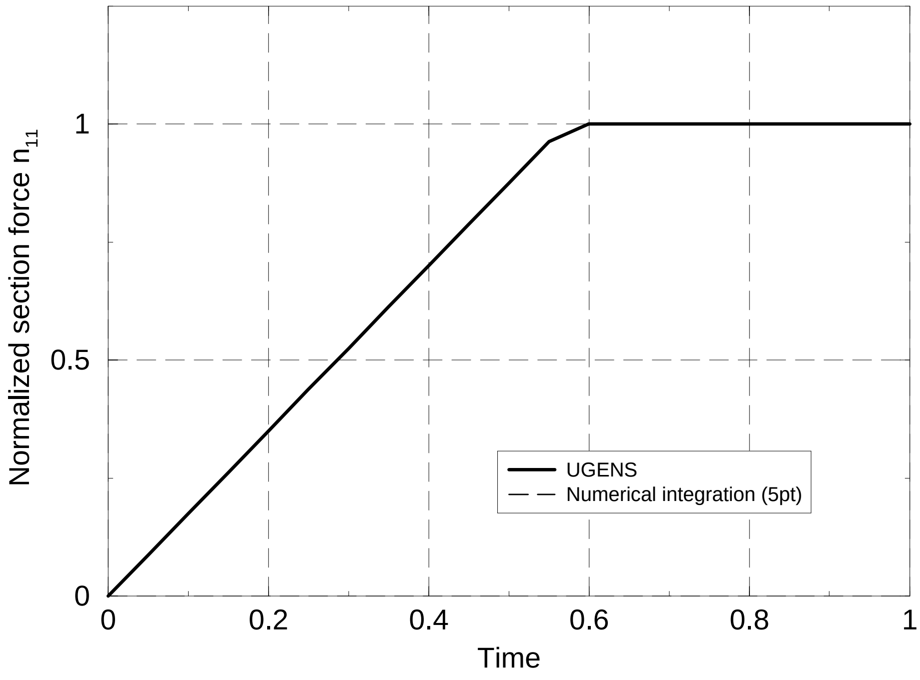

Figure 7.5: Single element test: uniaxial tension

Concerning the number of iteration steps for the return mapping a maximum of two to three iterations is needed in general. The only exception is the first elastoplastic increment of load case 4, where 5 iteration steps are required to return back onto the yield surface. Some CPU-time reductions (of up to 20%) owing to the use of the full section material routine are also observed.[15]

7.3.2 Uniformly Loaded, Simply Supported Plate

A simply supported plate, loaded by a uniform transversal load q is considered next. The plate, which is discretized with 1224 four noded elements (see Figure 7.10), is assumed to have a side length a of 100 mm and a thickness h of 3 mm. The material data taken for the computations are: Young's modulus $E = 210\ 000\ \text{N/mm}^2$, yield stress $\sigma_y = 600\ \text{N/mm}^2$, Poisson's ratio $\nu = 0.3$. Geometrically linear as well as nonlinear analyses were performed. Results of the computations are shown in Figures 7.9 to 7.11.

---

[15] The current implementation, however, is intended rather for testing purposes than for providing a computationally efficient code. When "tuning" the source code appropriately, therefore, further efficiency improvements can be expected.

Table 7.3: Single element tests: input data, boundary conditions (applied as (linear) ramp functions between $t = 0$ and $t = 1$)

Input Data		
Young's modulus: 210 000 N/mm^2		
Poisson's ratio	:	0.3
Yield stress	:	600 N/mm^2
Side length l	:	100 mm
Shell thickness	:	7 mm

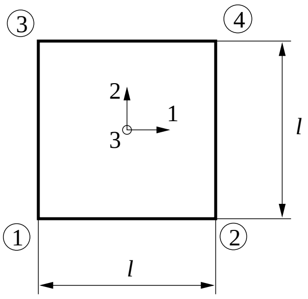

Magnitude of the prescribed boundary conditions (u_i ... displacement in i-direction [mm], ϕ_i ... rotation about i-axis [rad])									
Uniaxial tension					Uniaxial bending				
Node	1	2	3	4	Node	1	2	3	4
u_1	0	0.5	0	0.5	u_1	0	—	—	—
u_2	0	0	—	—	u_2	0	—	0	—
u_3	0	—	—	—	u_3	0	—	—	—
ϕ_1	0	—	—	—	ϕ_1	0	—	—	—
ϕ_2	0	—	—	—	ϕ_2	0	0.5	0	0.5
"Boundary" loading					General loading				
Node	1	2	3	4	Node	1	2	3	4
u_1	0	0.5	0	0.5	u_1	0	1.0	0	1.0
u_2	0	—	—	—	u_2	0	0	—	0.6
u_3	0	—	—	—	u_3	0	—	—	—
ϕ_1	0	—	—	—	ϕ_1	0	—	—	0.3
ϕ_2	0	0.1	0	0.1	ϕ_2	0	0.2	0	0.2

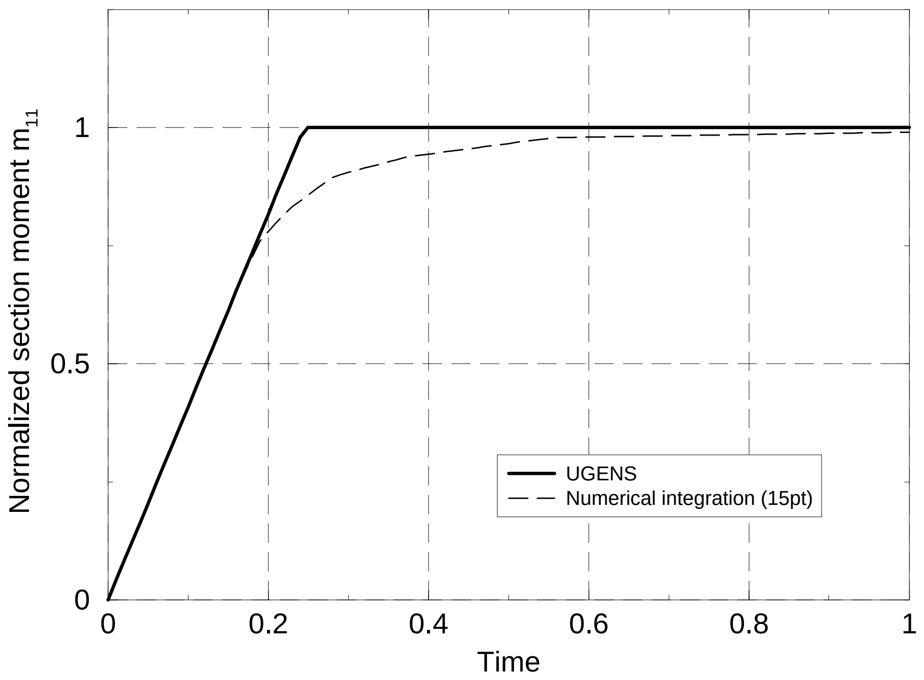

Figure 7.6: Single element test: uniaxial bending

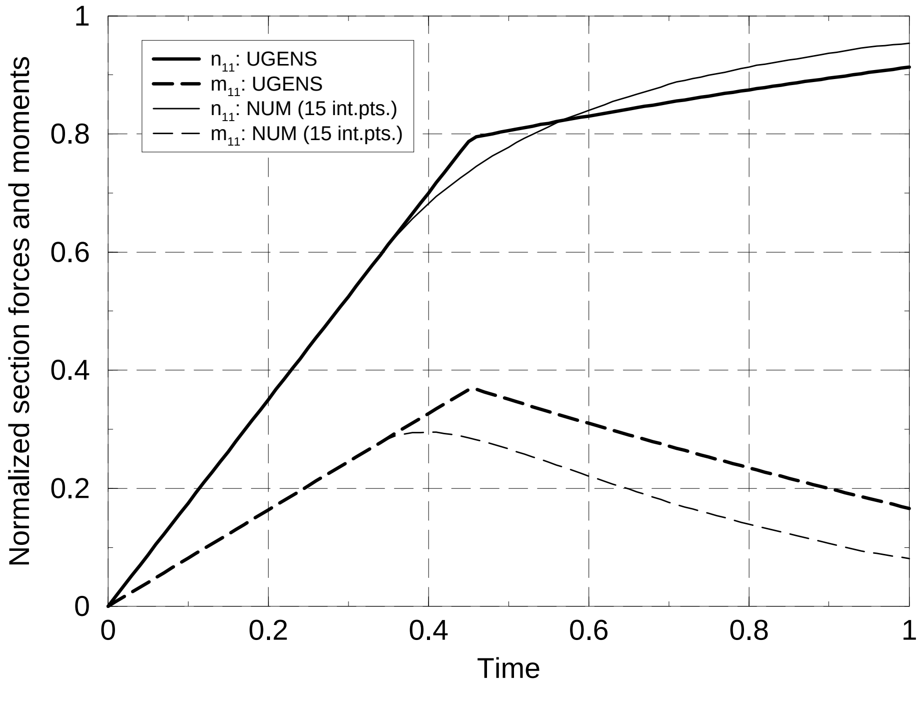

Figure 7.7: Single element test: general "boundary loading"

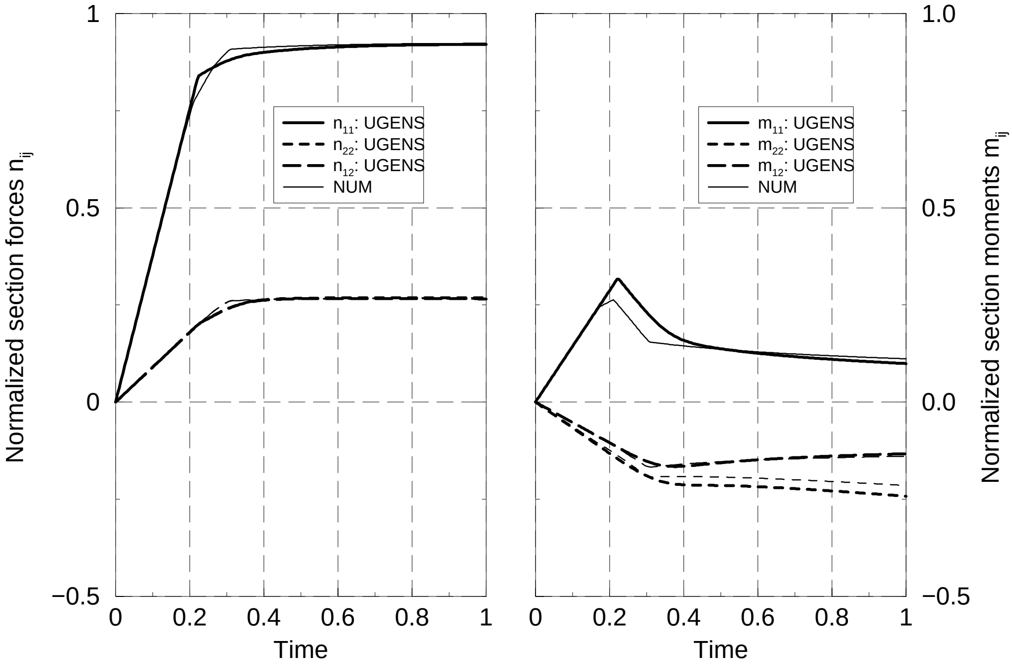

Figure 7.8: Single element test: general loading conditions

The uniformly loaded plate is a typical example for a (bending dominated) limit analysis problem, where approximate solutions for the upper and lower bounds of the critical collapse load are available. The corresponding values included in Figure 7.9 are taken from [Chen and Han, 1988].

It can be seen from the transversal load versus central deflection curves presented in Figure 7.9 that for geometrically linear analysis the application of the full section material routine leads to a markedly earlier approach to the elementary upper bound solution than the results based on a numerical thickness integration. For larger deflections, however, a close correspondence of these curves can also be observed. With respect to the position of the generalized stress points on the exact Ilyushin yield surface, these are for geometrically linear analysis confined to the point $Q_t = 0$, $Q_{tm} = 0$, $Q_m = 1$, i.e. no membrane effects are activated. For geometrically nonlinear analysis (and all boundary nodes totally constrained with respect to their displacement degrees of freedom), however, in-plane tensile forces are activated immediately. These membrane effects are essentially responsible that a much stiffer system response is observed in this case. Again, the results for the user subroutine UGENS reveal a stiffer force versus displacement behaviour than the results obtained by numerical thickness integration (which may also be traced back to neglecting fibre-yield within the full section material routine). With ongoing plastic deformations, however, some agreement between the simulation curves becomes visible again.

With respect to the kinematic mechanism underlying the analytical upper bound solution, a pyramidal mode of deformation, with plastic hinge lines developing along the diagonals of the plate, is assumed. The progression of the plastic zone, shown in Figure 7.10 for geometrically linear analysis, also shows this formation of plastic hinge lines very clearly. A larger spreading of the plastic zones (again being oriented along the diagonals of the square plate) is evident for the geometrically nonlinear results (Figure 7.11). In both cases, first yielding in the corner regions is caused by large twisting moments acting there.

Concerning the convergence behaviour of the return mapping step for these examples one to three iteration steps are needed in general. The CPU-time reductions due to the use of the full section material routine are about 33% for geometrically linear analysis and 22% for the geometrically nonlinear collapse simulation. Because the chosen number of integration points used for the numerical thickness integration is rather high (15 integration points were used to obtain a high resolution of fibre-yielding), however, the numerical efficiency improvements will (at least with the current implementation of the user subroutine) be less pronounced in practice.

7.3.3 Axial Crushing of a Square Tube

As a final example the large deformation plastic collapse behaviour of an axially compressed square tube is considered. Because for an initially straight column, however, the (generalized) internal stress state during axial compression is essentially restricted to inplane-loading (which, for the full section material routine, is critical from the numerical point of view, see above), with major bending contributions only developing with the ongoing crushing process, this example is a serious test for the proposed material routine.

Tube geometry and material behaviour are given by: side length $c = 38.6$ mm, wall thickness $h = 1.4$ mm, yield stress $\sigma_y = 300$ N/mm^2, Young's modulus $E = 210\,000$ N/mm^2, Poisson's ratio $\nu = 0.3$. Because only the formation of the first fold of a progressive crushing process is considered (without taking into account internal contact), a tube length of 60 mm is assumed for the simulations. The lower end of the tube is totally fixed. For the upper end a maximal axial displacement (10 mm) is prescribed, ramped linearly during the step — all other degrees of freedom of these boundary nodes are constrained to be zero. Due to the symmetry of both the geometry and the loading and boundary conditions

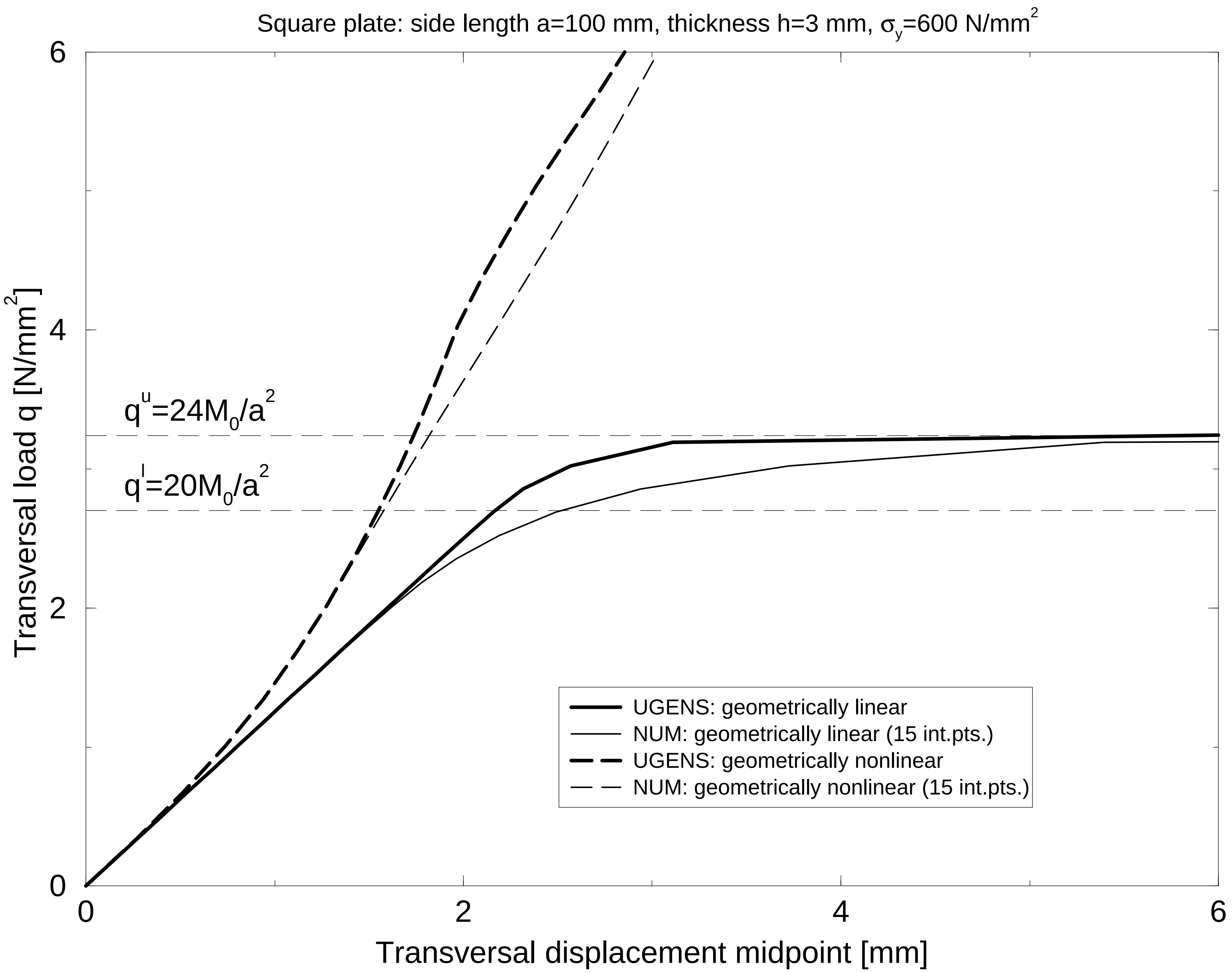

Figure 7.9: Uniformly loaded, simply supported plate: comparison of load versus lateral deflection curves

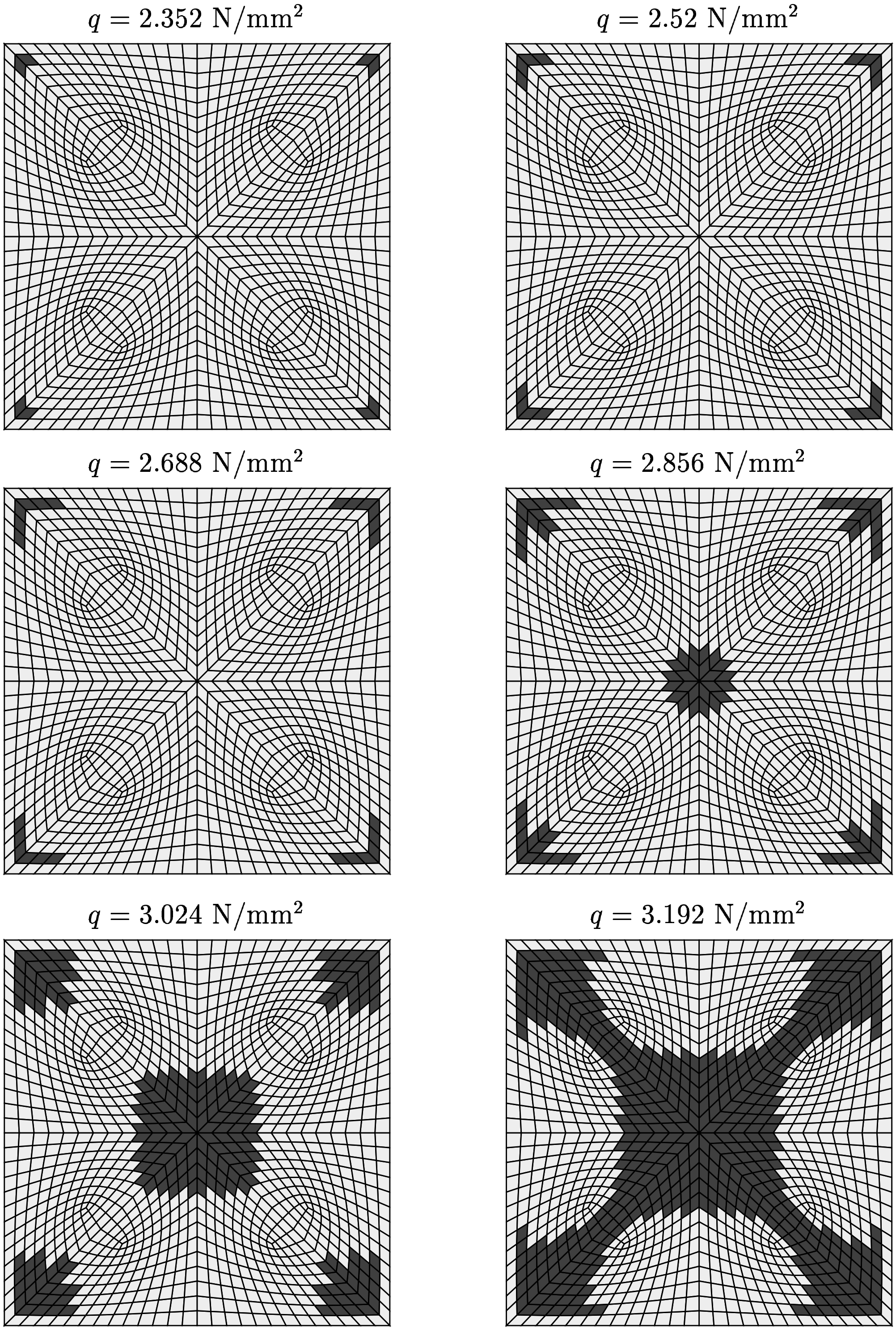

$q = 2.352$ N/mm^2

$q = 2.52$ N/mm^2

$q = 2.688$ N/mm^2

$q = 2.856$ N/mm^2

$q = 3.024$ N/mm^2

$q = 3.192$ N/mm^2

Figure 7.10: Uniformly loaded, simply supported plate — geometrically linear: progression of the plastic zone (light ... elastic, dark ... elasto-plastic material state)

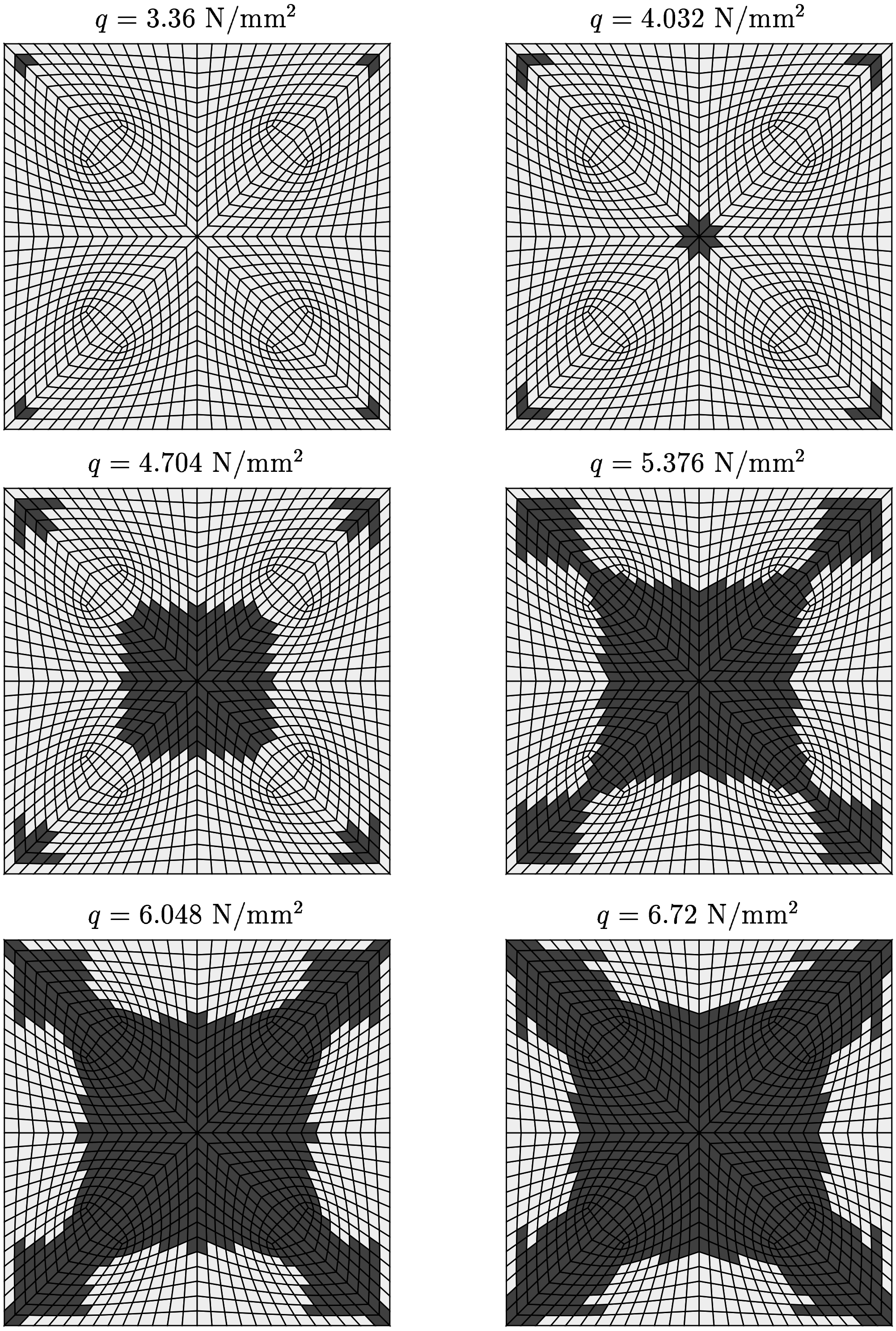

$q = 3.36$ N/mm^2

$q = 4.032$ N/mm^2

$q = 4.704$ N/mm^2

$q = 5.376$ N/mm^2

$q = 6.048$ N/mm^2

$q = 6.72$ N/mm^2

Figure 7.11: Uniformly loaded, simply supported plate — geometrically nonlinear: progression of the plastic zone (light … elastic, dark … elasto-plastic material state)

only one quarter of the tube is modelled (with 180 equally spaced elements). Buckling is triggered by initial imperfections. Initial and final FE geometry as well as the resulting axial load versus compression curves (obtained with the full section material routine and with a comparable numerical thickness integration material model) are shown in Figure 7.12.

It can be seen from the numerical results that the errors made by applying the full section material model remain rather small — only a slight overestimation is present compared to the results based on a numerical thickness integration. The reason for this good agreement may certainly be traced back to the fact that the collapse problem investigated here is essentially restricted to plastic deformations (leading to the formation of plastic hinge lines and a kinematic collapse mechanism, respectively). These dominant plastic deformations, however, are taken into account by the full section material model — confirming the initial statement that the application of such an approximative material description is appropriate for this type of problems.

With respect to the convergence behaviour of the return mapping algorithm (for this example the six-dimensional form in terms of $\Delta\hat{\boldsymbol{e}}^p$ and $\Delta\hat{\boldsymbol{k}}^p$ in combination with a Newton/Raphson integration scheme was applied), up to a maximum number of 7 iteration steps were required for in-plane dominant loading conditions, but valid solutions could always be obtained. Concerning the global convergence behaviour, however, some problems arose for very small imperfections, where the postbuckling range could not be reached in practice. For the solution included in Figure 7.12 a relatively large shift of 0.7 mm outside and inside from the perfect tube geometry was, therefore, applied on one circumferential row of nodes to initiate the progressive buckling mode (as can be seen from the FE models included in Figure 7.12). Besides this, the global convergence rate of the analysis must also be stated to be markedly below that of the numerical thickness integration material model (even leading to an increase in computing time). This, however, indicates that refinements with respect to the definition of the tangential stiffness matrix for the full section material routine should be considered. Furthermore, the principal applicability of a plastic limit yield criterion for plastic instability phenomena should also be investigated in more detail. The "parallel occurrence" of the singularity of the global stiffness matrix in combination with the full section material model (which also provides a singular stiffness contribution for the integration point under consideration) might be a major cause of numerical difficulties for this type of problems. Because collapse problems, however, are in general more conveniently solved with explicit codes (where neither equilibrium iterations are performed nor a tangential stiffness matrix has to be provided), the latter problems could possibly be

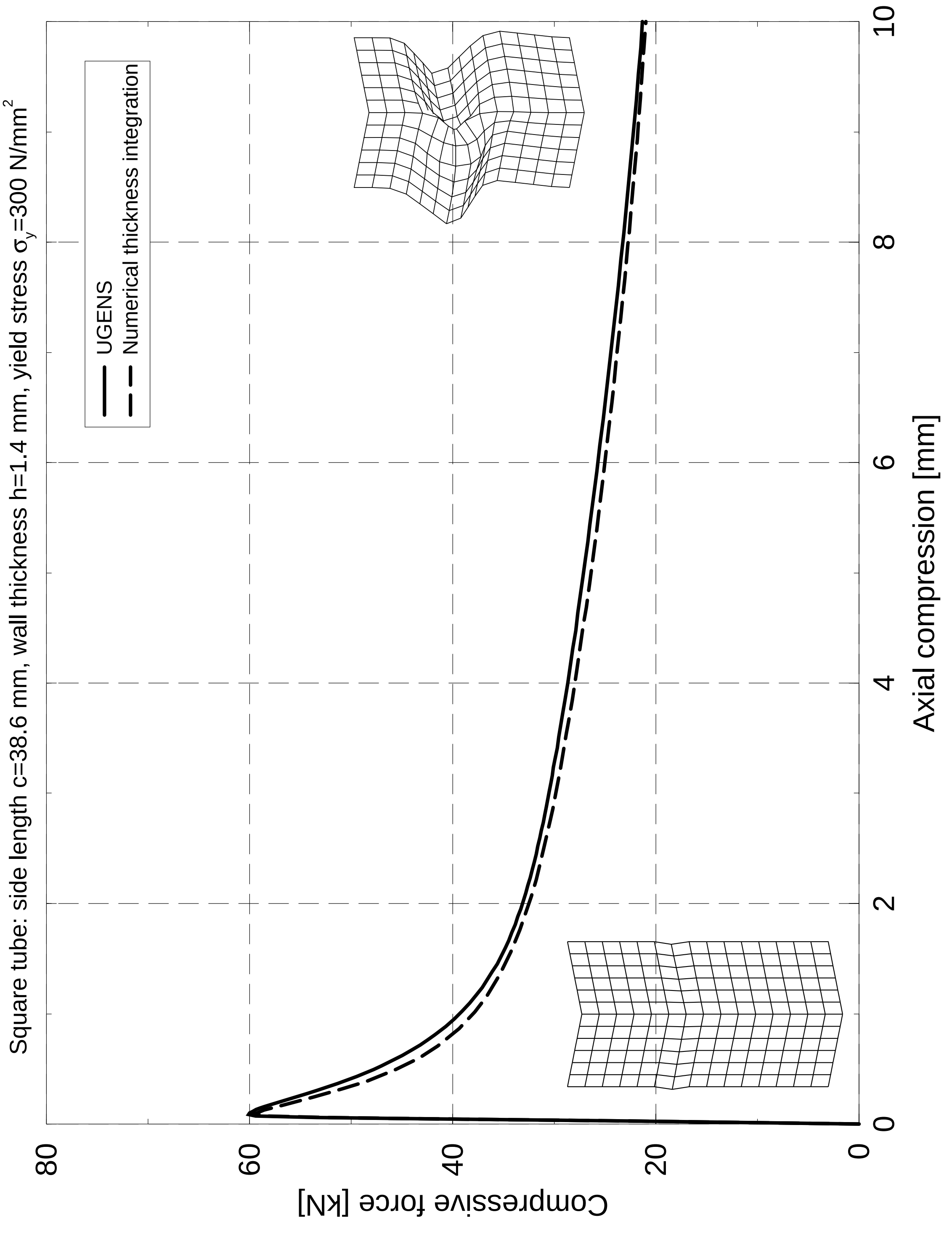

Figure 7.12: Axially compressed square tube: comparison of load versus compression curves, including the initial FE model and the deformed state after an axial compression of 10 mm

avoided if the proposed full section material routine is used in combination with an explicit time integration scheme.

7.4 Summary, Concluding Remarks

A full section material model, which is based on the exact Ilyushin yield criterion, was presented in this chapter. Many features considered as being essential for the definition of both a numerically stable and a computationally efficient formulation have been proposed and the main difficulties concerned with the implementation have been discussed. The basic requirements, pointed out for a successful implementation of the material routine (which is based on a predictor/corrector scheme), are:

- The application of a backward Euler integration scheme for the return mapping step is a natural choice because of the specific representation of the yield surface.
- The formulation of the subroutine in terms of deviatoric (i.e. transformed) quantities provides a computationally efficient, but (in parts) also an analytically tractable algorithmic structure.
- Several possible formulations for performing the return mapping step have been proposed. Experience reveals that
  - the six-dimensional formulations (in terms of $\Delta\overline{\hat{\boldsymbol{e}}}^p$ and $\Delta\hat{\boldsymbol{k}}^p$) provide rather robust algorithms, which are especially useful for development and testing purposes (the fixpoint algorithm, however, does not seem to offer advantages if compared to the Newton/Raphson solution procedure). For these formulations the numerical difficulties may essentially be confined to the nonlinear behaviour of the yield surface.
  - For the definition of a numerically efficient algorithm a formulation with (a minimum number of) three independent parameters should be applied. The formulation in terms of the (newly introduced) integral parameters $\Delta\xi_t$, $\Delta\xi_{tm}$ and $\Delta\xi_m$, but also the proposed algorithmic structure for the return mapping step (the formulation of which is closely related to standard plasticity algorithms) both seem to be appropriate for obtaining this goal. In contrast to the six-dimensional formulation, however, restrictions, which are imposed onto the

parameters, are not fulfilled identically. These must, therefore, also be taken into account if a general numerical solution scheme is applied.

- The fact that the exact Ilyushin yield criterion may only be stated in parametric form, renders it difficult to efficiently perform the initial check for yielding, but also to obtain accurate starting values for the return mapping algorithm. Here, however, the Ivanov yield criterion has proved to be applicable.
- Starting values quite close to the actual state are obtained with the proposed strategy, being essential for a good convergence behaviour of the applied numerical solution procedures.
- Use of the algorithmically consistent tangent stiffness matrix $\mathbf{C}_{tc}$ is a basic requirement for a rapid convergence behaviour of the overall equilibrium equations. A proper definition for $\mathbf{C}_{tc}$, being applicable for use with the exact Ilyushin yield surface, has also been proposed.

The test examples shown in the last part of this chapter confirm that the full section material routine is applicable for general finite element analyses, having the potential of markedly speeding up elastoplastic FE calculations (if compared to analyses which rely on a numerical thickness integration). This could clearly be shown for bending dominated problems, where maximal CPU-time reductions of more than 30% have been obtained. For in-plane dominated analyses, however, the convergence behaviour of the return mapping algorithm becomes markedly lower (mainly caused by the stronger nonlinearity of the yield surface). Hence, even for an "optimized" implementation, minor computational improvements must be expected for such load cases. In addition, the problem of an appropriate treatment of the slope discontinuity at the point $Q_t = 1$ remains to be solved. This is, however, expected to be one of the essential tasks for providing a practically useable implementation, delivering distinct CPU-time savings for all possible loading conditions.

Chapter 8

Summary and Conclusions

The subject of the present work is to provide contributions towards an efficient numerical analysis of the collapse process of thin-walled structures. Starting from a survey on the state of research the theoretical foundations underlying the proposed algorithms are summarized afterwards. Here, besides large deformation continuum mechanics and plastic extremum and bounding principles, special emphasis is put on the derivation and description of the exact Ilyushin yield surface, providing an important ingredient for the proposed algorithms. This plastic limit yield criterion (which is based on perfectly plastic material behaviour obeying the von Mises yield condition) provides a number of advantageous features, rendering the definition of both accurate and numerically efficient simulation tools for plastic collapse analysis possible. For example, interaction effects between the different stress resultant terms in shell structures are accounted for and the power of internal forces of a (rigid-perfectly plastic) Kirchhoff shell section may even be obtained in an exact way. Furthermore, due to the assumptions underlying the derivation of the yield surface it is fully consistent with plastic extremum and bounding principles, where it may in particular be utilized in combination with kinematics-oriented theorems, e.g. the Markov theorem or the upper bound theorem of limit analysis.

To gain more insight into the principles of the crushing phenomenon in a next step experimental results are presented and simplified analytically based collapse mechanisms proposed in the literature, which describe the quasistatic progressive buckling process of circular and multicornered prismatic profiles, are investigated in some detail. Comparisons with experiments and FE computations show that the ability of such mechanisms to describe the force-deflection characteristics of the whole deformation process is rather limited, even if the underlying kinematics seem to be well suited for the description of actual crushing processes. When the requirement for obtaining analytical solutions is dropped, several refinements and generalizations are possible. These essentially include a refined description of the constitutive behaviour (e.g. by application of the exact Ilyushin yield surface), and a more generalized kinematic description of the deformation mechanisms (e.g. an "FE-like" discretization of the geometry and the deformation field, respectively).

Starting from these considerations a computational model based on the upper bound theorem of limit analysis ("sequential limit analysis method") is presented in chapter 6, which allows to study the large deformation crushing behaviour of general axisymmetric shell structures. The kinematic description is chosen such that continuous and discontinuous plastic deformations can be considered. The large deformation process is described in an incremental manner, where each increment is solved by mathematical programming techniques. Due to the application of the exact Ilyushin yield surface the power of internal forces can be taken into account very accurately. It is also shown that with the proposed method frictionless internal contact can be accounted for easily. Furthermore, most of the analytically based kinematic mechanisms proposed in the literature for the concertina mode buckling of cylindrical shells can be regarded as special cases, thus allowing to study the effects of different simplifications used in these models. Several examples confirming the generality and suitability of the method for simplified plastic collapse analysis are included, too.

As a final possible tool for simplified (however, general) finite element based collapse and limit load analysis of shell structures a full section material model, which is based on the exact Ilyushin yield criterion, is investigated in chapter 7. Many features considered as being essential for the definition of both a numerically stable and a computationally efficient formulation are proposed and the main difficulties concerned with the implementation are discussed. This not only includes the reformulation of standard plasticity algorithms (being required, because the exact Ilyushin yield criterion may only be stated in parametric form), but also an appropriate definition and choice of internal parameters used for the local stress update. The test examples confirm that the proposed full section material routine in principle is applicable for general finite element analyses and even has the potential of speeding up FE based limit and collapse analyses. This holds especially true for bending dominated problems, where marked improvements could be obtained. For in-plane dominated loading conditions, but also for elastoplastic buckling phenomena, however, such improvements are not pronounced and further investigations to refine the implemented algorithms are required.

Appendices

Appendix A

Folding Mechanisms — Details

A.1 Axial Crushing of Multicorner Columns

This chapter summarizes the essential relations required for describing the axial crushing process of multicornered prismatic columns (energy rate and energy terms, D_i and W_i, axial compression kinematics), as outlined in section 5.3. The input variables characterizing the corner element (side length C, wall thickness h, opening angle $\pi - 2\psi_0$), are shown in Figure A.1. Initially unknown parameters, which are determined by minimization of the mean crushing force, are the folding length H, the switching angle $\overline{\alpha}$, and a small bending radius b, used for describing the cylindrical and toroidal parts of the mechanism. The rotation angle α is used as the process parameter, ranging from 0 to $\alpha_f = \pi/2$. For details of the derivation and the kinematic description the reader is referred to the literature (e.g. [Abramowicz and Wierzbicki, 1989] or the diploma theses [Wintschnig, 1996; Willminger, 1999]).

Extension in the toroidal surface

$$D_1 = 16 M_0 \frac{bH}{h} \cos\alpha \int_0^{\beta(\alpha)} \frac{1}{\sqrt{\tan^2\psi_0 + \cos^2\phi}} d\phi \, \dot{\alpha} \ , \tag{A.1}$$

where ϕ is the integration variable and $\beta(\alpha)$ is given by

$$\beta(\alpha) = \arctan\left(\frac{\tan\alpha}{\sin\psi_0}\right) \ ; \tag{A.2}$$

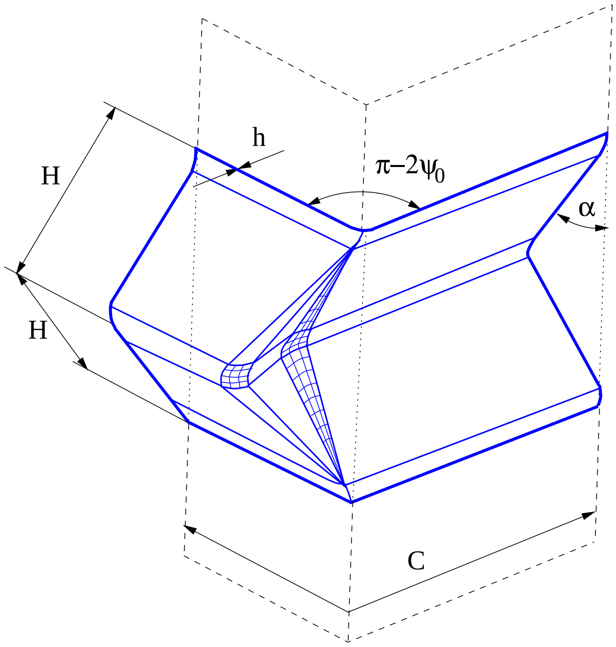

Figure A.1: Generalized folding mechanism for multicorner columns: variables definition

$$W_1 = 16 M_0 \frac{bH}{h} I_1(\psi_0, \overline{\alpha}) \ , \tag{A.3}$$

with

$$I_1(\psi_0, \overline{\alpha}) = \int_0^{\overline{\alpha}} \cos\alpha \left[\int_0^{\beta(\alpha)} \frac{1}{\sqrt{\tan^2\psi_0 + \cos^2\phi}} d\phi \right] d\alpha \ . \tag{A.4}$$

Bending along horizontal hinge lines

$$D_2 + D_5 = 4 M_0 C \dot{\alpha} \ ; \tag{A.5}$$

$$W_2 + W_5 = 4 M_0 C \alpha_f \ . \tag{A.6}$$

The derivation of these relations is based on the assumption that clamped boundary conditions act at the upper and lower end. Other types of boundary conditions, however, may simply be realized by appropriately changing the numerical coefficients.

Bending along inclined travelling hinge lines

$$D_3 = 4M_0 \frac{H^2}{b} \cot^2 \psi_0 \cos\alpha \sqrt{\tan^2 \psi_0 + \sin^2 \alpha}\ \dot{\alpha}\ ; \tag{A.7}$$

$$W_3 = 4M_0 \frac{H^2}{b} I_3(\psi_0, \overline{\alpha})\ , \tag{A.8}$$

with

$$I_3(\psi_0, \overline{\alpha}) = \cot^2 \psi_0 \int_0^{\overline{\alpha}} \cos\alpha \sqrt{\tan^2 \psi_0 + \sin^2 \alpha}\ d\alpha\ . \tag{A.9}$$

Remark: In [Abramowicz and Wierzbicki, 1989] the resulting equations for D_3 and I_3, respectively, are stated with a linear dependence with respect to $\cot\psi_0$. A rederivation of the kinematics of the crushing process, which was performed by Willminger [1999], however, indicates that a quadratic dependence, as included above, should be used instead. Because all other kinematic quantities used for the derivation of expressions (A.7) and (A.9) coincide, it is plausible that the difference may just be traced back to some printing error.

Stretching in the conical surfaces

$$D_4 = 8M_0 \frac{H^2}{h} \Phi(\alpha, \overline{\alpha}, \psi_0)\ \dot{\alpha}\ , \tag{A.10}$$

with

$$\Phi(\alpha, \psi_0, \overline{\alpha}) = \frac{\sin\overline{\alpha} \tan\psi_0 \sin 2\alpha}{2(\sin^2 \overline{\alpha} + \tan^2 \psi_0 \sin^2 \alpha)} + (\psi(\alpha) - \psi_0)\cos\alpha\ , \tag{A.11}$$

where

$$\psi(\alpha) = \arctan\left(\frac{\sin\alpha}{\sin\overline{\alpha}} \tan\psi_0\right)\ ; \tag{A.12}$$

$$W_4 = 8M_0 \frac{H^2}{h} I_4(\psi_0, \overline{\alpha})\ , \tag{A.13}$$

with

$$I_4(\psi_0, \overline{\alpha}) = \int_{\overline{\alpha}}^{\alpha_f} \Phi(\alpha, \psi_0, \overline{\alpha})\ d\alpha\ . \tag{A.14}$$

Bending along stationary inclined hinge lines

$$D_6 = 4M_0H\cot\psi_0\,\frac{\sin\overline{\alpha}\left(\sin^2\overline{\alpha}+\tan^2\psi_0\right)}{\sin^2\overline{\alpha}+\tan^2\psi_0\sin^2\alpha}\dot{\alpha}\ ; \tag{A.15}$$

$$W_6 = 4M_0HI_6(\psi_0,\overline{\alpha})\ , \tag{A.16}$$

with

$$I_6(\psi_0,\overline{\alpha}) = \cot\psi_0\int_{\overline{\alpha}}^{\alpha_f}\frac{\sin\overline{\alpha}\left(\sin^2\overline{\alpha}+\tan^2\psi_0\right)}{\sin^2\overline{\alpha}+\tan^2\psi_0\sin^2\alpha}d\alpha\ . \tag{A.17}$$

Axial compression kinematics

The axial crushing distance u_{c} is given by

$$u_{\mathrm{c}} = 2H(1-\cos\alpha)\ , \tag{A.18}$$

from which the compression velocity follows as

$$v_{\mathrm{c}} = 2H\sin\alpha\ \dot{\alpha}\ . \tag{A.19}$$

With these, the final crushing distance would be given as $u_{\mathrm{f}} = 2H$. In order to account for the finite bending radii of the crushing mechanism, however, a correction factor may be included for evaluating the external energy dissipation. Effective crushing distance and compression velocity are, therefore, given by

$$\begin{aligned} u_{\mathrm{c,eff}} &= \delta_{\mathrm{eff}}u_{\mathrm{c}}\ , \\ v_{\mathrm{c,eff}} &= \delta_{\mathrm{eff}}v_{\mathrm{c}}\ , \end{aligned} \tag{A.20}$$

replacing u_{c} and v_{c}, respectively. A value of $\delta_{\mathrm{eff}} = 0.73$ has e.g. been proposed for square columns [Abramowicz and Wierzbicki, 1989].

Appendix B

Exact Ilyushin Yield Surface — Details

B.1 Normalized Shell Quantities

The representation of the exact Ilyushin yield surface and the descriptions of its applications for limit load and collapse analyses are given in terms of normalized stress and strain quantities. In the following, therefore, several relations between physical and normalized values, which were used in the preceding chapters, are derived.

Reference Quantities

Section forces and moments are normalized with respect to the plastic limit loads in uniaxial tension and bending, respectively (yield stress σ_y, shell thickness h):

$$N_0 = \sigma_y h \ , \qquad M_0 = \sigma_y \frac{h^2}{4} \ . \tag{B.1}$$

Physical strain values are referred to a reference strain ε_0. A convenient measure for ε_0 (also used by Burgoyne and Brennan [1993b]) is given by

$$\varepsilon_0 = \frac{\sigma_y(1-\nu^2)}{E} \ , \tag{B.2}$$

with E being the Young's modulus and ν the Poisson's ratio of a linear elastic, isotropic material. ε_0 corresponds to the plastic limit strain of an uniaxially stretched plate.

The reference curvature κ_0 is defined by assuming the relation

$$N_0 \varepsilon_0 = M_0 \kappa_0 \tag{B.3}$$

to hold, which delivers

$$\kappa_0 = \frac{4\varepsilon_0}{h} \, . \tag{B.4}$$

A dimensionless thickness coordinate $\overline{z}$ is used for through-thickness integrations. The relation between $\overline{z}$ and the thickness coordinate s_3 is given by

$$\overline{z} = \frac{s_3}{h} \, . \tag{B.5}$$

Stress Quantities

Physical and normalized (dimensionless) stress vectors for a state of plane stress are given by

$$\boldsymbol{\sigma} = \begin{pmatrix} \sigma_{11} \\ \sigma_{22} \\ \sigma_{12} \end{pmatrix} \qquad \text{and} \qquad \overline{\boldsymbol{\sigma}} = \frac{1}{\sigma_y} \begin{pmatrix} \sigma_{11} \\ \sigma_{22} \\ \sigma_{12} \end{pmatrix} \, , \tag{B.6}$$

respectively. From these, the normalized section force and moment vectors $\boldsymbol{n}$ and $\boldsymbol{m}$ can be obtained according to

$$\begin{aligned} \boldsymbol{n} &= \frac{1}{N_0} \begin{pmatrix} N_{11} \\ N_{22} \\ N_{12} \end{pmatrix} = \frac{1}{N_0} \int_{-h/2}^{h/2} \boldsymbol{\sigma} \, ds_3 = \frac{1}{\sigma_y h} \int_{-1/2}^{1/2} \boldsymbol{\sigma} h \, d\overline{z} = \int_{-1/2}^{1/2} \overline{\boldsymbol{\sigma}} \, d\overline{z} \, , \\ \boldsymbol{m} &= \frac{1}{M_0} \begin{pmatrix} M_{11} \\ M_{22} \\ M_{12} \end{pmatrix} = \frac{1}{M_0} \int_{-h/2}^{h/2} \boldsymbol{\sigma} s_3 \, ds_3 = \frac{4}{\sigma_y h^2} \int_{-1/2}^{1/2} \boldsymbol{\sigma} h \overline{z} h \, d\overline{z} = 4 \int_{-1/2}^{1/2} \overline{\boldsymbol{\sigma}} \, \overline{z} \, d\overline{z} \, . \end{aligned} \tag{B.7}$$

The terms $N_{\alpha\beta}$ $(\alpha, \beta \in \{1, 2\})$ are the physical section force and moment components of a Kirchhoff shell (their arrangement in vector form being denoted as $\boldsymbol{N}$ and $\boldsymbol{M}$).

The quadratic form of the plane stress von Mises yield condition,

$$f(\boldsymbol{\sigma}) = \boldsymbol{\sigma}^T \mathbf{P} \boldsymbol{\sigma} - \sigma_y^2 = 0 \, , \qquad \mathbf{P} = \begin{pmatrix} 1 & -\frac{1}{2} & 0 \\ -\frac{1}{2} & 1 & 0 \\ 0 & 0 & 3 \end{pmatrix} \, , \tag{B.8}$$

directly follows from the definition of the normalized stress vector, Eq. (B.6), as

$$f(\overline{\boldsymbol{\sigma}}) = \overline{\boldsymbol{\sigma}}^T \mathbf{P} \overline{\boldsymbol{\sigma}} - 1 = 0 \, . \tag{B.9}$$

Strain Quantities

The physical strain and curvature vectors

$$\boldsymbol{\varepsilon} = \begin{pmatrix} \varepsilon_{11} \\ \varepsilon_{22} \\ 2\varepsilon_{12} \end{pmatrix} \qquad \text{and} \qquad \boldsymbol{\kappa} = \begin{pmatrix} \kappa_{11} \\ \kappa_{22} \\ 2\kappa_{12} \end{pmatrix} \tag{B.10}$$

are normalized with respect to ε_0 and κ_0, which gives

$$\boldsymbol{e} = \frac{1}{\varepsilon_0} \begin{pmatrix} \varepsilon_{11} \\ \varepsilon_{22} \\ 2\varepsilon_{12} \end{pmatrix} \qquad \text{and} \qquad \boldsymbol{k} = \frac{1}{\kappa_0} \begin{pmatrix} \kappa_{11} \\ \kappa_{22} \\ 2\kappa_{12} \end{pmatrix} . \tag{B.11}$$

With the physical midplane strain vector $\overline{\boldsymbol{\varepsilon}}$ (= $\boldsymbol{\varepsilon}(s_3 = 0)$ the Kirchhoff hypothesis in its standard (non-normalized) form is written as

$$\boldsymbol{\varepsilon}(s_3) = \overline{\boldsymbol{\varepsilon}} + s_3\, \boldsymbol{\kappa} . \tag{B.12}$$

Introduction of $\overline{z}$ (Eq. (B.5)) and division by ε_0 gives

$$\frac{1}{\varepsilon_0}\boldsymbol{\varepsilon} = \frac{1}{\varepsilon_0}\overline{\boldsymbol{\varepsilon}} + \overline{z}\frac{4}{\kappa_0}\boldsymbol{\kappa} , \tag{B.13}$$

where, in addition, the relation $\varepsilon_0 = h\kappa_0/4$ (Eq. (B.4)) has been used. It follows that the Kirchhoff hypothesis may in normalized form be written as

$$\boldsymbol{e}(\overline{z}) = \overline{\boldsymbol{e}} + 4\overline{z}\, \boldsymbol{k} . \tag{B.14}$$

Stress-Strain Relations

For elastoplastic material behaviour the tangential stress-strain relations for a Kirchhoff shell may be stated as

$$\begin{pmatrix} d\boldsymbol{N} \\ d\boldsymbol{M} \end{pmatrix} = \begin{pmatrix} \mathbf{C} & \mathbf{B} \\ \mathbf{B} & \mathbf{D} \end{pmatrix} \begin{pmatrix} d\overline{\boldsymbol{\varepsilon}} \\ d\boldsymbol{\kappa} \end{pmatrix} . \tag{B.15}$$

where $\mathbf{B}$, $\mathbf{C}$ and $\mathbf{D}$ are submatrices of the physical tangential stiffness matrix (all assumed to be symmetric). Introduction of the normalized generalized stress and strain quantities gives

$$\begin{pmatrix} d\boldsymbol{n} \\ d\boldsymbol{m} \end{pmatrix} = \begin{pmatrix} \frac{\varepsilon_0}{N_0}\mathbf{C} & \frac{\kappa_0}{N_0}\mathbf{B} \\ \frac{\varepsilon_0}{M_0}\mathbf{B} & \frac{\kappa_0}{M_0}\mathbf{D} \end{pmatrix} \begin{pmatrix} d\overline{\boldsymbol{e}} \\ d\boldsymbol{k} \end{pmatrix} = \begin{pmatrix} \mathbf{C}^* & \mathbf{B}^* \\ \mathbf{B}^* & \mathbf{D}^* \end{pmatrix} \begin{pmatrix} d\overline{\boldsymbol{e}} \\ d\boldsymbol{k} \end{pmatrix} , \tag{B.16}$$

i.e. the normalized stiffness matrix (submatrices $\mathbf{B}^*$, $\mathbf{C}^*$ and $\mathbf{D}^*$) is obtained from the physical one by multiplying the submatrices with

$$\begin{aligned} \frac{\varepsilon_0}{N_0} &= \frac{1}{h}\frac{1-\nu^2}{E}\,, & \frac{\kappa_0}{N_0} &= \frac{4}{h^2}\frac{1-\nu^2}{E}\,, \\ \frac{\varepsilon_0}{M_0} &= \frac{4}{h^2}\frac{1-\nu^2}{E}\,, & \frac{\kappa_0}{M_0} &= \frac{16}{h^3}\frac{1-\nu^2}{E}\,. \end{aligned} \tag{B.17}$$

For purely elastic material behaviour, the stiffness matrix is given by

$$\begin{aligned} \mathbf{B} &= \mathbf{0}\,, \\ \mathbf{C} &= h\frac{E}{1-\nu^2}\mathbf{E}\,, \qquad \text{with} \qquad \mathbf{E} = \begin{pmatrix} 1 & \nu & 0 \\ \nu & 1 & 0 \\ 0 & 0 & \frac{1-\nu}{2} \end{pmatrix}\,, \\ \mathbf{D} &= \frac{h^3}{12}\frac{E}{(1-\nu^2)}\mathbf{E}\,, \end{aligned} \tag{B.18}$$

from which the elastic constitutive law in normalized (and incremental) form follows as

$$\begin{pmatrix} d\boldsymbol{n} \\ d\boldsymbol{m} \end{pmatrix} = \begin{pmatrix} \mathbf{E} & \mathbf{0} \\ \mathbf{0} & \frac{4}{3}\mathbf{E} \end{pmatrix} \begin{pmatrix} d\overline{\boldsymbol{e}} \\ d\boldsymbol{k} \end{pmatrix}\,. \tag{B.19}$$

B.2 Algorithmic Details

Numerical Evaluation of the J_i-Integrals

A crucial point when using the exact Ilyushin yield surface in its general form is the numerical evaluation of the integral terms

$$J_i = \frac{1}{\sqrt{3}}\int_{-1/2}^{1/2} \frac{\overline{z}^i}{\sqrt{P_\varepsilon + 2P_{\varepsilon\kappa}\overline{z} + P_\kappa\overline{z}^2}}\,d\overline{z} \tag{B.20}$$

for any point of the yield surface, including the boundary.[1] The essential ingredients for a subroutine allowing for such a numerical treatment are discussed in the following.

A) $\underline{P_\kappa = 0}$:

For $P_\kappa = 0$ (and consequently, $P_{\varepsilon\kappa} = 0$) the integrals are simply given by

$$J_0 = \frac{1}{\sqrt{3P_\varepsilon}}\,, \qquad J_1 = 0 \quad \text{and} \qquad J_2 = \frac{1}{12\sqrt{3P_\varepsilon}} \tag{B.21}$$

(see also Eqs. (3.98)).

---

[1] As was noted in section 3.4 the integral values J_i may become infinite there.

B) $\underline{P_\kappa > 0}$:

The numerical evaluation of the J_i-integrals for $P_\kappa > 0$ is conveniently performed via the K_i-terms, all being related by

$$J_i = \frac{1}{\sqrt{3P_\kappa}} K_i \tag{B.22}$$

(see Eq. (3.88)). From Eq. (3.90) it becomes obvious that the only critical term which has to be controlled for the evaluation of the K_i-terms is the integral K_0. In terms of β and γ this is written as

$$K_0 = \int_{-1/2}^{1/2} \frac{1}{\sqrt{(\overline{z}-\beta)^2+\gamma}} d\overline{z}\ . \tag{B.23}$$

This equation, however, reveals that within the integration limits ($\overline{z} \in [-1/2, 1/2]$) the integrand function will become indefinite (at $\overline{z} = \beta$) and, accordingly, $K_0 = \infty$, only if both $|\beta| \leq 0.5$ and $\gamma = 0$ are fulfilled. Consequently, as long as γ is not exactly set to zero, but to some small positive number, a "regularized" evaluation of points at the boundary may be obtained. For example, with $\beta = 0.3$ and $\gamma = 10^{-12}$ the evaluation of Eqs. (3.90) delivers $K_0 = 27.185$, $K_1 = 7.555$ and $K_2 = 2.427$.

A further numerical difficulty arises at the boundary ($\gamma = 0$), when β becomes larger than 0.5. In this case Eq. (3.90) leads to

$$K_0 = \ln\left|\frac{(\beta-0.5)+(0.5-\beta)}{(0.5+\beta)-(0.5+\beta)}\right| = \ln\frac{0}{0}\ , \tag{B.24}$$

and even for small, but positive γ-values a numerically ill-conditioned expression is obtained, if β becomes sufficiently large.[2] Because, however, the identities

$$\begin{aligned} K_0(\beta) &= K_0(-\beta)\ , \\ K_1(\beta) &= -K_1(-\beta)\ , \\ K_2(\beta) &= K_2(-\beta) \end{aligned} \tag{B.25}$$

hold, and for $\beta < -0.5$ and $\gamma = 0$ the K_0-integral is well defined,

$$K_0 = \ln\left|\frac{(0.5-\beta)+(0.5-\beta)}{(-0.5-\beta)-(0.5+\beta)}\right| = \ln\frac{1-2\beta}{-1-2\beta}\ , \tag{B.26}$$

numerical evaluations for the K_i-terms, which are restricted to one half of the yield surface ($\beta < 0$) are sufficient to avoid the above mentioned difficulties.

---

[2] It is interesting to note that $|\beta| > 0.5$ and $\gamma = 0$ just describe the point of discontinuity of the yield surface (at $Q_t = 1$), where each β-value corresponds to a definite normal direction at this singular point.

Based upon these restrictions, a simple routine for computing $J_i(P_\varepsilon, P_{\varepsilon\kappa}, P_\kappa)$ may thus be defined as follows:

```
IF $(P_\varepsilon > \alpha_{\max} P_\kappa)$ THEN
  – Compute $J_i$ according to Eqs. (3.98)            Pure plastic inplane deformations
ELSE
  – Compute $\beta$ and $\gamma$ (Eqs. 3.86)
  – $c_\beta = 1$                                      Ensure that the the numerical evaluation
  – IF $(\beta > 0)$ THEN                              of the $J_i$-terms is always done for one
        $\beta = -\beta$                               half of the yield surface ($\beta < 0$)
        $c_\beta = -1$
    ENDIF
  – IF $((\gamma < \delta_\gamma)$.AND.$(|\beta| < (0.5 + \delta_\beta)))$   $\gamma = \delta_\gamma$   Regularization step
  – Compute $K_i$ according to Eqs. (3.90)
  – $K_1 = c_\beta K_1$                                Account for actual half of yield surface
  – Compute $J_i = \frac{1}{\sqrt{3P_\kappa}} K_i$ (Eqs. (3.88))
ENDIF
```

Here a threshold value $\alpha_{\max}$ is used to distinguish between general and pure plastic inplane deformations, δ_β and δ_γ are tolerance parameters, and c_β is a parameter containing information for a possible internal change of the sign of β (as described above).

Inversion of a Square Matrix Composed of Diagonal Submatrices

The introduction of generalized "deviatoric" stress/plastic strain increment vectors for the full section material routine (described in chapter 7) leads to matrices, which are composed of four diagonal submatrices each. Provided these matrices are nonsingular, a componentwise and thus computationally very efficient inversion may be performed. From the general statement

$$\begin{pmatrix} \mathbf{D}_1 & \mathbf{D}_2 \\ \mathbf{D}_3 & \mathbf{D}_4 \end{pmatrix} \begin{pmatrix} \overline{\mathbf{D}}_1 & \overline{\mathbf{D}}_2 \\ \overline{\mathbf{D}}_3 & \overline{\mathbf{D}}_4 \end{pmatrix} = \begin{pmatrix} \mathbf{I} & \mathbf{0} \\ \mathbf{0} & \mathbf{I} \end{pmatrix} \tag{B.27}$$

($\mathbf{D}_i$ and $\overline{\mathbf{D}}_i$ are square matrices of dimension $n/2$, $\mathbf{I}$ is the corresponding identity matrix) the inverted submatrices $\overline{\mathbf{D}}_i$ may be obtained according to

$$\begin{aligned} \overline{\mathbf{D}}_2 &= -[\mathbf{D}_1 - \mathbf{D}_2\mathbf{D}_4^{-1}\mathbf{D}_3]^{-1}\mathbf{D}_2\mathbf{D}_4^{-1} \ , \\ \overline{\mathbf{D}}_3 &= -[\mathbf{D}_4 - \mathbf{D}_3\mathbf{D}_1^{-1}\mathbf{D}_2]^{-1}\mathbf{D}_3\mathbf{D}_1^{-1} \ , \\ \overline{\mathbf{D}}_1 &= \mathbf{D}_1^{-1}[\mathbf{I} - \mathbf{D}_2\overline{\mathbf{D}}_3] \ , \\ \overline{\mathbf{D}}_4 &= \mathbf{D}_4^{-1}[\mathbf{I} - \mathbf{D}_3\overline{\mathbf{D}}_2] \ . \end{aligned} \tag{B.28}$$

If now all submatrices are diagonal, then it finally follows that each (diagonal) component of the inverted submatrices is given by (the diagonal components $\mathbf{D}_{j,ii}$ are written as $\mathbf{D}_{j,i}$, etc.)

$$\begin{aligned} \overline{\mathbf{D}}_{1,i} &= \frac{\mathbf{D}_{4,i}}{\mathbf{D}_{1,i}\mathbf{D}_{4,i} - \mathbf{D}_{2,i}\mathbf{D}_{3,i}} \ , \\ \overline{\mathbf{D}}_{2,i} &= \frac{-\mathbf{D}_{2,i}}{\mathbf{D}_{1,i}\mathbf{D}_{4,i} - \mathbf{D}_{2,i}\mathbf{D}_{3,i}} \ , \\ \overline{\mathbf{D}}_{3,i} &= \frac{-\mathbf{D}_{3,i}}{\mathbf{D}_{1,i}\mathbf{D}_{4,i} - \mathbf{D}_{2,i}\mathbf{D}_{3,i}} \ , \\ \overline{\mathbf{D}}_{4,i} &= \frac{\mathbf{D}_{1,i}}{\mathbf{D}_{1,i}\mathbf{D}_{4,i} - \mathbf{D}_{2,i}\mathbf{D}_{3,i}} \ , \end{aligned} \tag{B.29}$$

delivering exactly the same algorithmic structure (for each component i) as the analytical matrix inversion of a (2 × 2)-matrix. A simple Fortran implementation may thus (without checking for singularity) be realized as:

```
DO i=1,n/2
   const=D1(i)*D4(i)-D2(i)*D3(i)
   DINV1(i)=D4(i)/const
   DINV2(i)=-D2(i)/const
   DINV3(i)=-D3(i)/const
   DINV4(i)=D1(i)/const
ENDDO
```

B.3 Revised Derivation of the Continuum Tangential Stiffness Matrix

The tangential stiffness matrix, which relates changes of strain resultant increments to changes of stress resultant increments, is of the general form

$$\begin{pmatrix} d\boldsymbol{n} \\ d\boldsymbol{m} \end{pmatrix} = \mathbf{C}_t \begin{pmatrix} d\bar{\boldsymbol{e}} \\ d\boldsymbol{k} \end{pmatrix} = \begin{pmatrix} \mathbf{C}^* & \mathbf{B}^* \\ \mathbf{B}^* & \mathbf{D}^* \end{pmatrix} \begin{pmatrix} d\bar{\boldsymbol{e}} \\ d\boldsymbol{k} \end{pmatrix} . \tag{B.30}$$

For perfectly plastic material behaviour, the submatrices $\mathbf{B}^*$, $\mathbf{C}^*$ and $\mathbf{D}^*$ are symmetric and indeterminate. The following derivation of the continuum tangential stiffness matrix does not make use of the stress resultant yield surface and the normal direction to it (Burgoyne and Brennan [1993a] showed that in this case the matrix $\mathbf{B}^*$ is not itself symmetrical, see the remarks in section 7.2.2), but is related to the stresses and the normality rule in stress space. The only assumption used here is once again the validity of the Kirchhoff hypothesis for the plastic strain resultant increments, Eq. (3.69).

When plastic loading takes place, in the limit in each point over the thickness of a shell the incremental form of Hooke's law,

$$d\bar{\boldsymbol{\sigma}} = \mathbf{E}(d\boldsymbol{e} - d\xi \frac{\partial f}{\partial \bar{\boldsymbol{\sigma}}}) \; , \tag{B.31}$$

and the plastic consistency condition

$$df = \left(\frac{\partial f}{\partial \bar{\boldsymbol{\sigma}}}\right)^T d\bar{\boldsymbol{\sigma}} = 0 \tag{B.32}$$

are valid. These equations are sufficient for determining the plastic multiplier $d\xi$ and to establish a relationship of the form

$$d\bar{\boldsymbol{\sigma}} = \mathbf{E}^* d\boldsymbol{e} \; , \tag{B.33}$$

where

$$\mathbf{E}^* = \mathbf{E} - \frac{\mathbf{E} \, \frac{\partial f}{\partial \bar{\boldsymbol{\sigma}}} \left(\frac{\partial f}{\partial \bar{\boldsymbol{\sigma}}}\right)^T \mathbf{E}}{\left(\frac{\partial f}{\partial \bar{\boldsymbol{\sigma}}}\right)^T \mathbf{E} \, \frac{\partial f}{\partial \bar{\boldsymbol{\sigma}}}} \; . \tag{B.34}$$

If the assumption of linearly varying strains (Eq. (3.69)) is put into Eq. (B.33), and the stress increments are integrated over the thickness (in order to obtain $d\boldsymbol{n}$ and $d\boldsymbol{m}$), then the submatrices $\mathbf{B}^*$, $\mathbf{C}^*$ and $\mathbf{D}^*$ can be obtained as

$$\begin{aligned} \mathbf{C}^* &= \int_{-1/2}^{1/2} \mathbf{E}^* \, d\overline{z} \;, \\ \mathbf{B}^* &= 4 \int_{-1/2}^{1/2} \mathbf{E}^* \overline{z} \, d\overline{z} \;, \\ \mathbf{D}^* &= 16 \int_{-1/2}^{1/2} \mathbf{E}^* \overline{z}^2 \, d\overline{z} \;, \end{aligned} \tag{B.35}$$

which all are symmetric and indeterminate (because of the properties of $\mathbf{E}^*$).

For a single layer analysis it should be possible to obtain the stiffness matrix as a function only of stress or strain resultant quantities. Therefore, the term $\partial f / \partial \overline{\boldsymbol{\sigma}}$, which is necessary for obtaining $\mathbf{E}^*$, must be expressed with such quantities. This can be done by simply expressing the plastic strain increments in the normality law in stress space with the corresponding strain resultant increment quantities:

$$d\boldsymbol{e}^p = d\xi \frac{\partial f}{\partial \overline{\boldsymbol{\sigma}}} = d\overline{\boldsymbol{e}}^p + 4\overline{z} \; d\boldsymbol{k}^p \tag{B.36}$$

and, therefore,

$$\frac{\partial f}{\partial \overline{\boldsymbol{\sigma}}} = \frac{1}{d\xi} (d\overline{\boldsymbol{e}}^p + 4\overline{z} \; d\boldsymbol{k}^p) \; . \tag{B.37}$$

After inserting this relation in Eq. (B.34) $\mathbf{E}^*$ can be expressed as

$$\mathbf{E}^* = \mathbf{E} - \frac{\mathbf{E}_\varepsilon + 8\mathbf{E}_{\varepsilon\kappa}\overline{z} + 16\mathbf{E}_\kappa \overline{z}^2}{R_\varepsilon + 8R_{\varepsilon\kappa}\overline{z} + 16R_\kappa \overline{z}^2} \;, \tag{B.38}$$

with

$$\begin{aligned} \mathbf{E}_\varepsilon &= \mathbf{E} \; d\overline{\boldsymbol{e}}^p (d\overline{\boldsymbol{e}}^p)^T \mathbf{E} \;, \\ \mathbf{E}_{\varepsilon\kappa} &= \frac{1}{2} (\mathbf{E} \; d\overline{\boldsymbol{e}}^p (d\boldsymbol{k}^p)^T \mathbf{E} + \mathbf{E} \; d\boldsymbol{k}^p (d\overline{\boldsymbol{e}}^p)^T \mathbf{E}) \;, \\ \mathbf{E}_\kappa &= \mathbf{E} \; d\boldsymbol{k}^p (d\boldsymbol{k}^p)^T \mathbf{E} \;, \end{aligned} \tag{B.39}$$

and

$$\begin{aligned} R_\varepsilon &= (d\overline{\boldsymbol{e}}^p)^T \mathbf{E} \; d\overline{\boldsymbol{e}}^p \quad (\geq 0) \;, \\ R_{\varepsilon\kappa} &= (d\overline{\boldsymbol{e}}^p)^T \mathbf{E} \; d\boldsymbol{k}^p \;, \\ R_\kappa &= (d\boldsymbol{k}^p)^T \mathbf{E} \; d\boldsymbol{k}^p \quad (\geq 0) \;, \end{aligned} \tag{B.40}$$

subject to the condition

$$R_\varepsilon R_\kappa \geq R^2_{\varepsilon\kappa} \; . \tag{B.41}$$

With Eq. (B.34) the integrals for the determination of the elastoplastic stiffness matrix (Eqs. (B.35)) can be evaluated analytically to obtain

$$\begin{aligned} \mathbf{C}^* &= \mathbf{E} - (L_0\mathbf{E}_\varepsilon + 2L_1\mathbf{E}_{\varepsilon\kappa} + L_2\mathbf{E}_\kappa) \; , \\ \mathbf{B}^* &= -(L_1\mathbf{E}_\varepsilon + 2L_2\mathbf{E}_{\varepsilon\kappa} + L_3\mathbf{E}_\kappa) \; , \\ \mathbf{D}^* &= \frac{4}{3}\mathbf{E} - (L_2\mathbf{E}_\varepsilon + 2L_3\mathbf{E}_{\varepsilon\kappa} + L_4\mathbf{E}_\kappa) \; , \end{aligned} \tag{B.42}$$

where

$$L_i = \int_{-1/2}^{1/2} \frac{(4\overline{z})^i}{R_\varepsilon + 8R_{\varepsilon\kappa}\overline{z} + 16R_\kappa\overline{z}^2} d\overline{z} \; . \tag{B.43}$$

The integrals L_i are well defined for $R_\varepsilon R_\kappa - R^2_{\varepsilon\kappa} > 0$. For $R_\varepsilon R_\kappa - R^2_{\varepsilon\kappa} = 0$ (which corresponds to the boundary of the exact yield surface) the matrix $\mathbf{E}^*$ can be shown to be independent of $\overline{z}$, in which case

$$\mathbf{C}^* = \mathbf{E}^* \; , \qquad \mathbf{B}^* = 0 \qquad \text{and} \qquad \mathbf{D}^* = \frac{4}{3}\mathbf{E}^* \; , \tag{B.44}$$

with

$$\begin{aligned} \mathbf{E}^* &= \mathbf{E} - \frac{\mathbf{E}_\kappa}{R_\kappa} \qquad \text{for} \qquad d\boldsymbol{k}^p \neq 0 \; , \\ \mathbf{E}^* &= \mathbf{E} - \frac{\mathbf{E}_\varepsilon}{R_\varepsilon} \qquad \text{for} \qquad d\boldsymbol{k}^p = 0 \; . \end{aligned} \tag{B.45}$$

The derivation procedure sketched above relies on the assumption of infinitesimally small increments, leading to the continuum tangential material matrix. If finite increments are to be considered, then the algorithmically consistent tangential material matrix should be used in order to retain the quadratic convergence rate of the overall Newton/Raphson scheme. With respect to the definition of the consistent tangential stiffness matrix according to this revised derivation procedure, the elastic stiffness matrix $\mathbf{E}$ in Eq. (B.34) must be replaced by the algorithmic elastic stiffness matrix $\overline{\mathbf{E}}$:

$$\overline{\mathbf{E}}(\overline{z}) = (\mathbf{E}^{-1} + 2d\xi(\overline{z})\mathbf{P})^{-1} \; . \tag{B.46}$$

Because, however, the plastic consistency parameter $d\xi$, used therein, depends on the through-the-thickness position $\overline{z}$ (see Eq. (3.70)), an analytical thickness integration is no longer possible and one must resort to a numerical evaluation of Eqs. (B.35) in order to obtain the consistent tangential stiffness matrix for the plastically deforming shell section.

Bibliography

Aamlid, O., McGeorge, D. and Nilson, L. (1993). Collision properties of high speed craft. In: Moan et al. (eds.), *Proc. Structural Dynamics – EURODYN93*, pp. 505–512. Balkema, Rotterdam.

Abramowicz, W. (1996). Extremal paths in progressive plasticity. *Int. J. Impact. Eng.* **18**(7/8), pp. 753–764.

Abramowicz, W. and Jones, N. (1986). Dynamic progressive buckling of circular and square tubes. *Int. J. Impact. Eng.* **4**(4), pp. 243–270.

Abramowicz, W. and Wierzbicki, T. (1988). Axial crushing of foam-filled columns. *Int. J. Mech. Sci.* **30**(3/4), pp. 263–271.

Abramowicz, W. and Wierzbicki, T. (1989). Axial crushing of multicorner sheet metal columns. *J. Appl. Mech.* **56**, pp. 113–120.

Achtziger, W. (1998). Methods of non-smooth optimization: Algorithms and applications. In: *Advanced Topics in Structural Optimization*, Technical Report S 81. Danish Center for Applied Mathematics and Mechanics, Technical University of Denmark.

Albertini, C., Del Grande, A., Delzano, A., Kiefer, R., Montagnani, M., Murarotto, M., Pizzinato, E. V., Rodis, A. and Schnabel, A. W. (1993). New approach to crashworthiness studies of automotive and aerospace thin sheet metal structures by a large Hopkinson bar method. In: Moan et al. (eds.), *Proc. Structural Dynamics – EURODYN93*, pp. 539–545. Balkema, Rotterdam.

Alexander, J. M. (1960). An approximate analysis of the collapse of thin cylindrical shells under axial loading. *Quart. J. Mech. Appl. Math.* **13**(1), pp. 10–15.

Anselm, D. (1997). *Die PKW-Karosserie: Konstruktion, Deformationsverhalten, Unfallinstandsetzung.* Vogel Buchverlag, Würzburg.

Armero, F. and Garikipati, K. (1995). Recent advances in the analysis and numerical simulation of strain localization in inelastic solids. In: Owen et al. (eds.), *Computational Plasticity – Fundamentals and Applications. Proc. 4th Int. Conf., Barcelona, 3-6 April 1995*, pp. 547–561 (Part 1). Pineridge Press, Swansea.

Auricchio, F. and Taylor, R. L. (1994). A generalized elastoplastic plate theory and its algorithmic implementation. *Int. J. Num. Meth. Eng.* **37**, pp. 2583–2608.

Başar, Y. and Krätzig, W. B. (1985). *Mechanik der Flächentragwerke.* Vieweg & Sohn, Braunschweig, Wiesbaden.

Berstad, T., Langseth, M. and Hopperstad, O. S. (1995). Crashworthiness of thin-walled aluminium extrusions. In: Owen et al. (eds.), *Computational Plasticity – Fundamentals and Applications. Proc. 4th Int. Conf., Barcelona, 3-6 April 1995*, pp. 1901–1912 (Part 2). Pineridge Press, Swansea.

Bisagni, C. (1998). Energy absorption of riveted structures. In: *Proc. Int. Crashworthiness Conf. IJCRASH'98, September 9–11, 1998, Dearborn, USA*, pp. 420–431. Woodhead Publ. Ltd., Cambridge, England.

Bonet, J. (1998). Recent developments in the incremental flow formulation for the numerical simulation of metal forming processes. *Eng. Comp.* **15**(3), pp. 345–356.

Borges, L. A., Zouain, N. and Huespe, A. E. (1996). A nonlinear optimization procedure for limit analysis. *Eur. J. Mech., A/Solids,* **15**(3), pp. 487–512.

Bravo, P., Larrodé, E., Ullod, J. and Alba, J. J. (1993). Analysis of crash absorbing elements for automotive applications. In: A. Miravete (ed.), *Proc. 9. Int. Conf. on Comp. Mat. (ICCM/9, Madrid). Volume V: Composites behaviour*, pp. 374–385. Univ. of Zaragoza, Woodhead Publishing Ltd., Cambridge.

Bronstein, I. N., Semendjajew, K. A., Musiol, G. and Mühlig, H. (1995). *Taschenbuch der Mathematik.* Verlag Harry Deutsch, Thun, Frankfurt, 2nd edition.

Burgoyne, C. J. and Brennan, M. G. (1993a). Calculation of elasto-plastic rigidities using the exact Ilyushin yield surface. *Int. J. Sol. Struct.* **30**(8), pp. 1133–1145.

Burgoyne, C. J. and Brennan, M. G. (1993b). Exact Ilyushin yield surface. *Int. J. Sol. Struct.* **30**(8), pp. 1113–1131.

Capsoni, A. and Corradi, L. (1997a). A finite element formulation for rigid-plastic limit analyis of plates. In: D. R. J. Owen, E. Onate and E. Hinton (eds.), *Computational Plasticity – Fundamentals and Applications. Proc. 5th Int. Conf., Barcelona, 1997*, pp. 1865–1872. CIMNE, Barcelona.

Capsoni, A. and Corradi, L. (1997b). A finite element formulation of the rigid-plastic limit analysis problem. *Int. J. Num. Meth. Eng.* **40**, pp. 2063–2086.

Chen, W. F. and Han, D. J. (1988). *Plasticity for Structural Engineers.* Springer-Verlag, New York.

Chou, C. H., Pan, I. and Tang, S. C. (1994). Analysis of sheet metal forming operations by a stress resultant constitutive law. *Int. J. Num. Meth. Eng.* **37**, pp. 717–735.

Chung, J. and Lee, J. M. (1994). A new family of explicit time integration methods for linear and non-linear structural dynamics. *Int. J. Num. Meth. Eng.* **37**, pp. 3961–3976.

Cimpoeru, S. J. and Murray, N. W. (1993). The large-deflection pure bending properties of a square thin-walled tube. *Int. J. Mech. Sci.* **35**(3/4), pp. 247–256.

Cléon, L.-M. (1993). Résistance passive – application au TGV 2N. *Revue générale des chemins de fer* (November 93), pp. 45–57.

Cléon, L.-M. and Lagneau, H. (1993). Physique du choc et accidentologie. *Revue générale des chemins de fer* (November 93), pp. 29–33.

CrashCad (1995). *Crash Cad User's Manual, Version 3.2.* Impact Design, Europe, Inc., Michalowice 05-816, Poland.

Crisfield, M. A. (1980). Finite element analysis for combined material and geometric nonlinearities. Report, Transport and Road Research Lab. (TRRL), Crowthorne, Berkshire, England.

Crisfield, M. A. (1991). *Non-Linear Finite Element Analysis of Solids and Structures*, volume 1: Essentials. John Wiley & Sons Ltd., Chichester, England.

Crisfield, M. A. (1997). *Non-Linear Finite Element Analysis of Solids and Structures*, volume 2: Advanced Topics. John Wiley & Sons Ltd., Chichester, England.

de Buhan, P. and Maghous, S. (1995). A straightforward numerical method for evaluating the ultimate loads of structures. *Eur. J. Mech., A/Solids,* **14**(2), pp. 309–328.

Desjardins, S. P. et al. (1989). Aircraft crash survival design guide. USAAVSCOM TR 89-D-22A-E, Vol. I-IV.

Drazétic, P., Markiewicz, E. and Ravalard, Y. (1993). Application of kinematic models to compression and bending in simplified crash calculations. *Int. J. Mech. Sci.* **35**(3/4), pp. 179–191.

Drazétic, P., Tassin, R. and Ravalard, Y. (1995). A tool for rigid multibody modelling of impacted structures. *Eng. Comp.* **12**, pp. 21–34.

Feng, Z. Q. and de Saxcé, G. (1996). Rigid-plastic implicit integration scheme for analysis of metal forming. *Eur. J. Mech., A/Solids,* **15**(1), pp. 51–66.

Gao, D. Y. (1995). Limit analysis of plastic shells subjected to large deformations. *Eur. J. Mech., A/Solids,* **14**(3), pp. 459–472.

GMRT2100 (1997). GM/RT2100 Railway Group Standard: Structural requirements for railway vehicles. Railtrack Safety and Standards Directorate, London. Issue 2.

Grzebieta, R. H. (1990). An alternative method for determining the behaviour of round stocky tubes subjected to an axial crush load. *Thin-Walled Structures* **9**, pp. 61–89.

Gupta, N. K. and Khullar, A. (1993). Collapse of square and rectangular tubes in transverse loading. *Arch. Appl. Mech.* **63**, pp. 479–490.

Gupta, N. K. and Velmurugan, R. (1995). An analysis of axi-symmetric axial collapse of round tubes. *Thin-Walled Structures* **22**, pp. 261–274.

Haberl, J. and Eichinger, S. (1990). Insassenschutz, Partnerschutz und Fahrzeugschutz des BMW 850i. *Automobiltechnische Zeitschrift* **92**(11), pp. 628–643.

Harding, J. (1991). Mechanical properties of metals and constitutive relationships. In: *Lecture Notes for the Short Course on Mechanical Properties at High Rates of Strain, University of Oxford, 6 – 8 March.*

Haug, E., Arnaudeau, F., Dubois, J., de Rouvray, A. and Chedmail, J. F. (1983). Static and dynamic finite element analysis of structural crashworthiness in the automotive and aerospace industries. In: N. Jones and T. Wierzbicki (eds.), *Structural Crashworthiness*, chapter 7, pp. 175–217. Butterworth, London.

Hayduk, R. J. and Wierzbicki, T. (1984). Extensional collapse modes of structural members. *Computers and Structures* **18**(3), pp. 447–458.

HKS (1997). *Introduction to ABAQUS/Explicit.* Hibitt, Karlsson, Sorensen, Inc., Pawtucket, Rhode Island. Lecture notes.

HKS (1998a). *ABAQUS Theory Manual, Version 5.8.* Hibitt, Karlsson, Sorensen, Inc., Pawtucket, Rhode Island.

HKS (1998b). *ABAQUS/Explicit User's Manual, Version 5.8.* Hibitt, Karlsson, Sorensen, Inc., Pawtucket, Rhode Island.

HKS (1998c). *ABAQUS/Standard User's Manual, Version 5.8.* Hibitt, Karlsson, Sorensen, Inc., Pawtucket, Rhode Island.

Hu, X., Wagoner, R. H. and Daehn, G. S. (1994). Comparison of explicit and implicit finite element methods in the quasistatic simulation of uniaxial tension. *Comm. Num. Meth. Eng.* **10**, pp. 993–1003.

Hwan, C.-L. (1997). Plane strain extrusion by sequential limit analysis. *Int. J. Mech. Sci.* **39**(7), pp. 807–817.

Ibrahimbegović, A. and Frey, F. (1993). An efficient implementation of stress resultant plasticity in analysis of Reissner-Mindlin plates. *Int. J. Num. Meth. Eng.* **36**, pp. 303–320.

Ibrahimbegović, A. and Frey, F. (1994). Stress resultant geometrically non-linear shell theory with drilling rotations. Part III: Linearized kinematics. *Int. J. Num. Meth. Eng.* **37**, pp. 3659–3683.

Ilyushin, A. A. (1948). *Plasticity.* Gostekhizdat, Moscow. In Russian.

Ismar, H. and Mahrenholtz, O. (1979). *Technische Plastomechanik.* Vieweg, Braunschweig, Wiesbaden.

Ivanov, G. V. (1967). Approximating the final relationship between the forces and moments of shells under the Mises plasticity condition. *Inzhenernyi Zhurnal Mekhanika Tverdogo Tela* **6**, pp. 74–75. In Russian.

Jones, N. (1989a). Recent studies on the dynamic plastic behavior of structures. *Appl. Mech. Rev.* **42**(4), pp. 95–115.

Jones, N. (1989b). *Structural Impact.* Cambridge University Press, Cambridge, UK.

Kaufman, Jr., E. H., Leeming, D. J. and Taylor, G. D. (1995). An ODE-based approach to nonlinearly constrained minimax problems. *Numerical Algorithms* **9**, pp. 25–37.

Kecman, D. (1983). Bending collapse of rectangular and square section tubes. *Int. J. Mech. Sci.* **25**(9/10), pp. 623–636.

Kecman, D. (1997). An engineering approach to crashworthiness of thin-walled beams and joints in vehicle structures. *Thin-Walled Structures* **28**(3/4), pp. 309–320.

Kindervater, C. M. and Georgi, H. (1993). Composite strength and energy absorption as an aspect of structural crash resistance. In: N. Jones and T. Wierzbicki (eds.), *Structural Crashworthiness and Failure*, chapter 6, pp. 189–235. Elsevier Applied Science, London, New York.

Kindervater, C. M., Kohlgrüber, D. and Johnson, A. (1998). Composite vehicle structural crashworthiness – a status of design methodology and numerical simulation techniques. In: *Proc. Int. Crashworthiness Conf. IJCRASH'98, September 9–11, 1998, Dearborn, USA*, pp. 444–460. Woodhead Publ. Ltd., Cambridge, England.

Kirk, N. E., Kalton, A. F., Candy, E. G., Newell, G. C., Nicholson, C. E. and Wilson, C. (1998). Modifications to existing rolling stock to improve crashworthiness. In: *Proc. Int. Crashworthiness Conf. IJCRASH'98, September 9–11, 1998, Dearborn, USA*, pp. 239–250. Woodhead Publ. Ltd., Cambridge, England.

Kobayashi, S. (1977). Application of the variational principle to the analysis of metal-forming processes. In: H. Lippmann (ed.), *Engineering Plasticity: Theory of Metal Forming Processes*, volume 1 of *CISM Courses and Lectures No. 139*, pp. 25–79. Springer-Verlag, Wien, New York.

Kotelko, M. and Królak, M. (1993). Collapse behaviour of triangular cross-section girders subject to pure bending. *Thin-Walled Structures* **15**, pp. 127–141.

Kreißig, R. (1992). *Einführung in die Plastizitätstheorie: mit technischen Anwendungen.* Fachbuchverlag, Leipzig, Köln.

Kuntsevich, A. and Kappel, F. (1997). *SolvOpt — The Solver for Local Nonlinear Optimization Problems, Version 1.1.* Institute for Mathematics, Karl-Franzens University of Graz, Graz (A).

Lai, W. M., Rubin, D. and Krempl, E. (1993). *Introduction to Continuum Mechanics.* Pergamon Press, Oxford, New York, 3rd edition.

Larsson, R., Runesson, K. and Åknesson, M. (1995). Embedded localization band based on regularized strong discontinuity. In: Owen et al. (eds.), *Computational Plasticity – Fundamentals and Applications. Proc. 4th Int. Conf., Barcelona, 3-6 April 1995*, pp. 599–609 (Part 1). Pineridge Press, Swansea.

Larsson, R., Runesson, K. and Samuelsson, A. (1993). Numerical simulation of plastic localisation using FE-mesh realignment. In: E. Stein (ed.), *Progress in Computational Analysis of Inelastic Structures. CISM Courses and Lectures No. 321*, pp. 79–113. Springer Verlag, Wien.

Lewis, J. H. (1994). Development of crashworthy vehicle structures for railways. Technical report, British Rail Research – Structures Group, PO Box 2, London Road, Derby DE24 8YB, UK.

Lewis, J. H. (1998). Railway vehicle crashworthiness — the role of analysis and testing in the design process. In: *Proc. Int. Crashworthiness Conf. IJCRASH'98, September 9–11, 1998, Dearborn, USA*, pp. 207–215. Woodhead Publ. Ltd., Cambridge, England.

Lu, F. and Sherbourne, A. N. (1992). Moving hinge in large-displacement problems. *J. Eng. Mech. ASCE* **118**(9), pp. 1840–1849.

Lü, H., Tang, L. and Wang, X. (1993). The upper bound on the collapse load of plate bending by using a quasi-conforming element and the Monte-Carlo method. *Finite Elements in Analysis and Design* **12**, pp. 65–73.

Lubliner, J. (1990). *Plasticity Theory.* MacMillan, New York.

Maier, M., Klipfel, W. and Neitzel, M. (1990). Simulation des Crashverhaltens von Verbundwerkstoffen – Rechnung und Versuch. In: *Proc. 23.AVK-Tagung Mainz*, pp. A10/1–A10/13.

Malvern, L. E. (1969). *Introduction to the Mechanics of a Continuous Medium.* Prentice-Hall, Inc., Englewood Cliffs, New Jersey.

Markov, A. A. (1947). On variational principles in the theory of plasticity. *Prikladnaia Matematika i Mekhanika* **11**, pp. 339–350. In Russian.

McGregor, I. J., Meadows, D. J., Scott, C. E. and Seeds, A. D. (1993). Impact performance of aluminium structures. In: N. Jones and T. Wierzbicki (eds.), *Structural Crashworthiness and Failure*, chapter 10, pp. 385–421. Elsevier Science Publishers Ltd.

MilStd1290 (1988). Light fixed wing and rotary wing aircraft crash resistance. Military Standard MIL-STD-1290 A (AV).

Mori, K., Wang, C. C. and Osakada, K. (1996). Inclusion of elastic deformation in rigid-plastic Finite-Element analysis. *Int. J. Mech. Sci.* **38**(6), pp. 621–631.

Murray, N. W. (1985). *Introduction to the Theory of Thin-Walled Structures.* Clarendon Press, Oxford.

Murray, N. W. (1995). Some effects arising from impact loading of thin-walled structures. In: J. B. Obrebsky (ed.), *Proc. Lightweight Struct. in Civil Eng., 25–29 September, 1995, Warsaw, Poland*, pp. 389–394 (Part II). Faculty of Civil Engineering, Warsaw Univ. of Techn.

Nemat-Nasser, S., Li, Y. F. and Isaacs, J. B. (1994). Experimental/computational evaluation of flow stress at high strain rates with application to adiabatic shear banding. *Mech. Mat.* **17**, pp. 111–134.

Oliver, J. (1995). Continuum modelling of strong discontinuities in solid mechanics. In: Owen et al. (eds.), *Computational Plasticity – Fundamentals and Applications. Proc. 4th Int. Conf., Barcelona, 3-6 April 1995*, pp. 455–479 (Part 1). Pineridge Press, Swansea.

Ortiz, M. and Popov, E. P. (1985). Accuracy and stability of integration algorithms for elastoplastic constitutive relations. *Int. J. Num. Meth. Eng.* **21**, pp. 1561–1576.

Paefgen, F.-J., Kreiner, H. and Wilmers, G. (1994). Der neue Audi A8 – Teil 1. *Automobiltechnische Zeitschrift* **96**(4), pp. 198–211.

Press, W. H., Teukolsky, S. A., Vetterling, W. T. and Flannery, B. P. (1992). *Numerical Recipes in Fortran 77: The Art of Scientific Computing*, volume 1. Cambridge University Press, Cambridge, 2nd edition.

Reddy, T. Y. and Al-Hassani, S. T. S. (1993). Axial crushing of wood-filled square metal tubes. *Int. J. Mech. Sci.* **35**(3/4), pp. 231–246.

Reid, S. R. (1993). Plastic deformation mechanisms in axially compressed metal tubes used as impact energy absorbers. *Int. J. Mech. Sci.* **35**(12), pp. 1035–1052.

Robinson, M. (1971). A comparison of yield surfaces for thin shells. *Int. J. Mech. Sci.* **13**, pp. 345–354.

Seiffert, U. (1997). Möglichkeiten und Grenzen der neuen Frontal- und Seitenaufprall-Gesetzgebung. *Automobiltechnische Zeitschrift* **99**(9), pp. 494–504.

Seitzberger, M. and Rammerstorfer, F. G. (1998a). Study of axisymmetric crushing mechanisms by sequential limit analysis. In: *Proc. Int. Crashworthiness Conf. IJCRASH'98, September 9–11, 1998, Dearborn, Michigan (USA)*, pp. 509–521. Woodhead Publ. Ltd., Cambridge, England.

Seitzberger, M. and Rammerstorfer, F. G. (1998b). Über die Anwendung der exakten Ilyushin Fließfläche in Traglastuntersuchungen von Schalenstrukturen. In: *Proc. 6. Workshop "Numerische Methoden der Plastomechanik", June 22–24, 1998, Neustadt am Rübenberge (D).*

Seitzberger, M., Rammerstorfer, F. G., Degischer, H.-P. and Gradinger, R. (1997a). Crushing of axially compressed steel tubes filled with aluminium foam. *Acta Mechanica* **125**, pp. 93–105.

Seitzberger, M., Rammerstorfer, F. G., Gradinger, R., Degischer, H.-P., Blaimschein, M. and Walch, C. (1999). Experimental studies on the quasi-static axial crushing of steel columns filled with aluminium foam. *Int. J. Sol. Struct.* In Print.

Seitzberger, M., Wintschnig, S. and Rammerstorfer, F. G. (1997b). On the plastic collapse behaviour of tubular steel structures under axial compression. In: *Proc. Int. Conf. on Carrying Capacity of Steel Shell Structures (eds: V. Křupka, P. Schneider), October 1–3, 1997, Brno (CZ)*, pp. 64–70.

Seki, W. and Atluri, S. N. (1995). A new formulation of assumed stress hybrid elements and the applications for strain localization problems. In: S. N. Atluri, G. Yagawa and T. A. Cruse (eds.), *Computational Mechanics' 95. Theory and Applications. Proc. Int. Conf. on Comp. Eng. Science, July 30 – August 3, Hawaii, USA*, pp. 2474–2478. Springer Verlag, Berlin, Heidelberg, New York.

Sherbourne, A. N. and Lu, F. (1993). Strain hardening in the moving hinge method. *Int. J. Sol. Struct.* **30**(24), pp. 3475–3489.

Shi, G. and Atluri, S. N. (1988). Elasto-plastic large deformation analysis of space-frames: a plastic hinge and stress-based explicit derivation of tangent stiffnesses. *Int. J. Num. Meth. Eng.* **26**, pp. 589–615.

Shi, G. and Voyiadjis, G. Z. (1992). A simple non-layered finite element for the elasto-plastic analysis of shear flexible plates. *Int. J. Num. Meth. Eng.* **33**, pp. 85–99.

Shor, N. Z. (1985). *Minimization Methods for Non-Differentiable Functions*, volume 3 of *Springer Series in Computational Mathematics.* Springer-Verlag, Berlin.

Simo, J. C. (1992). Algorithms for static and dynamic multiplicative plasticity that preserve the classical return mapping schemes of the infinitesimal theory. *Comput. Methods Appl. Mech. Eng.* **99**, pp. 61–112.

Simo, J. C. (1993a). On a stress resultant geometrically exact shell model. Part VII: Shell intersections with 5/6-DOF finite element formulations. *Comput. Methods Appl. Mech. Eng.* **108**, pp. 319–339.

Simo, J. C. (1993b). Recent developments in the numerical analysis of plasticity. In: E. Stein (ed.), *Progress in Computational Analysis of Inelastic Structures*, pp. 115–173. CISM Courses and Lectures Nr. 321, Springer-Verlag, Wien, New York.

Simo, J. C. and Fox, D. D. (1989). On a stress resultant geometrically exact shell model. Part I: Formulation and optimal parametrization. *Comput. Methods Appl. Mech. Eng.* **72**, pp. 267–304.

Simo, J. C., Fox, D. D. and Rifai, M. S. (1989). On a stress resultant geometrically exact shell model. Part II: The linear theory: Computational aspects. *Comput. Methods Appl. Mech. Eng.* **73**, pp. 53–92.

Simo, J. C., Fox, D. D. and Rifai, M. S. (1990a). On a stress resultant geometrically exact shell model. Part III: Computational aspects of the nonlinear theory. *Comput. Methods Appl. Mech. Eng.* **79**, pp. 21–70.

Simo, J. C. and Kennedy, J. G. (1992). On a stress resultant geometrically exact shell model. Part V: Nonlinear plasticity: Formulation and integration algorithms. *Comput. Methods Appl. Mech. Eng.* **96**, pp. 133–171.

Simo, J. C., Kennedy, J. G. and Govindjee, S. (1988). Non-smooth multisurface plasticity and viscoplasticity. Loading/Unloading conditions and numerical algorithms. *Int. J. Num. Meth. Eng.* **26**, pp. 2161–2185.

Simo, J. C., Rifai, M. S. and Fox, D. D. (1990b). On a stress resultant geometrically exact shell model. Part IV: Variable thickness shells with through-the-thickness stretching. *Comput. Methods Appl. Mech. Eng.* **81**, pp. 91–126.

Simo, J. C., Rifai, M. S. and Fox, D. D. (1992). On a stress resultant geometrically exact shell model. Part VI: Conserving algorithms for non-linear dynamics. *Int. J. Num. Meth. Eng.* **34**, pp. 117–164.

Simo, J. C. and Taylor, R. L. (1986). A return mapping algorithm for plane stress elastoplasticity. *Int. J. Num. Meth. Eng.* **22**, pp. 649–670.

Smith, D. L. (ed.) (1990). *Mathematical Programming Methods in Structural Plasticity.* CISM Courses and Lectures No. 299. Springer-Verlag, Wien, New York.

Sonzogni, V. E. and Géradin, M. (1994). A hinge model with elastoplastic behaviour. *Eng. Comp.* **11**, pp. 227–256.

Toi, Y. and Isobe, D. (1996). Finite element analysis of quasi-static and dynamic collapse behaviors of framed structures by the adaptively shifted integration technique. *Computers and Structures* **58**(5), pp. 947–955.

Toi, Y. and Yang, H. J. (1991). Shifted integration technique and its applications to the finite element crush analysis of framed structures. *Naval Architecture and Ocean Eng.* **29**, pp. 113–127.

Tsuta, T., Okamoto, S. and Kobayashi, T. (1993). Collision and crash penetration analysis by the rigid plastic finite element method. In: Moan et al. (eds.), *Proc. Structural Dynamics – EURODYN93*, pp. 521–528. Balkema, Rotterdam.

Turgeman, S., Guessab, B. and Guessasma, M. (1998). Yield design theory: an efficient static method formulation. *Eur. J. Mech., A/Solids,* **17**(3), pp. 499–513.

Vasudevan, S., Okada, H. and Atluri, S. N. (1995). Development of new frame finite elements for aircraft crash analysis. In: S. N. Atluri, G. Yagawa and T. A. Cruse (eds.), *Computational Mechanics' 95. Theory and Applications. Proc. Int. Conf. on Comp. Eng. Science, July 30 – August 3, Hawaii, USA*, pp. 2189–2194 (Volume 2). Springer Verlag, Berlin, Heidelberg, New York.

Washizu, K. (1968). *Variational Methods in Elasticity and Plasticity.* Pergamon Press, Oxford.

Wierzbicki, T. and Abramowicz, W. (1983). On the crushing mechanics of thin-walled structures. *J. Appl. Mech.* **50**, pp. 727–734.

Wierzbicki, T. and Abramowicz, W. (1989). The mechanics of deep plastic collapse of thin-walled structures. In: T. Wierzbicki and N. Jones (eds.), *Structural Failure*, pp. 281–329. Wiley, New York.

Wierzbicki, T., Bhat, S. U., Abramowicz, W. and Brodkin, D. (1992). Alexander revisited – a two folding elements model of progressive crushing of tubes. *Int. J. Sol. Struct.* **29**(24), pp. 3269–3288.

Wierzbicki, T. and Huang, J. (1991). Initiation of plastic folding mechanisms in crushed box columns. *Thin-Walled Structures* **13**, pp. 115–143.

Wierzbicki, T., Recke, L., Abramowicz, W. and Gholami, T. (1994a). Stress profiles in thin-walled prismatic columns subjected to crush loading — I. Compression. *Computers and Structures* **51**(6), pp. 611–623.

Wierzbicki, T., Recke, L., Abramowicz, W., Gholami, T. and Huang, J. (1994b). Stress profiles in thin-walled prismatic columns subjected to crush loading — II. Bending. *Computers and Structures* **51**(6), pp. 625–641.

Willminger, S. (1999). Zur Analyse des Kollapsverhaltens axialgedrückter schaumgefüllter Profile. Heft ILFB – 2/99, Institute of Lightweight Structures and Aerospace Engineering, Vienna University of Technology, Vienna.

Wintschnig, S. (1996). Analytische, numerische und experimentelle Untersuchungen von Versagensmechanismen verschiedener Hohlprofile. Heft ILFB – 1/96, Institute of Lightweight Structures and Aerospace Engineering, Vienna University of Technology, Vienna.

Yang, W. H. (1993). Large deformation of structures by sequential limit analysis. *Int. J. Sol. Struct.* **30**(7), pp. 1001–1013.

Yu, H. S., Sloan, S. W. and Kleeman, P. W. (1994). A quadratic element for upper bound limit analysis. *Eng. Comp.* **11**, pp. 195–212.

Zaouk, A. K., Marzougui, D. and Kan, C. D. (1998). Development of detailed vehicle finite element model. Part II: material characterization and component testing. In: *Proc. Int. Crashworthiness Conf. IJCRASH'98, September 9–11, 1998, Dearborn, USA*, pp. 195–206. Woodhead Publ. Ltd., Cambridge, England.

Zhang, Y. G., Zhang, P. and Xue, W. M. (1994). Limit analysis considering initial constant loadings and proportional loadings. *Computational Mechanics* **14**, pp. 229–234.

Zhong, Z.-H. (1993). *Finite Element Procedures for Contact-Impact Problems.* Oxford University Press, Oxford, New York.

Zhou, J. L., Tits, A. L. and Lawrence, C. T. (1997). *User's Guide for FFSQP Version 3.7: A FORTRAN Code for Solving Constrained Nonlinear (Minimax) Optimization Problems, Generating Iterates Satisfying All Inequality and Linear Constraints.* Electrical Engineering Department and Institute for Systems Research, University of Maryland, College Park, MD 20742 (Systems Research Center TR-92-107r2).

Zouain, N., Herskovits, J., Borges, L. A. and Feijóo, R. A. (1993). An iterative algorithm for limit analysis with nonlinear yield functions. *Int. J. Sol. Struct.* **30**(10), pp. 1397–1417.

Zwoliński, J. (1995). Min-Max approach to shakedown and limit load analysis for elastic perfectly plastic and kinematic hardening materials. In: Z. Mróz et al. (eds.), *Inelastic behaviour of Structures under Variable Loads*, pp. 363–380. Kluwer Academic Publishers.

Curriculum Vitae

Name : Markus Seitzberger
Date of birth : December 1, 1965
Place of birth : Göstling/Ybbs, Austria
Citizenship : Austrian

Education

1980 – 1984	“Bundesoberstufenrealgymnasium”, Wiener Neustadt (A);
July 84 – Feb. 85	Compulsory military service;
1985 – 1992	Studies of mechanical engineering (specialization: automotive engineering) at the Vienna University of Technology (A). Diploma thesis: “FE-Analyse des instationären Temperaturfeldes beim Laserschweißen” (FE analysis of the transient temperature field during laser welding);
June 1992	Graduated with honours with the degree of Diplomingenieur;
since 1992	Doctoral student at the Institute of Lightweight Structures and Aerospace Engineering (ILFB), Vienna University of Technology (A).

Professional Development

Oct. 91 – Feb. 92	“Studienassistent” at the ILFB. Task: Implementation of an eigenvalue solver into a linear FE code;
Oct. 92 – Sept. 96	“Universitätsassistent” at the ILFB;
March 97 – Feb. 99	Research assistant within the research project “Crushing Simulation of Thin-Walled Structures”, sponsored by the Austrian “Fonds zur Förderung der wissenschaftlichen Forschung (FWF)”, at the ILFB;
since March 99	Research assistant at the ILFB. Field of work: project coordination and execution within the pilot phase for the “Austrian Aerospace Competence Network”.